Issue: 34
SCOPUS
UNIVERSIDAD POLITÉCNICA SALESIANA **ECUADOR**

pISSN: 1390-650X
eISSN: 1390-860X
july / december 2025

INGENIUS

Revista de Ciencia y Tecnología

34

INGENIUS

- Implementation of microservices in IoT projects with arduino

Pag. 9

- Effect of process variable on the mechanical and thermal behavior of a polypropylene composite reinforced with short bamboo fibers by hot compression

Pag. 20

- IoT and MQTT-based cardiovascular parameter monitoring system for medical alerts

Pag. 75

- Modeling of an electromagnetic cannon usind ATP-EMTP and ATPDRAW

Pag. 103

Indexed in: SCOPUS

Ingenius

Ingenius • Issue 34 • july-december 2025. Journal of Science and Tecnology of the Universidad Politécnica Salesiana of Ecuador. Publication dedicated to studies related to the Sciences of Mechanical Engineering, Electrical Engineering, Electronic Engineering, Mechatronic Engineering, Systems Engineering and Industrial Engineering.

Editors Board

Rafael Antonio Balart Gimeno, PhD, Universidad Politécnica de Valencia, España – Editor-in-chief.
John Ignacio Calle Siguencia, PhD, Universidad Politécnica Salesiana, Ecuador – Editor-in-chief.
Mariela Cerrada Lozada, PhD, Universidad Politécnica Salesiana, Ecuador – Associate Editor.
Teodiano Freire Bastos Filho, PhD, (Universidade Federal do Espírito Santo, Brasil – Associate Editor.
Marlon Xavier Quinde Abril, MSc, Universidad Politécnica Salesiana, Ecuador – Associate Editor.

Scientific board

Juan López Martínez, PhD, Universidad Politécnica de Valencia, España.

Elena Fortunati, PhD, Universidad de Perugia, Italia.

Gustavo Rovelo Ruiz, PhD, Hasselt University, Diepenbeek, Bélgica.

Franklin Gavilanez Alvarez, PhD, American University, Estados Unidos.

Piedad Gañan Rojo, PhD, Universidad Pontificia Bolivariana, Colombia.

José Alex Restrepo, PhD, Universidad Simón Bolívar, Venezuela.

Sergio Lujan Mora, PhD, Universidad de Alicante, España.

Martha Zequera Díaz, PhD, Pontificia Universidad Javeriana, Colombia.

Grover Zurita, PhD, Universidad Privada Boliviana, Bolivia.

Vladimir Robles, PhD, Universidad Politécnica Salesiana, Ecuador.

Germán Arévalo, PhD, Universidad Politécnica Salesiana, Ecuador.

Wilbert Aguilar, PhD, Universidad de las Fuerzas Armadas, ESPE, Ecuador.

Jack Bravo Torres, PhD, Universidad Politécnica Salesiana, Ecuador.

Walter Orozco, PhD, Universidad Politécnica Salesiana, Ecuador.

Mariela Cerrada, PhD, Universidad Politécnica Salesiana, Ecuador.

Julio César Viola, PhD, Universidad Politécnica Salesiana, Ecuador.

Sergio Gamboa Sánchez, PhD, Universidad Nacional Autónoma de México, México.

Roger Abdón Bustamante Plaza, PhD, Universidad de Chile, Chile.

Christian Blum, PhD, Consejo Superior de Investigaciones Científicas, España.

Silvia Noemi Schiaffino, PhD, Universidad Nacional del Centro de la Provincia de Buenos Aires, Argentina.

Analía Adriana Amandi, PhD, Universidad Nacional del Centro de la Provincia de Buenos Aires, Argentina.

Rubén de Jesús Medina Molina, PhD, Universidad de Los Andes, Venezuela.

Johnny Josué Bullón Torrealba, PhD, Universidad de Los Andes, Venezuela.

Rodrigo Palma Hillerns, PhD, Universidad de Chile, Chile.

Gerardo Espinoza Pérez, PhD, Universidad Nacional Autónoma de México, México.

Alexandre Mendes Abrão, PhD, Universidad Federal de Minas Gerais, Brasil.

Kamla Abdel Radi Ismail, PhD, Universidad Estatal de Campinas Unicamp, Brasil.

Arnaldo Da Silva, PhD, Universidad Estatal de Campinas Unicamp, Brasil.

Álvaro Rocha, PhD, Universidad de Coimbra, Portugal.

José Antenor Pomilio, PhD, Universidad Estatal de Campinas Unicamp, Brasil.

Luis Paulo Reis, PhD, Universidad de Minho, Portugal.

Luís Fernandes, PhD, Escuela Superior Náutica Infante d. Henrique, Portugal.

Aníbal Traça de Almeida, PhD, Universidad de Coimbra, Portugal.

Jorge Sá Silva, PhD, Universidad de Coimbra, Portugal.

Pedro Manuel Soares Moura, PhD, Universidad de Coimbra, Portugal.

Sérgio Manuel Rodrigues Lopes, PhD, Universidad de Coimbra, Portugal.

Ricardo Madeira Soares Branco, PhD, Universidad de Coimbra, Portugal.

Carlos Alexandre Bento Capela, PhD, Universidad de Coimbra, Portugal.

Filipe Araujo, PhD, Universidad de Coimbra, Portugal.

Luis Manuel Guerra Silva Rosa, PhD, Universidad de Lisboa, Portugal.

Hélder de Jesus Fernandes, Puga, PhD, Universidad de Minho, Portugal.

Filipe Samuel, Pereira da Silva, PhD, Universidad de Minho, Portugal.

César Sequeira, PhD, Universidad de Lisboa, Portugal.

José Teixeira Estêvão Ferreira, PhD, Universidad de Coimbra, Portugal.

Nuno Laranjeiro, PhD, Universidad de Coimbra, Portugal.

Luís Amaral, PhD, Universidad de Lisboa, Portugal.

Jorge Henriques, PhD, Universidad de Coimbra, Portugal.

William Ipanaque, PhD, Universidad de Piura, Perú.

Lorenzo Leija Salas, PhD, Centro de Investigación y Estudios Avanzados del Instituto Politécnico Nacional, México.

Valeri Kontorovich Mazover, PhD, Centro de Investigación y de Estudios Avanzados del Instituto Politécnico Nacional, México.

Alejandro Ávila García, PhD, Centro de Investigación y de Estudios Avanzados del Instituto Politécnico Nacional, México.

Paolo Bellavista, PhD, Universidad de Bologna, Italia.

Carlos Rubio, PhD, Centro de Ingeniería y Desarrollo Industrial, México.

Fernando Hernández Sánchez, PhD, Centro de Investigación Científica de Yucatán, México.

Emilio Muñoz Sandoval, PhD, Instituto Potosino de Investigación Científica y Tecnológica, México.

Yasuhiro Matsumoto Kuwabara, PhD, Centro de Investigación y de Estudios Avanzados del Instituto Politécnico Nacional, México.

David Zumoffen, PhD, Centro Internacional Franco Argentino de Ciencias de la Información y de Sistemas, Argentina.

Vicente Rodríguez González, PhD, Instituto Potosino de Investigación Científica y Tecnológica, México.

Alejandro Rodríguez Ángeles, PhD, Centro de Investigación y de Estudios Avanzados del Instituto Politécnico Nacional, México.

Alistair Borthwick, PhD, Universidad de Edimburgo, Reino Unido.

Copyright. Ingenius 2025, Universidad Politécnica Salesiana. The total or partial reproduction of this journal is allowed, citing the source.

Reviewers board

Federico Dominguez, PhD, Escuela Superior Politécnica del Litoral, Ecuador.

Enrique Carrera, PhD, Universidad de las Fuerzas Armadas, ESPE, Ecuador.

Andrés Tello, MSc, Universidad de Cuenca, Ecuador.

Cristian García Bauza, PhD, Universidad Nacional del Centro de la Provincia de Buenos Aires, Argentina.

Osvaldo Añó, PhD, Universidad Nacional de San Juan, Argentina.

Thalía San Antonio, PhD, Universidad Técnica de Ambato, Ecuador.

Victor Saquicela, PhD, Universidad de Cuenca, Ecuador.

Gonzalo Olmedo, PhD, Universidad de las Fuerzas Armadas, ESPE, Ecuador.

Román Lara, PhD, Universidad de las Fuerzas Armadas, ESPE, Ecuador.

Guillermo Soriano, PhD, Escuela Superior Politécnica del Litoral, Ecuador.

María Fernanda Granda, PhD, Universidad de Cuenca, Ecuador.

Ricardo Cayssials, PhD, Universidad Tecnológica Nacional, Argentina.

Leonardo Solaque Guzman, PhD, Universidad Militar Nueva Granada, Colombia.

José Di Paolo, PhD, Universidad Nacional de Entre Ríos, Argentina.

Astrid Rubiano Fonseca, PhD, Universidad Militar Nueva Granada, Colombia.

Robinson Jiménez, PhD, Universidad Militar Nueva Granada, Colombia.

Alfonso Zozaya, PhD, Universidad de Carabobo, Venezuela.

Mauricio Mauledoux, PhD, Universidad Militar Nueva Granada, Colombia.

Luis Medina, PhD, Universidad Simón Bolivar, Venezuela.

Ernesto Cuadros-Vargas, PhD, Universidad Católica San Pablo, Perú.

Samuel Sepúlveda Cuevas, PhD, Universidad de la Frontera, Chile.

Carlos Cares, PhD, Universidad de la Frontera, Chile.

Rafael Sotelo, PhD, Universidad de Montevideo, Uruguay.

Omar Lopez, PhD, Universidad de Los Andes, Colombia.

Job Flores-Godoy, PhD, Universidad Católica del Uruguay, Uruguay.

Luis Mario Mateus, PhD, Universidad de los Andes, Colombia.

Amadeo Argüelles Cruz, PhD, Instituto Politécnico Nacional, México.

Santiago Bentancourt Parra, PhD, Universidad Pontificia Bolivariana, Colombia.

Germán Zapata, PhD, Universidad Nacional de Colombia, Colombia.

Pedro García, PhD, Universidad Autónoma de Barcelona, España.

Arturo Conde Enríquez, PhD, Universidad Autónoma de Nuevo León, México.

Alberto Cavazos González, PhD, Universidad Autónoma de Nuevo León, México.

Ernesto Vázquez Martínez, PhD, Universidad Autónoma de Nuevo León, México.

Miguel Díaz Rodriguez, PhD, Universidad de Los Andes, Venezuela.

Efraín Alcorta García, PhD, Universidad Autónoma de Nuevo León, México.

Luis Chirinos Garcia, PhD, Pontificia Universidad Católica de Perú, Perú.

Oscar Avilés, PhD, Universidad Militar Nueva Granada, Colombia.

Dora Martínez Delgado, PhD, Universidad Autónoma de Nuevo León, México.

David Ojeda, PhD, Universidad Técnica del Norte, Ecuador.

Irene Beatríz Steinmann, PhD, Universidad Tecnológica Nacional, Argentina.

Mario Serrano, Universidad Nacional de San Juan, Argentina.

Cornelio Posadas Castillo, PhD, Universidad Autónoma Nuevo León, México.

Mario Alberto Rios Mesias, PhD, Universidad de Los Andes, Colombia.

Yudith Cardinale Villarreal, PhD, Universidad Simón Bolivar, Venezuela.

Jose Eduardo Ochoa Luna, PhD, Universidad Católica San Pablo, Perú.

Dante Angel Elias Giordano, PhD, Pontificia Universidad Católica de Perú, Perú.

Manuel Pelaez Samaniego, PhD, Universidad de Cuenca, Ecuador.

Juan Espinoza Abad, PhD, Universidad de Cuenca, Ecuador.

Pietro Codara, PhD, Universidad de Milan, Italia.

Alberto Soria, PhD, Centro de Investigación y de Estudios Avanzados del Instituto Politécnico Nacional, México.

José M. Aller, PhD, Universidad Politécnica Salesiana, Ecuador.

Ferney Amaya F., PhD, Universidad Pontificia Bolivariana, Medellin, Colombia.

Santiago Arango Aramburo, PhD, Universidad Nacional de Colombia, Colombia.

Diego Arcos–Avilés, PhD, Universidad de las Fuerzas Armadas, ESPE, Ecuador.

Pablo Arevalo, PhD, Universidad Politécnica Salesiana, Ecuador.

Roberto Beltran, MSc, Universidad de las Fuerzas Armadas, ESPE, Ecuador.

Leonardo Betancur, PhD, Universidad Pontificia Bolivariana, Medellin, Colombia.

Roberto Gamboa, PhD, Universidad de Lisboa, Portugal.

Paulo Lopes dos Santos, PhD, Universidad do Porto, Portugal.

Pedro André Dias Prates, PhD, Universidad de Coimbra, Portugal.

José Manuel Torres Farinha, PhD, Universidad de Coimbra, Portugal.

Celso de Almeida, PhD, Universidad Estatal de Campinas Unicamp, Brasil.

Ramon Molina Valle, PhD, Universidad Federal de Minas Gerais, Brasil.

Cristina Nader Vasconcelos, PhD, Universidad Federal Fluminense, Brasil.

João M. Ferreira Calado, PhD, Universidad de Lisboa, Portugal.

Guilherme Luz Tortorella, PhD, Universidad Federal de Santa Catarina, Brasil.

Mauro E. Benedet, PhD, Universidad Federal de Santa Catarina, Brasil.

Artemis Marti Ceschin, PhD, Universidade de Brasilia, Brasil.

Gilmar Barreto, PhD, Universidad Estatal de Campinas Unicamp, Brasil.

Ricardo Emilio F. Quevedo Nogueira, PhD, Universidad Federal de Ceará, Brasil.

Weslley Luiz da Silva Assis, PhD, Universidad Federal Fluminense, Brasil.

Ana P. Martinazzo, PhD, Universidad Federal Fluminense, Brasil.

Jorge Bernardino, PhD, Universidad de Coimbra, Portugal.

Luis Geraldo Pedroso Meloni, PhD, Universidad Estatal de Campinas Unicamp, Brasil.

Facundo Almeraya Calderón, PhD, Universidad Autónoma de Nuevo León, México.

Freddy Villao Quezada, PhD, Escuela Superior Politécnica del Litoral, Ecuador.

Jose Manrique Silupu, MSc, Universidad de Piura, Perú.

Germán Ariel Salazar, PhD, Instituto de Investigaciones en Energía no Convencional, Argentina.

José Mahomar Jananías, PhD, Universidad del BIOBIO, Chile.

Arnaldo Jélvez Caamaño, PhD, Universidad del BIOBIO, Chile.

Jorge Andrés Uribe, MSc, Centro de Ingeniería y Desarrollo Industrial, México.

Ricardo Beltran, PhD, Centro de Investigación en Materiales Avanzados, México.

Adi Corrales, MSc, Centro de Ingeniería y Desarrollo Industrial, México.

Jorge Uribe Calderón, PhD, Centro de Investigación Científica de Yucatán, México

José Trinidad Holguín Momaca, MSc, Centro de Investigación en Materiales Avanzados, México.

Juan Manuel Alvarado Orozco, PhD, Centro de Ingeniería y Desarrollo Industrial, México.

Arnaldo Jélvez Caamaño, PhD, Universidad del BIOBIO, Chile.

Javier Murillo, PhD, Centro Internacional Franco Argentino de Ciencias de la Información y de Sistemas, Argentina.

Lucas Daniel Terissi, PhD, Universidad Nacional de Rosario, Argentina.

Rene Vinicio Sanchez Loja, MSc, Universidad Politécnica Salesiana, Ecuador.

Freddy Leonardo Bueno Palomeque, MSc, Universidad Politécnica Salesiana, Ecuador.

Diego Cabrera Mendieta, MSc, Universidad Politécnica Salesiana, Ecuador.

Edwuin Jesus Carrasquero, PhD, Universidad Técnica de Machala, Ecuador.

Carlos Mauricio Carrillo Rosero, MSc, Universidad Técnica de Ambato, Ecuador.

Diego Carrion Galarza, MSc, Universidad Politécnica Salesiana, Ecuador.

Carmen Celi Sanchez, MSc, Universidad Politécnica Salesiana, Ecuador.

Diego Chacon Troya, MSc, Universidad Politécnica Salesiana, Ecuador.

Paul Chasi, MSc, Universidad Politécnica Salesiana, Ecuador.

Juan Chica, MSc, Universidad Politécnica Salesiana, Ecuador.

Diego Marcelo Cordero Guzmán, MSc, Universidad Católica de Cuenca, Ecuador.

Luis Javier Cruz, PhD, Universidad Pontificia Bolivariana, Medellin, Colombia.

Fabricio Esteban Espinoza Molina, MSc, Universidad Politécnica Salesiana, Ecuador.

Jorge Fajardo Seminario, MSc, Universidad Politécnica Salesiana, Ecuador.

Patricia Fernandez Morales, PhD, Universidad Pontificia Bolivariana, Medellin, Colombia.

Marcelo Flores Vazquez, MSc, Universidad Politécnica Salesiana, Ecuador.

Carlos Flores Vázquez, MSc, Universidad Católica de Cuenca, Ecuador.

Carlos Franco Cardona, PhD, Universidad Nacional de Colombia, Colombia.

Cristian García García, MSc, Universidad Politécnica Salesiana, Ecuador.

Teonila García Zapata, PhD, Universidad Nacional Mayor de San Marcos, Perú.

Luis Garzón Mñoz, PhD, Universidad Politécnica Salesiana, Ecuador.

Natalia Gonzalez Alvarez, MSc, Universidad Politécnica Salesiana, Ecuador.

Ernesto Granado, PhD, Universidad Simón Bolívar, Venezuela.

Adriana del Pilar Guaman, MSc, Universidad Politécnica Salesiana, Ecuador.

Juan Inga Ortega, MSc, Universidad Politécnica Salesiana, Ecuador.

Esteban Inga Ortega, PhD, Universidad Politécnica Salesiana, Ecuador.

Paola Ingavélez, MSc, Universidad Politécnica Salesiana, Ecuador.

Cesar Isaza Roldan, PhD, Universidad Pontificia Bolivariana.

Nelson Jara Cobos, MSc, Universidad Politécnica Salesiana, Ecuador.

Ruben Jerves, MSc, Universidad Politécnica Salesiana, Ecuador.

Victor Ramon Leal, PhD, Investigador de PDVSA, Venezuela

Gabriel Leon, MSc, Universidad Politécnica Salesiana, Ecuador.

Edilberto Llanes, PhD, Universidad Internacional SEK, Ecuador.

Luis López, MSc, Universidad Politécnica Salesiana, Ecuador.

Carlos Mafla Yépez, MSc, Universidad Técnica del Norte, Ecuador.

Hader Martínez, PhD, Universidad Pontificia Bolivariana, Medellin, Colombia

Javier Martínez, PhD, Instituto Nacional de Eficiencia Energética y Energías Renovables, Ecuador.

Alex Mayorga, MSc, Universidad Técnica de Ambato, Ecuador.

Jimmy Molina, MSc, Universidad Técnica de Machala, Ecuador.

Andres Montero, PhD, Universidad de Cuenca, Ecuador.

Vicente Morales, MSc, Universidad Tecnica de Ambato, Ecuador.

Fabián Morales, MSc, Universidad Técnica de Ambato, Ecuador.

Diego Morales, MSc, Ministerio de Electricidad y Energías Renovables del Ecuador.

Yoandrys Morales Tamayo, PhD, Universidad Técnica de Cotopaxi, Cotopaxi

Olena Leonidivna Naidiuk, MSc, Universidad Politécnica Salesiana, Ecuador.

Oscar Naranjo, MSc, Universidad del Azuay, Ecuador.

Paul Narvaez, MSc, Universidad Politécnica Salesiana, Ecuador.

Hernán Navas Olmedo, MSc, Universidad Técnica de Cotopaxi, Ecuador.

Cesar Nieto, PhD, Universidad Pontificia Bolivariana, Medellin, Colombia

Fabio Obando, MSc, Universidad Politécnica Salesiana, Ecuador.

Luis Ortiz Fernandez, MSc, Universidade Federal de Rio Grande del Norte, Brasil

Pablo Parra, MSc, Universidad Politécnica Salesiana, Ecuador.

Paulo Peña Toro, PhD, Ministerio de Productividad, Ecuador.

Patsy Prieto Velez, MSc, Universidad Politécnica Salesiana, Ecuador.

Diego Quinde Falconi, MSc, Universidad Politécnica Salesiana, Ecuador.

Diana Quintana Espinoza, MSc, Universidad Politécnica Salesiana, Ecuador.

William Quitiaquez Sarzosa, MSc, Universidad Politécnica Salesiana, Ecuador.

Flavio Quizhpi Palomeque, MSc, Universidad Politécnica Salesiana, Ecuador.

Washington Ramirez Montalvan, MSc, Universidad Politécnica Salesiana, Ecuador.

Fran Reinoso Avecillas, MSc, Universidad Politécnica Salesiana, Ecuador.

Néstor Rivera Campoverde, MSc, Universidad Politécnica Salesiana, Ecuador.

Jorge Romero Contreras, MSc, Universidad de Carabobo, Venezuela

Fabian Saenz Enderica, MSc, Universidad de las Fuerzas Armadas, ESPE, Ecuador.

Luisa Salazar Gil, PhD, Universidad Simón Bolivar, Venezuela

Gustavo Salgado Enríquez, Msc, Universidad Central del Ecuador., Ecuador.

Juan Carlos Santillán Lima, MSc, Universidad Nacional de Chimborazo

Jonnathan Santos Benítez, MSc, Universidad Politécnica Salesiana, Ecuador.

Andrés Sarmiento Cajamarca, MSc, Universidad Federal de Santa Catarina, Brasil

Luis Serpa Andrade, MSc, Universidad Politécnica Salesiana, Ecuador.

Cristian Timbi Sisalima, MSc, Universidad Politécnica Salesiana, Ecuador.

Milton Tipan Simbaña, MSc, Universidad Politécnica Salesiana, Ecuador.

Paul Torres Jara, MSc, Universidad Politécnica Salesiana, Ecuador.

Rodrigo Tufiño Cárdenas, MSc, Universidad Politécnica Salesiana, Ecuador.

Fernando Urgiles Ortíz, MSc, Universidad Politécnica Salesiana, Ecuador.

Juan Valladolid Quitoisaca, MSc, Universidad Politécnica Salesiana, Ecuador.

Efrén Vázquez Silva, PhD, Universidad Politécnica Salesiana, Ecuador.

Julio Verdugo, MSc, Universidad Politécnica Salesiana, Ecuador.

Mary Vergara Paredes, PhD, Universidad de los Andes, Merida, Venezuela

Jennifer Yepez Alulema, MSc, Universidad Politécnica Salesiana, Ecuador.

Julio Zambrano Abad, MSc, Universidad Politécnica Salesiana, Ecuador.

Patricia Zapata Molina, MSc, Universidad Politécnica Salesiana, Ecuador.

Publications board

General Editor

Technical board

Publications Service

Editorial

Editorial Abya Yala (Quito-Ecuador),
Av. 12 de octubre N422 y Wilson,
Bloque A, UPS Quito, Ecuador.
Casilla 17-12-719 Teléfonos: (593-2) 3962800 ext. 2638
email: editorial@abyayala.org

Printing: 800 copies

Typographic system used in the composition of this document LaTeX.

Ingenius

Revista de Ciencia y Tecnologia

Issue 34

july – december 2025

ISSN impreso 1390-650X / ISSN electrónico 1390-860X

The administration of the journal is done through the following parameters:

The journal uses the academic anti-plagiarism system

The articles have an identification code (Digital Object Identifier)

The editorial process is managed through the Open Journal System

The articles of the present edition can be consulted in
http://revistas.ups.edu.ec/index.php/ingenius

Universidad Politécnica Salesiana del Ecuador

INGENIUS Journal, is indexed in the following Databases and scientific information systems:

SELECTIVE DATABASES

Scopus

Emerging Sources Citation Index

Google scholar

SciELO Ecuador

BASE

EBSCOhost Fuente Académica Plus

SIS Scientific Indexing Services

EuroPub

REVIEWS EVALUATION PLATFORMS

MIAR

Quality Open Access Market

I2OR

SELECTIVE DIRECTORIES

latindex

Journal Seeker Research Bible

AcademicKeys

Science Library Index

ULRICHSWEB™ GLOBAL SERIALS DIRECTORY

SELECTIVE SERIAL LIBRARY

redalyc.org

REDIB Red Iberoamericana de Innovación y Conocimiento Científico

refseek

SCIENTIFIC LITERATURE SEARCHERS OPEN ACCESS

DOAJ DIRECTORY OF OPEN ACCESS JOURNALS

EXALEAD

WorldWideScience.org

Journals for Free

OTHER BIBLIOGRAPHICAL DATABASES

Dialnet

JournalTOCs

PKP|INDEX

CATALOG OF INTERNATIONAL UNIVERSITY LIBRARIES

UNIVERSITÄT PASSAU
Fakultät für Informatik und Mathematik

BSB Bayerische StaatsBibliothek
Information in erster Linie

Deutsches Museum

Hochschule Rosenheim
University of Applied Sciences

HOCHSCHULE LANDSHUT
HOCHSCHULE FÜR ANGEWANDTE WISSENSCHAFTEN

HOCHSCHULE
FÜR ANGEWANDTE
WISSENSCHAFTEN
MÜNCHEN

HOCHSCHULE
WEIHENSTEPHAN-TRIESDORF
UNIVERSITY OF APPLIED SCIENCES

TUM
Technische Universität München

Universität der Bundeswehr München

LMU
LUDWIG-MAXIMILIANS-UNIVERSITÄT MÜNCHEN

Technische Hochschule Ingolstadt

Hochschule Augsburg
University of Applied Sciences

Hochschule Kempten
University of Applied Sciences

HNU
HOCHSCHULE NEU-ULM
UNIVERSITY
OF APPLIED SCIENCES

OTH
OSTBAYERISCHE
TECHNISCHE HOCHSCHULE
REGENSBURG

Ostbayerische Technische Hochschule
Amberg-Weiden

Staatliche Bibliothek
Neuburg an der Donau

sbr
Staatliche Bibliothek
Regensburg

Staats- und
Stadtbibliothek
Augsburg

GEORG-SIMON-OHM
HOCHSCHULE NÜRNBERG

Universitätsbibliothek Augsburg
UBA

KATHOLISCHE UNIVERSITÄT
EICHSTÄTT-INGOLSTADT

UR
Universität
Regensburg

HOCHSCHULE
ANSBACH

COBURG UNIVERSITY
of applied sciences and arts

hochschule
hof
University of Applied Sciences

HOCHSCHULE
MERSEBURG (FH)
University of Applied Sciences

ThULB
THÜRINGER UNIVERSITÄTS- UND
LANDESBIBLIOTHEK JENA

EZB
Elektronische
Zeitschriftenbibliothek

UNIVERSITY OF BAMBERG
OTTO-FRIEDRICH-UNIVERSITÄT BAMBERG

UNIVERSITÄT BAMBERG

UNIVERSITÄT
BAYREUTH

FAU
FRIEDRICH-ALEXANDER
UNIVERSITÄT
ERLANGEN-NÜRNBERG

Bauhaus-
Universität
Weimar

UB
WÜ

Freie Universität Berlin

FHE
FACHHOCHSCHULE
ERFURT UNIVERSITY
OF APPLIED SCIENCES

h2
Hochschule
Magdeburg • Stendal

htw
Hochschule für Technik
und Wirtschaft Berlin
University of Applied Sciences

UB
Braunschweig

STIFTUNG
TIERÄRZTLICHE HOCHSCHULE HANNOVER
1778

GOTTFRIED WILHELM LEIBNIZ BIBLIOTHEK
NIEDERSÄCHSISCHE LANDESBIBLIOTHEK

EDITORIAL

Dear readers,

Issue 34 of our scientific journal reaffirms our commitment to fostering innovative, collaborative, and multidisciplinary knowledge in science and technology. This edition stands out for the diversity of its contributions, which tackle contemporary issues from multiple perspectives and disciplines, reflecting the dynamism and breadth of current scientific thinking.

A defining element of this issue is the clear interdisciplinary nature of the articles. From implementing microservices in IoT systems using Arduino, to exploring deep generative models for medical data enhancement, including studies on composite materials, cardiovascular monitoring systems, renewable energy, and electric mobility analysis—each research effort provides solutions from technical, environmental, biomedical, and social perspectives.

The geographic diversity of the authors further enriches this volume. Researchers from Mexico, Colombia, Ecuador, Peru, Uruguay, Spain, Chile, India, and Canada converge in a scientific synergy that transcends borders, fostering the exchange of experiences, methodologies, and knowledge. This international scope not only enhances the quality of the studies, but also illustrates the growing importance of global networks in scientific production.

In terms of themes, there is a strong focus on sustainability, technological innovation, and health, all highly relevant in today's global context. The analysis of biodiesel use in diesel vehicles, intelligent charging management for electric vehicles, and the development of hydroelectric power in Africa exemplify how research can actively contribute to the Sustainable Development Goals (SDGs). Meanwhile, medical applications of IoT and advanced modeling of electromagnetic and robotic systems highlight the role of engineering as a bridge between science and human well-being.

We invite our readers to explore this issue with a critical and collaborative mindset, confident that they will find inspiration, scientific rigor, and a broad vision of the challenges facing our society.

John Calle-Siguencia, PhD
Editor in Chief

Table of contents

Scientific Paper / Artículo Científico

UNIVERSIDAD POLITÉCNICA SALESIANA ECUADOR
INGENIUS
Revista de Ciencia y Tecnología
https://doi.org/10.17163/ings.n34.2025.01
pISSN: 1390-650X / eISSN: 1390-860X

IMPLEMENTATION OF MICROSERVICES IN IOT PROJECTS WITH ARDUINO

IMPLEMENTACIÓN DE MICROSERVICIOS EN PROYECTOS DE IOT CON ARDUINO

Marco Antonio Celis Crisóstomo[1,*], Francisco Miguel Hernández López[1], Jorge Alberto Cárdenas Magaña[1], Emmanuel Vega Negrete[1]

Received: 14-08-2024, Received after review: 14-01-2025, Accepted: 12-03-2025, Published: 01-07-2025

Abstract

This article focuses on the implementation of a system to send and receive data using an Arduino MEGA and an Ethernet Shield, with an emphasis on communication with a microservices-based API. The relevance of this study lies in the growing demand for accessible technological solutions for automation and education, allowing the integration of low-cost systems with modern data management tools. The objective is to provide a detailed description of the components and configurations required to establish this communication, offering practical examples of the most common HTTP services: GET, POST, PUT, and DELETE. For the creation of the microservices, a MAMP server is used, and PHP is programmed using the Slim Framework. A comprehensive explanation is provided on how to implement each of these methods in Arduino projects, accompanied by code examples and practical demonstrations that facilitate understanding and application in various contexts. The results obtained demonstrate the viability of this technology in educational and automation projects, highlighting the effectiveness of combining Arduino with microservices for real-time data management. In conclusion, the combination of Arduino and microservices presents itself as an effective and adaptable solution for implementing technological projects in educational and automation contexts, offering a robust and efficient alternative for data handling.

Keywords: Arduino, Microservices, Automation, Communication, Data, Programming

Resumen

Este artículo aborda la implementación de un sistema para el envío y recepción de datos mediante un Arduino MEGA y un Ethernet Shield, con énfasis en la comunicación con una API basada en microservicios. La relevancia de este estudio se encuentra en la creciente demanda de soluciones tecnológicas accesibles para la automatización y la educación, lo que permite la integración de sistemas de bajo costo con herramientas modernas de gestión de datos. El objetivo principal es describir detalladamente los componentes y configuraciones necesarias para establecer esta comunicación, proporcionando ejemplos prácticos de los servicios HTTP más comunes: GET, POST, PUT y DELETE. Para la creación de los microservicios, se utiliza un servidor MAMP y se programa en PHP junto con el microframework Slim. Se detalla la implementación de cada uno de estos métodos en proyectos con Arduino, incluyendo ejemplos de código y demostraciones prácticas que facilitan su comprensión y aplicación en diversos contextos. Los resultados obtenidos evidencian la viabilidad de esta tecnología en proyectos educativos y de automatización, destacando la eficacia de combinar Arduino con microservicios para la gestión de datos en tiempo real. En conclusión, la combinación de Arduino y microservicios se presenta como una solución eficaz y adaptable para el desarrollo de proyectos tecnológicos en contextos educativos y de automatización, proporcionando una alternativa robusta y eficiente para la gestión de datos.

Palabras clave: Arduino, microservicios, automatización, comunicación, datos, programación

---

[1,*] Instituto Tecnológico José Mario Molina Pasquel y Henríquez Unidad Académica Tamazula, México.
Corresponding author ✉: marco.celis@tamazula.tecmm.edu.mx.

Suggested citation: M. A. Celis Crisóstomo, F. M. Hernández López, J. A. Cárdenas Magaña, and E. Vega Negrete, "Implementation of microservices in IoT projects with arduino," *Ingenius, Revista de Ciencia y Tecnología*, N.° 34, pp. 9-19, 2025, DOI: https://doi.org/10.17163/ings.n34.2025.01.

1. Introduction

The Internet of Things (IoT) has experienced remarkable growth in recent years, becoming an integral component across various sectors, including smart agriculture and home automation. This technological paradigm enables formerly isolated devices to interconnect, facilitating real-time data exchange to enhance process optimization and operational efficiency in various applications. In the agricultural domain, for example, IoT-enabled sensors continuously monitor critical environmental parameters such as soil moisture and temperature, thereby enabling data-driven decisions to improve the precision of irrigation and fertilization strategies [1]. Similarly, in smart home environments, the integration of devices such as thermostats, security cameras, and intelligent lighting systems has contributed to increased energy efficiency and enhanced security [2].

Despite the widespread adoption of Internet of Things (IoT) technologies, their effective implementation continues to pose significant challenges, particularly in terms of connectivity and data management [3]. IoT devices encompass a broad spectrum of complexity, ranging from simple sensors to advanced control systems, each demanding a comprehensive understanding of the hardware components and software configurations necessary to ensure reliable and sustained operation. Moreover, seamless communication between these devices and the servers responsible for data processing and storage constitutes a critical requirement for the successful deployment of any IoT system [4, 5].

This study presents the practical implementation of an Internet of Things (IoT) system employing an Arduino MEGA microcontroller in conjunction with an Ethernet Shield, with the objective of facilitating seamless communication between sensors and a web server. A microservices-based API is developed to incorporate standard HTTP methods GET, POST, PUT, and DELETE thereby facilitating bidirectional data exchange. This API allows devices, such as the soil moisture sensors used in this work, to transmit and receive data efficiently, supporting real-time monitoring and control [6].

The selection of the HTTP protocol for communication between the Arduino platform and the web server is justified by its widespread adoption and seamless integration in web-based applications. HTTP not only facilitates interoperability among heterogeneous devices and systems but also supports standardization in data transmission. This is particularly advantageous in the context of the Internet of Things (IoT), where ensuring that data is both accessible and manipulable across diverse applications and platforms is essential [7].

In this project, HTTP services were implemented to carry out CRUD operations create, read, update, and delete on data, utilizing a MAMP server and PHP programming within the Slim framework [8]. This architecture not only establishes a clear and organized structure for data management but also offers scalability and flexibility, which are critical requirements in Internet of Things (IoT) applications [9].

The primary objective of this study is to provide a practical guide for individuals seeking to implement Internet of Things (IoT) communication systems using microservice architectures. It presents a comprehensive overview of the required hardware and software configurations, the development of microservices, and their integration with an Arduino-based platform [10]. Furthermore, the study includes practical examples and demonstrations that illustrate the real-time management of sensor-acquired data, an aspect particularly relevant in educational and automation-focused applications [11].

The implementation demonstrates the feasibility of employing microservices in Internet of Things (IoT) projects, emphasizing the effectiveness of integrating Arduino with a microservices architecture for real-time data management [12]. This technological approach is applicable not only in educational settings but also holds significant potential for industrial and commercial environments, where the efficient management of large volumes of data is essential [13].

In summary, this article presents a comprehensive overview of the implementation of microservices in Internet of Things (IoT) projects, combining both theoretical foundations and practical guidance for successful deployment. This approach enhances the existing body of knowledge in the IoT domain by offering an accessible and efficient solution for real-time data management, one that is both adaptable and scalable to meet the specific requirements of diverse applications [14].

2. Materials and methods

This study presents a formal investigation centered on the programming and implementation of software for Internet of Things (IoT) applications. The methodology adopted is outlined in the following sections:

2.1. Project architecture

To enable communication between the Arduino microcontroller and a web server, a system architecture was designed with a focus on data transmission using the HTTP protocol. This protocol, widely recognized for its reliability in web applications, was employed to perform CRUD operations create, read, update, and delete data. These operations were implemented on a server using PHP Slim, a microframework that streamlines the development of web applications and RESTful APIs. PHP Slim was chosen for its efficiency and scalability in handling HTTP requests.

Figure 1 illustrates the key components of the project: the circuit design and the web server configuration. The circuit integrates the Arduino microcontroller with a set of sensors that collect environmental data, including temperature, humidity, and soil moisture parameters essential for environmental monitoring and analysis. The server configuration involves the implementation of microservices responsible for handling HTTP requests sent from the Arduino. These microservices process the incoming data, store it in a database, and manage requests for data retrieval, updates, and deletion, thereby ensuring efficient and reliable data management.

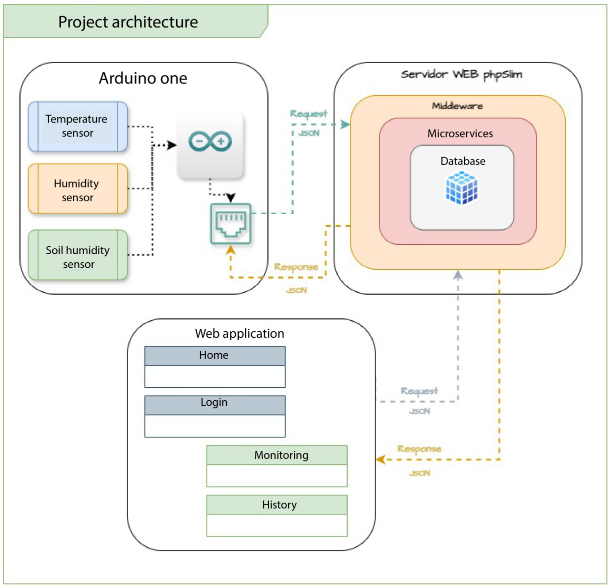

Figure 1. General architecture

Communication within the system is established through the HTTP protocol, which serves as a foundational standard for data exchange over the web. Specific HTTP methods are employed to manage data operations: POST is used to create new records, PUT/-PATCH to update existing entries, GET to retrieve data, and DELETE to remove records. Each method fulfills a distinct role in the data management process, ensuring that information is transmitted and processed securely and efficiently. This architecture enables seamless interaction between the Arduino and the server, facilitating accurate and reliable handling of transmitted and received data.

2.2. Implemented circuit diagram

The construction of the circuit and the configuration of the server were essential stages in the system's implementation. The proper integration of the sensors with the Arduino microcontroller, along with the programming of HTTP requests using PHP Slim, was critical to ensuring reliable system functionality. Figure 2 presents a visual representation of the component connections and the server setup for handling incoming requests. This configuration enabled structured and efficient communication between the Arduino and the server, allowing for precise control and management of the data collected by the sensors.

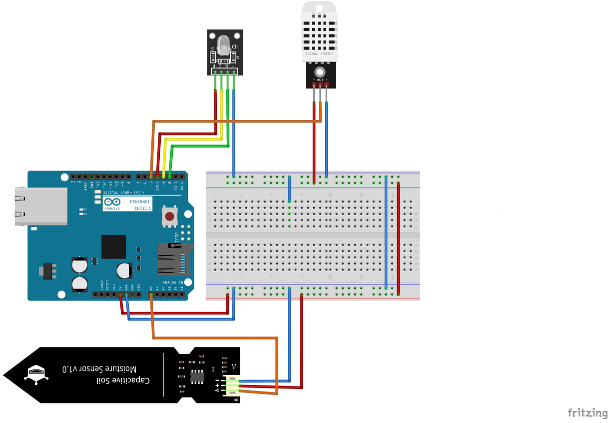

Figure 2. Implemented circuit

2.3. Database design

To store the collected data, a sequential database was implemented to handle requests from lightweight clients, such as the Arduino, web clients, or mobile applications, depending on the operations performed on the database records. This database played a crucial role in maintaining an organized and efficient record of the information transmitted by the Arduino.

Figure 3 highlights the management of the AntEmisoras table, which stores the location of the Arduino device responsible for generating the data transmitted to the server. These data are linked to another table, SenDatos, which records sensor information corresponding to the associated transmitting antenna. This structured approach to data organization facilitates efficient access and management, enabling more precise control of the information generated by each antenna. Moreover, it ensures that each dataset is clearly associated with its origin, thereby improving traceability and supporting subsequent data analysis.

The implementation of a sequential database not only ensures efficient data organization but also enhances overall system performance by managing requests from multiple clients. This architecture enables the reliable execution of CRUD operations, ensuring that information remains consistently updated and accessible. Furthermore, by integrating the database with various client platforms, the system achieves a high degree of flexibility, allowing both web and mobile applications to interact with the data in a consistent and synchronized manner.

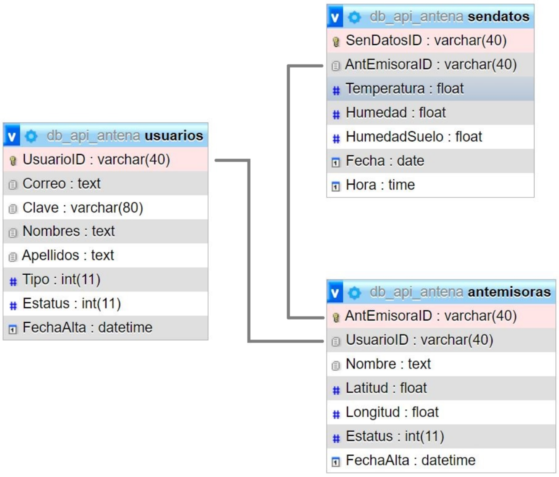

Figure 3. Database structure

2.4. Microservices developed

Four types of services were implemented to enable the Arduino to issue various HTTP requests. Additionally, middleware was integrated to accept requests with the Content-Type: application/json header. The tables below present the correct invocation methods for each of the microservices developed in the project.

Table 1. GET microservice for antenna status retrieval

Method	GET
Endpoint	/ v1/webadmin/antemisoras/arduino/
Request	None
Response	{json "Estatus": bool, "Codigo": int, "EstAntEmisora": int}
Args	ID (in URL)
Description	Retrieves the status of the antenna to determine whether it is in one of the following states: 0 installing, 1 operating, 2 maintenance, 3 relocating, or 4 deleted.

Table 2. POST microservice for sensor data submission

Method	POST
Endpoint	/v1/webadmin/sendatos
Request	json {" AEID ": UUID, "Tem": float, "Hum": float, “HumSuelo”: float}
Response	json {"Estatus":bool, "Codigo":int, "Data":textt}
Args	None
Description	Transmits the data generated by each sensor.

Table 3. PUT microservice for device location update

Method	PUT
Endpoint	/v1/webadmin/antemisoras/ubicacion
Request	json {"AEID ": UUID, "Lat": float, "Log": float}
Response	json {"Estatus":bool, "Codigo":int, "Data":text}
Args	None
Description	The latitude and longitude values are updated automatically when the device's physical location changes.

Table 4. DELETE microservice for record deletion

Method	DELETE
Endpoint	/v1/webadmin/antemisoras/
Request	Ninguno
Response	json {"Estatus":bool}
Args	ID (in URL)
Description	This microservice allows the user to delete all data generated throughout the day up to the current time.

These microservices were implemented using the PHP Slim microframework and integrated with an SQL database for efficient record management.

3. Results and discussion

This section presents the results obtained from the implementation and testing of the bidirectional communication system between an Arduino microcontroller and a web server utilizing a microservices-based architecture. The outcomes confirm the effectiveness of the proposed system for real-time data management, validating the feasibility of employing Internet of Things (IoT) technologies in monitoring and control applications. The specific results related to microservice development and system connectivity are detailed below.

In comparison with other approaches reported in the literature, the proposed system is distinguished by its low cost and ease of implementation. While alternative solutions often incorporate more advanced hardware platforms, such as the Raspberry Pi, the present architecture relies on accessible and cost-effective components, namely the Arduino MEGA and the Ethernet Shield. Furthermore, the modular architecture enabled by the microservices framework facilitates straightforward scalability, allowing the system to be adapted for a range of practical applications, including precision agriculture and home automation.

3.1. Microservice development using the PHP slim framework

A local web server was configured using MAMP, which provides an integrated suite of services, including Apache, Nginx, MySQL, PHP, phpMyAdmin, and support for Python and Perl, along with system management and monitoring tools. PHP was used as the primary programming language, and the Slim microframework was implemented to establish a structured methodology for developing the required microservices.

Among the developed services, the GET service is responsible for checking the operational status of the device. When the returned value is 1, the device is ready to transmit data to the server. This information supports the scheduling of maintenance or corrective actions, ensuring reliable communication and enabling interventions to be planned when the device is idle and available, see figure 4.

```php
<?php
$app->group('/v1/webadmin/antemisoras', function ($app) {
    $app->get('/arduino/{AntEmisoraID}', function ($request, $response, $args) {
        try {
            $AntEmisoraID = $args['AntEmisoraID'];
            $sql = "SELECT * FROM AntEmisoras WHERE (AntEmisoraID = '$AntEmisoraID' AND Estatus != 4);";
            $dbc = new db();
            $dbc = $dbc->connect();
            $stmt = $dbc->query($sql);
            $AntEmisoras = $stmt->fetchAll(PDO::FETCH_OBJ);
            $dbc = null;
            $json = json_encode(['Estatus' => true, 'EstatusAntEmisora' => (int) $AntEmisoras[0]->Estatus]);
        } catch(PDOException $error) {
            $msg = $error->getMessage();
            $json = json_encode(['Estatus' => false, 'Codigo' => 400, 'Datos' => $msg]);
        }
        $response->getBody()->write($json);
        return $response;
    });
});
?>
```

Figure 4. PHP slim implementation of the GET request

To store data on the server, the POST method was implemented. This method receives a set of data in the request body and creates a corresponding record for each device based on predefined specifications, see figure 5.

```php
<?php
$app->group('/v1/webadmin/sendatos', function ($app) {
    $app->post('', function ($request, $response, $args) {
        try {
            $Datos = $request->getParsedBody();

            $SenDatosID = GenUUID();
            $Fecha = GenFecha();
            $Hora = GenHora();
            $sql = "INSERT INTO SenDatos (SenDatosID, AntEmisoraID, Temperatura, Humedad, HumedadSuelo, Fecha, Hora )
                        VALUES (:SenDatosID, :AntEmisoraID, :Temperatura, :Humedad, :HumedadSuelo, :Fecha, :Hora );";
            $dbc = new db();
            $dbc = $dbc->connect();
            $stmt = $dbc->prepare($sql);
            $stmt->bindParam("SenDatosID", $SenDatosID);
            $stmt->bindParam("AntEmisoraID", $Datos['AntEmisoraID']);
            $stmt->bindParam("Temperatura", $Datos['Temperatura']);
            $stmt->bindParam("Humedad", $Datos['Humedad']);
            $stmt->bindParam("HumedadSuelo", $Datos['HumedadSuelo']);
            $stmt->bindParam("Fecha", $Fecha);
            $stmt->bindParam("Hora", $Hora);
            $stmt->execute();
            $dbc = null;
            $json = json_encode(['Estatus' => true, 'Codigo' => 200, 'Datos' => $SenDatosID]);

         } catch(PDOException $error) {
            $msg = $error->getMessage();
            $json = json_encode(['Estatus' => false, 'Codigo' => 400, 'Datos' => $msg]);
        }
        $response->getBody()->write($json);
        return $response;
    });
});
?>
```

Figure 5. PHP slim implementation of the POST request

The PUT method is used to update the device's geolocation, specifically its latitude and longitude coordinates. This method is invoked to ensure that the location data remains accurate and up to date, see figure 6.

```php
<?php
$app->group('/v1/webadmin/antemisoras', function ($app) {
    $app->put('/ubicacion', function ($request, $response, $args) {
        try {
            $Datos = $request->getParsedBody();
            if (isset($Datos['Latitud']) && isset( $Datos['Longitud']) && isset($Datos['AntEmisoraID']) )  {
                $sql = "UPDATE AntEmisoras SET Latitud=:Latitud, Longitud=:Longitud WHERE
(AntEmisoraID=:AntEmisoraID);";
                $dbc = new db();
                $dbc = $dbc->connect();
                $stmt = $dbc->prepare($sql);
                $stmt->bindParam("Latitud", $Datos['Latitud']);
                $stmt->bindParam("Longitud", $Datos['Longitud']);
                $stmt->bindParam("AntEmisoraID", $Datos['AntEmisoraID']);
                $stmt->execute();
                $dbc = null;
                $json = json_encode(['Estatus' => true, 'Codigo' => 200, 'Datos' => "Reubicada"]);
            } else {
                $json = json_encode(['Estatus' => false, 'Codigo' => 200, 'Datos' => "Faltan parametros"]);
            }
         } catch(PDOException $error) {
            $msg = $error->getMessage();
            $json = json_encode(['Estatus' => false, 'Codigo' => 400, 'Datos' => $msg]);
        }
        $response->getBody()->write($json);
        return $response;
    });
});
?>
```

Figure 6. PHP slim implementation of the PUT request

To delete data, this microservice is invoked by the device and removes all information generated up to the date and time the delete request is issued. This method ensures that the device-specific data is properly removed according to the user's request, see figure 7.

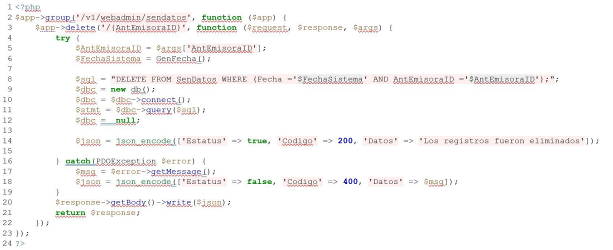

```php
<?php
$app->group('/v1/webadmin/sendatos', function ($app) {
    $app->delete('/{AntEmisoraID}', function ($request, $response, $args) {
        try {
            $AntEmisoraID = $args['AntEmisoraID'];
            $FechaSistema = GenFecha();

            $sql = "DELETE FROM SenDatos WHERE (Fecha ='$FechaSistema' AND AntEmisoraID ='$AntEmisoraID');";
            $dbc = new db();
            $dbc = $dbc->connect();
            $stmt = $dbc->query($sql);
            $dbc =  null;

            $json = json_encode(['Estatus' => true, 'Codigo' => 200, 'Datos' => 'Los registros fueron eliminados']);

        } catch(PDOException $error) {
            $msg = $error->getMessage();
            $json = json_encode(['Estatus' => false, 'Codigo' => 400, 'Datos' => $msg]);
        }
        $response->getBody()->write($json);
        return $response;
    });
});
?>
```

Figure 7. PHP slim implementation of the DELETE request

The microservices were developed using version 3.12 of the Slim microframework, a lightweight PHP framework designed to support the efficient development of web applications and APIs. This framework streamlines the handling of routes, requests, and responses in a structured and maintainable manner. Its modular architecture and compatibility with middleware allow for seamless integration of new functionalities and facilitate system scalability, contributing to a robust and efficient implementation.

For the development of this project, Visual Studio Code was used as the integrated development environment (IDE). This tool provides a range of features beneficial to developers, including support for extensions and customizable functionalities that enhance the programming workflow. Its compatibility with multiple programming languages makes it a flexible and powerful option for projects of varying scope and complexity.

3.2. Verification of service connectivity using postman

The functionality of each microservice was verified using Postman, a widely used testing tool that enabled the validation of multiple operations, including GET, POST, PUT, and DELETE. Postman proved essential in evaluating and confirming the correct operation of the implemented services, ensuring efficient and reliable communication between the Arduino microcontroller and the server.

Figure 8 demonstrates the verification of the GET method's functionality, including the validation of required parameters for communication and data processing. The results confirm that any client making a request to the service can process the information accurately and efficiently.

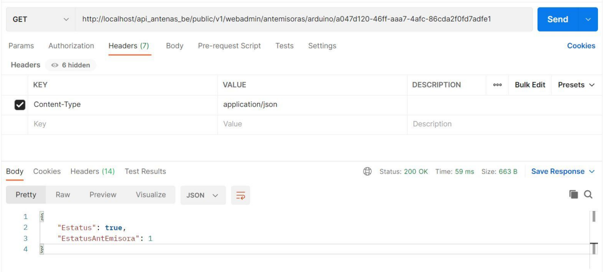

```
GET http://localhost/api_antenas_be/public/v1/webadmin/antemisoras/arduino/a047d120-46ff-aaa7-4afc-86cda2f0fd7adfe1
```

	KEY	VALUE	DESCRIPTION
☑	Content-Type	application/json	
	Key	Value	Description

Status: 200 OK Time: 59 ms Size: 663 B

```
{
    "Estatus": true,
    "EstatusAntEmisora": 1
}
```

Figure 8. Verification of GET method functionality

For data transmission to the server, the information is structured in a request in a JSON-formatted request. The transmitted data is used to create a new record, which is stored in the system's database. Additionally, the server's response includes the operation status, indicating whether the process was successful or encountered an error, see figure 9.

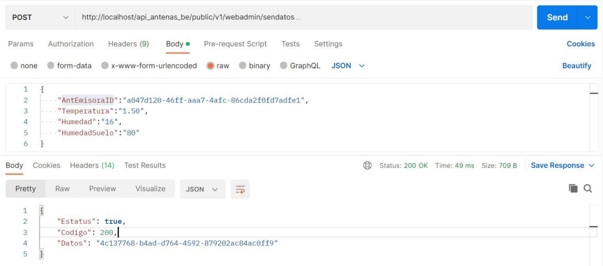

```
POST http://localhost/api_antenas_be/public/v1/webadmin/sendatos ...
```

```
{
    "AntEmisoraID":"a047d120-46ff-aaa7-4afc-86cda2f0fd7adfe1",
    "Temperatura":"1.50",
    "Humedad":"16",
    "HumedadSuelo":"80"
}
```

Status: 200 OK Time: 49 ms Size: 709 B

```
{
    "Estatus": true,
    "Codigo": 200,
    "Datos": "4c137768-b4ad-d764-4592-879202ac84ac0ff9"
}
```

Figure 9. Verification of POST method functionality

To verify communication using the update (PUT) method, the parameters are transmitted in JSON format. The data is then modified accordingly, and the server responds with a confirmation indicating that the changes were successfully applied, see figure 10.

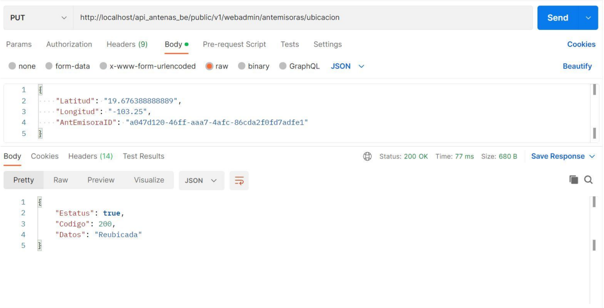

```
PUT http://localhost/api_antenas_be/public/v1/webadmin/antemisoras/ubicacion
```

```
{
    "Latitud": "19.676388888889",
    "Longitud": "-103.25",
    "AntEmisoraID": "a047d120-46ff-aaa7-4afc-86cda2f0fd7adfe1"
}
```

Status: 200 OK Time: 77 ms Size: 680 B

```
{
    "Estatus": true,
    "Codigo": 200,
    "Datos": "Reubicada"
}
```

Figure 10. Verification of PUT method functionality

The record deletion service, triggered by the device, removes data based on the date on which the request is made. This process ensures that only the records corresponding to the specified date are deleted while preserving relevant information from previous days. This functionality contributes to maintaining an organized database and prevents the unnecessary accumulation of outdated data, thereby facilitating more efficient management of the information generated by the devices, see figure 11.

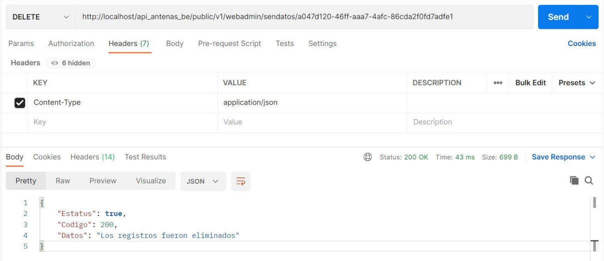

```
DELETE http://localhost/api_antenas_be/public/v1/webadmin/sendatos/a047d120-46ff-aaa7-4afc-86cda2f0fd7adfe1
```

	KEY	VALUE	DESCRIPTION
☑	Content-Type	application/json	
	Key	Value	Description

Status: 200 OK Time: 43 ms Size: 699 B

```
{
    "Estatus": true,
    "Codigo": 200,
    "Datos": "Los registros fueron eliminados"
}
```

Figure 11. Verification of DELETE method functionality

3.3. Arduino code implementation for communication with microservices

The Arduino programs were developed to interact with the server side microservices in accordance with predefined communication protocols, supplying the required data for each service. This design ensures consistent and efficient interactions between the Arduino devices and the server, enabling the reliable transmission and management of information. Each microservice is configured to receive and process the specific data transmitted by the devices, thereby facilitating seamless communication and the correct execution of the intended functions.

3.3.1. Internet connectivity code implementation

The following code modules enable the automated establishment of internet connectivity. This functionality ensures that devices connect to the network efficiently and reliably, facilitating uninterrupted data transmission without the need for manual intervention, see figure 12.

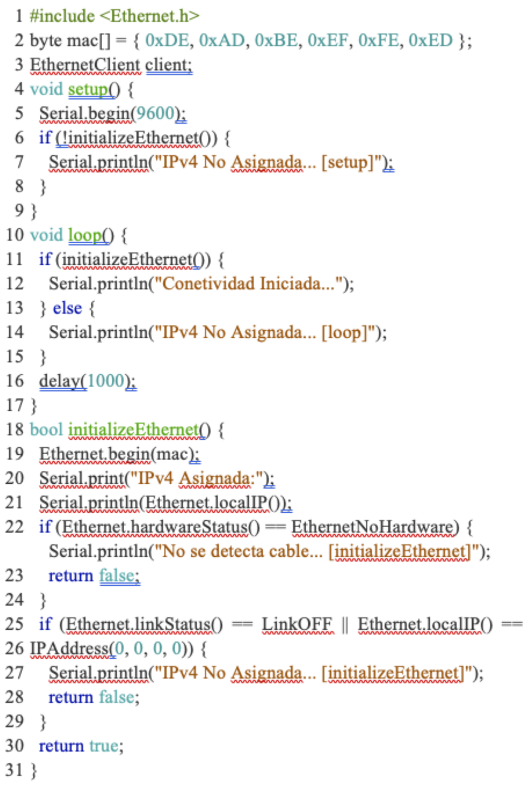

```
#include <Ethernet.h>
byte mac[] = { 0xDE, 0xAD, 0xBE, 0xEF, 0xFE, 0xED };
EthernetClient client;
void setup() {
  Serial.begin(9600);
  if (!initializeEthernet()) {
    Serial.println("IPv4 No Asignada... [setup]");
  }
}
void loop() {
  if (initializeEthernet()) {
    Serial.println("Conetividad Iniciada...");
  } else {
    Serial.println("IPv4 No Asignada... [loop]");
  }
  delay(1000);
}
bool initializeEthernet() {
  Ethernet.begin(mac);
  Serial.print("IPv4 Asignada:");
  Serial.println(Ethernet.localIP());
  if (Ethernet.hardwareStatus() == EthernetNoHardware) {
    Serial.println("No se detecta cable... [initializeEthernet]");
    return false;
  }
  if (Ethernet.linkStatus() == LinkOFF || Ethernet.localIP() ==
IPAddress(0, 0, 0, 0)) {
    Serial.println("IPv4 No Asignada... [initializeEthernet]");
    return false;
  }
  return true;
}
```

Figure 12. Arduino code for internet connectivity

3.3.2. Functions for executing arduino based communication

The following functions are executed only when an internet connection has been successfully established. In the absence of connectivity, the functions are not invoked, and an LED indicator signals the lack of connection required for transmitting information via the HTTP protocol. Communication with the server is performed using JSON format.

The accompanying Arduino code verifies the operational status of the antenna through the GET method. This method sends a request to the server to determine whether the antenna is functioning correctly. If a valid internet connection is available, the code initiates the request and processes the server's response to assess the antenna's status, see figure 13.

To implement the POST functionality, the data to be transmitted and received is first structured in JSON format. This approach ensures a clear and consistent framework for data exchange between the device and the server, see figure 14.

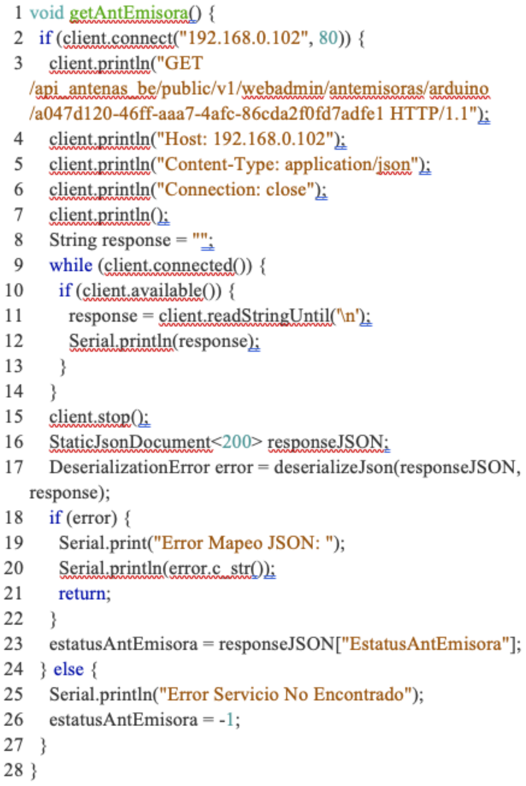

```
void getAntEmisora() {
 if (client.connect("192.168.0.102", 80)) {
  client.println("GET
/api_antenas_be/public/v1/webadmin/antemisoras/arduino
/a047d120-46ff-aaa7-4afc-86cda2f0fd7adfe1 HTTP/1.1");
  client.println("Host: 192.168.0.102");
  client.println("Content-Type: application/json");
  client.println("Connection: close");
  client.println();
  String response = "";
  while (client.connected()) {
   if (client.available()) {
    response = client.readStringUntil('\n');
    Serial.println(response);
   }
  }
  client.stop();
  StaticJsonDocument<200> responseJSON;
  DeserializationError error = deserializeJson(responseJSON,
response);
  if (error) {
   Serial.print("Error Mapeo JSON: ");
   Serial.println(error.c_str());
   return;
  }
  estatusAntEmisora = responseJSON["EstatusAntEmisora"];
 } else {
  Serial.println("Error Servicio No Encontrado");
  estatusAntEmisora = -1;
 }
}
```

Figure 13. Arduino code for GET method

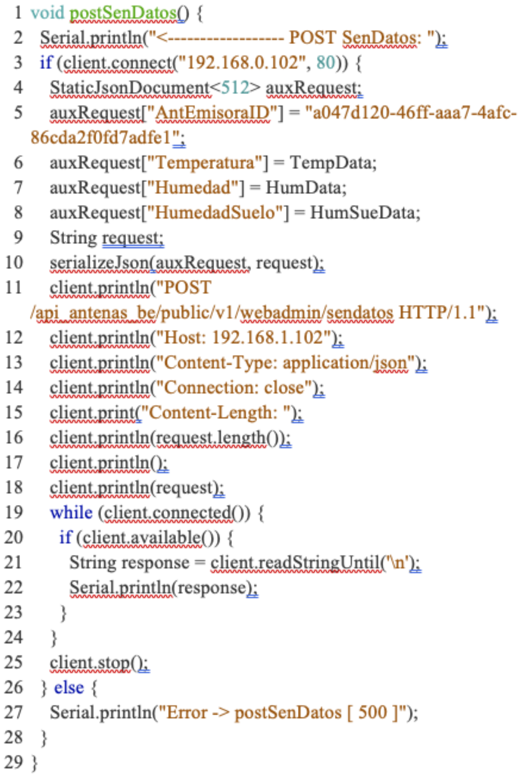

```
void postSenDatos() {
 Serial.println("<------------------ POST SenDatos: ");
 if (client.connect("192.168.0.102", 80)) {
  StaticJsonDocument<512> auxRequest;
  auxRequest["AntEmisoraID"] = "a047d120-46ff-aaa7-4afc-
86cda2f0fd7adfe1";
  auxRequest["Temperatura"] = TempData;
  auxRequest["Humedad"] = HumData;
  auxRequest["HumedadSuelo"] = HumSueData;
  String request;
  serializeJson(auxRequest, request);
  client.println("POST
/api_antenas_be/public/v1/webadmin/sendatos HTTP/1.1");
  client.println("Host: 192.168.1.102");
  client.println("Content-Type: application/json");
  client.println("Connection: close");
  client.print("Content-Length: ");
  client.println(request.length());
  client.println();
  client.println(request);
  while (client.connected()) {
   if (client.available()) {
    String response = client.readStringUntil('\n');
    Serial.println(response);
   }
  }
  client.stop();
 } else {
  Serial.println("Error -> postSenDatos [ 500 ]");
 }
}
```

Figure 14. Arduino code for POST method

To update the device's geographic position based on latitude and longitude coordinates, the PUT method was implemented to modify the stored location. The data is structured in JSON format prior to transmission, see figure 15.

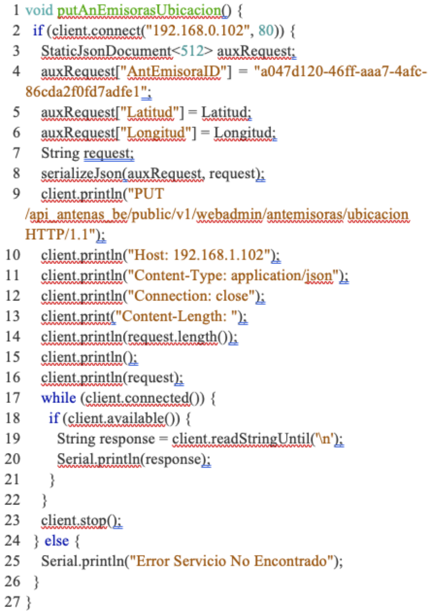

```
void putAnEmisorasUbicacion() {
 if (client.connect("192.168.0.102", 80)) {
  StaticJsonDocument<512> auxRequest;
  auxRequest["AntEmisoraID"] = "a047d120-46ff-aaa7-4afc-
86cda2f0fd7adfe1";
  auxRequest["Latitud"] = Latitud;
  auxRequest["Longitud"] = Longitud;
  String request;
  serializeJson(auxRequest, request);
  client.println("PUT
/api_antenas_be/public/v1/webadmin/antemisoras/ubicacion
HTTP/1.1");
  client.println("Host: 192.168.1.102");
  client.println("Content-Type: application/json");
  client.println("Connection: close");
  client.print("Content-Length: ");
  client.println(request.length());
  client.println();
  client.println(request);
  while (client.connected()) {
   if (client.available()) {
    String response = client.readStringUntil('\n');
    Serial.println(response);
   }
  }
  client.stop();
 } else {
  Serial.println("Error Servicio No Encontrado");
 }
}
```

Figure 15. Arduino code for PUT method

To implement the DELETE functionality, a physical button was incorporated that, when pressed, triggers the deletion of data recorded on the current day without affecting previously stored information, see figure 16.

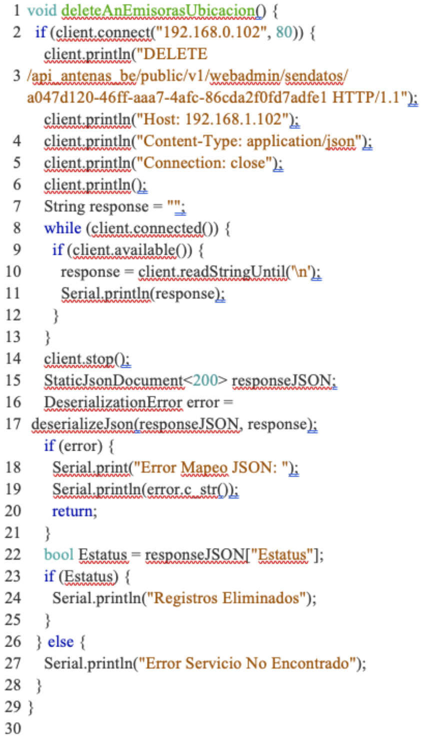

```
void deleteAnEmisorasUbicacion() {
 if (client.connect("192.168.0.102", 80)) {
  client.println("DELETE
/api_antenas_be/public/v1/webadmin/sendatos/
a047d120-46ff-aaa7-4afc-86cda2f0fd7adfe1 HTTP/1.1");
  client.println("Host: 192.168.1.102");
  client.println("Content-Type: application/json");
  client.println("Connection: close");
  client.println();
  String response = "";
  while (client.connected()) {
   if (client.available()) {
    response = client.readStringUntil('\n');
    Serial.println(response);
   }
  }
  client.stop();
  StaticJsonDocument<200> responseJSON;
  DeserializationError error =
deserializeJson(responseJSON, response);
  if (error) {
   Serial.print("Error Mapeo JSON: ");
   Serial.println(error.c_str());
   return;
  }
  bool Estatus = responseJSON["Estatus"];
  if (Estatus) {
   Serial.println("Registros Eliminados");
  }
 } else {
  Serial.println("Error Servicio No Encontrado");
 }
}
```

Figure 16. Arduino code for DELETE method

To implement the aforementioned functions, the Arduino Json library was employed, as it facilitates the conversion of textual data into JSON format. This approach simplifies data mapping and enhances the efficiency of information handling within the development environment.

3.4. Case study: moisture monitoring in agricultural crops

The proposed system was applied in a case study focused on monitoring soil moisture in agricultural crops. Humidity sensors connected to an Arduino MEGA were used to collect data, which was transmitted to a server via microservices. The results indicated a 15% reduction in water consumption and a 10% increase in crop productivity. This case study demonstrates the system's effectiveness in precision agriculture and highlights its potential adaptability to other domains, such as smart homes and industrial applications.

3.5. Comparison with existing approaches

Compared to other approaches reported in the literature, the proposed scheme offers several notable advantages:

1. **Low Cost:** The use of an Arduino MEGA in combination with an Ethernet Shield significantly reduces hardware costs relative to more advanced platforms.
2. **Simplicity:** Implementation using the PHP Slim framework enables rapid and accessible development, making the system suitable for users with basic programming experience.
3. **Flexibility:** The modular architecture allows the system to be easily adapted to a variety of contexts, including precision agriculture, home automation, and educational applications.
4. **Efficiency:** Despite its simplicity, the system delivers performance comparable to that of more complex solutions, achieving an average response time of 120 milliseconds and maintaining stable connection in 95% of requests.

3.6. Discussion

The findings of this study confirm the effectiveness of a microservices-based architecture for real-time data management in Internet of Things (IoT) applications. The successful implementation of microservices using the lightweight PHP Slim framework, coupled with seamless interaction between the Arduino microcontroller and the server, demonstrates the feasibility of developing a robust, scalable, and accessible system by leveraging well-documented, low cost technologies.

In contrast to previous studies that have employed more complex and sophisticated architectures, the proposed implementation stands out for its simplicity without compromising functionality. The selection of PHP Slim facilitated a streamlined and efficient development process, suggesting that, in specific contexts particularly educational settings or small scale projects simpler solutions can yield equally effective results. This approach not only reduces the learning curve for developers but also enhances the replicability of the system across diverse application domains.

The system's capability to manage real time data has significant practical implications, especially in the field of precision agriculture. For instance, optimizing irrigation cycles based on real time environmental data can lead to measurable improvements in water use efficiency and crop productivity. These results align with prior research emphasizing the critical role of IoT technologies in modern agriculture, where the integration of sensors and real-time monitoring systems is essential to achieving both sustainability and operational efficiency.

Nevertheless, this study presents several limitations that should be acknowledged. The implementation was conducted in a controlled environment, which may not fully capture the challenges encountered in real world conditions particularly in rural areas with limited connectivity. Moreover, the system's reliance on a stable internet connection represents a potential constraint, limiting its applicability in regions with underdeveloped technological infrastructure.

To address these limitations and guide future work, the following research directions are recommended:

- **Integration of additional sensors:** Extend the system's functionality by incorporating sensors for monitoring variables such as air quality, ambient light, or atmospheric pressure, thereby broadening its applicability.

- **Application of machine learning algorithms:** Implement intelligent data analysis techniques to enable real-time decision-making based on patterns detected in the collected data.

- **Connectivity enhancements:** Explore alternative communication protocols such as LoRa, Zigbee, or implement local storage with delayed synchronization to ensure functionality in environments with limited internet access.

- **Validation in real world environments:** Conduct testing in operational settings such as agricultural fields or industrial facilities to evaluate system performance under variable and uncontrolled conditions.

4. Conclusions

The implementation of a microservices based architecture was essential for enabling efficient interaction with the database. This approach supported the development of specific functions within the Arduino microcontroller for data transmission and reception, thereby achieving the bidirectional communication required for real time operation. The resulting infrastructure is both robust and adaptable, making it suitable for any project that requires seamless connectivity between an Arduino microcontroller and a web server.

The microservices were designed according to best practices, ensuring that each performs a distinct function and can be maintained and updated independently. Version 3.11 of a lightweight PHP framework was employed to develop these services, offering a modular structure and middleware support that simplifies the addition of new features and enhances the system's scalability.

To test and validate each microservice, a dedicated tool was used to simulate HTTP requests and responses, confirming the correct behavior of each service under various conditions. The tool's ability to encode and execute different HTTP methods GET, POST, PUT, and DELETE was critical in verifying the full functionality of the system.

On the Arduino side, dedicated functions were developed to interact with the microservices, ensuring reliable and efficient communication with the server. Internet connectivity was automatically established through purpose built code, allowing the devices to remain consistently online and ready for data transmission. Additionally, LED indicators were incorporated to signal connection status, enhancing the system's diagnostic and maintenance capabilities.

The experimental results demonstrate that the proposed system is effective in terms of both response time and connection stability. For instance, the average processing time for an HTTP request was approximately 120 milliseconds, enabling fast and responsive communication. Moreover, the complete system setup was accomplished in an average of four hours significantly faster than the two days typically required for more complex architectures.

Tools used

Visual Studio Code is a highly configurable source code editor developed by Microsoft. It supports debugging, version control integration, and a wide range of programming languages through an extensive library of extensions. More information is available at [15].

Postman is a widely used tool for API development and testing. It enables the execution of HTTP requests, the creation and management of test collections, and the automation ofAPI workflows. For more details, visit [16].

Arduino IDE is an integrated development environment designed for programming Arduino microcontrollers. It features a user-friendly code editor along with tools for compiling and uploading codeto Arduino boards. Learn more at [17].

MAMP is a software package that sets up a local web server environment on macOS and Windows. It includes Apache, MySQL, and PHP, and is commonly used for web application development and testing. More information can be found at [18].

Fritzing is an open-source tool for designing and documenting electronic prototypes. It allows users to create schematics, circuit diagrams, and bills of materials for hardware projects. Learn more at [19].

Draw.io (also known as diagrams.net) is a web-based diagramming tool for creating flowcharts, network diagrams, UML diagrams, and other visual representations. It is especially useful for system design and project documentation. For more details visit [20].

Contributor Roles

- **Marco Antonio Celis Crisóstomo:** Programming, software development, designing computer programs.
- **Francisco Miguel Hernández López:** Programming, software development, implementation of the computer code and supporting algorithms.
- **Jorge Alberto Cárdenas Magaña:** Programming, software development.
- **Emmanuel Vega Negrete:** Oversight and leadership responsibility for the research activity planning and execution.

References

[1] J. P. Tovar Soto, J. S. Solórzano Suárez, A. Badillo Rodríguez, and G. O. Rodríguez Cainaba, “Internet de las cosas aplicado a la agricultura: estado actual,” *Lámpsakos*, no. 22, pp. 86–105, Nov. 2019. [Online]. Available: https://doi.org/10.21501/21454086.3253

[2] B. A. Quintana G., V. R. Pereira Poveda, and C. N. Vega S., “Automatización en el hogar: un proceso de diseño para viviendas de interés social,” *Revista Escuela de Administración de Negocios*, no. 78, pp. 108–121, Jul. 2015. [Online]. Available: https://doi.org/10.21158/01208160.n78.2015.1193

[3] C. A. Laura Mamani, “Pruebas de software para microservicios,” *Innovación y Software*, vol. 4, no. 1, pp. 151–160, Mar. 2023. [Online]. Available: http://dx.doi.org/10.48168/innosoft.s11.a86

[4] P. Gutiérrez Prada, G. B. de Corso-Sicilia, and W. G. Jiménez-Barbosa, “Impacto social del internet de las cosas (IdC): una reflexión conceptual,” *Jangwa Pana*, vol. 21, no. 3, pp. 254–270, Nov. 2022. [Online]. Available: https://doi.org/10.21676/16574923.4719

[5] L. G. Viera Molina and C. O. Guilcaso Molina, “Utilización de sensores iot para la automatización de sistemas de riego,” *Dominio de las Ciencias*, vol. 9, no. 4, pp. 1731–1748, 2023. [Online]. Available: https://upsalesiana.ec/ing34ar1r5

[6] L. García, L. Parra, J. M. Jimenez, J. Lloret, and P. Lorenz, “IoT-based smart irrigation systems: An overview on the recent trends on sensors and iot systems for irrigation in precision agriculture,” *Sensors*, vol. 20, no. 4, p. 1042, Feb. 2020. [Online]. Available: https://doi.org/10.3390/s20041042

[7] S. K. Mousavi, A. Ghaffari, S. Besharat, and H. Afshari, “Improving the security of internet of things using cryptographic algorithms: a case of smart irrigation systems,” *Journal of Ambient Intelligence and Humanized Computing*, vol. 12, no. 2, pp. 2033–2051, Jul. 2020. [Online]. Available: https://doi.org/10.1007/s12652-020-02303-5

[8] B. Parvathi Sangeetha, N. Kumar, A. P. Ambalgi, S. L. Abdul Haleem, K. Thilagam, and P. Vijayakumar, “IoT based smart irrigation management system for environmental sustainability in India,” *Sustainable Energy Technologies and Assessments*, vol. 52, p. 101973, Aug. 2022. [Online]. Available: https://doi.org/10.1016/j.seta.2022.101973

[9] J. Yang, A. Sharma, and R. Kumar, “IoT-based framework for smart agriculture,” *International Journal of Agricultural and Environmental Information Systems*, vol. 12, no. 2, pp. 1–14, Apr. 2021. [Online]. Available: http://doi.org/10.4018/ijaeis.20210401.oa1

[10] J. Ruan, Y. Wang, F. T. S. Chan, X. Hu, M. Zhao, F. Zhu, B. Shi, Y. Shi, and F. Lin, “A life cycle framework of green IoT-based agriculture and its finance, operation, and management issues,” *IEEE Communications Magazine*, vol. 57, no. 3, pp. 90–96, Mar. 2019. [Online]. Available: http://doi.org/10.1109/mcom.2019.1800332

[11] J. M. Talavera, L. E. Tobón, J. A. Gómez, M. A. Culman, J. M. Aranda, D. T. Parra,

L. A. Quiroz, A. Hoyos, and L. E. Garreta, "Review of IoT applications in agro-industrial and environmental fields," *Computers and Electronics in Agriculture*, vol. 142, pp. 283–297, Nov. 2017. [Online]. Available: http://doi.org/10.1016/j.compag.2017.09.015

[12] R. Kumar, R. Mishra, H. P. Gupta, and T. Dutta, "Smart sensing for agriculture: Applications, advancements, and challenges," *IEEE Consumer Electronics Magazine*, vol. 10, no. 4, pp. 51–56, Jul. 2021. [Online]. Available: https://doi.org/10.1109/MCE.2021.3049623

[13] M. S. Farooq, S. Riaz, A. Abid, T. Umer, and Y. B. Zikria, "Role of IoT technology in agriculture: A systematic literature review," *Electronics*, vol. 9, no. 2, p. 319, Feb. 2020. [Online]. Available: http://doi.org/10.3390/electronics9020319

[14] V. K. Patil, A. Jadhav, S. Gavhane, and V. Kapare, "IoT based real time soil nutrients detection," in *2021 International Conference on Emerging Smart Computing and Informatics (ESCI)*. IEEE, Mar. 2021, pp. 737–742. [Online]. Available: http://doi.org/10.1109/esci50559.2021.9396860

[15] Visual Studio Code. (2024) *Your code editor. Redefined with AI.* Visual Studio Code. [Online]. Available: https://upsalesiana.ec/ing34ar1r15

[16] Postman. (2024) AI is powered by APIs. APIs are powered by Postman,. Postman. Inc. [Online]. Available: https://upsalesiana.ec/ing34ar1r16

[17] Arduino. (2024) Arduino IDE 2.3.4. Arduino. [Online]. Available: https://upsalesiana.ec/ing34ar1r17

[18] MAMP. (2024) MAMP PRO & MAMPYour web development tool. MAMP GmbH. [Online]. Available: https://upsalesiana.ec/ing34ar1r18

[19] Fritzing. (2024) Fritzing home page. Fritzing Electronics Made Easy. [Online]. Available: https://upsalesiana.ec/ing34ar1r19

[20] Draw.io. (2024) Diagrams on line. J Graph. Ltd. [Online]. Available: https://upsalesiana.ec/ing34ar1r20

Scientific Paper / Artículo Científico

UNIVERSIDAD POLITÉCNICA SALESIANA ECUADOR
INGENIUS
Revista de Ciencia y Tecnología
https://doi.org/10.17163/ings.n34.2025.02
pISSN: 1390-650X / eISSN: 1390-860X

EFFECT OF PROCESS VARIABLE ON THE MECHANICAL AND THERMAL BEHAVIOR OF A POLYPROPYLENE COMPOSITE REINFORCED WITH SHORT BAMBOO FIBERS BY HOT COMPRESSION

EFECTO DE VARIABLES DE PROCESO EN EL COMPORTAMIENTO MECÁNICO Y TÉRMICO DE UN COMPOSITE DE POLIPROPILENO REFORZADO CON FIBRAS CORTAS DE BAMBÚ POR COMPRESIÓN EN CALIENTE

Leidy Quintero[1], Alexis García[2], Alejandro Alcaraz[1], Jorge Fajardo[3], Luis Cruz[1,*]

Received: 12-05-2023, Received after review: 17-03-2025, Accepted: 26-03-2025, Published: 01-07-2025

Abstract

This study investigates the effect of fiber content and coupling agent concentration on the mechanical and thermal behavior of a polypropylene-based composite. The materials were fabricated via hot compression molding using pellets composed of polypropylene (PP) modified with maleic anhydride-grafted polypropylene (MAPP) and reinforced with short bamboo fibers derived from Guadua angustifolia Kunth (GAK). The fibers were previously extracted through the steam explosion technique. The research was carried out in two stages: first, the composite materials were produced; second, their mechanical and thermal properties were comprehensively characterized. The incorporation of GAK fibers and MAPP significantly altered the mechanical performance of the PP matrix, yielding stiffer composites with improved flexural strength and impact resistance. The optimal formulation, containing 50 wt% GAK fibers and 4 wt% MAPP, resulted in a 322% increase in elastic modulus (2.9 GPa) compared to neat polypropylene (0.7 GPa). Both variables, fiber content and compatibilizer concentration, were found to exert a substantial influence on the mechanical behavior of the resulting composites.

Keywords: Natural fibers, bamboo, polymeric composites, hot compression, mechanical characterization, thermal characterization.

Resumen

En este trabajo se estudió el efecto de la concentración del refuerzo y del agente de acople en el comportamiento mecánico y térmico de un material compuesto, procesado mediante la técnica de moldeo por compresión en caliente (MCC), a partir de una matriz de polipropileno (PP) modificada con anhídrido maleico injertado en polipropileno (MAPP) y reforzada con fibras cortas de bambú de la especie Guadua angustifolia Kunth (GAK). Las fibras fueron extraídas previamente mediante la técnica de *steam explosion*. La investigación se desarrolló en dos etapas. En la primera, se elaboraron los materiales compuestos poliméricos y, en la segunda, se realizó la caracterización mecánica y térmica de los mismos. La adición de las fibras de GAK y del agente de acople (MAPP) al polipropileno, modificó el comportamiento mecánico de la matriz, obteniéndose materiales más rígidos, con una mayor resistencia a la flexión y mayor absorción de la energía de impacto. La mejor configuración del material compuesto fue con el 50 % p/p de fibras de GAK y el 4 % p/p de MAPP, lo que permitió obtener un incremento sustancial en el módulo de elasticidad del 322 % (2,9 GPa) en relación con el PP virgen (0,7 GPa). Ambos factores tuvieron un efecto significativo en el comportamiento mecánico del *composite*.

Palabras clave: fibras naturales, bambú, composites poliméricos, compresión en caliente, caracterización mecánica, caracterización térmica

---

[1,*] Facultad de Ingeniería Mecánica, Universidad Pontificia Bolivariana, Colombia.
Corresponding author ✉: luis.cruz@upb.edu.co.

[2] Centro de diseño y manufactura del cuero - SENA, Colombia.

[3] Facultad de Ingeniería Mecánica, Universidad Politécnica Salesiana, Cuenca, Ecuador.

Suggested citation: L. Quintero, A. García, A. Alcaraz, J. Fajardo, and L. Cruz, "Effect of process variable on the mechanical and thermal behavior of a polypropylene composite reinforced with short bamboo fibers by hot compression," *Ingenius, Revista de Ciencia y Tecnología*, N.° 34, pp. 20-30, 2025, DOI: https://doi.org/10.17163/ings.n34.2025.02.

1. Introduction

In recent decades, natural fibers such as kenaf, jute, and hemp have garnered increasing attention as renewable alternatives for the development of bio-based composite materials. Their appeal lies in the potential to replace non-biodegradable, difficult-to-dispose synthetic resources in the fabrication of functional components, where key performance attributes include high stiffness and low weight [1].

These bio-derived fibers offer multiple advantages, including low cost, reduced energy consumption during production, widespread availability, renewability, non-toxicity, low density, and high specific mechanical properties, comparable in some cases to those of glass fibers [2, 3].

In particular, natural fibers derived from Guadua angustifolia Kunth (GAK) represent a promising reinforcement alternative for composite materials, owing to their high tensile strength and elevated modulus of elasticity. Furthermore, these fibers are environmentally sustainable and exhibit rapid growth, reaching maturity in approximately three years, a comparatively short cultivation cycle [4–6].

Natural fiber-reinforced composite materials are well-suited for processing through various conventional techniques, including extrusion molding, injection molding, thermoforming, and hot compression molding. Moreover, they fulfill both technical and economic requirements for the production of functional components suitable for a wide range of industrial applications [7, 8].

However, several challenges hinder the widespread adoption of these materials, including the variability in the mechanical properties of natural fibers [6], their susceptibility to moisture [9], and the poor interfacial adhesion between the fibers and the polymer matrix, an issue arising from the intrinsic incompatibility between the hydrophilic nature of the fibers and the hydrophobic character of the matrix [10].

With respect to this latter issue, it is important to note that the incompatibility between the hydrophilic fibers and the hydrophobic matrix not only presents processing challenges [5], but also significantly impairs the mechanical performance of the resulting composite material [11]. To address this, various chemical, physical, and biological surface treatments have been developed to reduce the hydrophilicity of natural fibers, enhance their surface area, and improve interfacial bonding with the polymer matrix [12–14].

Similarly, in composite materials, surface modification techniques such as esterification, etherification, and benzylation have been employed, along with the incorporation of compatibilizing agents during manufacturing processes. According to the scientific literature, the most commonly used compatibilizers for thermoplastic polymers reinforced with short natural fibers include maleic anhydride-grafted polypropylene (MAPP), maleic anhydride-grafted polyethylene (MAPE), and silanes [15].

Similarly, [16, 17] developed polypropylene-based composite materials reinforced with bamboo fibers, applying surface treatments with NaOH and silanes, and calcium carbonate, respectively, to enhance their mechanical performance. The authors reported improvements in key properties such as tensile strength and elastic modulus.

In line with these approaches, [18,19] proposed alkaline treatments using NaOH and $NaClO_2$ to remove surface impurities from Guadua angustifolia Kunth (GAK) fibers and enhance polymer–fiber adhesion. These treatments also increased surface roughness and fiber crystallinity, while reducing both fiber weight and diameter.

In contrast, Kumar and Das [2] developed a composite laminate using an unsaturated polyester matrix reinforced with Guadua angustifolia Kunth (GAK) fibers, proposing its use in semi-structural components. They evaluated mechanical properties, including tensile strength, Young's modulus, flexural strength, and flexural modulus, and reported that all values decreased relative to the reference material. This reduction was attributed to the lack of fiber orientation control during fabrication, as well as the absence of coupling agents to mitigate the incompatibility between the hydrophilic nature of the fibers and the hydrophobic character of the polymer matrix.

Among the limited studies available on hybrid polymer matrices, the work of Ying-Chen et al. [20] is particularly noteworthy. The authors employed the extrusion technique to fabricate composite materials comprising a hybrid polypropylene/polylactic acid (PP/PLA) matrix reinforced with bamboo fibers. MAPP was introduced as a coupling agent to improve the fiber–matrix interfacial compatibility, and the resulting composites were evaluated for their morphological, thermal, and rheological properties.

The authors attributed the improvement in these properties to enhanced interaction at the hybrid fiber–matrix interface resulting from the incorporation of MAPP. They also reported an increase in the crystallinity of the composites compared to the unreinforced polymers, which was ascribed to the nucleating effect of natural fibers.

As highlighted in the literature, the behavior of short fiber-reinforced composite materials is governed by numerous factors, the most significant of which include: fiber type and content, coupling agent type and concentration, reinforcement orientation, fiber length, fiber–matrix interfacial adhesion, and processing technique [21].

It is noteworthy that the scientific literature lacks studies analyzing the fabrication of these materials via hot compression molding (HCM), as well as research on the behavior of natural composites reinforced with short fibers extracted through the steam explosion technique.

To address this gap in the literature, this study investigated the effects of varying fiber content and coupling agent concentration (MAPP) on the mechanical and thermal behavior of a composite fabricated via hot compression molding (HCM), using polypropylene, MAPP, and short Guadua angustifolia Kunth (GAK) fibers. Mechanical tests (tensile, flexural, and impact) and thermal analyses (DSC and TGA) were conducted, and the optimal composite formulation was identified based on the results obtained.

2. Materials and Methods

The polymeric matrix used in this study was HOPELEN H1500 homopolymer polypropylene pellets (injection grade), with a density of 0.9 g/cm^3 and a melt flow index of 12 g/10 min, supplied by LOTTE CHEMICAL.

Short bamboo fibers from Guadua angustifolia Kunth (GAK), extracted via steam explosion at a severity factor of 3.3 [22], were used as the reinforcing material.

For compatibilization between the fibers and the polymer matrix, maleic anhydride-grafted polypropylene (MAPP) pellets, supplied by SIGMA-ALDRICH, were employed.

2.1. Processing of Composite Materials

The fibers extracted via steam explosion were dried at 105 °C for 2 hours to remove residual moisture. Subsequently, their size was reduced using a blade mill operating at 1440 rpm, with a 4 mm sieve used to retain the processed material. The milled fibers were then classified using a sieve shaker. For composite fabrication, fibers retained on mesh 60 (250 µm) and mesh 100 (150 µm) were selected, in accordance with ASTM E11 standards.

For the fabrication of the composite materials, the hot compression molding (HCM) technique was employed, with controlled variations in fiber content (30%, 40%, and 50% w/w) and MAPP concentration (0%, 4%, and 8% w/w), to evaluate the influence of these variables on the composites' mechanical and thermal behavior. Based on the test results, the optimal composite formulation was identified.

The percentages of reinforcing material and compatibilizer were established based on findings from the scientific literature. For example, studies such as [23] on bamboo fiber-reinforced polypropylene composites have demonstrated that incorporating fibers in the range of 30% to 50% w/w can lead to significant improvements in mechanical properties, including tensile strength and elastic modulus.

Similarly, studies such as [24] have reported that increasing the content of pineapple leaf fibers, which share structural similarities with Guadua angustifolia Kunth (GAK) fibers, enhances the elastic modulus. However, fiber contents exceeding 50% w/w may compromise the toughness of the composite.

In contrast, studies such as [25] have concluded that the use of coupling agents like maleic anhydride-grafted polypropylene (MAPP) enhances interfacial adhesion between the polypropylene (PP) matrix and natural fibers, thereby improving both mechanical strength and thermal stability. Specifically, a coupling agent concentration of 4% w/w has proven effective in promoting adhesion without adversely affecting the homogeneity of the mixture.

Thus, three levels of MAPP were established to evaluate potential improvements or saturation effects in the composite's properties.

Prior to sheet fabrication, the raw materials, manually pre-mixed, were fed into a single-screw extruder to produce homogeneous premixes corresponding to the different composite formulations.

The extruder's temperature profile was set to 170 °C, 180 °C, 190 °C and 200 °C. across its heating zones. The screw speed was maintained at 60 rpm. The extruder was equipped with a 3 mm diameter pelletizer, and the resulting pellets were cut into granules with an average length of 5 mm.

Subsequently, the pellets were hot-pressed in multiple stages using the hot compression molding (HCM) technique, as illustrated in Figure 1, to produce plates measuring 150 × 100 × 3mm. Test specimens for mechanical characterization were then machined from these plates using a CNC router.

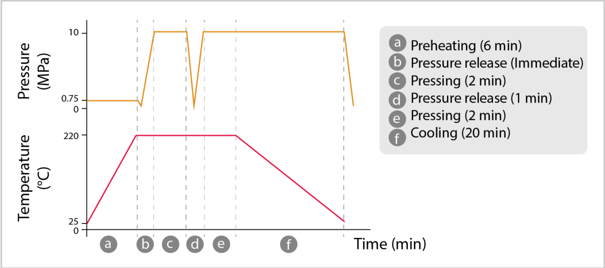

Figure 1. Temperature and pressure curves used in the hot compression molding process.

2.1.1. Mechanical Characterization of Composite Materials

Tensile tests were conducted using an INSTRON 5582 universal testing machine, in accordance with ASTM D638-14, employing Type IV specimens to determine tensile strength, elastic modulus, and maximum elongation at break. An Instron 2630-105 axial extensometer with a gauge length of 25 mm was used to measure deformation.

Additionally, the fiber-matrix interface of the composites was qualitatively analyzed after tensile testing using a scanning electron microscope (SEM, JEOL JCM-6000Plus) operated at 15 kv under high vacuum conditions. Prior to imaging, the samples were coated by cathodic sputtering to ensure surface conductivity.

Three-point bending tests were conducted using an INSTRON 5582 universal testing machine, in accordance with ASTM D790-10, Procedure A, to determine flexural strength and flexural modulus.

Impact tests were conducted using an Izod-type pendulum impact tester (SATEC Systems), in accordance with ASTM D256-10.

For each composite formulation, eight replicates were tested.

Surface hardness was evaluated using a Shore D durometer (Bareiss) with an analog scale ranging from 0 to 100, following the procedure described in ASTM D2240-15. Prior to testing, the samples were conditioned at 22 °C and 55% relative humidity for 40 hours, as specified in ASTM D618-13.

2.1.2. Thermal Characterization of Composite Materials

Thermal properties of the composite materials, including melting temperature, crystallization temperature, and the enthalpies of melting and crystallization, were determined using differential scanning calorimetry (DSC).

Samples of approximately 6 mg were analyzed under an inert nitrogen atmosphere, with a flow rate of 50 mL/min and a heating rate of 10 °C/min.

It is important to highlight that, prior to data collection, a thermal erasure step was performed to eliminate the thermal processing history of the samples.

Additionally, thermogravimetric analysis (TGA) was used to determine the maximum thermal degradation temperature of the composite materials.

Samples of approximately 9 mg were analyzed under an inert nitrogen atmosphere, with a flow rate of 50 ml/min. The heating range extended from ambient temperature to 800 °C, with a heating rate of 30 °C/min.

3. Results and Discussion

Figure 2 presents the results of the tensile tests conducted on both the polypropylene matrix and the composite materials, with and without the coupling agent.

Regarding tensile strength, Figure 2a shows that the polypropylene (PP) matrix achieved the highest value, at 34.3 MPa. In contrast, uncompatibilized composites reinforced with 30% w/w fiber reached a maximum tensile strength of 18.6 MPa. Similarly, compatibilized composites with 50% w/w fiber and 4% w/w MAPP achieved a maximum of 24.8 MPa, representing reductions of 46% and 28%, respectively, compared to the NetApp matrix.

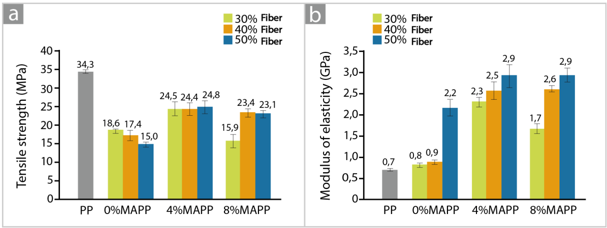

Figure 2. Tensile properties of composite materials with and without a coupling agent: a) Tensile strength and b) Elastic modulus.

As observed in the results, the tensile strength of composites without a coupling agent tends to decrease as the fiber content increases. This behavior is attributed to the hydrophilic nature of the fibers and the hydrophobic character of the polypropylene matrix, which results in poor interfacial compatibility and, consequently, weak fiber - matrix adhesion - an effect that becomes more pronounced at higher reinforcement levels [26, 27].

However, the addition of 4% w/w coupling agent to the composites results in improved tensile strength compared to the uncompatibilized formulations, as MAPP enhances fiber–matrix interfacial adhesion.

In contrast, increasing the MAPP content to 8% w/w does not yield further improvements; in fact, a slight decrease in tensile strength is observed. Fuqua and Ulven [28] attribute this behavior to the formation of weak van der Waals bonds between the residual coupling agent and the polypropylene matrix, which undermines the mechanical integrity of the composite.

Based on these results, none of the composites, reinforced, with or without a coupling agent, achieved the tensile strength exhibited by neat polypropylene. This outcome is attributed to the hot compression molding (HCM) technique, which does not promote fiber alignment in a preferred direction but instead produces a random fiber orientation. As a result, the reinforcing effect of the fibers is significantly reduced.

This same phenomenon has been reported by other authors [29], who attribute it to the random distribution of fibers within the matrix and the reduced aspect ratio (length-to-diameter) of the fibers after processing. During fabrication, the fibers experience significant breakage due to shear stresses generated by the processing equipment (e.g., mill and extruder), resulting in shorter fibers that limit efficient stress transfer within the composite.

Additionally, after processing, the fibers exhibit lengths shorter than the critical threshold required for effective reinforcement in the bamboo-PP system, which, according to [26], is approximately 3.5 mm.

Regarding the elastic modulus (figure 2b), a significant increase is observed upon incorporation of short GAK fibers into the polypropylene matrix, an effect that is further enhanced by the addition of the coupling agent (MAPP).

Quantified relative to virgin polypropylene (0.7 GPa) , the elastic modulus increased by 212% (reaching 2.2 GPa) with 50% w/w fiber, and up to 322% (2.9GPa) when an additional 4% w/w MAPP was incorporated at the same fiber concentration. These results are consistent with the findings reported by [30].

These authors attribute this improvement to the intrinsic rigidity of the fibers and the high reinforcement content in the composite, as the elastic modulus is strongly influenced by the fiber volume fraction.

Additionally, the incorporation of the coupling agent results in higher elastic modulus values compared to composites without a compatibilizer. This improvement is attributed to the formation of covalent bonds between the anhydride groups of MAPP and the hydroxyl groups of the GAK fibers, as well as interactions between the non-polar segments of MAPP and the polypropylene matrix, as reported by Chattopadhyay et al. [23].

This enhanced interfacial adhesion between the fiber and the matrix facilitates more efficient stress transfer from the matrix to the fibers [23].

However, despite the positive effects associated with the addition of the compatibilizer, increasing the MAPP content to 8% w/w does not result in further improvements; in fact, it may lead to a slight reduction in this property, as previously reported [28].

Additionally, a qualitative analysis of the fiber-matrix interface of the composites was conducted using SEM imaging of the fracture surfaces following tensile testing to identify potential interfacial defects or failure mechanisms.

As shown in figures 3a and 3b, the incorporation of the coupling agent resulted in improved matrix wettability and enhanced fiber impregnation, as clearly observed in the compatibilized composite (figure 3b).

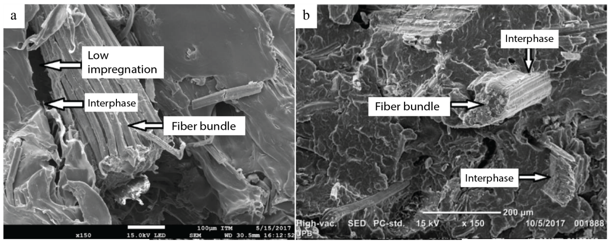

Figure 3. Scanning electron microscopy (SEM) images of the fracture surfaces of the composite materials after tensile testing: (a) 30% w/w fiber and 0% w/w MAPP; (b) 30% w/w fiber and 4% w/w MAPP.

The addition of MAPP modifies the fiber-matrix interface by enhancing interfacial interactions between the two phases, thereby improving stress transfer from the matrix to the fibers and ultimately enhancing the mechanical performance of the compatibilized composites.

Figure 4 presents the results of the three-point bending tests conducted on virgin polypropylene (PP) and the reinforced composite materials, both with and without the coupling agent. The highest flexural strength value, 34.0 MPa (figure 4a), was observed in the formulation containing 40% w/w fiber and 4% w/w MAPP.

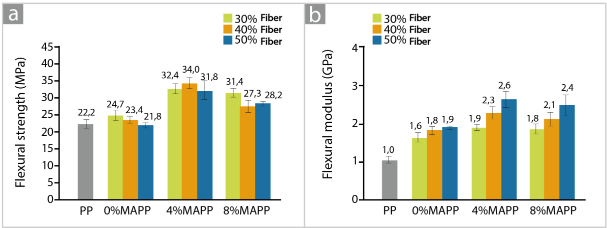

Figure 4. Flexural properties of the composite materials with and without a coupling agent: a) Flexural strength, and b) Flexural modulus.

In the case of the composites reinforced without a coupling agent, an 11.46% increase in flexural strength was observed with 30% w/w fiber, reaching 24.7 MPa. In contrast, with the addition of 40% w/w fiber and 4% w/w MAPP, the improvement rose to 53.34% (34.0 MPa) relative to virgin PP.

Flexural strength shows a slight increase with rising fiber content in composites without compatibilization; however, this trend reverses when the fiber loading exceeds 40% w/w. This decline has also been reported by other authors [27], who attribute it to the incompatibility between the hydrophobic polymer matrix and the hydrophilic reinforcement, as well as to less uniform fiber distribution at higher concentrations.

In contrast, compatibilization of the matrix with MAPP leads to a significant improvement in flexural strength, attributed to enhanced interfacial adhesion between the fiber and the matrix, which facilitates more efficient stress transfer along the fiber-matrix interface [23].

However, increasing the MAPP concentration to 8% w/w results in a slight decrease in flexural strength, a trend similar to that observed for tensile strength [28].

Regarding flexural modulus (figure 4b), the composites without a coupling agent exhibited a maximum increase of approximately 83% (1.9 GPa), while the compatibilized composites reached a 154% increase (2.6 GPa) both relative to virgin polypropylene (1.0 GPa).

These results highlight the improvement in flexural modulus achieved through fiber reinforcement, which increases significantly with the addition of the coupling agent.

According to the findings reported in [30], the behavior of the flexural modulus mirrors that of the elastic modulus, both increasing with the incorporation of MAPP. This indicates that these properties are sensitive to interfacial adhesion between the GAK fibers and the polypropylene matrix. A similar trend was also observed in [9], supporting the idea of more efficient stress transfer from the matrix to the fibers, along with increased composite stiffness. This is attributed to the inherently high elastic modulus of GAK fibers, which, at higher reinforcement levels, requires greater force to achieve equivalent deformation.

However, as previously noted, the coupling agent at a concentration of 8 wt% does not positively influence this property. This behavior is attributed to residual MAPP molecules that do not form covalent bonds with the fibers and the matrix [17].

Figure 5 presents the results of the impact strength tests, with a maximum value of 47.2 J/m observed for the composite containing 50 wt% fiber and 0 wt% MAPP. This corresponds toan increase of approximately 50% compared to virgin polypropylene (31.4 J/m).

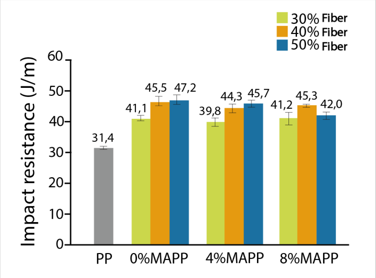

Figure 5. Impact strength of the manufactured composite materials.

According to the literature, the increase in impact strength is associated with mechanical interlocking at the fiber–matrix interface, which promotes more efficient stress transfer between the two phases. Additionally, the linear increase in this property with fiber content is attributed to the greater interfacial area available for stress distribution [23].

Likewise, the addition of reinforcement enhances energy absorption, driven by fracture mechanisms such as fiber pull-out, sliding, fragmentation, and partial fracture of the matrix material [31, 32].

However, the composites compatibilized with 4 wt% MAPP exhibit slightly lower impact strength compared to those without accoupling agent.

According to [33], this reduction is consistent with enhanced interaction and adhesion at the fiber–matrix interface, driven by the formation of a stronger chemical bond that replaces the previous mechanical interlocking. As interfacial bonding increases, a more rigid and cohesive composite structure is formed, resulting in greater stiffness and hardness but reduced toughness, thereby requiring less energy to initiate fracture.

Similarly, higher MAPP contents (8 wt%) do not enhance impact strength. According to [34], an excess of coupling agent may lead to the formation of a macromolecular layer within the composite, generating a weak region rich in MAPP that facilitates crack initiation and reduces the material's overall toughness.

Figure 6 presents the surface hardness results for the fabricated composites. The composite containing 50 wt% GAK fiber and no MAPP exhibited a 5% increase in hardness (78.13 Shore D) compared tovirgin polypropylene (74.13 Shore D).

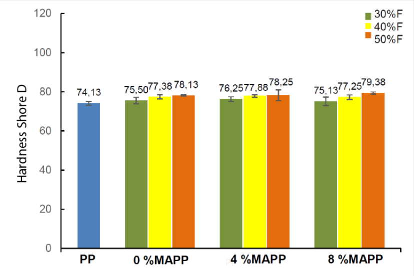

Figure 6. Shore D surface hardness of the fabricated composite materials.

This increase is attributed to the reinforcing effect of the GAK fibers embedded in the polymer matrix. When 8 wt% MAPP is incorporated as a compatibilizing agent, at the same fiber loading, a progressive increase in hardness is observed, reaching a maximum value of 79.38 Shore D. This represents a 7% improvement compared to virgin polypropylene.

Although the measured hardness values remain close to that of virgin polypropylene, this is expected since the test assesses only the surface of the composite, where PP is the dominant phase. Nonetheless, the slight increase suggests that the compatibilizer enhances interfacial adhesion between the fibers and the matrix, contributing to improved surface cohesion and greater resistance to penetration and wear.

Figure 7 presents the DSC thermograms of the fabricated composite materials, both with and without the coupling agent, using virgin polypropylene as a reference.

These tests were used to assess the influence of fiber content and MAPP concentration on the thermal behavior of the composites.

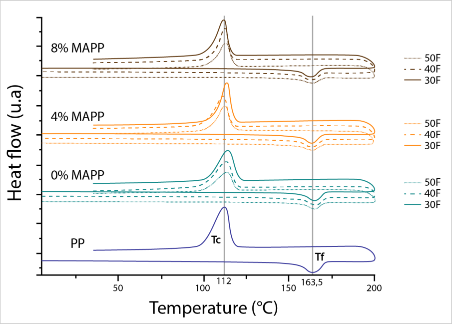

Figure 7. DSC curves of the fabricated composite materials.

The melting and crystallization temperatures of virgin polypropylene were observed around 163.5 °C and 112 °C, respectively. Upon incorporating the reinforcement and the coupling agent, no significant change in melting temperature was observed compared to virgin PP, with only a slight increase of about2 °C.

This slight increase is attributed to the fibers' higher heat absorption capacity compared to the polymer. However, the addition of MAPP at 4 wt% and 8 wt% did not havea significant effect on this property [9], [35, 36].

Regarding crystallization temperature, an increase in fiber content results in a slight upward shift in this property, as the fibers serve as heterogeneous nucleation sites that accelerate the crystallization process [9], [37]. Additionally, incorporating higher amounts of bamboo fiber reduces the free volume available for polymer chain mobility, thereby promoting crystallization at higher temperatures during the cooling cycle [38].

However, as shown in Table 1, the enthalpy of fusion decreases with increasing reinforcement content, as the fibers act as inert fillers and, additionally, reduce the proportion of polypropylene in the composite, thereby lowering the energy required to induce melting [39].

Nevertheless, this thermal property exhibits higher values in composites compatibilized with 4 wt% MAPP compared to those with 0 wt% and 8 wt%, indicating that, at this concentration, fiber–matrix interactions are enhanced, thereby improving the thermal stability of the composites.

On the other hand, when MAPP is added at a concentration of 8 wt%, the presence of residual coupling agent in the matrix reduces thermal stability, as MAPP has a lower melting temperature than virgin polypropylene [35].

A similar trend is observed for crystallization enthalpy, which decreases with increasing reinforcement content due to the lower proportion of polypropylene in the composite, as shown in Table 1 [35].

Table 1. Fusion and crystallization enthalpies of the fabricated composite materials.

Sample	Fusion enthalpy (J/g)	Crystallization enthalpy (J/g)
PP	114.5	104
30 % p/p F/0 % p/p MAPP	79.95	78.16
40 % p/p F/0 % p/p MAPP	65.32	75.44
50 % p/p F/0 % p/p MAPP	55.11	51.7
30 % p/p F/0 % p/p MAPP	75.95	71.21
40 % p/p F/0 % p/p MAPP	72.69	83.39
50 % p/p F/0 % p/p MAPP	77.8	72.9
30 % p/p F/0 % p/p MAPP	72.04	81.51
40 % p/p F/0 % p/p MAPP	71.94	60.96
50 % p/p F/0 % p/p MAPP	58.94	49.88

In the composites compatibilized with 4 wt% MAPP, crystallization enthalpy follows a similar trend to that observed for fusion enthalpy, indicating improved interfacial adhesion between the fibers and the matrix.

At a MAPP concentration of 8 wt%, the same trend observed for fusion enthalpy is maintained.

Figure 8 presents the DTG curves obtained from TGA analyses performed on a sheet of virgin polypropylene and on reinforced composites with and without the coupling agent, all evaluated at a heating rate of 30 °C/min.

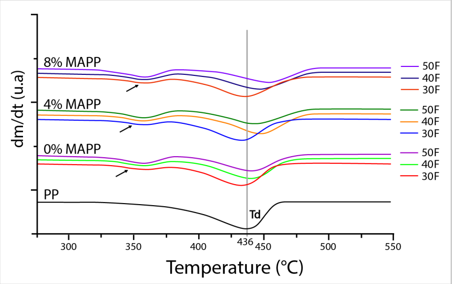

Figure 8. DTG curves of the fabricated composite materials.

The polypropylene sheet exhibits single-stage thermal decomposition, initiating at approximately 365 °C and completing around 436 °C. When bamboo fibers are incorporated, a second degradation stage appears at lower temperatures (see arrow), corresponding to the thermal decomposition of the reinforcement. This secondary stage becomes more pronounced with increasing fiber content, due to the breakdown of low-molecular-weight constituents in the natural fibers, primarily cellulose and hemicellulose, which are more abundant at higher reinforcement levels [35].

However, as shown in the graph and previously discussed, increasing the fiber content slightly enhances the thermal stability of the composites [9] [35]. Additionally, the degradation temperatures of the reinforced composites, both with and without the coupling agent, are slightly higher than those of virgin polypropylene, indicating a slower degradation process. This behavior is attributed to the greater heat absorption capacity of the reinforcement, which is further amplified in composites compatibilized with MAPP, reflecting improved interfacial adhesion due to more effective fiber–matrix bonding [35], [37].

4. Conclusions

The tensile strength of the fabricated composites decreased with increasing fiber content. In contrast, the elastic modulus increased significantly up to 322% with the incorporation of 4 wt% MAPP.

Scanning electron microscopy confirmed that the incorporation of MAPP enhances the fiber–matrix interface by promoting stronger interactions between the two phases. This finding aligns with the tensile test results, which showed improved mechanical performance in compatibilized composites.

Flexural strength and flexural modulus also improved relative to the neat polypropylene matrix, with maximum increases of 55% and 154%, respectively, observed in composites containing MAPP. Similarly, impact resistance increased by up to 50% with the addition of GAK fibers, even in the absence of the coupling agent, specifically in the formulation with 50 WT% fiber and 0 wt% MAPP.

Regarding surface hardness, a slight increase of 7% was observed compared to virgin polypropylene in the composite containing 50 wt% fiber and 8 wt% MAPP. This result highlights the reinforcing effect of the GAK fibers and also suggests that the compatibilizer enhances fiber–matrix interfacial adhesion, contributing to improved resistance to penetration and wear.

The incorporation of GAK fibers and MAPP had little effect on melting and crystallization temperatures. However, fusion and crystallization enthalpies tended to decrease with increasing fiber and compatibilizer content, likely due to the reduced proportion of polypropylene available for these phase transitions.

The degradation temperatures of the polymer increased slightly with the incorporation of GAK fibers and MAPP. This effect is attributed to the higher energy absorption capacity of the fibers and the improved interfacial adhesion between the fiber and matrix provided by the compatibilizer. Together, these factors contribute to a greater energy requirement for the thermal degradation of the polymer.

Overall, higher MAPP concentrations (8 wt%) did not lead to further improvements in mechanical or thermal performance, confirming that 4 wt% is the optimal compatibilizer content.

The addition of GAK fibers and the coupling agent (MAPP) to polypropylene modified the mechanical behavior of the matrix, resulting in stiffer composites with enhanced flexural strength and greater energy absorption capacity under impact. Based on the results of this study, the best-performing formulation corresponds to the composite containing 50 wt% GAK fiber and 4 wt% MAPP.

This composite material is recommended for application in the automotive industry for the fabrication of semi-structural components, including door panels, seat backs, trunk linings, floor trays, and dashboards, which are traditionally manufactured from neat polypropylene in many vehicle models.

Reinforcing these components with GAK fibers would improve their mechanical performance relative to the virgin polypropylene matrix, while also contributing to overall vehicle weight reduction.

Acknowledgments

The authors gratefully acknowledge the Research Center for Development and Innovation (CIDI) at the Pontificia Bolivariana University, Medellín campus, for funding this research under project reference 439B-08/15-18. We also extend our sincere thanks to the Agricultural Engineering Research Group at the National University of Colombia, Medellín campus, for their valuable support in supplying the raw materials used in this study.

Contributor Roles

- **Leidy Quintero:** Conceptualization, investigation, methodology, validation, formal analysis, writing – original draft, writing – review and editing, visualization.
- **Alexis García:** Writing – original draft, writing – review and editing, formal analysis, validation.
- **Alejandro Alcaraz:** Writing – original draft, writing – review and editing, formal analysis, validation.
- **Jorge Fajardo:** Review and editing, formal analysis, validation.
- **Luis Cruz:** Conceptualization, writing – original draft, writing – review and editing, project administration, supervision, funding acquisition.

References

[1] H. Abdul Khalil, I. Bhat, M. Jawaid, A. Zaidon, D. Hermawan, and Y. Hadi, “Bamboo fibre reinforced biocomposites: A

review,” *Materials & Design*, vol. 42, pp. 353–368, Dec. 2012. [Online]. Available: https://doi.org/10.1016/j.matdes.2012.06.015

[2] N. Kumar and D. Das, “Fibrous biocomposites from nettle (girardinia diversifolia) and poly(lactic acid) fibers for automotive dashboard panel application,” *Composites Part B: Engineering*, vol. 130, pp. 54–63, Dec. 2017. [Online]. Available: https://doi.org/10.1016/j.compositesb.2017.07.059

[3] Y. Wu, C. Xia, L. Cai, A. C. García, and S. Q. Shi, “Development of natural fiber-reinforced composite with comparable mechanical properties and reduced energy consumption and environmental impacts for replacing automotive glass-fiber sheet molding compound,” *Journal of Cleaner Production*, vol. 184, pp. 92–100, May 2018. [Online]. Available: https://doi.org/10.1016/j.jclepro.2018.02.257

[4] L. C. Botero Cortés, *Reproducción de la Guadua angustifolia por el método de chusquines*. Organisation Internationale pour le Bambou et le Rotin. [Online]. Available: https://upsalesiana.ec/ing34ar2r4

[5] L. Osorio, E. Trujillo, A. Van Vuure, and I. Verpoest, “Morphological aspects and mechanical properties of single bamboo fibers and flexural characterization of bamboo/ epoxy composites,” *Journal of Reinforced Plastics and Composites*, vol. 30, no. 5, pp. 396–408, Mar. 2011. [Online]. Available: https://doi.org/10.1177/0731684410397683

[6] A. U. Md Shah, M. T. H. Sultan, M. Jawaid, F. Cardona, and A. R. Abu Talib, “A review on the tensile properties of bamboo fiber reinforced polymer composites,” *BioResources*, vol. 11, no. 4, pp. 10 654–10 676, Sep. 2016. [Online]. Available: http://dx.doi.org/10.15376/biores.11.4.Shah

[7] V. K. Thakur and M. K. Thakur, “Processing and characterization of natural cellulose fibers/thermoset polymer composites,” *Carbohydrate Polymers*, vol. 109, pp. 102–117, Aug. 2014. [Online]. Available: https://doi.org/10.1016/j.carbpol.2014.03.039

[8] F. M. AL-Oqla, S. Sapuan, M. Ishak, and A. Nuraini, “Predicting the potential of agro waste fibers for sustainable automotive industry using a decision making model,” *Computers and Electronics in Agriculture*, vol. 113, pp. 116–127, Apr. 2015. [Online]. Available: https://doi.org/10.1016/j.compag.2015.01.011

[9] C. Wang and S. Ying, “A novel strategy for the preparation of bamboo fiber reinforced polypropylene composites,” *Fibers and Polymers*, vol. 15, no. 1, pp. 117–125, Jan. 2014. [Online]. Available: https://doi.org/10.1007/s12221-014-0117-z

[10] F. M. AL-Oqla and S. Sapuan, “Natural fiber reinforced polymer composites in industrial applications: feasibility of date palm fibers for sustainable automotive industry,” *Journal of Cleaner Production*, vol. 66, pp. 347–354, Mar. 2014. [Online]. Available: https://doi.org/10.1016/j.jclepro.2013.10.050

[11] M. Sood and G. Dwivedi, “Effect of fiber treatment on flexural properties of natural fiber reinforced composites: A review,” *Egyptian Journal of Petroleum*, vol. 27, no. 4, pp. 775–783, Dec. 2018. [Online]. Available: https://doi.org/10.1016/j.ejpe.2017.11.005

[12] T. H. Nam, S. Ogihara, H. Nakatani, S. Kobayashi, and J. I. Song, “Mechanical and thermal properties and water absorption of jute fiber reinforced poly(butylene succinate) biodegradable composites,” *Advanced Composite Materials*, vol. 21, no. 3, pp. 241–258, Jun. 2012. [Online]. Available: https://doi.org/10.1080/09243046.2012.723362

[13] A. A. El-Fattah, A. G. M. EL Demerdash, W. A. Alim Sadik, and A. Bedir, “The effect of sugarcane bagasse fiber on the properties of recycled high density polyethylene,” *Journal of Composite Materials*, vol. 49, no. 26, pp. 3251–3262, Dec. 2014. [Online]. Available: https://doi.org/10.1177/0021998314561484

[14] S. R. Ferreira, F. d. A. Silva, P. R. L. Lima, and R. D. Toledo Filho, “Effect of fiber treatments on the sisal fiber properties and fiber–matrix bond in cement based systems,” *Construction and Building Materials*, vol. 101, pp. 730–740, Dec. 2015. [Online]. Available: https://doi.org/10.1016/j.conbuildmat.2015.10.120

[15] A. El-Sabbagh, “Effect of coupling agent on natural fibre in natural fibre/polypropylene composites on mechanical and thermal behaviour,” *Composites Part B: Engineering*, vol. 57, pp. 126–135, Feb. 2014. [Online]. Available: https://doi.org/10.1016/j.compositesb.2013.09.047

[16] W. Chunhong, L. Shengkai, and Y. Zhanglong, “Mechanical, hygrothermal ageing and moisture absorption properties of bamboo fibers reinforced with polypropylene composites,” *Journal of Reinforced Plastics and Composites*, vol. 35, no. 13, pp. 1062–1074, Mar. 2016. [Online]. Available: https://doi.org/10.1177/0731684416637681

[17] W. Liu, T. Chen, X. Wen, R. Qiu, and X. Zhang, "Enhanced mechanical properties and water resistance of bamboo fiber–unsaturated polyester composites coupled by isocyanatoethyl methacrylate," *Wood Science and Technology*, vol. 48, no. 6, pp. 1241–1255, Sep. 2014. [Online]. Available: https://doi.org/10.1007/s00226-014-0668-6

[18] M. Das and D. Chakraborty, "Evaluation of improvement of physical and mechanical properties of bamboo fibers due to alkali treatment," *Journal of Applied Polymer Science*, vol. 107, no. 1, pp. 522–527, Sep. 2007. [Online]. Available: https://doi.org/10.1002/app.26155

[19] J. T. Kang and S. H. Kim, "Improvement in the mechanical properties of polylactide and bamboo fiber biocomposites by fiber surface modification," *Macromolecular Research*, vol. 19, no. 8, pp. 789–796, Jul. 2011. [Online]. Available: https://doi.org/10.1007/s13233-011-0807-y

[20] Z. Ying-Chen, W. Hong-Yan, and Q. Yi-Ping, "Morphology and properties of hybrid composites based on polypropylene/polylactic acid blend and bamboo fiber," *Bioresource Technology*, vol. 101, no. 20, pp. 7944–7950, Oct. 2010. [Online]. Available: https://doi.org/10.1016/j.biortech.2010.05.007

[21] O. Faruk, A. K. Bledzki, H.-P. Fink, and M. Sain, "Biocomposites reinforced with natural fibers: 2000–2010," *Progress in Polymer Science*, vol. 37, no. 11, pp. 1552–1596, Nov. 2012. [Online]. Available: https://doi.org/10.1016/j.progpolymsci.2012.04.003

[22] J. Fajardo Seminario, L. Quintero, J. García, D. Londoño Mesa, and L. Cruz, "Estudio de las propiedades mecánicas de los haces de fibras de *Guadua angustifolia* kunth ecuatoriana extraída a partir de diferentes métodos," in *XIII Congreso Nacional de Corrosión y IV Congreso Internacional de Integridad estructural*, Aug. 2016, xIII Congreso Nacional de Corrosión y IV Congreso Internacional de Materiales e Integridad Estructural, ASCOR 2016 ; Conference date: 24-08-2016 Through 26-08-2016. [Online]. Available: https://upsalesiana.ec/ing34ar2r23

[23] S. K. Chattopadhyay, R. K. Khandal, R. Uppaluri, and A. K. Ghoshal, "Bamboo fiber reinforced polypropylene composites and their mechanical, thermal, and morphological properties," *Journal of Applied Polymer Science*, vol. 119, no. 3, pp. 1619–1626, Aug. 2010. [Online]. Available: https://doi.org/10.1002/app.32826

[24] A. N. Kasim, M. Z. Selamat, N. Aznan, S. N. Sahadan, M. A. Mohd Daud, R. Jumaidin, and S. Salleh, "Effect of pineapple leaf fiber loading on the mechanical properties of pineapple leaf fiber – polypropylene composite," *Jurnal Teknologi*, vol. 77, no. 21, Dec. 2015. [Online]. Available: https://doi.org/10.11113/jt.v77.6617

[25] C. Kakou, F. Arrakhiz, A. Trokourey, R. Bouhfid, A. Qaiss, and D. Rodrigue, "Influence of coupling agent content on the properties of high density polyethylene composites reinforced with oil palm fibers," *Materials & Design*, vol. 63, pp. 641–649, Nov. 2014. [Online]. Available: https://doi.org/10.1016/j.matdes.2014.06.044

[26] S. Nahar, R. Khan, K. Dey, B. Sarker, A. Das, and S. Ghoshal, "Comparative studies of mechanical and interfacial properties between jute and bamboo fiber-reinforced polypropylene-based composites," *Journal of Thermoplastic Composite Materials*, vol. 25, no. 1, pp. 15–32, Jul. 2011. [Online]. Available: https://doi.org/10.1177/0892705711404725

[27] M. R. Rahman, S. Hamdan, D. M. A. Hashim, M. S. Islam, and H. Takagi, "Bamboo fiber polypropylene composites: Effect of fiber treatment and nano clay on mechanical and thermal properties," *Journal of Vinyl and Additive Technology*, vol. 21, no. 4, pp. 253–258, Jul. 2014. [Online]. Available: https://doi.org/10.1002/vnl.21407

[28] M. A. Fuqua and C. A. Ulven, "Preparation and characterization of polypropylene composites reinforced with modified lignocellulosic corn fiber," in *2008 Providence, Rhode Island, June 29 - July 2, 2008*, ser. prov2008. American Society of Agricultural and Biological Engineers, 2008. [Online]. Available: http://doi.org/10.13031/2013.24770

[29] S. Huda and Y. Yang, "A novel approach of manufacturing light-weight composites with polypropylene web and mechanically split cornhusk," *Industrial Crops and Products*, vol. 30, no. 1, pp. 17–23, Jul. 2009. [Online]. Available: https://doi.org/10.1016/j.indcrop.2008.12.007

[30] R. Karnani, *Kenaf-reinforced polypropylene composites*. Departmanet of Chemical Engineering, Michigan State, 1996. [Online]. Available: https://upsalesiana.ec/ing34ar2r31

[31] M. A. Hidalgo-Salazar, M. F. Muñoz, and J. H. Mina, "Influence of incorporation of natural fibers on the physical, mechanical, and thermal properties of composites ldpe-al reinforced with fique fibers," *International Journal of Polymer Science*, vol. 2015, pp. 1–8, 2015. [Online]. Available: https://doi.org/10.1155/2015/386325

[32] N.-M. Barkoula, B. Alcock, N. Cabrera, and T. Peijs, "Fatigue properties of highly oriented polypropylene tapes and all-polypropylene composites," *Polymers and Polymer Composites*, vol. 16, no. 2, pp. 101–113, Feb. 2008. [Online]. Available: https://doi.org/10.1177/096739110801600203

[33] L. Rodríguez Sepulveda, *Elaboración de un material biocompuesto a partir de la fibra de plátano*. Universidad Nacional de Manizales, 2014. [Online]. Available: https://upsalesiana.ec/ing34ar2r35

[34] X. Zhou, Y. Yu, Q. Lin, and L. Chen, "Effects of maleic anhydride-grafted polypropylene (mapp) on the physico-mechanical properties and rheological behavior of bamboo powder-polypropylene foamed composites," *BioResources*, vol. 8, no. 4, Oct. 2013. [Online]. Available: http://dx.doi.org/10.15376/biores.8.4.6263-6279

[35] S.-Y. Lee, I.-A. Kang, B.-S. Park, G.-H. Doh, and B.-D. Park, "Effects of filler and coupling agent on the properties of bamboo fiber-reinforced polypropylene composites," *Journal of Reinforced Plastics and Composites*, vol. 28, no. 21, pp. 2589–2604, Sep. 2008. [Online]. Available: https://doi.org/10.1177/0731684408094070

[36] N. T. Phuong, C. Sollogoub, and A. Guinault, "Relationship between fiber chemical treatment and properties of recycled pp/bamboo fiber composites," *Journal of Reinforced Plastics and Composites*, vol. 29, no. 21, pp. 3244–3256, Aug. 2010. [Online]. Available: https://doi.org/10.1177/0731684410370905

[37] V. Srebrenkoska, G. B. Gaceva, M. Avella, M. E. Ericco, and G. Gentile, "Utilization of recycled polypropylene for production of eco-composites," *Polymer-Plastics Technology and Engineering*, vol. 48, no. 11, pp. 1113–1120, Oct. 2009. [Online]. Available: https://doi.org/10.1080/03602550903147247

[38] J. Lisperguer, X. Bustos, Y. Saravia, C. Escobar, and H. Venegas, "Efecto de las características de harina de madera en las propiedades físico-mecánicas y térmicas de polipropileno reciclado," *Maderas. Ciencia y tecnología*, no. ahead, pp. 0–0, 2013. [Online]. Available: http://dx.doi.org/10.4067/S0718-221X2013005000025

[39] I. Baroulaki, O. Karakasi, G. Pappa, P. Tarantili, D. Economides, and K. Magoulas, "Preparation and study of plastic compounds containing polyolefins and post used newspaper fibers," *Composites Part A: Applied Science and Manufacturing*, vol. 37, no. 10, pp. 1613–1625, Oct. 2006.

Scientific Paper / Artículo Científico

UNIVERSIDAD POLITÉCNICA SALESIANA ECUADOR
INGENIUS
Revista de Ciencia y Tecnología
https://doi.org/10.17163/ings.n34.2025.03
pISSN: 1390-650X / eISSN: 1390-860X

CHARACTERIZATION OF GRAPHENE OXIDE SYNTHESIZED THROUGH A MODIFIED HUMMERS METHOD

CARACTERIZACIÓN DE ÓXIDO DE GRAFENO SINTETIZADO MEDIANTE UN MÉTODO DE HUMMERS MODIFICADO

Wilson Navas-Pinto[1,*,2], Duncan E. Cree[3], Lee D. Wilson[4],
Germán Omar Barrionuevo[1,5], Xavier Sánchez-Sánchez[1], Héctor Calvopiña[1]

Received: 08-10-2024, Received after review: 25-03-2025, Accepted: 27-03-2025, Published: 01-07-2025

Abstract

Graphene oxide (GO) has garnered significant interest due to its exceptional and tunable properties, which make it a promising candidate for a wide range of engineering applications, including composite material fabrication and water treatment. In this study, GO was synthesized from graphite flakes using a modified Hummers method involving a reduced amount of sulfuric acid. The resulting material was characterized using scanning electron microscopy (SEM), Fourier transform infrared spectroscopy (FTIR), and X-ray photoelectron spectroscopy (XPS). These techniques enabled a clear differentiation between the morphology of the synthesized GO and that of the original graphite. The GO exhibited a substantially altered structure, with increased thickness likely due to the incorporation of oxygen-containing functional groups on its basal plane.

Resumen

El óxido de grafeno ha despertado un creciente interés debido a sus propiedades únicas y potencialmente ajustables, las cuales abarcan aplicaciones que van desde la fabricación de materiales compuestos hasta el tratamiento de aguas. Por esta razón, se desarrolló un proceso de síntesis de óxido de grafeno basado en el método de Hummers con una reducción en la cantidad de ácido sulfúrico empleada. El material obtenido fue caracterizado mediante diferentes técnicas, incluyendo microscopía electrónica de barrido (MEB), espectroscopía infrarroja transformada de Fourier (IR-TF) y espectrometría fotoelectrónica por rayos X (XPS). Estas técnicas experimentales permitieron distinguir las diferencias morfológicas entre el óxido de grafeno sintetizado y el grafito utilizado como precursor. Adicionalmente, se determinó la composición química del polvo obtenido, así como la relación entre carbono y oxígeno, con el fin de evaluar su viabilidad para aplicaciones específicas. Se observó que la morfología del óxido de grafeno difiere significativamente de la del grafito de partida. En particular, el espesor de las láminas de óxido de grafeno se incrementó debido a la incorporación de grupos funcionales oxigenados en el plano basal.

[1,*] Department of Energy and Mechanical Sciences, Universidad de las Fuerzas Armadas ESPE, Quito, Ecuador
Corresponding Author ✉: wmnavas1@espe.edu.ec.

[2] Department of Mechanical Engineering University of Saskatchewan, Saskatoon, Canadá

[3] Department of Mechanical Engineering, McMaster University, Hamilton, Canadá

[4] Department of Chemistry, University of Saskatchewan, Saskatoon, Canadá

[5] Engineering Department, Universidad Católica de Uruguay, Montevideo, Uruguay

Suggested citation: Navas-Pinto, W.; Cree, D.; Wilson, L.; Barrionuevo, G.; Sánchez-Sánchez, X. and Calvopiña, H. "Characterization of graphene oxide synthesized through a modified Hummers method," *Ingenius, Revista de Ciencia y Tecnología*, N.° 34, pp. 31-42, 2025, DOI: https://doi.org/10.17163/ings.n34.2025.03.

FTIR analysis confirmed the presence of characteristic functional groups such as hydroxyl, carbonyl, and carboxyl. XPS analysis revealed that the elemental composition of the synthesized GO consisted of approximately 69.7% carbon and 29.9% oxygen, with a trace amount of sulfur attributed to the reagents used in the synthesis. The observed changes in morphology and composition suggest the successful synthesis of GO with potential for functionalization and application in diverse engineering contexts.

Keywords: Graphene oxide, synthesis, functional groups, FTIR, SEM, XPS

El espectro FTIR del óxido de grafeno confirmó la presencia de diversos grupos funcionales, como el hidroxilo (-OH), carbonilo (C-O) y carboxilo (-COOH). Por su parte, la espectroscopía XPS reveló que la composición química del óxido de grafeno obtenido fue de 69,7 % de carbono y 29,9 % de oxígeno, con una traza mínima de azufre atribuida a los reactivos empleados durante el proceso de síntesis.

Palabras clave: óxido de grafeno, síntesis, grupos funcionales, IR-TF, MEB, XPS

1. Introduction

Graphene oxide (GO) consists of a single-atom-thick hexagonal carbon basal plane decorated with randomly distributed oxygen-containing functional groups [1, 2], as illustrated in Figure 1. Previous studies have reported that the thickness of GO typically ranges between 0.7 and 1.6 nm [3, 4] while its lateral dimensions can vary significantly from a few nanometers to several micrometers [1], [5].

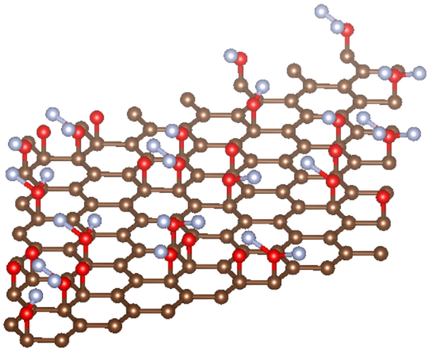

Figure 1. Schematic representation of the graphene oxide (GO) structure

Numerous studies have been conducted to assess the feasibility of graphene oxide (GO) in a broad range of applications, owing to its high surface area [6], favorable mechanical properties [7, 8], the presence of diverseoxygen-containing functional groups [9–11], and even its potential antibacterial activity [12–14]. As a result, GO has been explored for use inflexible electronic sensors [15, 16], supercapacitors [17–19], energy storage and conversion systems [20, 21], biomedical devices [22, 23], composite materials [24, 25], water treatment technologies [26], and microbial activity control [27].

For instance, Liang et al. [16] developed reduced graphene oxide (rGO) humidity sensors and reported rapid response and recovery times, attributed to the inhibition of water molecule aggregation due to the structural characteristics of rGO. Similarly, Kerli et al. [17] synthesized silver-doped rGO polyaniline (PANI) composites and evaluated their specific capacitance, observing a maximum improvement of 17% compared to conventional materials. Eftekhari et al. [21] investigated the fabrication of GO-based membranes for electrochemical energy storage, highlighting the superior diffusion of water molecules through GO, which enhanced membrane performance in acidic electrolyte environments. GO has also been incorporated into polymer matrices at low concentrations, resulting in improved mechanical properties compared to neat polymer samples [24]. In biomedical applications, GO has demonstrated potential for promoting periodontal tissue regeneration and reducing inflammation when integrated into collagen scaffolds [23]. Additionally, GO-based membranes have been tested for water filtration, where the incorporation of GO into chitosan enhanced both water permeability and dye rejection properties [26]. Regarding antimicrobial activity, Yu et al. [27] evaluated the effectiveness of different GO solutions in controlling the proliferation of Streptococcus mutans and found that GO particle size had a direct influence on antimicrobial efficacy.

The synthesis of graphene oxide (GO) involves a strong oxidation process in which graphite flakes are treated with various oxidizing agents as raw materials [11], [28]. This procedure results in the formation of graphite oxide, from which GO is subsequently obtained through an exfoliation or sonication step that separates individual layers to yield a single-layered material [21], [29]. The mechanical properties of GO are highly dependent on its synthesis conditions, which influence its structure, degree of oxidation, chemical composition, and carbon-to-oxygen (C/O) ratio. Several studies have reported the mechanical performance of monolayer GO; for instance, its tensile strength has been measured at approximately 77 ± 20 MPa, and its elastic modulus falls within the range of 150 to 250 GPa [2], [30]. In comparison, pristine graphene exhibits significantly higher mechanical properties, with a tensile strength ranging from 50 to 60 GPa and an elastic modulus close to 1 TPa [31]. Despite its relatively lower mechanical strength, GO exhibits superior chemical reactivity due to the presence of functional groups on its basal plane, which makes it highly amenable to bonding with other materials. This reactivity facilitates the development of advanced composite and hybrid materials [32, 33].

Graphene oxide (GO) has been synthesized using various methods, each differing primarily in the type and concentration of oxidizing agents employed [34–38], as illustrated in Figure 2.

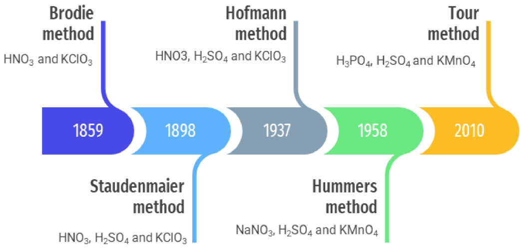

Figure 2. Timeline of GO synthesis methods and their corresponding oxidizing agents

In 1859, Brodie [34] conducted the first documented attempt to oxidize graphite. For this purpose, a solution was prepared using a 3:1 ratio of potassium chlorate ($KClO_3$) and nitric acid (HNO_3), which was then mechanically stirred with a measured quantity of graphite. Once a homogeneous mixture was achieved, the solution was heated to 60 °C and continuously stirred for 72 hours or until the evolution of yellow fumes had ceased. Following the reaction, multiple washing steps were carried out by adding deionized water and decanting the mixture to eliminate any residual unreacted reagents. The resulting substance, initially referred to as graphitic acid, was found to be partially soluble in deionized water, but insoluble in both pure water and acidic solutions.

Staundemaier [35] reported an alternative method for synthesizing graphene oxide (GO) by incorporating sulfuric acid (H_2SO_4) into the original solution developed by Brodie. In this procedure, a mixture of H_2SO_4 and nitric acid (HNO_3) in a 1:3 volume ratio was stirred until the emission of fumes was observed. The fuming mixture was then added to graphite flakes, which were maintained in an ice bath and stirred for 30 minutes. Subsequently, potassium chlorate ($KClO_3$) was slowly added to prevent a rapid increase in temperature. The solution was then transferred to ambient conditions and stirred continuously for an additional 96 hours. Finally, several decantation and washing steps were carried out using hydrochloric acid (HCl) and demineralized water to remove any supernatant.

Similarly, Hofmann and König [36] carried out an oxidation process on graphite flakes, introducing temperature variation as a key parameter during the synthesis. Initially, a solution consisting of sulfuric acid (H_2SO_4) and nitric acid (HNO_3) in a 1:3 volume ratio was prepared and placed in an ice bath to suppress gas evolution. Graphite flakes were then added gradually, with continuous stirring maintained throughout the cooling stage. Subsequently, potassium chlorate ($KClO_3$) was slowly introduced over a period of approximately 30 minutes. The resulting mixture was then subjected to magnetic stirring for 96 hours at room temperature. Finally, a hydrochloric acid (HCl) solution at 5% by volume was added to eliminate residual sulfate ions, followed by multiple washing steps withdeionized water.

In 1958, Hummers and Offeman [37] introduced a direct method for synthesizing graphene oxide (GO) using sulfuric acid (H_2SO_4), sodium nitrate ($NaNO_3$), and potassium permanganate ($KMnO_4$) as oxidizing agents. In this procedure, a beaker was placed in an ice bath prior to the addition of 100 g of graphite flakes, 50 g of $NaNO_3$, and 2.3 liters of concentrated H_2SO_4. The mixture was vigorously stirred until a homogeneous dispersion was achieved. Subsequently, 300 g of $KMnO_4$ was gradually added while maintaining the temperature below 20 °C The reaction mixture was then transferred to an oil bath at 35 °C and stirred for 30 minutes. This step was followed by the addition of 4.6 liters of demineralized water, which induced vigorous effervescence and elevated the temperature to approximately 98 °C. Next, 14 liters of a solution composed of warm water and 3% hydrogen peroxide (H_2O_2) were added to neutralize any remaining oxidizing agents. The final steps involved repeated washing with deionized water, followed by centrifugation and vacuum drying of the resulting slurry at 40 °C.

In 2010, Marcano et al. [38] developed a modified synthesis route for graphene oxide (GO) based on the Hummers method. In this approach, the amount of potassium permanganate ($KMnO_4$) was increased, and the reaction was carried out using a 9:1 volumetric mixture of sulfuric acid (H_2SO_4) and phosphoric acid (H_3PO_4). This modification effectively suppressed the generation of hazardous fumes and yielded GO with an increased oxygen content.

In addition to conventional methods, several novel approaches have been explored to synthesize graphene oxide (GO) powder. For instance, Chen et al. [39] proposed a modified version of the Hummers method in which sodium nitrate ($NaNO_3$) was excluded from the reaction mixture to prevent the formation of potentially toxic nitrogen-based gases. This alternative protocol effectively oxidized graphite, yielding results comparable to those obtained with the original Hummers method.

Given the extensive research dedicated to synthesizing graphene oxide (GO) from graphite and its potential applications in future engineering technologies, this study focuses on the characterization and morphological analysis of GO powder synthesized via a modified Hummers method. Comprehensive characterization of the resulting material was carried out using scanning electron microscopy (SEM), Fourier-transform infrared spectroscopy (FTIR), and X-ray photoelectron spectroscopy (XPS).

2. Materials and Methods

2.1. Materials

Graphite powder (325 mesh, 99.9995% metals basis) was obtained from Thermo Scientific Chemicals. Potassium permanganate ($KMnO_4$), sodium nitrate ($NaNO_3$), and concentrated sulfuric acid (H_2SO_4) were supplied by Fisher Chemical^{TM}. All reagents were used as received without further purification.

2.2. GO Synthesis

Graphene oxide (GO) was synthesized using a modified Hummers method, in which the amount of sulfuric acid (H_2SO_4) was reduced to minimize the residual sulfur content in the final product. The procedure began by adding 5 g of graphite powder, 2.5 g of sodium nitrate ($NaNO_3$), and 105 mL of concentrated H_2SO_4 to a beaker. The quantity of sulfuric acid was decreased by approximately 10% compared to the original Hummers method [37] to assess the extent to which this modification reduces the presence of residual sulfurin the synthesized GO [40]. The resulting mixture was magnetically stirred for 45 minutes until a homogeneous solution was obtained. It was then placed in an ice bath and stirred for an additional hour. Subsequently, 15 g of potassium permanganate ($KMnO_4$), was gradually added with continuous stirring, carefully maintaining the temperature to prevent a rapid rise. The solution was then transferred to a cold-water bath at approximately 15 °C and stirred for another 30 minutes, with ice added as necessary to keep the temperature below 20 °C. The reaction mixture was next placed in a warm water bath (approximately 35 °C), and 230 mL of deionized water was added slowly in small increments. After the complete addition, the solution was transferred to an oil bath at 98 °C and stirred for 20 minutes. This was followed by the addition of 400 mL of distilled water, which caused a visible color change from dark brown to light brown, with stirring continued for an additional 20 minutes. Subsequently, 50 mL of hydrogen peroxide (H_2O_2) was introduced to terminate the reaction. Finally, the suspension was stirred at room temperature for 12 hours to complete the oxidation process, see figure 3.

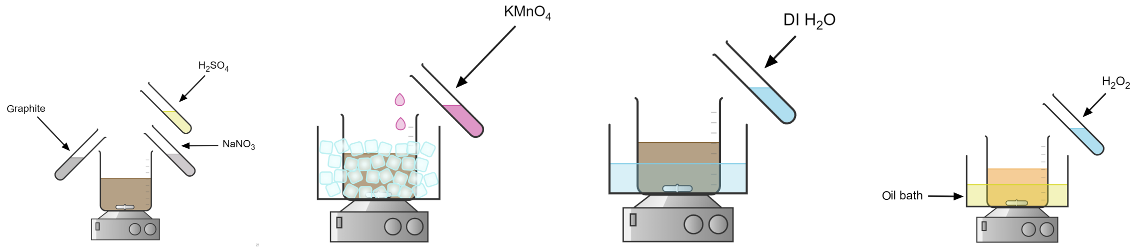

(a) (b) (c) (d)

Figure 3. Schematic representation of the GO synthesis process. a) Initial stage involving the addition of the primary reagents. b) Ice bath stage, during which potassium permanganate is gradually introduced. c) Addition of deionized water to the reaction mixture.d) Final stage involving the addition of hydrogen peroxide to complete the oxidation process

Once the synthesis was complete, a multi-step purification process was carried out to remove unreacted chemicals and ensure the appropriate purity of the synthesized graphene oxide (GO). Each initial purification stage involved the addition of 500 mL of deionized water, followed by stirring for 60 minutes. The suspension was then allowed to precipitate, and the supernatant was carefully decanted. This stage was repeated four times, during which a progressive darkening of the solution was observed. Subsequently, 200 mL of a 30% (v/v) hydrochloric acid (HCl) solution was added and stirred for 60 minutes. After precipitation, the supernatant was again removed. This was followed by the addition of 200 mL of ethanol (C_2H_5OH), which was stirred for an additional hour before decanting. Two final washing steps were conducted using 400 mL of deionized water in each cycle to complete the purification. The resulting solution was then poured into Petri dishes to form thin films approximately 1–2 mm thick and dried in a vacuum oven at 30 °C until dry membranes were obtained. These membranes were manually ground and sieved using a 100-mesh screen to ensure a uniform particle size distribution. The yield of each synthesis batch ranged from 6.8 to 7.2 g of GO powder, with minor variations attributed to unintentional losses during supernatant removal.

2.3. GO characterization

To confirm the successful synthesis of graphene oxide (GO) powder, a series of characterization techniques were employed. Fourier-transform infrared (FT-IR) spectroscopy was used to assess the presence of characteristic functional groups [41, 42]. For this purpose, both the starting graphite powder and the synthesized GO powder were analyzed using a Bio-RAD FTS-40 infrared spectrometer [43]. Each sample was mixed with potassium bromide (KBr) in a 1:10 weight ratio. In addition, scanning electron microscopy (SEM) was used to compare the morphology of the two materials. SEM images were acquired using a JEOL JSM-6010 LV microscope operating at an acceleration voltage of 10 kV. Image processing software was utilized to measure particle dimensions, and the average particle size was determined using statistical analysis tools. X-ray photoelectron spectroscopy (XPS) was conducted to evaluate the degree of oxidation in the GO samples via the carbon-to-oxygen (C/O) ratio. Measurements were performed using a Kratos AXIS Supra system equipped with an Al K-α monochromator (1486,66 eV), operating at an acceleration voltage of 15 kV and an emission current of 15 mA. Survey scans were recorded in the range of 0-1200 eV with a step size of 1eV and a pass energy of 160 eV. The acquired spectra were analyzed using CASA XPS software. The density of the GO powder was measured using a Micromeritics AccuPyc 1340 helium gas pycnometer. Prior to analysis, the instrument was calibrated by placing a stainless-steel sphere of known volume (V_C) in the sample chamber. The GO powder was then weighed (m_S) and placed in the chamber, which was subsequently filled with helium until reaching a pressure of 110 MPa (P_2). Simultaneously, a second steel sphere with known volume (V_R) was placed in the reference chamber, and its pressure (P_1) was recorded. The sample volume was calculated using Equation (1), and the process was repeated five times to ensure accuracy. Reported values represent the average of these measurements.

$$V_S = V_C - V_R\left(\frac{P_1}{P_2} - 1\right) \tag{1}$$

Finally, the density of the GO powder was calculated using Equation (2).

$$\rho_{GO} = \frac{m_S}{V_S} \tag{2}$$

3. Results and Discussion

3.1. FT-IR Spectral Analysis

The FT-IR spectra of both the raw graphite powder and the synthesized graphene oxide (GO) are presented in Figure 4. The spectrum of graphite (light gray) exhibits an almost constant absorbance between 0.71 and 1, with no prominent peaks, indicating the chemically inert nature of graphite [44,45]. In contrast, the FT-IR spectrum of GO displays several characteristic absorption bands, confirming the presence of various oxygen-containing functional groups on the basal plane of the material [9], [46]. A broad absorption band centered around 3300 cm^{-1} corresponds to the $C - OH$ stretching vibration, indicating the presence of hydroxyl groups [46,47]. The band near 2300 cm^{-1} corresponds to CH_2 stretching vibrations [48]. A well-defined peak observed at approximately 1700 cm^{-1} is attributed to C=O stretching, indicative of carbonyl groups [44,47]. Similarly, the peak around 1600 cm^{-1} is associated with C=C stretching vibrations [47], [49]. The absorption band at 1050 cm^{-1} is related to C–O and C–C stretching modes [45], while the band near 700 cm^{-1} corresponds to O–H out-of-plane bending [48,49].

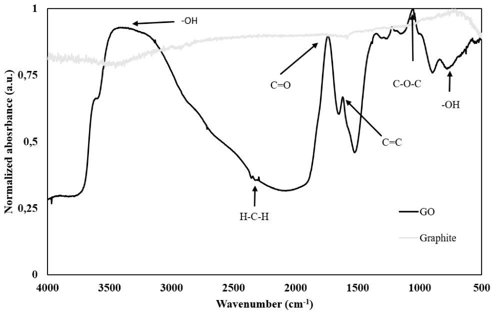

Figure 4. FTIR spectra of graphite and GO powder

3.2. SEM Analysis

Figure 5a displays the SEM micrograph of the as-received graphite powder at 500× magnification, while Figure 5b presents the micrograph of the ground graphene oxide (GO) obtained under the same conditions. The graphite particles exhibit uniformly sized structures with smooth surfaces. In contrast, the GO sample shows a broader distribution of particle sizes, ranging approximately from 60 to 200 μm. Furthermore, GO particles exhibit more irregular and rougher surface morphologies compared to the pristine graphite. The increased thickness observed in the GO particles is likely attributed to the incorporation of oxygen-containing functional groups on the basal plane [5], [50,51].

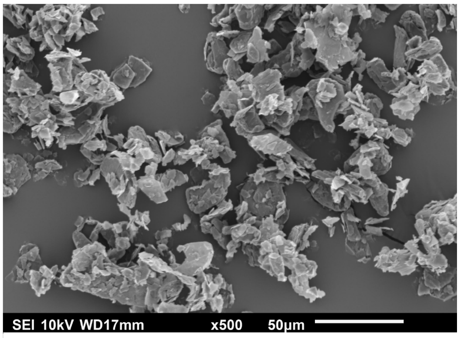

(a)

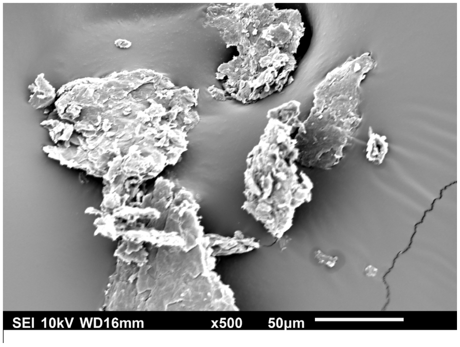

(b)

Figure 5. SEM micrographs a) graphite powder 500x, b) synthesized GO 500x

Numerous studies have evaluated the influence of reinforcement particle size on the mechanical properties of composite materials [52, 53]. To determine the average particle size of the synthesized graphene oxide (GO), a scanning electron microscopy (SEM) image captured at 60 × magnification was analyzed, as shown in Figure 6. The dimensions of all visible particles were measured, and a histogram illustrating the particle size distribution is presented in Figure 7. Based on the measurements, the average particle size was calculated to be 86.144 ± 11.47 μm.

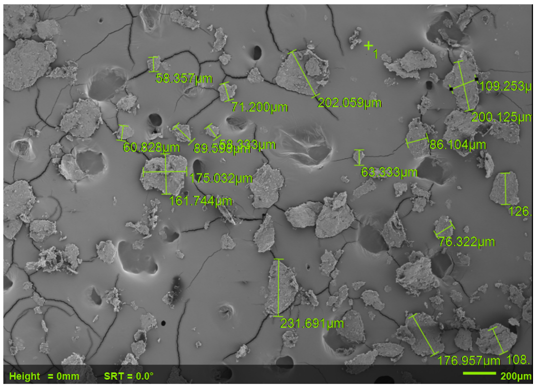

Figure 6. SEM micrograph of GO at 60× magnification, used for particle size analysis

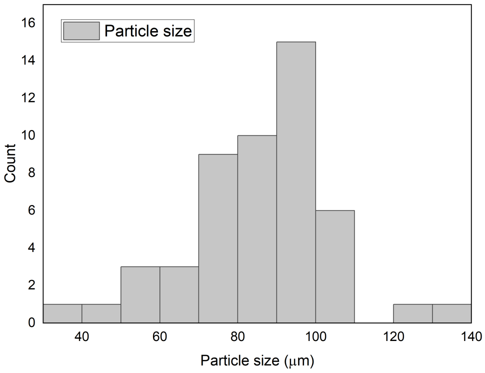

Figure 7. Histogram showing the particle size distribution of GO

3.3. XPS Analysis

Figures 8a and 8b present the X-ray photoelectron spectroscopy (XPS) spectra of pristine graphite and the synthesized graphene oxide (GO), respectively. In the case of graphite, a prominent peak appears at approximately 283 eV, corresponding to the C1s peak. The elemental composition of the graphite sample was determined to be approximately 99% carbon and 1% oxygen. The elevated oxygen content, compared to the material datasheet, is likely attributed to exposure to atmospheric conditions prior to analysis [54]. In contrast, the GO spectrum exhibits several distinct peaks. Alongside the C1s peak, characteristic oxygen-related signals are observed at around 520 eV and 980 eV, corresponding to the O1s and O KLL transitions, respectively. The elemental composition of the synthesized GO was found to be approximately 69.7% carbon, 29.9% oxygen, and a trace amount of sulfur (0.4%), resulting in a carbon-to-oxygen (C/O) ratio of 2.3. This value falls within the range reported in the literature, typically between 1.8 [10] and 2.77 [55], for GO synthesized via Hummers-based methods.

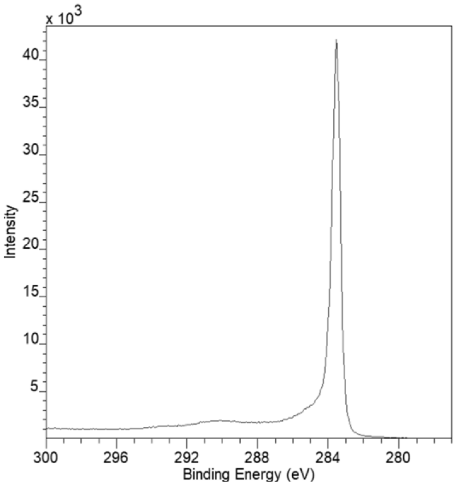

(a)

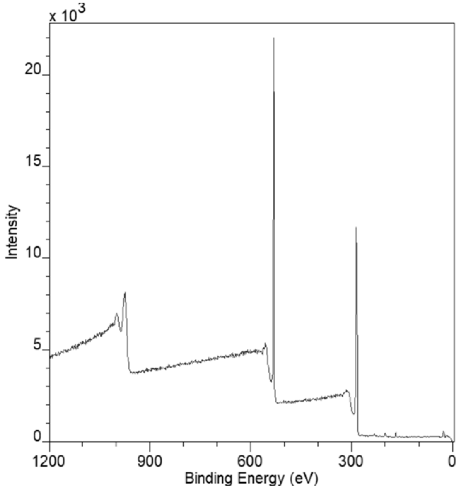

(b)

Figure 8. XPS spectra of a) graphite and b) synthesized GO

High-resolution scans were acquired with a step size of 50 meV to further characterize the synthesized graphene oxide (GO), as illustrated in Figure 9. The spectra were deconvoluted using CASA XPS software, revealing four prominent peaks located at approximately 284, 286, 288, and 289 eV. These peaks correspond to sp^2 hybridized carbon $C = C$, epoxy/hydroxyl groups, carbonyl functionalities, and carboxylates, respectively. Notably, the latter three peaks represent carbon atoms bonded to oxygen-containing functional groups, which collectively account for approximately 47% of the total carbon content in the GO sample. In contrast, the first peak corresponds to carbon atoms bonded exclusively to other carbon atoms.

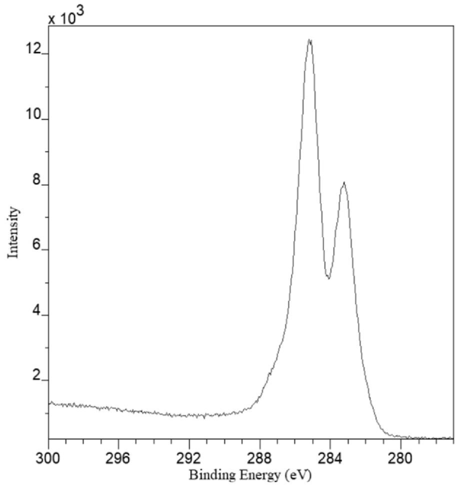

Figure 9. High-resolution XPS spectrum of the synthesized GO

3.4. Density Measurement

The graphene oxide (GO) sample was first weighed, yielding a consistent mass of 4.775 g across five repeated measurements. Following volume determination, the density of the synthesized GO powder was calculated to be 2,084 ± 0,03 g/cm^3.

4. Conclusions

In this study, graphene oxide (GO) was successfully synthesized using a modified Hummers method, and the resulting material was thoroughly characterized to evaluate its potential for engineering applications. The main conclusions are as follows:

Graphene oxide (GO) can be synthesized using various methods employing different ratios of oxidizing agents. The Hummers method is one of the most widely used; however, its reliance on concentrated sulfuric acid often results in trace sulfur contamination in the final product. To mitigate this issue, the present study adopted a modified synthesis protocol in which the amount of sulfuric acid was reduced by approximately 10%.

The FT-IR spectrum of the synthesized GO exhibited characteristic absorption bands at 3300, 2300, 1700, 1600, 1050 and 700 cm^1, confirming the success of the synthesis process. These peaks correspond to hydroxyl (–OH) groups, CH_2 stretching vibrations, carbonyl (C=O) groups, C=C stretching, carboxylate (O–O–C) groups, and out-of-plane O–H bending, respectively.

SEM analysis revealed pronounced morphological differences between pristine graphite and the synthesized GO. The GO displayed a more irregular and rougher surface, along with increased thickness, attributed to the presence of oxygen-containing functional groups.

XPS analysis revealed that the elemental composition of the synthesized GO was approximately 69.7% carbon, 29.9% oxygen, and 0.4% sulfur, resulting in a carbon-to-oxygen (C/O) ratio of 2.3.

High-resolution XPS spectra revealed that approximately 47% of the carbon atoms in the synthesized GO were bonded to oxygen-containing functional groups, while the remaining carbon atoms were bonded exclusively to other carbon atoms within the graphene lattice.

The presence of oxygen-containing functional groups enhances the potential of GO for chemical bonding with polymer matrices, particularly those containing epoxide groups, thereby improving the mechanical performance of the resulting composites. Furthermore, the particle size of the synthesized GO suggests its suitability as an effective reinforcing agent in polymer matrix composites.

The density of the synthesized graphene oxide (GO) powder was determined to be 2.084 ± 0,03 g/cm^3 using helium gas pycnometry.

Contributor Roles

- **Wilson Navas-Pinto:** Data curation, formal analysis, investigation, methodology, writing – original draft.
- **Duncan E. Cree:** Conceptualization, formal analysis, funding acquisition, project administration, resources, supervision, validation, writing – review and editing.
- **Lee D. Wilson:** Conceptualization, formal analysis, funding acquisition, project administration, resources, supervision, validation, writing – review and editing.
- **Germán Omar Barrionuevo:** Data curation, methodology, investigation, software, visualization, writing – original draft.
- **Xavier Sánchez-Sánchez:** Formal analysis, resources, software, methodology, validation, visualization, writing – original draft.

- **Héctor Calvopiña:** Methodology, project administration, software, visualization, writing – original draft, writing – review and editing.

References

[1] K. Gao, *Graphene Oxide: Reduction Recipes, Spectroscopy, and Applications*. Springer International Publishing, 2015. [Online]. Available: https://doi.org/10.1007/978-3-319-15500-5

[2] J. W. Suk, R. D. Piner, J. An, and R. S. Ruoff, "Mechanical properties of monolayer graphene oxide," *ACS Nano*, vol. 4, no. 11, pp. 6557–6564, Oct. 2010. [Online]. Available: https://doi.org/10.1021/nn101781v

[3] S. Stankovich, D. A. Dikin, R. D. Piner, K. A. Kohlhaas, A. Kleinhammes, Y. Jia, Y. Wu, S. T. Nguyen, and R. S. Ruoff, "Synthesis of graphene-based nanosheets via chemical reduction of exfoliated graphite oxide," *Carbon*, vol. 45, no. 7, pp. 1558–1565, Jun. 2007. [Online]. Available: https://doi.org/10.1016/j.carbon.2007.02.034

[4] M. Moazzami Gudarzi and F. Sharif, "Enhancement of dispersion and bonding of graphene-polymer through wet transfer of functionalized graphene oxide," *Express Polymer Letters*, vol. 6, no. 12, pp. 1017–1031, 2012. [Online]. Available: http://dx.doi.org/10.3144/expresspolymlett.2012.107

[5] K. A. Mkhoyan, A. W. Contryman, J. Silcox, D. A. Stewart, G. Eda, C. Mattevi, S. Miller, and M. Chhowalla, "Atomic and electronic structure of graphene-oxide," *Nano Letters*, vol. 9, no. 3, pp. 1058–1063, Feb. 2009. [Online]. Available: https://doi.org/10.1021/nl8034256

[6] W. Zięba, K. Jurkiewicz, A. Burian, M. Pawlyta, S. Boncel, G. S. Szymański, J. Kubacki, P. Kowalczyk, K. Krukiewicz, A. Furuse, K. Kaneko, and A. P. Terzyk, "High-surface-area graphene oxide for next-generation energy storage applications," *ACS Applied Nano Materials*, vol. 5, no. 12, pp. 18 448–18 461, Dec. 2022. [Online]. Available: http://dx.doi.org/10.1021/acsanm.2c04281

[7] X. Mu, X. Wu, T. Zhang, D. B. Go, and T. Luo, "Thermal transport in graphene oxide – from ballistic extreme to amorphous limit," *Scientific Reports*, vol. 4, no. 1, Jan. 2014. [Online]. Available: https://doi.org/10.1038/srep03909

[8] X. Shen, X. Lin, J. Jia, Z. Wang, Z. Li, and J.-K. Kim, "Tunable thermal conductivities of graphene oxide by functionalization and tensile loading," *Carbon*, vol. 80, pp. 235–245, Dec. 2014. [Online]. Available: https://doi.org/10.1016/j.carbon.2014.08.062

[9] Z. Li, R. J. Young, R. Wang, F. Yang, L. Hao, W. Jiao, and W. Liu, "The role of functional groups on graphene oxide in epoxy nanocomposites," *Polymer*, vol. 54, no. 21, pp. 5821–5829, Oct. 2013. [Online]. Available: https://doi.org/10.1016/j.polymer.2013.08.026

[10] C. Botas, P. Álvarez, P. Blanco, M. Granda, C. Blanco, R. Santamaría, L. J. Romasanta, R. Verdejo, M. A. López-Manchado, and R. Menéndez, "Graphene materials with different structures prepared from the same graphite by the hummers and brodie methods," *Carbon*, vol. 65, pp. 156–164, Dec. 2013. [Online]. Available: https://doi.org/10.1016/j.carbon.2013.08.009

[11] R. K. Singh, R. Kumar, and D. P. Singh, "Graphene oxide: strategies for synthesis, reduction and frontier applications," *RSC Advances*, vol. 6, no. 69, pp. 64 993–65 011, 2016. [Online]. Available: https://doi.org/10.1039/C6RA07626B

[12] S. Jaworski, B. Strojny-Cieślak, M. Wierzbicki, M. Kutwin, E. Sawosz, M. Kamaszewski, A. Matuszewski, M. Sosnowska, J. Szczepaniak, K. Daniluk, A. Lange, M. Pruchniewski, K. Zawadzka, M. Łojkowski, and A. Chwalibog, "Comparison of the toxicity of pristine graphene and graphene oxide, using four biological models," *Materials*, vol. 14, no. 15, p. 4250, Jul. 2021. [Online]. Available: https://doi.org/10.3390/ma14154250

[13] P. Kumar, P. Huo, R. Zhang, and B. Liu, "Antibacterial properties of graphene-based nanomaterials," *Nanomaterials*, vol. 9, no. 5, p. 737, May 2019. [Online]. Available: https://doi.org/10.3390/nano9050737

[14] N. Mushahary, A. Sarkar, F. Basumatary, S. Brahma, B. Das, and S. Basumatary, "Recent developments on graphene oxide and its composite materials: From fundamentals to applications in biodiesel synthesis, adsorption, photocatalysis, supercapacitors, sensors and antimicrobial activity," *Results in Surfaces and Interfaces*, vol. 15, p. 100225, May 2024. [Online]. Available: https://doi.org/10.1016/j.rsurfi.2024.100225

[15] S. Wang, H. Yan, H. Zheng, Y. He, X. Guo, S. Li, and C. Yang, "Fast response humidity sensor based on chitosan/graphene oxide/tin dioxide composite," *Sensors and Actuators B: Chemical*, vol. 392, p. 134070, Oct. 2023. [Online]. Available: https://doi.org/10.1016/j.snb.2023.134070

[16] T. Liang, W. Hou, J. Ji, and Y. Huang, "Wrinkled reduced graphene oxide humidity sensor with fast

response/recovery and flexibility for respiratory monitoring," *Sensors and Actuators A: Physical*, vol. 350, p. 114104, Feb. 2023. [Online]. Available: https://doi.org/10.1016/j.sna.2022.114104

[17] S. Kerli, S. Bhardwaj, W. Lın, and R. K. Gupta, "Silver-doped reduced graphene oxide/-Pani composite synthesis and their supercapacitor applications," *Journal of Organometallic Chemistry*, vol. 995, p. 122725, Aug. 2023. [Online]. Available: https://doi.org/10.1016/j.jorganchem.2023.122725

[18] S. Nagarani, G. Sasikala, M. Yuvaraj, S. Balachandran, R. Dhilip Kumar, and M. Kumar, "Cost effective, metal free reduced graphene oxide sheet for high performance electrochemical capacitor application," *Materials Science and Engineering: B*, vol. 284, p. 115852, Oct. 2022. [Online]. Available: https://doi.org/10.1016/j.mseb.2022.115852

[19] S. Nagarani, J.-H. Chang, M. Yuvaraj, S. Balachandran, M. Kumar, and S. Kanimozhi, "Well-organized metal-free chemically reduced graphene oxide sheets as electrocatalysts for enhanced oxygen reduction reactions in alkaline media," *Materials Letters*, vol. 357, p. 135705, Feb. 2024. [Online]. Available: https://doi.org/10.1016/j.matlet.2023.135705

[20] J. A. Arévalo, J. E. Alfonso, O. J. Suárez, J. J. Olaya, and L. C. Moreno-Aldana, "Growth and physical-chemical characterization of manganese oxide and graphene-manganese oxide films for potential applications in energy store devices," *Results in Materials*, vol. 22, p. 100574, Jun. 2024. [Online]. Available: https://doi.org/10.1016/j.rinma.2024.100574

[21] A. Eftekhari, Y. M. Shulga, S. A. Baskakov, and G. L. Gutsev, "Graphene oxide membranes for electrochemical energy storage and conversion," *International Journal of Hydrogen Energy*, vol. 43, no. 4, pp. 2307–2326, Jan. 2018. [Online]. Available: https://doi.org/10.1016/j.ijhydene.2017.12.012

[22] A. Joy, G. Unnikrishnan, M. Megha, M. Haris, J. Thomas, A. Deepti, P. Baby Chakrapani, E. Kolanthai, and S. Muthuswamy, "A novel combination of graphene oxide/palladium integrated polycaprolactone nanocomposite for biomedical applications," *Diamond and Related Materials*, vol. 136, p. 110033, Jun. 2023. [Online]. Available: https://doi.org/10.1016/j.diamond.2023.110033

[23] A. M. Sindi, "Applications of graphene oxide and reduced graphene oxide in advanced dental materials and therapies," *Journal of Taibah University Medical Sciences*, vol. 19, no. 2, pp. 403–421, Apr. 2024. [Online]. Available: https://doi.org/10.1016/j.jtumed.2024.02.002

[24] A. Loeffen, D. E. Cree, M. Sabzevari, and L. D. Wilson, "Effect of graphene oxide as a reinforcement in a bio-epoxy composite," *Journal of Composites Science*, vol. 5, no. 3, p. 91, Mar. 2021. [Online]. Available: https://doi.org/10.3390/jcs5030091

[25] J. Zhou, Z. Yao, Y. Chen, D. Wei, Y. Wu, and T. Xu, "Mechanical and thermal properties of graphene oxide/phenolic resin composite," *Polymer Composites*, vol. 34, no. 8, pp. 1245–1249, Jun. 2013. [Online]. Available: http://dx.doi.org/10.1002/pc.22533

[26] L. Yang, F. Jia, Z. Juan, D. Yu, L. Sun, Y. Wang, L. Huang, and J. Tang, "Bioinspired graphene oxide nanofiltration membranes with ultrafast water transport and selectivity for water treatment," *FlatChem*, vol. 36, p. 100450, Nov. 2022. [Online]. Available: https://doi.org/10.1016/j.flatc.2022.100450

[27] C.-H. Yu, G.-Y. Chen, M.-Y. Xia, Y. Xie, Y.-Q. Chi, Z.-Y. He, C.-L. Zhang, T. Zhang, Q.-M. Chen, and Q. Peng, "Understanding the sheet size-antibacterial activity relationship of graphene oxide and the nano-bio interaction-based physical mechanisms," *Colloids and Surfaces B: Biointerfaces*, vol. 191, p. 111009, Jul. 2020. [Online]. Available: https://doi.org/10.1016/j.colsurfb.2020.111009

[28] H. L. Poh, F. Šaněk, A. Ambrosi, G. Zhao, Z. Sofer, and M. Pumera, "Graphenes prepared by Staudenmaier, Hofmann and Hummers methods with consequent thermal exfoliation exhibit very different electrochemical properties," *Nanoscale*, vol. 4, no. 11, p. 3515, 2012. [Online]. Available: https://doi.org/10.1039/C2NR30490B

[29] N. Zaaba, K. Foo, U. Hashim, S. Tan, W.-W. Liu, and C. Voon, "Synthesis of graphene oxide using modified Hummers method: Solvent influence," *Procedia Engineering*, vol. 184, pp. 469–477, 2017. [Online]. Available: https://doi.org/10.1016/j.proeng.2017.04.118

[30] C. Gómez-Navarro, M. Burghard, and K. Kern, "Elastic properties of chemically derived single graphene sheets," *Nano Letters*, vol. 8, no. 7, pp. 2045–2049, Jun. 2008. [Online]. Available: https://doi.org/10.1021/nl801384y

[31] K. Cao, S. Feng, Y. Han, L. Gao, T. Hue Ly, Z. Xu, and Y. Lu, "Elastic straining of free-standing monolayer graphene," *Nature Communications*,

vol. 11, no. 1, Jan. 2020. [Online]. Available: https://doi.org/10.1038/s41467-019-14130-0

[32] S. Stankovich, D. A. Dikin, G. H. B. Dommett, K. M. Kohlhaas, E. J. Zimney, E. A. Stach, R. D. Piner, S. T. Nguyen, and R. S. Ruoff, "Graphene-based composite materials," *Nature*, vol. 442, no. 7100, pp. 282–286, Jul. 2006. [Online]. Available: https://doi.org/10.1038/nature04969

[33] M. Mehrabi Kooshki and A. Jalali-Arani, "High performance graphene oxide/epoxy nanocomposites fabricated through the solvent exchange method," *Polymer Composites*, vol. 39, no. S4, Feb. 2018. [Online]. Available: https://doi.org/10.1002/pc.24803

[34] B. Collins Brodie, "XIII. On the atomic weight of graphite," *Philosophical Transactions of the Royal Society of London*, vol. 149, pp. 249–259, Dec. 1859. [Online]. Available: https://doi.org/10.1098/rstl.1859.0013

[35] L. Staudenmaier, "Verfahren zur Darstellung der Graphitsäure," *Berichte der deutschen chemischen Gesellschaft*, vol. 31, no. 2, pp. 1481–1487, May 1898. [Online]. Available: https://doi.org/10.1002/cber.18980310237

[36] U. Hofmann and E. König, "Untersuchungen über graphitoxyd," *Zeitschrift für anorganische und allgemeine Chemie*, vol. 234, no. 4, pp. 311–336, Dec. 1937. [Online]. Available: https://doi.org/10.1002/zaac.19372340405

[37] W. S. Hummers and R. E. Offeman, "Preparation of graphitic oxide," *Journal of the American Chemical Society*, vol. 80, no. 6, pp. 1339–1339, Mar. 1958. [Online]. Available: https://doi.org/10.1021/ja01539a017

[38] D. C. Marcano, D. V. Kosynkin, J. M. Berlin, A. Sinitskii, Z. Sun, A. Slesarev, L. B. Alemany, W. Lu, and J. M. Tour, "Improved synthesis of graphene oxide," *ACS Nano*, vol. 4, no. 8, pp. 4806–4814, Jul. 2010. [Online]. Available: https://doi.org/10.1021/nn1006368

[39] J. Chen, B. Yao, C. Li, and G. Shi, "An improved Hummers method for eco-friendly synthesis of graphene oxide," *Carbon*, vol. 64, pp. 225–229, Nov. 2013. [Online]. Available: https://doi.org/10.1016/j.carbon.2013.07.055

[40] Y. Zhu, G. Kong, Y. Pan, L. Liu, B. Yang, S. Zhang, D. Lai, and C. Che, "An improved Hummers method to synthesize graphene oxide using much less concentrated sulfuric acid," *Chinese Chemical Letters*, vol. 33, no. 10, pp. 4541–4544, Oct. 2022. [Online]. Available: https://doi.org/10.1016/j.cclet.2022.01.060

[41] G. Surekha, K. V. Krishnaiah, N. Ravi, and R. Padma Suvarna, "FTIR, Raman and XRD analysis of graphene oxide films prepared by modified Hummers method," *Journal of Physics: Conference Series*, vol. 1495, no. 1, p. 012012, Mar. 2020. [Online]. Available: http://dx.doi.org/10.1088/1742-6596/1495/1/012012

[42] Rattana, S. Chaiyakun, N. Witit-anun, N. Nuntawong, P. Chindaudom, S. Oaew, C. Kedkeaw, and P. Limsuwan, "Preparation and characterization of graphene oxide nanosheets," *Procedia Engineering*, vol. 32, pp. 759–764, 2012. [Online]. Available: https://doi.org/10.1016/j.proeng.2012.02.009

[43] M. Sabzevari, D. E. Cree, and L. D. Wilson, "Mechanical properties of graphene oxide-based composite layered-materials," *Materials Chemistry and Physics*, vol. 234, pp. 81–89, Aug. 2019. [Online]. Available: https://doi.org/10.1016/j.matchemphys.2019.05.091

[44] L.-L. Tan, W.-J. Ong, S.-P. Chai, and A. R. Mohamed, "Reduced graphene oxide-TiO_2 nanocomposite as a promising visible-light-active photocatalyst for the conversion of carbon dioxide," *Nanoscale Research Letters*, vol. 8, no. 1, Nov. 2013. [Online]. Available: https://doi.org/10.1186/1556-276X-8-465

[45] D. Galpaya, M. Wang, G. George, N. Motta, E. Waclawik, and C. Yan, "Preparation of graphene oxide/epoxy nanocomposites with significantly improved mechanical properties," *Journal of Applied Physics*, vol. 116, no. 5, Aug. 2014. [Online]. Available: https://doi.org/10.1063/1.4892089

[46] E. Aliyev, V. Filiz, M. M. Khan, Y. J. Lee, C. Abetz, and V. Abetz, "Structural characterization of graphene oxide: Surface functional groups and fractionated oxidative debris," *Nanomaterials*, vol. 9, no. 8, p. 1180, Aug. 2019. [Online]. Available: https://doi.org/10.3390/nano9081180

[47] F. Ren, G. Zhu, P. Ren, Y. Wang, and X. Cui, "In situ polymerization of graphene oxide and cyanate ester–epoxy with enhanced mechanical and thermal properties," *Applied Surface Science*, vol. 316, pp. 549–557, Oct. 2014. [Online]. Available: https://doi.org/10.1016/j.apsusc.2014.07.159

[48] M. S. A. Sher Shah, A. R. Park, K. Zhang, J. H. Park, and P. J. Yoo, "Green synthesis of biphasic tio_2–reduced graphene oxide nanocomposites with highly enhanced photocatalytic activity," *ACS Applied Materials Interfaces*, vol. 4, no. 8, pp. 3893–3901, Jul. 2012. [Online]. Available: https://doi.org/10.1021/am301287m

[49] I. O. Faniyi, O. Fasakin, B. Olofinjana, A. S. Adekunle, T. V. Oluwasusi, M. A. Eleruja, and E. O. B. Ajayi, "The comparative analyses of reduced graphene oxide (RGO) prepared via green, mild and chemical approaches," *SN Applied Sciences*, vol. 1, no. 10, Sep. 2019. [Online]. Available: https://doi.org/10.1007/s42452-019-1188-7

[50] S. Kwon, K. E. Lee, H. Lee, S. J. Koh, J.-H. Ko, Y.-H. Kim, S. O. Kim, and J. Y. Park, "The effect of thickness and chemical reduction of graphene oxide on nanoscale friction," *The Journal of Physical Chemistry B*, vol. 122, no. 2, pp. 543–547, Oct. 2017. [Online]. Available: https://doi.org/10.1021/acs.jpcb.7b04609

[51] S. Gadipelli and Z. X. Guo, "Graphene-based materials: Synthesis and gas sorption, storage and separation," *Progress in Materials Science*, vol. 69, pp. 1–60, Apr. 2015. [Online]. Available: https://doi.org/10.1016/j.pmatsci.2014.10.004

[52] S.-Y. Fu, X.-Q. Feng, B. Lauke, and Y.-W. Mai, "Effects of particle size, particle/matrix interface adhesion and particle loading on mechanical properties of particulate–polymer composites," *Composites Part B: Engineering*, vol. 39, no. 6, pp. 933–961, Sep. 2008. [Online]. Available: https://doi.org/10.1016/j.compositesb.2008.01.002

[53] S. Siraj, A. H. Al-Marzouqi, M. Z. Iqbal, and W. Ahmed, "Impact of micro silica filler particle size on mechanical properties of polymeric based composite material," *Polymers*, vol. 14, no. 22, p. 4830, Nov. 2022. [Online]. Available: https://doi.org/10.3390/polym14224830

[54] L. H. Grey, H.-Y. Nie, and M. C. Biesinger, "Defining the nature of adventitious carbon and improving its merit as a charge correction reference for XPS," *Applied Surface Science*, vol. 653, p. 159319, Apr. 2024. [Online]. Available: https://doi.org/10.1016/j.apsusc.2024.159319

[55] R. Al-Gaashani, A. Najjar, Y. Zakaria, S. Mansour, and M. Atieh, "XPS and structural studies of high quality graphene oxide and reduced graphene oxide prepared by different chemical oxidation methods," *Ceramics International*, vol. 45, no. 11, pp. 14 439–14 448, Aug. 2019. [Online]. Available: https://doi.org/10.1016/j.ceramint.2019.04.165

Scientific Paper / Artículo Científico

UNIVERSIDAD POLITÉCNICA SALESIANA ECUADOR
INGENIUS
Revista de Ciencia y Tecnología
https://doi.org/10.17163/ings.n34.2025.04
pISSN: 1390-650X / eISSN: 1390-860X

OPERATIVE ANALYSIS OF CONTROLLED CHARGING MANAGEMENT FOR ELECTRIC VEHICLES: CENTRALIZED AND DECENTRALIZED COORDINATION

ANÁLISIS OPERATIVO DE LA GESTIÓN DE CARGA CONTROLADA EN VEHÍCULOS ELÉCTRICOS: COORDINACIÓN CENTRALIZADA Y DESCENTRALIZADA

Carlos W. Villanueva-Machado[1,*], Jaime E. Luyo[1], Alberto Ríos-Villacorta[2]

Received: 24-07-2024, Received after review: 25-03-2025, Accepted: 23-04-2025, Published: 01-07-2025

Abstract

Electric vehicle (EV) charging management can be implemented through centralized or decentralized strategies. Strategic coordination between these approaches enhances system efficiency and balances energy loads, thereby supporting the widespread adoption of EVs and fostering a sustainable, emissions-free society. In this study, distribution network operators (DNOs), acting as centralized charging managers, are responsible for mitigating the lack of coordination among electric vehicle aggregators (EVAs), which represent decentralized managers. The primary objective of the centralized management in this research is to constrain each decentralized optimization model, characterized using Monte Carlo simulations. Three EV adoption scenarios–comprising 2,000, 2,500, and 3,750 vehicles–are evaluated by comparing decentralized charging management with an unregulated charging baseline in the IEEE 14-bus power system. Improvements are required only in the highest adoption scenario, where the proposed centralized coordination model is applied. The study models energy trading constraints for each EVA, assigning one aggregator per load-bearing bus in the system. Transmission-level results are analyzed and then synthesized for application in the IEEE 13-bus distribution power system. Findings demonstrate that coordinated centralized and decentralized charging management significantly improves operational conditions in both transmission and distribution networks without necessitating changes to travel behavior.

Keywords: Electric Vehicles, Electric Vehicle Aggregators, Monte Carlo Simulation, Optimal Power Flow, Distribution Network Operator, Power System

Resumen

La gestión de la carga controlada de vehículos eléctricos se aplica de forma centralizada y descentralizada. La coordinación estratégica entre ambas optimiza la eficiencia y equilibra la carga de los sistemas energéticos, promoviendo tanto la adopción de vehículos eléctricos, así como una sociedad sostenible y libre de emisiones. Los operadores de las redes de distribución (gestores de carga centralizada) deben controlar la descoordinación entre los agregadores de vehículos eléctricos (gestores descentralizados seleccionados para este estudio). El objetivo de gestión centralizada de esta investigación es acotar cada modelo de optimización descentralizada (caracterizado mediante simulación de Monte Carlo). La gestión descentralizada, se compara con la carga desregulada en el sistema de potencia IEEE de 14 barras para 3 escenarios de adopción de vehículos eléctricos (2000, 2500, 3750 vehículos eléctricos), requiriendo mejoras únicamente en el último escenario, al cual se le aplica la coordinación en gestión centralizada propuesta. El estudio modela las restricciones en la energía comercializada por cada agregador de vehículos eléctricos (uno por barra del sistema eléctrico con carga). Los resultados en transmisión se analizan, sintetizan y aplican al modelo de sistema de potencia de distribución IEEE de 13 barras. Los sistemas de transmisión y distribución de energía coordinan entre la gestión de carga centralizada y descentralizada mejoran las condiciones de operación en los sistemas de potencia sin requerir cambios en los patrones de manejo.

Palabras clave: agregadores de vehículos eléctricos, flujo óptimo de potencia, operador de redes de distribución, simulación Monte Carlo, sistemas eléctricos, vehículos eléctricos

---

[1,*]Faculty of Mechanical Engineering, Universidad Nacional de Ingeniería, Perú
Corresponding author ✉: cwvillanuevam@uni.pe.

[2]Faculty of Systems Electronics and Industrial Engineering, Universidad Técnica de Ambato, Ecuador

Suggested citation: C. W. Villanueva-Machado, J. E. Luyo and A. Ríos-Villacorta “Operative Analysis of Controlled Charging Management for Electric Vehicles: Centralized and Decentralized Coordination,” *Ingenius, Revista de Ciencia y Tecnología*, N.° 34, pp. 43-60, 2025, DOI: https://doi.org/10.17163/ings.n34.2025.04.

1. Introduction

The increasing adoption of electric vehicles (EVs) has intensified interest in the development of effective charging management strategies. Proper management of EV charging is essential for promoting sustainable electric mobility and reducing reliance on conventional energy sources within power grids.

Previous research [1] has characterized the rise in power system demand caused by EV integration using Monte Carlo simulation. According to that study, distribution network operators (DNOs) must implement centralized electric vehicle charging management (CEVCM) to maintain system stability. Such centralized approaches enable distributed renewable energy sources to meet the additional load imposed by EV charging. In related work, a vehicle-to-grid (V2G) scheduling method has been proposed [2], which incorporates battery protection objectives while utilizing renewable energy in microgrid environments. This approach aims to reduce battery degradation and encourage the use of local renewable generation. Additionally, research by [3] explores the deployment of on-site wind power generation to support EV charging in building-level microgrids. This strategy leverages a Markov decision process and a policy improvement framework based on distributed simulation, demonstrating strong scalability and operational effectiveness.

1.1. Electric Vehicle Charging Optimization

The study presented in [4] highlights the critical role of electric vehicle (EV) charging and discharging management in the context of smart homes and intelligent grids. Similarly, [5] explores the complexity of administering EV charging within smart-home energy management systems. The research conducted in [6] underscores the importance of integrated EV charging management strategies that incorporate enhancements in energy storage infrastructure. In [7], it is emphasized that coordinated interaction between EVs and the grid enables the provision of regulation reserve services while compensating EV owners for battery degradation, thereby reducing overall system operation costs.

Additional studies have proposed frameworks for electric vehicle charge-discharge management (EVCDM). For example, [8] introduces a model utilizing photovoltaic energy outputs to reduce residential energy costs, demonstrating its effectiveness through simulation. In [9], an online coordination method is employed within an EVCDM framework to manage the charging of plug-in electric vehicles (PEVs) in intelligent distribution networks.

Further contributions include [10], which presents a transactive energy framework based on sensitivity analysis to coordinate EV charging with voltage control in low-voltage distribution systems. Complementarily, [11] develops a distributed algorithm for the charging control of plug-in hybrid and electric vehicles. This algorithm eliminates the need for a centralized control unit, increases resilience to single-node or link failures, and scales efficiently with an increasing number of charging points.

Moreover, [12] proposes a peak load management model for scheduling EV charging and discharging based on queuing theory, supported by extensive MATLAB-based simulations. Finally, [13] evaluates a multi-timescale framework under uncertainty conditions, applying a real-time coordinated scheduling method for active distribution networks incorporatingsoft open points and PEVs.

1.2. Electric Vehicle Charging Impact on Power Systems

Efficient communication between centralized electric vehicle charging management (CEVCM) and decentralized systems, such as electric vehicle aggregators (EVAs) or parking facilities, is essential for the reliable operation of modern power systems [14]. Similar to the approach in [4], this study addresses the coordination of charging and discharging operations. A 2% increase in NO_x emissions has been observed when communication in decentralized smart charging systems is infrequent, leading to higher operational costs and increased capacity demands on the electrical network. Additionally, study [15] highlights how EVAs influence the pace and pattern of electric vehicle adoption.

Both centralized and decentralized management strategies are necessary to maintain power system stability. Study [16] proposes a coordinated EV management system for low-voltage residential networks, aiming to minimize electricity costs under grid constraints through a multi-agent system architecture. Research [17] supports this objective by reducing energy costs and preventing transformer overloads during EV charging. It introduces the MASCO architecture, which adapts to varying tariff structures using multi-agent, multi-objective reinforcement learning based on energy pricing.

Further contributions include a real-time smart load management (RT-SLM) strategy in [18], which lowers costs and grid losses by incorporating time-varying electricity prices and priority-based charging for plug-in electric vehicles (PEVs). Study [19] suggests a market-based coordination model involving EV owners, fleet operators, and distribution system operators, considering driving needs, costs, and system constraints. Study [20] presents a methodology designed to maximize aggregator profits while maintaining the operational integrity of distribution networks.

Study [21] models EVA participation in both day-ahead and real-time electricity markets, accounting for battery degradation. Similarly, study [22] introduces a demand response program coordinated by aggregators within a reconfigured, grid-connected microgrid, which includes EV charging stations, renewable energy sources, and diesel generators. Building on this line of research, study [23] presents a multi-objective optimization model for managing local multi-energy systems that incorporate PEVs.

Finally, study [24] explores the optimal operation of a grid-connected AC microgrid using stochastic optimization, while study [25] proposes a hybrid decentralized framework that combines robust optimization with stochastic programming to coordinate the management of EVAs and energy hubs under uncertainty.

1.3. Electric Vehicle Adoption Analysis

According to [26], electric vehicle (EV) sales data from 2022 show that China leads the global EV market. In Latin America, reference [27] identifies three primary categories of EV incentives implemented in 2019: purchase incentives, use and circulation incentives, and other promotional measures. Reference [28] notes that several Latin American countries exhibit high levels of EV imports, while [29] reports the number of EV chargers available by country.

Figure 1 summarizes this information, indicating an average global growth of 17% in EV adoption. North America experienced a 46% year-over-year increase, while other regions recorded an 81% rise compared to the previous year. On a global scale, the COVID-19 pandemic temporarily slowed the growth of EV and hybrid vehicle adoption, with recovery progressing gradually through 2023. Brazil, Mexico, and Colombia are currently increasing their rates of EV importation. The average ratio of electric vehicles per charging station is 18.75, with these stations distributed throughout power systems.

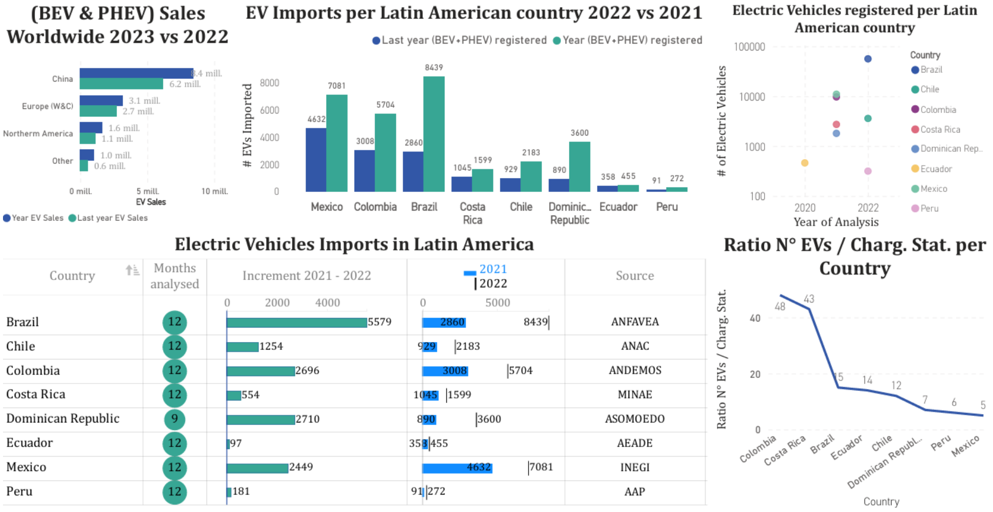

Country	Months analysed	Increment 2021 - 2022	2021	2022	Source
Brazil	12	5579	2860	8439	ANFAVEA
Chile	12	1254	929	2183	ANAC
Colombia	12	2696	3008	5704	ANDEMOS
Costa Rica	12	554	1045	1599	MINAE
Dominican Republic	9	2710	890	3600	ASOMOEDO
Ecuador	12	97	358	455	AEADE
Mexico	12	2449	4632	7081	INEGI
Peru	12	181	91	272	AAP

* Self -Elabotation, based in information from:
- MOVE, Interoperability of Electric Vehicles Charging in Latin America and Caribbean.
- ANDEMOS, Increment in Electric Vehicle and Hybrid penetration in Latin America during 2022.
- EV-Volumes - The Electric Vehicle World Sales Database

Figure 1. Adoption of Electric Vehicles worldwide and in LA

As noted in [30], the Peruvian Ministry of Energy and Mining issued a decree in August 2019 to promote the adoption of EVs and plug-in electric vehicles (PEVs). Reference [1] presents a Monte Carlo simulation analysis featuring three scenarios and two output variables, designed to characterize the stochastic behavior of EVs. These scenarios assess the operation of EVAs under conditions that do not adversely affect power system performance.

2. Materials and Methods

Figure 2 presents the flow diagram of the methodology employed in this research. The process begins with a Monte Carlo Simulation (MCS), which characterizes the geographic distribution and travel behavior of electric vehicle (EV) owners. These MCS-generated scenarios are then modeled within a decentralized electric vehicle charging management (DEVCM) framework. The outputs from the DEVCM model subsequently trigger a centralized electric vehicle charging management (CEVCM) analysis, evaluating its impact on the operation of the distribution network (DN). Based on this evaluation, modifications are introduced into the DEVCM model by incorporating coordination constraints between the decentralized and centralized charging strategies. The coordinated charging strategy is then tested on a distribution power system using the IEEE 13-bus network, as illustrated in Figure 3. The dataset used in this study is available at the following repository [31].

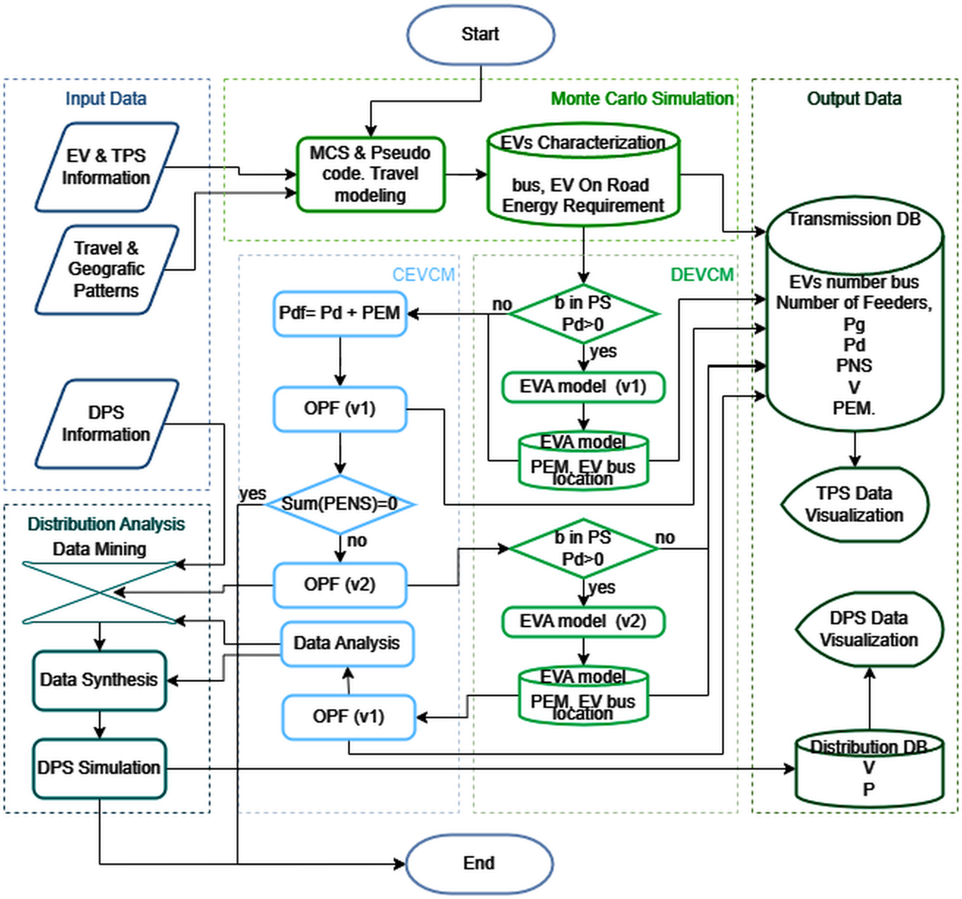

Figure 2. Method used by each EV adoption scenario

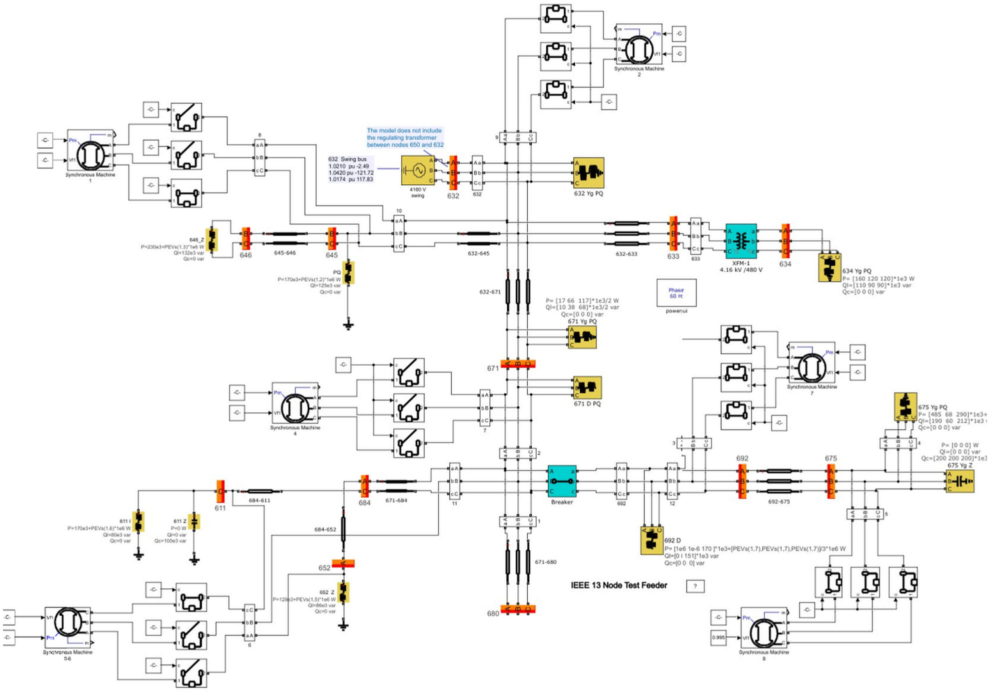

Figure 3. Distribution Power System (IEEE 13 bus) simulation

2.1. Scenario analysis and inputs

Following the approach in [1], this methodology models the stochastic behavior of electric vehicle (EV) charging. Reference [1] presents a centralized electric vehicle charging management (CEVCM) model applied in Peru across three scenarios. The present study builds upon that framework, comparing the same three scenarios involving 2,000, 2,500, and 3,750 EVs under controlled charging conditions. The primary objective of this research is to identify the coordination infrastructure required between decentralized (DEVCM) and centralized (CEVCM) charging management systems. Each scenario is evaluated using Monte Carlo Simulation to characterize the EVs' energy requirements. For each case, the simulation produces minimum and maximum output values, denoted as $s_{\min}$ and $s_{\max}$. respectively.

2.2. Monte Carlo Simulation

The study defines the departure and arrival points for each electric vehicle (EV) based on the EV aggregator (EVA) closest to the user's home and workplace. Table 1 reports the number of EVs assigned to each bus for both references–departure (Dep.) and arrival (Arr.)–as illustrated in Figure 4(a).

Previous studies have characterized EV travel patterns, such as the work in [32], which describes departure behavior, and [33], which presents arrival conditions for a subset of EV users. Figure 4(b)presents the probability distribution functions for home departure and arrival times. Accordingly, this research adopts normal distributions to model these stochastic variables, maintaining neutrality with respect to specific driving behavior policies.

Figure 4(c) draws from [1] to characterize regional travel patterns by categorizing trips into high-, medium-, and low-speed segments. The probabilistic characteristics of each speed category are shown in Figure 4(d). Together, these figures represent the stochastic modeling of the geographic variables used in this study.

Table 1. Geographical Distribution of EVs by Bus, Scenario, and Monte Carlo Simulation (MCS) Output

	Scenario 1				Scenario 2				Scenario 3			
EVs	minimum		maximum		minimum		maximum		minimum		maximum	
Bar	Dep.	Arr.	Dep.	Arr.	Dep.	Arr.	Dep.	Arr.	Dep.	Arr.	Dep.	Arr.
2	201	187	174	190	251	281	96	262	461	449	316	375
3	179	174	137	155	183	100	183	55	260	262	296	285
4	310	304	146	111	256	458	199	154	427	594	271	305
5	177	202	89	90	372	223	111	118	571	414	214	132
6	203	221	325	201	229	274	193	339	341	285	324	562
9	223	219	178	105	244	240	176	258	388	380	331	370
10	210	270	74	104	285	283	217	229	403	473	257	243
11	163	123	129	140	156	237	277	195	285	197	344	299
12	70	124	190	287	171	91	282	170	236	132	438	309
13	180	127	246	396	206	236	272	486	161	445	426	441
14	84	49	312	221	147	77	494	234	217	119	533	429

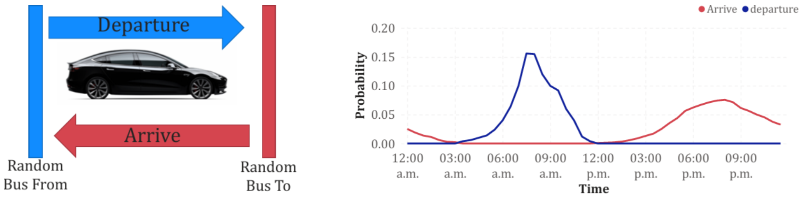

(a) Geographic patterns (b) Departure & Arrive data

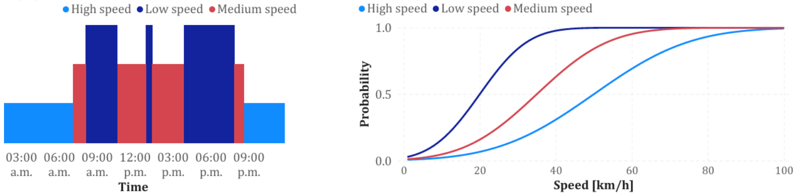

(c) Daily Traffic Speed (d) Cumulative Density Function of Speed

Figure 4. Electric vehicle behavior patterns

These stochastic variables define the departure times $\mathrm{dep_{v,s}}$, arrival times $\mathrm{arr_{v,s}}$, travel distance $td_{\mathrm{v,s}}$ and speed during the analyzed period $\mathrm{sv_{t,v,s}}$. In addition to this data, the methodology requires information about the energy exchanged between electric vehicles and their assigned EVA. Accordingly, the trip modeling presented in Figure 5 and detailed in Section 2.2.1, Pseudo Trip Modeling Code, incorporates a specific energy consumption variable $\mathrm{SC_{v,s}}$ expressed in kilowatt-hours per kilometer [kWh/km].

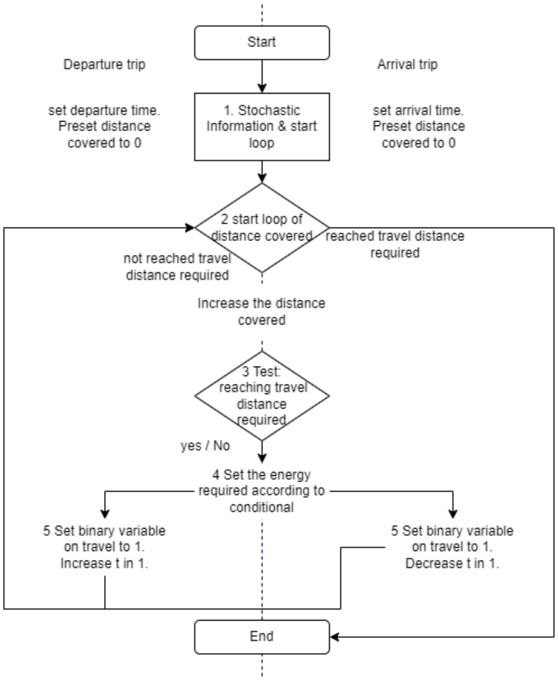

Figure 5. Trip Modeling

2.2.1. Pseudo code: trip modeling

1. 2. Initialize departure and arrival times, along with the time variable fordistance covered. $t = \mathrm{dep}_{v,s} \wedge \mathrm{rdt}_{v,s} = 0$ for the departure trip and $t = \mathrm{arr}_{v,s} \wedge \mathrm{rdt}_{v,s} = 0$ for the return trip.

2. Begin loop to accumulate distance traveled until the total trip distance is reached:

$$while\mathrm{rdt}_{v,s} \leq td_{v,s}$$

$$rdt_{v,s} = rdt_{v,s} + sv_{v,s} \times \frac{24}{T}$$

3. Evaluate the conditional statement to determine whether the final travel period has been reached–that is, whether the trip distance has been fully covered–and compute the energy required by the electric vehicle during travel:

$$ifrdt_{v,s} \leq td_{v,s}$$

$$R_{t,v,s} = \frac{sv_{v,s} \times SC_{v,s}}{n_{dsg}} \times \frac{24}{T}$$

4. Assign the energy demand required for the final segment of the trip, based on the remaining distance to be traveled:

$$else \left\{ R_{t,v,s} = (sv_{v,s} + td_{v,s} - rdt_{v,s}) \times \frac{SC_{v,s}}{n_{dsg}} \right\}$$

5. Assign the final departure time and initial arrival time, along with the binary variable representing the in-route state of the trip:

$$X_{t,v,s} = 1 \wedge t = +1 \Rightarrow \mathrm{de}_{v,s} = t \quad \text{(for dep. trip)}$$

$$X_{t,v,s} = 1 \wedge t = -1 \Rightarrow \mathrm{ai}_{v,s} = t \quad \text{(for arr. trip)}$$

2.2.2. MCS outputs

Once the trip is modeled, the binary variable$CS_{b,t,v,s}$ is used to assign each electric vehicle to a specific bus within the system. This variable also tracks the vehicle's charging stage on an hourly basis, enabling the corresponding EVA to collect energy demand information from all vehicles within its assigned area. The definitions and calculations for this variable are provided in equations(1) and (2).

$$CS_{Fr_{v,s},\, t,\, v,\, s} = 1 \quad \forall\, arr_{v,s} < t < dep_{v,s} \tag{1}$$

$$CS_{To_{v,s},\, t,\, v,\, s} = 1 \quad \forall\, de_{v,s} \leq t \leq ai_{v,s} \tag{2}$$

To characterize the daily charging requirements of electric vehicles (EVs), the Monte Carlo Simulation (MCS) process performs 1,000,000 micro-stochastic evaluations, comprising 200 samples of 2,000 EVs, 120 samples of 2,500 EVs, and 80 samples of 3,750 EVs. These evaluations correspond to three predefined scenarios. The MCS results provide aggregate system-level charging data, which serve as input for the decentralized charging management strategy.

The simulation aggregates the total energy required by all EVs under analysis, denoted as $GChR_s$, and allows for comparative analysis across the sampled scenarios. Equation (3) defines this cumulative energy requirement during travel. For each scenario, the MCS also identifies the minimum and maximum samples, denoted ass_{min} and s_{max} respectively.

$$GChR_s = \sum_{v} \sum_{t} R_{t,v,s} \tag{3}$$

2.3. Decentralized electric vehicle charging management

The methodology applies decentralized electric vehicle charging management (DEVCM) modeling through EV aggregators (EVAs) at each bus where feeder integration is permitted. This study models the interaction at aggregator busk, assuming that the EVAs involved (corresponding to the "from" and "to" buses) are owned by different entities. The model uses the variables $CS_{k,t,v,s}$ and $R_{t,v,s}$ to determine the location and energy demand of each electric vehicleover time.

The methodology incorporates the model proposed in [21], adapting it to account for uncertainty in EV departure and arrival times. While the departure and arrival locations remain fixed, the associated time variables are modified, as illustrated by the probability distributions in Figure 4(b) . Specifically, departure times are modeled using a normal distribution with a mean of 08:02 and a standard deviation of 01:11, while arrival times follow a normal distribution with a mean of 22:04 and a standard deviation of 04:18.

This study analyses a set of samples $s \in S$, as described in Section 2.2.1 (Pseudo Trip Modeling Code). In this case, the distance traveled $td_{v,s}$ remains unchanged, while only the departurede $p_{v,s}$ and arrival $arr_{v,s}$. At this stage, the sets ,used for the Monte Carlo simulation, is limited to its minimum and maximum output cases. During DEVCM optimization, the set $n \in N$ represents the samples used for real-time operation. Each sample is assigned an equal probability of occurrence $\pi_n = \frac{1}{N}$, reflecting the absence of historical data and the neutrality of policy assumptions. Finally, in line with the objectives of this study, the energy traded through EVAs must be regulated to ensure coordination and maintain power system (PS) capacity.

For this research, the parameter P_t^{SYScap} represents the upper bound of the total charging demand permitted within the power system. This constraint accounts for the aggregate energy traded in both the day-ahead (DA) and real-time (RT) electricity markets. As shown inequation (4), its initial value corresponds to the sum of power demands across all buses at the system's annual peak load hour:

$$P^{SYScap} = \sum_b Pd_b \tag{4}$$

The DEVCM formulation is primarily based on the model presented in [21]; however, this study refines the approach by modifying several constraints–specifically equations (7), (8), (10), (11), (14), (18), (20), (22), (23) and (24). Furthermore, equations (25) through (42) adapt the algorithm by transforming the original nonlinear model into a mixed-integer linear programming (MILP) formulation. A comprehensive terminology section follows the mathematical formulation, describing all sets, parameters, and variables used in the model.

$$\min C = DAEM - RTEM^{\downarrow} + RTEM^{\uparrow} + BATCOST \tag{5}$$

$$\text{DAEM} = \Delta t \sum_t^T \lambda_t \times P_t^{EM} \tag{6}$$

$$\text{RTEM}^{\uparrow} = \Delta t \sum_t^T \sum_n^N \pi_n \times \lambda_{t,n}^{\uparrow} \times P_{t,n}^{-} \tag{7}$$

$$\text{RTEM}^{\downarrow} = \Delta t \sum_t^T \sum_n^N \pi_n \times \lambda_{t,n}^{\downarrow} \times P_{t,n}^{+} \tag{8}$$

$$\text{BATCOST} = BC^{ES} \times \sum_t^T \sum_v^V \sum_n^N \frac{m_v}{100} \times \frac{soc_{t,v,n}^{deg}}{BC_v^{ES}} \times C_v^{ES} \tag{9}$$

$$0 \leq P_{t,n}^{+} + P_{t,n}^{-} \leq \sum_v^V P_{t,v,n}^{B2G} \times \eta^{dsg} \tag{10}$$

$$\sum_n^N \left(P_{t,n}^{-} - P_{t,n}^{+}\right) = 0 \tag{11}$$

$$\begin{aligned} P_t^{EM} = & \sum_v^V \left(P_{t,v,n}^{G2B} - P_{t,v,n}^{B2G} \times \eta^{dsg}\right) \times CS_{k,t,v,s} \\ & + P_{t,n}^{+} - P_{t,n}^{-} \quad \forall t \in T \wedge n \in N \end{aligned} \tag{12}$$

$$P_{t,v,n}^{B2R} \times \eta^{dsg} = R_{t,v,n} \tag{13}$$

$$0 \leq P_{t,v,n}^{G2B} + P_{t,v,n}^{B2G} \leq P^{max} \times CS_{k,t,v,s} \tag{14}$$

$$0 \leq P_{t,v,n}^{B2R} \leq P^{max} \times X_{t,v,n} \tag{15}$$

$$0 \leq P_{t,v,n}^{G2B}, \quad 0 \leq P_{t,v,n}^{B2G} \tag{16}$$

$$\begin{aligned} soc_{t,v,n} = soc_{t-1,v,n} + \Delta t \times \Big(& P_{t,v,n}^{G2B} \cdot n^{chg} \\ & - P_{t,v,n}^{B2G} - P_{t,v,n}^{B2R} \Big) \end{aligned} \tag{17}$$

$$\begin{aligned} soc_{1,v,n} = soc_{T,v,n} + \Delta t \times (& P_{1,v,n}^{G2B} \cdot n^{chg} \\ & - P_{1,v,n}^{B2G} - P_{1,v,n}^{B2R}) \end{aligned} \tag{18}$$

$$0 \leq \underline{SoC} \leq soc_{t,v,n} \leq \overline{SoC} \leq BC^{ES} \tag{19}$$

$$soc_{t=1} = SoC_{n,v}^{init} \tag{20}$$

$$soc^{deg}_{t,v,n} \times CS_{k,t,v,s} \geq \; soc_{t-1,v,n} \times CS_{k,t,v,s} - \; soc_{t,v,n} \times CS_{k,t,v,s} \tag{21}$$

$$DAEM = \Delta t \sum_{t=1}^{T} \sum_{b=1}^{B} (\lambda_b - \lambda_{b-1}) \times \left(P^{EMefective}_{t,b}\right) \tag{22}$$

$$RTEM^{\uparrow} = \Delta t \sum_{t=1}^{T} \sum_{s=1}^{S} \sum_{b=1}^{B} \pi_n \times (\lambda_b - \lambda_{b-1}) \times \left(P^{-efective}_{t,n,b}\right) \tag{23}$$

$$RTEM^{\downarrow} = \Delta t \sum_{t=1}^{T} \sum_{s=1}^{S} \sum_{b=1}^{B} \pi_n \times (\lambda_b - \lambda_{b-1}) \times \left(P^{+efective}_{t,n,b}\right) \tag{24}$$

$$P^{EM}_t = P^{EM+}_t - P^{EM-}_t \tag{25}$$

$$P^{EMefective}_{t,b} = P^{EMefective+}_{t,b} - P^{EMefective-}_{t,b} \tag{26}$$

$$P^{EM}_t + P^{Sys}_t \geq P^{PQP}_{b-1} \times PQP_{t,b} \tag{27}$$

$$P^{EM}_t + P^{-}_{t,n} - P^{+}_{t,n} + P^{Sys}_t \geq P^{PQP}_{b-1} \times PQP^{n}_{t,n,b} \tag{28}$$

$$P^{EM}_t + P^{Sys}_t \leq P^{SYScap} \tag{29}$$

$$P^{EM}_t + P^{-}_{t,n} - P^{+}_{t,n} + P^{Sys}_t \leq P^{SYScap} \tag{30}$$

$$P^{EMefect+}_{t,b} \geq P^{EM+}_t - M_{big} \times (1 - PQP_{t,b}) \tag{31}$$

$$P^{EMefect+}_{t,b} \leq P^{EM+}_t \tag{32}$$

$$P^{EMefect+}_{t,b} \leq M_{big} \times (1 - PQP_{t,b}) \tag{33}$$

$$P^{EMefect-}_{t,b} \geq P^{EM-}_t - M_{big} \times (1 - PQP_{t,b}) \tag{34}$$

$$P^{EMefect-}_{t,b} \leq P^{EM-}_t \tag{35}$$

$$P^{EMefect-}_{t,b} \leq M_{big} \times (1 - PQP_{t,b}) \tag{36}$$

$$P^{+efect}_{t,n,b} \geq P^{+}_{t,n} - M_{big} \times \left(1 - PQP^{n}_{t,n,b}\right) \tag{37}$$

$$P^{+\text{efect}}_{t,n,b} \leq P^{+}_{t,n} \tag{38}$$

$$P^{+efect}_{t,n,b} \leq M_{big} \times (1 - PQP^{n}_{t,n,b}) \tag{39}$$

$$P^{-efect}_{t,n,b} \geq P^{-}_{t,n} - M_{big} \times (1 - PQP^{n}_{t,n,b}) \tag{40}$$

$$P^{-efect}_{t,n,b} \leq P^{-}_{t,n} \tag{41}$$

$$P^{-efect}_{t,n,b} \leq M_{big} \times (1 - PQP^{n}_{t,n,b}) \tag{42}$$

Terminology:

Symbol	**Description**
C	Total cost associated with the Electric Vehicle Aggregator (EVA)
$DAEM$	Cost of energy purchased in the day-ahead electricity market (DA)
$RTEM$	Cost of energy traded in the real-time electricity market (RT)
$BATCOST$	Cost associated with battery lifetime degradation (TVB)
Sets, Universe	
n, N	Samples analyzed
t, T	Time
v, V	Electric vehicles
b, B	PQP probability steps
$\downarrow$	Surplus energy (energy available for sale)
$\uparrow$	Deficit energy (energy required for purchase)
Variables and Parameters	
$\lambda_t, \lambda^{\uparrow}_{t,s}, \lambda^{\downarrow}_{t,s}$	Unit prices of energy in the DA and RT markets
P^{EM}_t	Power traded in the DA electricity market
$P^{-}_{t,s}, P^{+}_{t,s}$	Power deficit and surplus traded in the RT market
m_v	Linear degradation rate associated with battery lifetime
C^{ES}_v	Cost of energy storage [\$/kWh]
BC^{ES}_v	Energy storage capacity
$soc^{deg}_{t,v,n}$	Battery degradation equivalent to state of charge
n^{chg}	Battery charging efficiency
n^{dsg}	Battery discharging efficiency
$P^{B2G}_{t,v,n}$	Power fed from the battery to the grid
$P^{G2B}_{t,v,n}$	Power fed from the grid to the battery
$P^{B2R}_{t,v,n}$	Battery power used during the trip
$R_{t,v,n}$	Energy consumption during the trip [kWh]
$X_{t,v,n}$	Binary variable indicating travel state
$P^{\max}$	Maximum allowed charging power

Symbol	Description
$P^{\max}$	Maximum allowed charging power
$\underline{SoC}$	Lower bound of the battery state of charge
$\overline{SoC}$	Upper bound of the battery state of charge
$SoC^{\text{init}}_{n,v}$	Initial battery state of charge (randomly assigned)
$P^{EMefect}_{t,b}$	Effective DA power for step b
$P^{-efect}_{t,n,b}$	Effective power deficit for step b
$P^{+efect}_{t,n,b}$	Effective power surplus for step b
$PQP_{t,b}$	Binary indicating whether total DA load $\leq P_b$
$PQP^{n}_{t,n,b}$	Binary indicating whether total RT load $\leq P_b$
M_{big}	Parameter used for algorithm constraints

The DEVCM incorporates these constraints to optimize its economic variables. As a result, each EVA reports to the distribution network operator (DNO) the required power $P^{EM}_{k,t,s}$ at busk during each periodt for the two representative scenarios: s_{min} and s_{max}. The DNO processes this informationas detailed in the following sections. Due to the computational complexity of the DEVCM, the decentralized electric vehicle charging models were executed using the NEOS Server, as supported by [34–36], for each load-carrying bus.

2.3.1. Electric vehicle aggregator data

The vehicle data used in this study is based on the Tesla Model 3, as reported in [21]. The specific energy consumption ranges between <0.19;0.25> kWh/km, and the battery capacity is BCES=80kWh. The battery degradation cost is defined as $C^{ES}_v =< 100 - 140 >$ MWh, and the linear approximation of battery lifetime is $m_v =< 0.0006, 0.0017 >$.

In addition, information related to the EVA charging stations includes a maximum charging power of $P_{max} = 150$ KW, with both charging and discharging efficiencies set at $n_{chg} = 90$ % and $n_{dsg} = 90$ %, respectively The state-of-charge (SoC) operating limits, as recommended by the manufacturer, range from 15% to 95%.

2.4. Centralized electric vehicle charging management

The centralized electric vehicle charging management (CEVCM) is formulated as an optimal power flow (OPF) problem that processes the aggregated power requests $P^{EM}_{k,t}$ collected from all network EV aggregators. This information modifies the day-ahead load planning of the power system. Equation (43) represents the impact of each aggregator on the system load: if electric vehicles require energy, the load increases; conversely, if the EVs inject energy into the power system ($P^{EM}_{k,t}$ with negative value), the load decreases accordingly.

$$Pd_{k,t,s} = Pdps_{k,t,s} + P^{EM}_{k,t,s} \quad \forall s \in \{s_{\min}, s_{\max}\} \tag{43}$$

The study in [1] presents a CEVCM model, which is refined in the present research. Both models rely on power flow analysis to ensure proper power system (PS) operation, incorporating a contingency variable and various types of constraints. For each period t , the CEVCM is modeled using the following equations. Equation (44) defines the objective function, which minimizes power losses and penalizes non-supplied energy (NSE). The equality constraints, represented by ($h(x) = 0$), are described in equations (45) through (48). Equation (49) introduces the inequality constraint $g(x)$ ($g(x) < 0$). Finally, equations (50) through (53) define the bounds on the control variables, expressed as ($\underline{x} < x < \overline{x}$). All of these equations are applied to each time interval analyzed.

$$of = \sum_{k=1}^{n_{bus}} (C_{pen} \cdot NSE_k) + Pg_{slack} \tag{44}$$

$$Pg_k + NSP_k = Pd_k + \sum_{m=1}^{n_{bus}} P_{km} \tag{45}$$

$$Qg_k = Qd_k + Qsh_k + \sum_{m=1}^{n_{bus}} Q_{km} \tag{46}$$

$$P_{km} = V_k V_m Y_{km} \cos(\theta_{km} + \delta_{km}) - V_k^2 \cos(\tau_{km}) \tag{47}$$

$$Q_{km} = -V_k V_m Y_{km} \sin(\theta_{km} + \delta_{km}) + V_k^2 Y_{km} \sin(\tau_{km}) \tag{48}$$

$$S_{km} = \sqrt{P_{km}^2 + Q_{km}^2} \leq S^{up}_{km} \tag{49}$$

$$V_i^{low} \leq V_i \leq V_i^{up} \tag{50}$$

$$d_i^{low} \leq d_i \leq d_i^{up} \tag{51}$$

$$P^{low}_{g_i} \leq P_{g_i} \leq P^{up}_{g_i} \tag{52}$$

$$Q^{low}_{g_i} \leq Q_{g_i} \leq Q^{up}_{g_i} \tag{53}$$

Terminology:

Symbol	**Description**
OPF	Optimal Power Flow
NSE	Not Supplied Energy
PS	Power System
NSP	Not Supplied Power
low	Lower limit
up	Upper limit
Subscripts, Universe	
b, nbus	Bar in the power system (also: i, j, k, m)
Variables and Parameters	
$Pdps_i$	PS initial active power demand parameter
Pd_i	Active power demand
Qd_i	Reactive power demand
Pg_i	Active power generation
Qg_i	Reactive power generation
P_{ij}	Active power flow from bus i to j
Q_{ij}	Reactive power flow from bus i to j
S_{ij}	Apparent power flow from bus i to j
V_i	Voltage magnitude
δ_{km}	Voltage angle difference between buses k and m
Y_{km}	Admittance matrix magnitude
θ_{km}	Admittance matrix angle

The application results indicate that some scenarios exhibit the presence of not supplied power (NSP). Consequently, CEVCM operators must regulate the exchange of information with the DEVCM in order to adjust the energy traded in the day-ahead (DA) electricity market. When the load exceeds the available power system (PS) capacity, distribution network operators (DNOs) activate the load limit calculation for the EVAs associated with the affected buses. For further details, refer to Section 3. Results and Discussion.

2.4.1. Coordination between centralized and decentralized Charging Management

EV aggregators (EVAs) must apply a predefined limit when energy is requested from the power system. To quantify this limit, distribution network operators (DNOs) incorporate an additional variable into their optimization model: $P^{EM}_{cap,k}$, representing the energy trading capacity. This variable functions similarly to the NSE variable, regulating the maximum amount of power that EVAs are allowed to request from the system. Accordingly, this model modifies equation (45) by replacing it with equation (54), which restricts the value of the energy traded by EVAs in relation to the final demand of the power system, as defined in equation (55).

$$Pg_k + NSP_k = Pd_k + P^{EM}_{cap,k} + \sum_m P_{km} \tag{54}$$

$$P^{EM}_{cap,k} \leq Pd_k \tag{55}$$

EVAs must update their models, specifically equations (29) and (30), by adjusting the corresponding constraints based on temporary data provided by the regulatory agent for each EVA. Accordingly, the model adopts the modified formulations given by equations(56) and (57).

$$P^{EM}_t \leq P^{EM}_{cap} \tag{56}$$

$$P^{EM}_t + P^-_{t,n} - P^+_{t,n} \leq P^{EM}_{cap} \tag{57}$$

2.4.2. Transmission power system analyzed

The transmission power system analyzed in this study is based on the IEEE 14-bus model, as presented in [37]. Additionally, power factor data from the SEIN system, as reported by COES-SINAC, was used to adapt the model for daily analysis. This data corresponds to weekdays (Monday through Friday) in February 2020, prior to the national impact of the SARS-CoV-19 outbreak, which began affecting the country in March 2020. The reference day for peak load conditions is February 19, 2020.

2.4.3. Distribution analysis

In addition to the transmission system analysis, this study evaluates the distribution network using the IEEE 13-bus power system. Figure 3 illustrates the layout of this distribution system. The distribution analysis incorporates outputs from the transmission-level simulation, including bus voltages and load requirements. To generate representative distribution-level data, a data mining process is applied, which uses a stochastic characterization of the transmission results. This is achieved through a Monte Carlo simulation, which produces statistical samples based on the transmission system outputs.

In Figure 3, the presence of generators simulates vehicle-to-grid (V2G) energy injections from electric vehicles at different buses in the distribution system. The high-voltage side of the main transformer is not modeled, as its primary role is voltage regulation, which could interfere with the objective of monitoring voltage behavior within the distribution network. Following the data analysis and mining process, the distribution analysis includes a data synthesis stage. This stage produces a variety of statistical samples that synthetically represent the behavior of the distribution network under the influence of V2G technology and the power demand imposed by EV aggregators (EVAs).

3. Results and Discussion

Research in [1] presents a CEVCM model applied to the Peruvian context under three adoption scenarios. Building upon that framework, this study explores the coordination infrastructure between decentralized (DEVCM) and centralized (CEVCM) electric vehicle charging management models by comparing the same three scenarios.

3.1. Decentralized Electric Vehicle Charging Management

The distribution network operator (DNO) requires the amount of energy to be traded in each period of the day-ahead (DA) market. Table 2 presents the total daily energy traded for each scenario, including the minimum and maximum outputs obtained from the Monte Carlo Simulation (MCS) analysis.

Figure 6 (a) displays the minimum MCS outputs, while Figure 6 (b) illustrates the maximum outputs. According to Table 2, the EVAs associated with buses 6, 9, 12, 13, and 14 cause deviations in scenarios 2 and 3.

The electric vehicle characterization conducted in this study enables future analysis of regulatory measures focused on travel behavior and geographic distribution. Study [5] also considers uncertainties related to power generation, load demand, and real-time electricity pricing; however, its analysis is limited to a typical residential household.

Table 2. Daily energy traded with the power system by EVA

PEM [MWh]	Scenario 1		Scenario 2		Scenario 3	
Bar	minimum	maximum	minimum	maximum	minimum	maximum
2	2.211	2.188	2.953	2.103	4.802	3.887
3	2.022	1.806	1.768	1.504	2.926	3.308
4	2.469	1.293	2.321	1.566	3.313	2.361
5	1.384	0.936	1.735	1.002	3.144	1.290
6	2.502	3.357	2.835	3.389	60.494	5.655
9	1.849	2.147	2.083	2.795	3.061	59.141
10	1.809	1.101	2.255	2.150	3.265	2.422
11	1.859	1.758	2.417	2.848	2.849	3.777
12	1.526	3.381	1.930	50.309	40.676	5.078
13	1.870	1.758	2.713	61.462	44.124	79.022
14	1.392	3.381	2.192	6.734	39.120	8.427

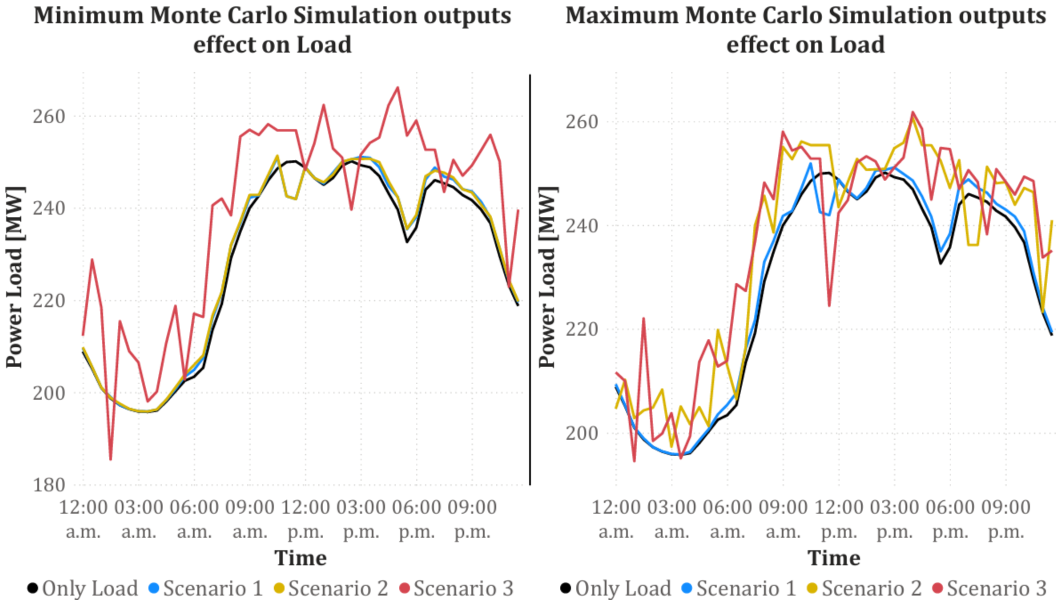

Figure 6. Power System Load per MCS output and scenario

Similarly, the work in [6] focuses on integrating cost savings and efficiency in electric vehicle charging infrastructure. Research in [7] emphasizes the interaction between electric vehicles and various energy markets. The present study extends this line of work by incorporating an optimization framework that combines day-ahead and real-time market dynamics with battery cost modeling.

3.2. Centralized Electric Vehicle Charging Management

Network operators are required to run optimal power flow (OPF) analyses. Table 3 presents the corresponding results, where the presence of not supplied energy (NSE) indicates that the EVA must adjust its daily load schedule. Figure 7 (a) illustrates OPF outcomes: the maximum output from the MCS analysis under Scenario 1 is shown in blue, and the minimum output from Scenario 3 is shown in red. These results demonstrate that the impact on daily system operation is minimal under Scenario 1, reflecting low EV adoption. In contrast, Scenario 3 highlights the negative consequences of poor coordination between CEVCM and DEVCM. The power system performance for Scenario 3 also reveals three instances of NSE (marked in red) and an increase in system losses of up to 7.79% compared to the business-as-usual (BAU) case.

Study [1] tests the same three scenarios under both unregulated charging and a centralized electric vehicle charging management (CEVCM) approach. In the case of unregulated EV charging, the resulting non-supplied energy (NSE) is 0.5 MWh for Scenario 1, 0.62 MWh for Scenario 2, and 2.74 MWh for Scenario 3. In this research, the application of DEVCM resolves power system operation issues for Scenarios 1 and 2. However, in Scenario 3, due to limited EV availability and the absence of coordination, the decentralized model results in 7.44 MWh of NSE. This highlights the necessity of coordinated management for systems with 3,750 EVs or more. The following section analyzes the impact of this coordination on the model.

Table 3. Centralized optimal power flow performance per scenario and MCS output

Bar	Without	Scenario 1		Scenario 2		Scenario 3	
	Evs	Min MCS	Max. MCS	Min MCS	Max. MCS	Min MCS	Max. MCS
Energy demand [MWh]	5486.08	5506.98	5509.18	5511.28	5654.06	5742.52	5672.24
Peak load [MW]	250.11	251.04	251.89	251.31	260.68	266.09	261.79
power factor	0.91	0.91	0.91	0.91	0.9	0.9	0.9
Power supplied [MWh]	5737.52	5760.42	5762.92	5765.14	5923.42	6013.54	5942.28
Losses [MWh]	251.44	253.46	253.74	253.86	269.36	271.02	270.04
ENS [MWh]	0	0	0	0	0	7.44	1.54
Maximum NSP [MW]	0	0	0	0	0	7.23	3.1
NSP Slash [#]						14	14

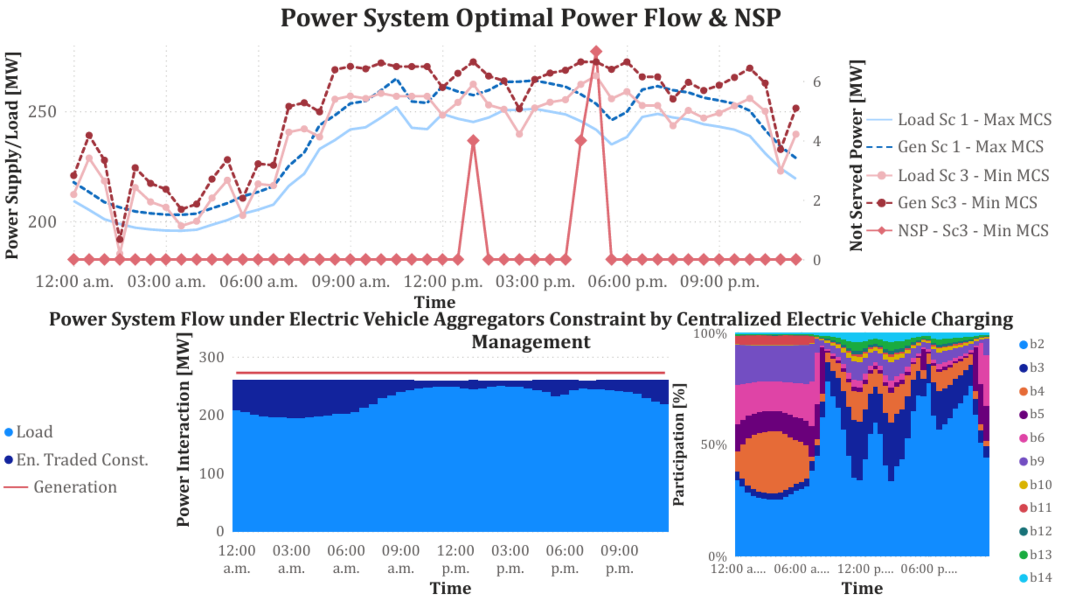

Figure 7. Power System operation performed by DNO

3.2.1. Coordination between centralized and decentralized management

The maximum amount of energy allowed for trading by each EVA serves as a constraint in the execution of decentralized charging management. Figure 7 (b) illustrates the energy trading limits established by distribution network operators (DNOs), while Figure 7 (c) shows the participation of each aggregator within those limits.

Scenario 3 is re-executed with these constraints applied to the EVAs. Table 4 presents the resulting energy traded between the aggregators and the DNO. Under this coordinated strategy, the DEVCM shifts battery charging to off-peak hours and maintains stability during peak demand periods. Figure 8 displays the response of the EVAs under these operating conditions, showing the minimum output in blue and the maximum output in red.

Table 4. Daily energy traded with the power system by EVA

Scenario 3	PEM [MWh]	
CR bar	min MCS	max MCS
2	74.891	71.135
3	12.277	10.419
4	30.783	2.248
5	30.180	18.688
6	14.582	19.129
9	22.681	30.668
10	2.992	3.092
11	7.193	7.663
12	2.468	4.367
13	4.257	5.713
14	3.714	7.084

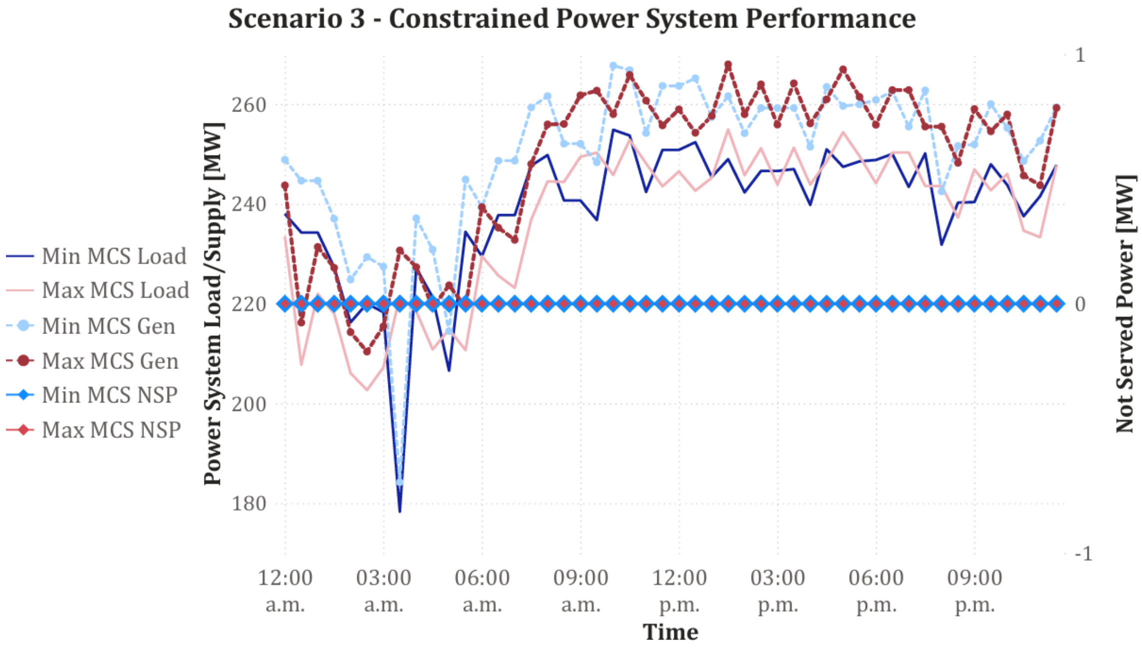

Figure 8. CEVCM coordination over DEVCM

For both MCS outputs under DNOs load regulation,no non-supplied energy (NSE) is observed, ensuring the system operates under normal conditions as long as the required energy transfer is achieved. The increase in charging activity may raise daily energy losses–up to 7.34% (shown in blue) and, to a lesser extent, up to 5.9% (shown in red). Power system variability decreases throughout the day due to the application of DEVCM. As a result, DNOs must plan for this operational behavior in the long term, aiming to reduce future peak-hour costs through increased base generation capacity. According to the reviewed literature, this additional capacity could be provided by renewable sources such as wind, hydro, or geothermal energy. Table 5 presents the CEVCM power system performance results.

Study [21] reports a positive economic impact on EVA charging management in the absence of geographical uncertainty and under the analysis of travel patterns for 500 electric vehicles. Additionally, the numerical results in [23] demonstrate that, under the most environmentally favorable scenario, excluding certain electric vehicles from the optimization process reduces emissions by 7% compared to the base case–while still yielding the highest profits for the operator. Similarly, the results in [24] propose a coordinated optimal operation strategy for a 33-node test system, achieving a reduction in operational costs from 17.74% to 17.53% and a decrease in system losses ranging from 29.49% to 31.36%.

Table 5. Centralized managed optimal power flow performance

Daily charge	Without SV	Scenario 3 CR	
		min MCS	max MCS
Energy demand [MWh]	5486.08	5734.54	5683.06
Maximum load [MW]	250.11	254.87	254.93
load factor	0.91	0.94	0.93
Power supplied [MWh]	5737.52	6004.56	5949.34
Losses [MWh]	251.44	270.02	266.28
ENS [MWh]	0	0	0
Maximum NSP [MW]	0	0	0
bar		0	0

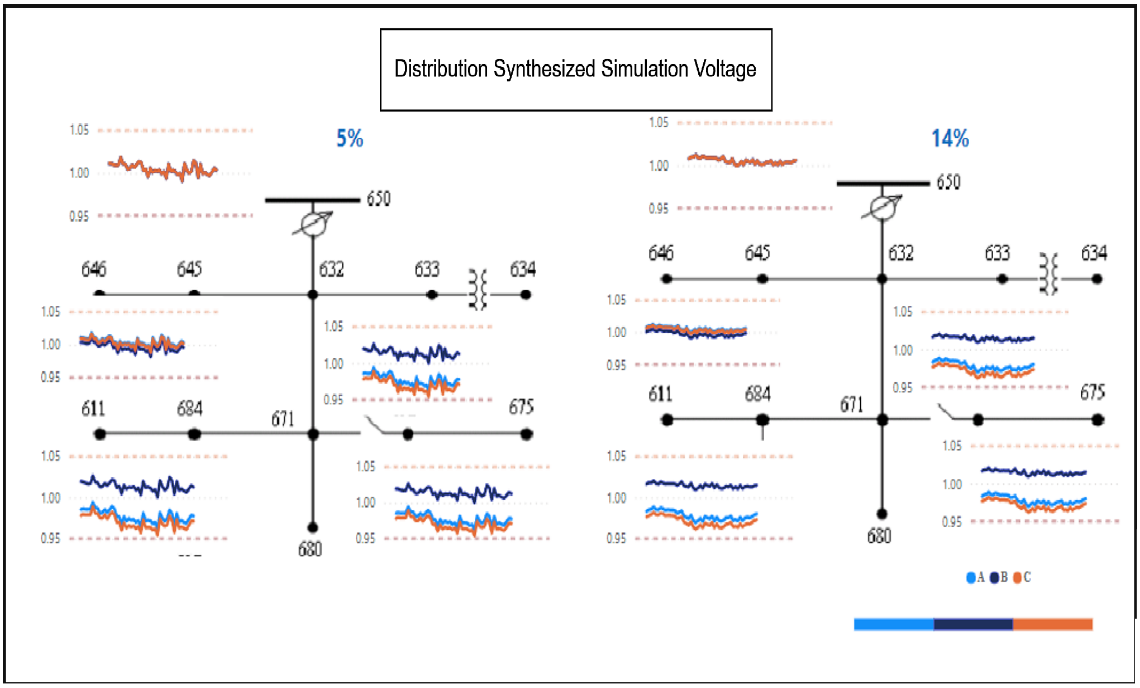

Figure 9. Distribution Power System (IEEE 13 bus) simulation

3.3. Distribution Analysis

Figure 9 presents the results for the 5% and 14% synthesized data sets, which showed the lowest error in the distribution analysis. The distribution network (DN) results reported in [1] indicate voltage levels approaching undervoltage conditions. In contrast, the findings of this study show that the voltage levels at the farthest buses (671, 675, 611, 684, 652, 680, and 692) are less prone to undervoltageissues.

4. Conclusions

The integration of decentralized electric vehicle charging management (DEVCM) into the transmission power system (PS) improves its operational performance compared to unregulated charging, as reported in [1] and illustrated inTable 3, Figure 6, and Figure 7. Under purely decentralized management, the power system performs well in Scenarios 1 and 2, even under maximum MCS outputs, without the need for additional energy management policies. However, Scenario 3–with higher EV penetration–demands additional policy interventions to maintain system stability.

This research introduces a novel Centralized Electric Vehicle Charging Management (CEVCM) system that operates independently of external influences, ensuring reliable and predictable EV charging behavior. By reducing stress on the power grid, it contributes to mitigating power outages and related safety risks. Moreover, CEVCM infrastructure can be deployed in phases, adapting to EV penetration rates and enabling geographically targeted placement based on observed travel patterns. As demonstrated in Table 5 and Figure 8, the CEVCM approach improves the daily operational performance of the power system.

This work also provides a valuable framework for addressing coordination challenges in current distributed energy management policies. The CEVCM model supports data-driven planning for charging environments, guided by actual EV usage behavior. This facilitates the optimization of power system infrastructure near substations experiencing high EV adoption but limited energy trading activity, as shown in Figure 7. Furthermore, this study evaluates the unbalanced IEEE 13-bus power system as a distribution network. The model demonstrates compliance with Peruvian voltage regulations, even at the most remote buses of the distribution system.

For future research, the proposed model, particularly the version incorporating the non-supplied energy (NSE) variable, offers significant potential for evaluating grid expansion needs associated with the integration of distributed renewable energy sources. Further studies could explore combining the CEVCM framework with centralized coordination mechanisms and EV-based generation planning. The data synthesis process could also be refined to focus on a targeted set of operational and contingency scenarios, thereby reducing computational complexity. Finally, a hybrid charging management approach that integrates both controlled and uncontrolled strategies, including day-ahead coordination, distributed generation, and real-time aggregator flexibility (e.g., demand response, EV battery state-of-charge control, and distributed generation management), may yield additional operational benefits.

Acknowledgments

The authors gratefully acknowledge the support of the "Program of Doctorates in Peruvian Universities," promoted by the Ministry of Education (MINEDU), the National Council of Science, Technology and Technological Innovation (CONCYTEC), and the National Fund for Scientific, Technological and Technological Innovation Development (FONDECYT).

Contributor Roles

- **Carlos W. Villanueva-Machado:** Conceptualization, data curation, formal analysis, investigation, methodology, software, visualization, writing – original draft, writing – review and editing.
- **Jaime E. Luyo:** Formal analysis, investigation, project administration, supervision, validation.
- **Alberto Rios-Villacorta:** Formal analysis, investigation, project administration, supervision, validation.

References

[1] C. W. Villanueva-Machado, J. E. Luyo, and A. Ríos-Villacorta, “Impacto de la simulación montecarlo de carga no controlada de vehículos eléctricos en la generación distribuida,” *Ingenius*, no. 30, pp. 120–134, Jul. 2023. [Online]. Available: https://doi.org/10.17163/ings.n30.2023.10

[2] S. Li, P. Zhao, C. Gu, J. Li, S. Cheng, and M. Xu, “Battery protective electric vehicle charging management in renewable energy system,” *IEEE Transactions on Industrial Informatics*, vol. 19, no. 2, pp. 1312–1321, Feb. 2023. [Online]. Available: https://doi.org/10.1109/TII.2022.3184398

[3] Y. Yang, Q.-S. Jia, G. Deconinck, X. Guan, Z. Qiu, and Z. Hu, “Distributed coordination of EV charging with renewable energy in a microgrid of buildings,” *IEEE Transactions on Smart Grid*, vol. 9, no. 6, pp.

6253–6264, Nov. 2018. [Online]. Available: https://doi.org/10.1109/TSG.2017.2707103

[4] A. J. Cheng, B. Tarroja, B. Shaffer, and S. Samuelsen, "Comparing the emissions benefits of centralized vs. decentralized electric vehicle smart charging approaches: A case study of the year 2030 California electric grid," *Journal of Power Sources*, vol. 401, pp. 175–185, Oct. 2018. [Online]. Available: https://doi.org/10.1016/j.jpowsour.2018.08.092

[5] S. Zeynali, N. Rostami, A. Ahmadian, and A. Elkamel, "Two-stage stochastic home energy management strategy considering electric vehicle and battery energy storage system: An ann-based scenario generation methodology," *Sustainable Energy Technologies and Assessments*, vol. 39, p. 100722, Jun. 2020. [Online]. Available: https://doi.org/10.1016/j.seta.2020.100722

[6] M. R. Sarker, H. Pandžić, K. Sun, and M. A. Ortega-Vázquez, "Optimal operation of aggregated electric vehicle charging stations coupled with energy storage," *IET Generation, Transmission & Distribution*, vol. 12, no. 5, pp. 1127–1136, Jan. 2018. [Online]. Available: https://doi.org/10.1049/iet-gtd.2017.0134

[7] M. R. Sarker, Y. Dvorkin, and M. A. Ortega-Vázquez, "Optimal participation of an electric vehicle aggregator in day-ahead energy and reserve markets," *IEEE Transactions on Power Systems*, vol. 31, no. 5, pp. 3506–3515, Sep. 2016. [Online]. Available: https://doi.org/10.1109/TPWRS.2015.2496551

[8] H. Kikusato, K. Mori, S. Yoshizawa, Y. Fujimoto, H. Asano, Y. Hayashi, A. Kawashima, S. Inagaki, and T. Suzuki, "Electric vehicle charge–discharge management for utilization of photovoltaic by coordination between home and grid energy management systems," *IEEE Transactions on Smart Grid*, vol. 10, no. 3, pp. 3186–3197, May 2019. [Online]. Available: http://dx.doi.org/10.1109/TSG.2018.2820026

[9] M. F. Shaaban, M. Ismail, E. F. El-Saadany, and W. Zhuang, "Real-time pev charging/discharging coordination in smart distribution systems," *IEEE Transactions on Smart Grid*, vol. 5, no. 4, pp. 1797–1807, Jul. 2014. [Online]. Available: http://dx.doi.org/10.1109/TSG.2014.2311457

[10] M. M. Hoque, M. Khorasany, R. Razzaghi, H. Wang, and M. Jalili, "Transactive coordination of electric vehicles with voltage control in distribution networks," *IEEE Transactions on Sustainable Energy*, vol. 13, no. 1, pp. 391–402, Jan. 2022. [Online]. Available: https://doi.org/10.1109/TSTE.2021.3113614

[11] N. Rahbari-Asr and M.-Y. Chow, "Cooperative distributed demand management for community charging of PHEV/PEVs based on KKT conditions and consensus networks," *IEEE Transactions on Industrial Informatics*, vol. 10, no. 3, pp. 1907–1916, Aug. 2014. [Online]. Available: https://doi.org/10.1109/TII.2014.2304412

[12] D. Said and H. T. Mouftah, "A novel electric vehicles charging/discharging management protocol based on queuing model," *IEEE Transactions on Intelligent Vehicles*, vol. 5, no. 1, pp. 100–111, Mar. 2020. [Online]. Available: https://doi.org/10.1109/TIV.2019.2955370

[13] X. Yang, C. Xu, Y. Zhang, W. Yao, J. Wen, and S. Cheng, "Real-time coordinated scheduling for ADNs with soft open points and charging stations," *IEEE Transactions on Power Systems*, vol. 36, no. 6, pp. 5486–5499, Nov. 2021. [Online]. Available: https://doi.org/10.1109/TPWRS.2021.3070036

[14] M. Shafie-Khah, P. Siano, D. Z. Fitiwi, N. Mahmoudi, and J. P. S. Catalao, "An innovative two-level model for electric vehicle parking lots in distribution systems with renewable energy," *IEEE Transactions on Smart Grid*, vol. 9, no. 2, pp. 1506–1520, Mar. 2018. [Online]. Available: https://doi.org/10.1109/TSG.2017.2715259

[15] M. Mohiti, H. Monsef, and H. Lesani, "A decentralized robust model for coordinated operation of smart distribution network and electric vehicle aggregators," *International Journal of Electrical Power & Energy Systems*, vol. 104, pp. 853–867, Jan. 2019. [Online]. Available: https://doi.org/10.1016/j.ijepes.2018.07.054

[16] M. S. H. Nizami, M. J. Hossain, and K. Mahmud, "A coordinated electric vehicle management system for grid-support services in residential networks," *IEEE Systems Journal*, vol. 15, no. 2, pp. 2066–2077, Jun. 2021. [Online]. Available: https://doi.org/10.1109/JSYST.2020.3006848

[17] F. L. Da Silva, C. E. H. Nishida, D. M. Roijers, and A. H. Reali Costa, "Coordination of electric vehicle charging through multiagent reinforcement learning," *IEEE Transactions on Smart Grid*, vol. 11, no. 3, pp. 2347–2356, May 2020. [Online]. Available: https://doi.org/10.1109/TSG.2019.2952331

[18] S. Deilami, A. S. Masoum, P. S. Moses, and M. A. S. Masoum, "Real-time coordination of plug-in electric vehicle charging in smart grids

to minimize power losses and improve voltage profile," *IEEE Transactions on Smart Grid*, vol. 2, no. 3, pp. 456–467, Sep. 2011. [Online]. Available: https://doi.org/10.1109/TSG.2011.2159816

[19] J. Hu, S. You, M. Lind, and J. Ostergaard, "Coordinated charging of electric vehicles for congestion prevention in the distribution grid," *IEEE Transactions on Smart Grid*, vol. 5, no. 2, pp. 703–711, Mar. 2014. [Online]. Available: https://doi.org/10.1109/TSG.2013.2279007

[20] M. R. Sarker, M. A. Ortega-Vázquez, and D. S. Kirschen, "Optimal coordination and scheduling of demand response via monetary incentives," *IEEE Transactions on Smart Grid*, vol. 6, no. 3, pp. 1341–1352, May 2015. [Online]. Available: https://doi.org/10.1109/TSG.2014.2375067

[21] J. Luyo, C. Villanueva, A. Delgado, and C. Carbajal, "Electric vehicles aggregator participation in energy markets considering uncertainty travel patterns," *International Journal of Innovative Technology and Exploring Engineering*, vol. 8, no. 12, pp. 4994–4998, Oct. 2019. [Online]. Available: http://dx.doi.org/10.35940/ijitee.L3747.1081219

[22] P. Harsh and D. Das, "Optimal coordination strategy of demand response and electric vehicle aggregators for the energy management of reconfigured grid-connected microgrid," *Renewable and Sustainable Energy Reviews*, vol. 160, p. 112251, May 2022. [Online]. Available: https://doi.org/10.1016/j.rser.2022.112251

[23] W. Yang, J. Guo, and A. Vartosh, "Retracted: Optimal economic-emission planning of multi-energy systems integrated electric vehicles with modified group search optimization," *Applied Energy*, vol. 311, p. 118634, Apr. 2022. [Online]. Available: https://doi.org/10.1016/j.apenergy.2022.118634

[24] S. Gupta, A. Maulik, D. Das, and A. Singh, "Coordinated stochastic optimal energy management of grid-connected microgrids considering demand response, plug-in hybrid electric vehicles, and smart transformers," *Renewable and Sustainable Energy Reviews*, vol. 155, p. 111861, Mar. 2022. [Online]. Available: https://doi.org/10.1016/j.rser.2021.111861

[25] A. Najafi, M. Pourakbari-Kasmaei, M. Jasinski, M. Lehtonen, and Z. Leonowicz, "A hybrid decentralized stochastic-robust model for optimal coordination of electric vehicle aggregator and energy hub entities," *Applied Energy*, vol. 304, p. 117708, Dec. 2021. [Online]. Available: https://doi.org/10.1016/j.apenergy.2021.117708

[26] EV Volumes. (2023) Global EV sales for 2023. EV Volumes Autovista Group. [Online]. Available: https://upsalesiana.ec/ing34ar4r26

[27] PNUMA, *Movilidad eléctrica: Avances 19 en América Latina y el Caribe 2019*. Programa de las Naciones Unidas para el Medioambiente, 2019. [Online]. Available: https://upsalesiana.ec/ing34ar4r27

[28] LNE. (2023) Aumentó la penetración de vehículos eléctricos e híbridos en América Latina durante el 2022. La nota económica. [Online]. Available: https://upsalesiana.ec/ing34ar4r28

[29] MOVELATAM, *Interoperability for recharging electric vehicles in Latin America and the Caribbean, practical guide of recommendations*. United Nations Environment Programme, 2022. [Online]. Available: https://upsalesiana.ec/ing34ar4r29

[30] AAP. (2019) Los protagonistas de la nueva era automotriz: Vehículos eléctricos e hibrídos en el perú. Asociación Automotríz del Perú. [Online]. Available: https://upsalesiana.ec/ing34ar4r30

[31] C. W. Villanueva. (2024) Operative analysis of electric vehicle controlled charging management: Centralized - decentralized coordination. Git-Hub. Inc. [Online]. Available: https://upsalesiana.ec/ing34ar4r37

[32] L. Wang, S. Sharkh, and A. Chipperfield, "Optimal decentralized coordination of electric vehicles and renewable generators in a distribution network using A* search," *International Journal of Electrical Power & Energy Systems*, vol. 98, pp. 474–487, Jun. 2018. [Online]. Available: https://doi.org/10.1016/j.ijepes.2017.11.036

[33] S. Pirouzi, J. Aghaei, T. Niknam, H. Farahmand, and M. Korpas, "Exploring prospective benefits of electric vehicles for optimal energy conditioning in distribution networks," *Energy*, vol. 157, pp. 679–689, Aug. 2018. [Online]. Available: https://doi.org/10.1016/j.energy.2018.05.195

[34] J. Czyzyk, M. Mesnier, and J. More, "The neos server," *IEEE Computational Science and Engineering*, vol. 5, no. 3, pp. 68–75, 1998. [Online]. Available: https://doi.org/10.1109/99.714603

[35] E. D. Dolan, *NEOS server 4.0 administrative guide.*, Jul. 2001. [Online]. Available: http://dx.doi.org/10.2172/822567

[36] W. Gropp and J. J. More, "Optimization environments and the NEOS server," in *Conference: 3. International Workshop on short*

term experiments under strongly reduced gravity conditions, Bremen (Germany), 8-11 Jul 1996. Argonne National Lab. (ANL), Argonne, IL (United States), 03 1997. [Online]. Available: https://upsalesiana.ec/ing34ar4r35

[37] PSCAD. (2018) IEEE 14 bus system. Manitoba Hydro International Ltd. [Online]. Available: https://upsalesiana.ec/ing34ar4r36

Scientific Paper / Artículo Científico

UNIVERSIDAD POLITÉCNICA SALESIANA ECUADOR
INGENIUS
Revista de Ciencia y Tecnología
https://doi.org/10.17163/ings.n34.2025.05
pISSN: 1390-650X / eISSN: 1390-860X

EVALUATION OF POLLUTANT EMISSIONS FROM DIESEL VEHICLES FUELED WITH BIODIESEL UNDER REAL-WORLD DRIVING CONDITIONS

EVALUACIÓN DE LAS EMISIONES CONTAMINANTES EN VEHÍCULOS DIÉSEL ALIMENTADOS CON BIODIÉSEL EN CONDICIONES REALES DE CONDUCCIÓN

Edilberto Antonio Llanes-Cedeño[1,*], Andrés Cárdenas-Yánez[1], Edwin Chamba[1], Juan Carlos Castelo[2], Juan Carlos Rocha-Hoyos[2]

Received: 22-02-2025, Received after review: 02-06-2025, Accepted: 05-06-2025, Published: 01-07-2025

Abstract

This study evaluates the impact of B10 and B20 biodiesel blends produced from waste frying oil on pollutant emissions when used in diesel-powered vehicles operating under real-world driving conditions at high altitudes, ranging from 2619 to 2877 meters above sea level, in the Metropolitan District of Quito, Ecuador. Comparative tests were conducted using two diesel vehicles: one equipped with a common rail direct injection (CRDI) system, designated as M2.5C, and another with an injection pump system, referred to as H2.5B. Both vehicles were initially fueled with conventional diesel to establish a baseline. Exhaust emissions were measured under hot-engine conditions using a Portable Emissions Measurement System (PEMS) along a 15.7 km route that included ascending, descending, and urban driving segments. The findings indicate that carbon monoxide (CO) emissions were lowest when pure diesel was used in both engine types. Hydrocarbon (HC) emissions were minimal when B20 biodiesel was employed, regardless of the vehicle. Nitrogen oxide (NO_x) emissions showed no significant differences across the fuels tested, and in urban driving conditions, NO_x levels remained consistently stable.

Keywords: fuel consumption index, air conditioning, efficient driving, fuel, schedule, driving cycle

Resumen

Esta investigación evalúa los efectos de las mezclas de biodiésel de aceite de fritura usado (B10 y B20) con combustible convencional, en términos de emisiones, a gran altitud (entre 2619 y 2877 m s. n. m.), bajo condiciones reales de conducción en el Distrito Metropolitano de Quito, Ecuador. Se realizaron ensayos comparativos con dos vehículos con motor diésel; el primer sistema CRDI de inyección directa de common rail denominado M2.5C; el segundo, con sistema de bomba de inyección, denominado H2.5B, ambos alimentados inicialmente con diésel puro como línea base. Las tasas de emisiones de escape se cuantificaron en caliente mediante el sistema portátil de medición de emisiones (PEMS), a lo largo de una ruta de 15,7 km que incluyó condiciones de ascenso, descenso por carretera y tramos urbanos. Los resultados permiten concluir que las emisiones mínimas de CO se registran al utilizar diésel convencional en ambos motores (H2.5B y M2.5C); las emisiones de HC son mínimas con la mezcla B20, y las emisiones de NO_x no presentan variaciones significativas, independientemente del combustible utilizado. En el circuito urbano, tampoco se observa una variación significativa de las emisiones de NO_x según el tipo de combustible.

Palabras clave: índice de consumo de combustible, aire acondicionado, conducción eficiente, combustible, horario, ciclo de conducción.

[1,*] Ingeniería Automotriz/Eficiencia, Impacto Ambiental e Innovación Grupo de Investigación en Industria y Transporte, Universidad Internacional SEK, Ecuador. Corresponding author ✉: antonio.llanes@uisek.edu.ec.

[2] Facultad de Mecánica / Grupo de Investigación en Producción Científica con Tecnología Moderna en el Campo Automotriz INVELECTRO, Escuela Superior Politécnica de Chimborazo, Ecuador.

Suggested citation: E. A. Llanes-Cedeño, A. Cárdenas-Yánez, E. Chamba, J. C. Castelo, and J. C. Rocha-Hoyos, "Evaluation of pollutant emissions from Diesel Vehicles Fueled with biodiesel under Real-World driving conditions," *Ingenius, Revista de Ciencia y Tecnología*, N.° 34, pp. 61-74, 2025, DOI: https://doi.org/10.17163/ings.n34.2025.05.

1. Introduction

The combustion of petroleum-derived fuels produces emissions that are both toxic and harmful to public health. According to the World Health Organization (WHO), nine out of ten people worldwide are exposed to polluted air, contributing to the premature deaths of approximately seven million individuals each year [1]. In Latin America and the Caribbean, over 100 million people are exposed to air pollution levels exceeding WHO-recommended thresholds [2, 3]. Importantly, emissions from diesel engines have been classified as carcinogenic to humans [4, 5]. The transport sector has overtaken the energy sector as the leading contributor to carbon emissions and other pollutants that significantly exacerbate the greenhouse effect and global warming [6]. According to the International Transport Forum, carbon dioxide (CO_2) emissions from transport account for 23% of global totals and represent 30% of all CO_2 emissions resulting from fossil fuel combustion [7]. Moreover, the transport sector is the primary source of conventional air pollutants responsible for elevated concentrations of ozone and particulate matter in urban environments [8].

Although there is extensive literature on vehicular emissions, most studies have been conducted in cities located at or near sea level [9]. In Ecuador, air pollution resulting from hydrocarbon combustion has reached alarming levels in recent years. One major contributing factor is the country's topography, with cities such as the Metropolitan District of Quito situated at an average altitude of 2,850 meters above sea level [10]. At high altitudes, combustion becomes less efficient, leading to increased emissions of nitrogen oxides (NO_x) and particulate matter (PM) [11]. Additionally, the diesel fuel used in Ecuador contains approximately 350 ppm of sulfur, which restricts the import of vehicles equipped with after-treatment technologies designed to reduce NO_x and PM emissions [11]. Higher altitudes are also associated with increased emissions of unburned hydrocarbons (HC), PM, and soot [12]. Furthermore, evidence suggests that real-world NO_x emissions from diesel vehicles have shown little improvement over time and often exceed regulatory limits by a wide margin [13, 14]. Altitude affects both intake and exhaust pressures, which can lead to clogging of air filters and diesel particulate filters (DPFs). Moreover, variations in spray and combustion characteristics in diesel engines have been observed across altitudes ranging from 0 to 4,500 meters, with injection pressure playing a significant role [15]. According to Fontaras et al. [16], the Worldwide Harmonized Light Vehicles Test Procedure (WLTP) provides CO_2 emission estimates that are more representative of real-world driving conditions than those from the New European Driving Cycle (NEDC). However, the Real Driving Emissions (RDE) test, designed to ensure regulatory compliance under on-road conditions, specifically targets the reduction of NO_x emissions in diesel vehicles using Portable Emissions Measurement Systems (PEMS) [17].

Traditionally, vehicular emissions are evaluated using standardized dynamometer-based test cycles, such as the New European Driving Cycle (NEDC), the Worldwide Harmonized Light Vehicles Test Cycle (WLTC), and the EPA Federal Test Procedure (FTP-75). However, studies have demonstrated that these laboratory protocols do not always capture the full range of emissions encountered under real-world operating conditions. As a result, on-road testing methodologies have gained prominence. These rely on Portable Emissions Measurement Systems (PEMS) to evaluate vehicle performance under everyday driving scenarios, including road gradients, traffic variability, ambient temperature fluctuations, and changes in driving speed. According to Kousoulidou et al. [18], real-world emissions of nitrogen oxides (NO_x) and particulate matter can be two to four times higher than those measured in controlled laboratory environments.

Diesel engines are widely recognized for their low installation cost, high energy efficiency, operational stability, and exceptional adaptability to diverse operating conditions [19, 20]. However, fossil fuel reserves are being rapidly depleted under current consumption trends [21]. This has spurred growing interest in the development of renewable, sustainable, and environmentally friendly alternative fuels. Among these, biofuels represent a promising energy source capable of enhancing energy, economic, and environmental security [22]. Biodiesel, in particular, has attracted global attention as both a blending component and a direct substitute for conventional fuels in internal combustion engines (ICEs) [23, 24]. To mitigate emissions of harmful pollutants, blends of diesel with biodiesel derived from oilseeds and other feedstocks have been proposed as viable alternatives [25]. Despite its potential, there is limited empirical evidence regarding the impact of biodiesel blends on the performance and emissions of diesel engines not originally designed for such fuels [26]. Furthermore, studies assessing the health impacts of biodiesel combustion must be interpreted in the context of rapid advances in diesel engine technology, which have evolved significantly in response to increasingly stringent emissions regulations [27, 28].

Biodiesel has emerged as a viable alternative to fossil fuels, garnering growing interest for its potential to reduce pollutant emissions and mitigate the environmental impact of compression ignition engines. Derived from renewable feedstocks such as vegetable oils, animal fats, and recycled cooking oils, this biofuel offers substantial advantages in terms of sustainability and greenhouse gas (GHG) mitigation [29, 30].

According to Demirbas [31], carbon dioxide (CO_2) emissions from biodiesel combustion can be reduced by up to 78% compared to conventional diesel. Additionally, biodiesel produces lower emissions of particulate matter, sulfur oxides (SO_x), and carbon monoxide (CO), thereby contributing to improved urban air quality [32]. However, its effect on nitrogen oxide (NO_x) emissions remains variable and depends on factors such ascombustion conditions and engine design.

This study aims to evaluate the impact of B10 and B20 biodiesel blends, derived from waste frying oil and mixed with conventional diesel, on vehicle emissions under high-altitude conditions ranging from 2,619 to 2,877 meters above sea level. The assessment was conducted through on-road testing to quantify emissions during real-world driving in the Metropolitan District of Quito, Ecuador.

2. Materials and Methods

The experimental work was carried out in two stages. The first stage involved the characterization of the base diesel fuel and its blends with biodiesel. The second stage consisted of evaluating the exhaust emissions from a diesel engine fueled with pure diesel and biodiesel–diesel blends (B10 and B20). All tests were performed at an altitude of 2,810 meters above sea level at the Laboratory for the Analysis of Vehicles and Sustainable Mobility (LIAVMS), located in Quito, Ecuador.

2.1. Characterization of waste cooking oil and biodiesel production.

A total of 100 liters of waste cooking oil was collected from a restaurant located near SEK University in Quito, Ecuador. The oil was centrifuged and filtered to remove suspended solids and then heated to reduce its water content. The collected oil had undergone at least ten frying cycles. Table 1 presents the physicochemical characteristics and selected fuel-related properties of the waste cooking oil [33].

The waste cooking oil was converted into fatty acid methyl esters (FAME) via base-catalyzed transesterification using potassium hydroxide (KOH) dissolved in methanol. The reaction was carried out in a thermal bath at 90 °C for 3 hours at a stirring rate of 900 rpm. Upon completion, the reaction mixture was filtered using Millipore equipment. To purify the filtrate, 5 mL of Milli-Q water was added for washing, followed by 2 mL of a hexane: diethyl ether mixture (80:20) to remove residual impurities, catalyst traces, and solvent. The mixture was then transferred to separating funnels and allowed to stand for 20 minutes to facilitate phase separation. The organic phase was subsequently collected in pre-weighed tubes and dried in an oven at 60 °C for 24 hours.

The production cost of one liter of biodiesel at the laboratory scale was approximately three U.S. dollars, a value that could be reduced under industrial-scale conditions. In comparison, the international market price for conventional diesel is around one dollar per liter, making biodiesel production economically unviable under laboratory-scale parameters. However, it is important to note that biodiesel is not typically used at 100% concentration (B100). The literature recommends blending levels of no more than 20% (B20) due to the associated reduction in engine torque and power output [3]. Therefore, one liter of biodiesel can be mixed with at least five liters of conventional diesel, which improves economic feasibility when applied under real-world blending practices.

Table 1. Physicochemical properties of waste cooking oil

Property	**Value**
Acidity	1,998±0,02
Kinematic viscosity (mm^2/s, a 313 K)	35,4±0,05
pH	2,9±0,0
Density (kg/L, at 288 K)	0,931±0,02
Water content (%)	0,46±0,01
Saponification value	124,31±0,03
ÍIodine value	30,85±0,01
Cetane number	47±0,1
Free fatty acid (mg KOH/g oil)	1,29±0,03

2.2. Characterization of diesel/biodiesel blends

Presents the physicochemical properties of the fuel samples, characterized in accordance with ASTM standards and compared against the limits established by Ecuadorian Technical Standard INEN 1489:2012 for diesel and biodiesel blends. All measured values complied with the specified requirements. According to the literature, a higher cetane number contributes to improved combustion performance in diesel engines [25], [32].

2.3. Test vehicles

Table 3 presents the technical specifications of the two test vehicles used in this study. The first vehicle, an MB-5 van from the 2015 model year, had an odometer reading of 55,000 km. The second, an H2.5 van also from 2015, had accumulated 143,365 km. Although the H2.5 is equipped with an older injection system, it was included in the study due to its continued presence in Ecuador's second-hand vehicle market. Moreover, this type of engine remains in use in certain heavy-duty applications, such as trucks, locomotives, and marine vessels, where durability and mechanical simplicity are critical.

Table 2. Physicochemical characterization of diesel and biodiesel blends.

Fuel properties	**Standard**	**Diesel Premium**	**Diesel / 10% biodiesel (B10)**	**Diesel / 20 % biodiesel (B20)**	**INEN Standard: 1489 2012**
Cetane number	ASTM D976	51.7	53.2	53.5	45 min.
Distillation curve T90 – 90 % evap„ (oC)	ASTM D88	336	336	343	360 max.
Flash Point (oC)	ASTM D93	61	63	66	51 min.
Sulfur content (ppm)	ASTM D4294	145.9	122.7	106.7	650 max.
Copper strip corrosion	ASTM D130	1A	1A	1A	3
Kinematic viscosity at 40 oC (mm^2/s)	ASTM D445	3.528	3.445	3.459	2-May
Water and sediment content (%)	ASTM D1796	<0,05	<0,05	<0,05	0.05 max.

Table 3. Main technical specifications of test vehicles.

Model	**Fuel system**	**Engine type**	**Displacement (cm^3)**	**Power**	**Torque**	**Compression ratio**
M2.5C Double Cabin Pick up	CRDI Common Rail Diesel Electronic Injection EURO 3	4 cylinders in line, DOHC	2499 cm^3	117.3 kW 3500 rpm	330 Nm 1800 rpm	18:01
H2.5B Van	Injection pump, type of bypass EURO 3	4 cylinders in line, SOHC, TCi (Injecting timing control)	2476 cm^3	73.08 kW 3800 rpm	392 Nm 2000 - 2500 rpm	21:01

Prior to the experimental tests, the vehicles underwent preventive maintenance, including oil changes, replacement of fuel filters, and injector cleaning. The selected vehicle model is commonly used in the mountainous regions of Ecuador due to the country's geographical variability and prevalence of third-order roads. Additionally, the vehicle brand ranks among the ten best-selling in Ecuador's national vehicle fleet, which adds relevance to its inclusion in the study [34]. Its engine displacement is representative of the average configuration for this class of vehicle, and it is equipped with a catalytic converter designed to reduce pollutant emissions.

2.4. Road circuit

The driving cycle used in this study was based on the route developed by Pisuña and Solís [35], with a total length of 15,673 meters, comprising 7,993 meters of suburban roadway and 7,680 meters of urban segments. Figure 1 illustrates the route selected for the on-board emissions tests, which was designed to evaluate vehicle performance in relation to altitude and pollutant emissions. The average elevation along the route is 2,610 meters above sea level [36]. The route is divided into two main sections. The first begins with an ascent along Avenida Rumiñahui, where data were collected for subsequent analysis, followed by a descent toward the Cloverleaf interchange, which provided a second set of measurements. The second section covers the urban portion of the route, extending from the Cloverleaf to Plaza Artigas. This phase of the study accounted for variables such as traffic density, number of circulating vehicles, ambient temperature, and weather conditions. The data collected enabled a comparative analysis of the different fuel alternatives and their environmental impacts under real-world driving conditions.

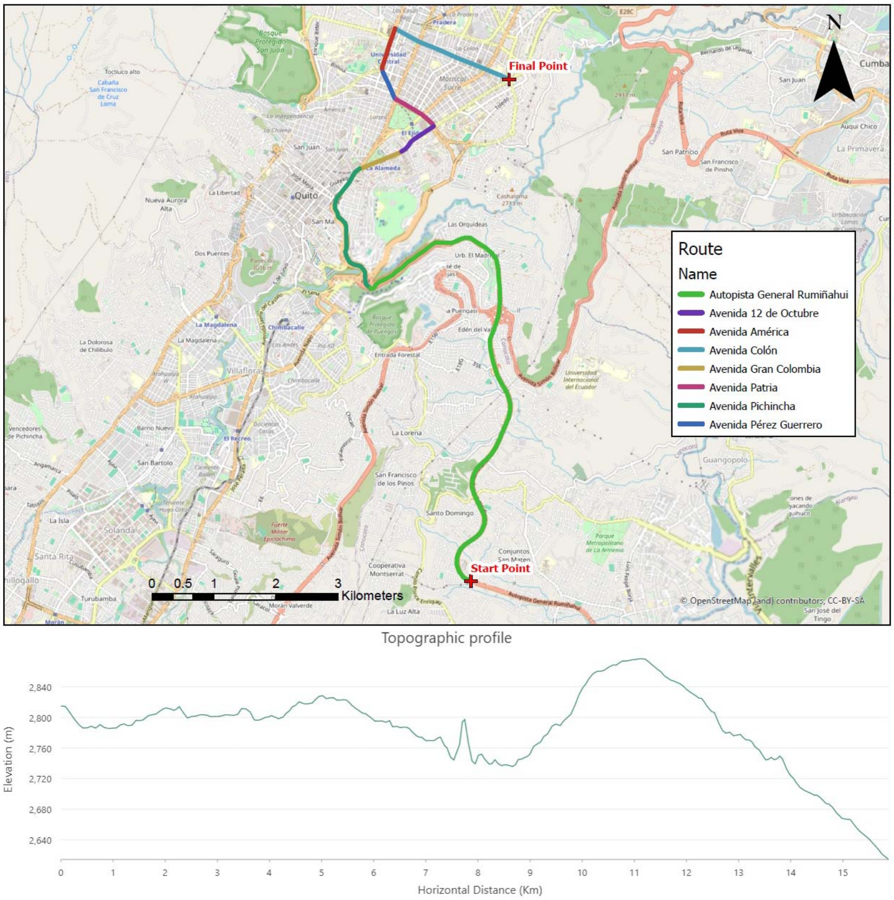

Figure 1. Driving route used for on-board emissions testing [35]

The study was designed to analyze the route in discrete sections rather than as a continuous whole, based on several technical considerations. These included variability in engine load, the need for accurate characterization of real-world driving behavior, improved calibration of simulation models, and the development of targeted mitigation strategies for segments associated with the highest emission levels, such as steep inclines or congested urban areas.

2.5. Portable emission data acquisition system

Exhaust gas measurements were conducted using the Axion OEM-2100AX model, which records volumetric concentrations of pollutants by interfacing with the vehicle's onboard diagnostic port (OBD2) [27]. Detailed technical specifications of the equipment are provided in Table 4.

Table 4. Especificaciones técnicas del sistema de medición de emisiones Axion OEM-2100AX

Parameter	**Measurement Range**	**Accuracy**	**Resolution**
Measuring O_2 (sensor)	Greater than or equal to (0,01 a 25 % vol.)	Greater than or equal 0,1 % abs.	Greater than or equal 0,01 % vol.
Measurement CO (NDIR)	Greater than or equal to (0,001 a 10 % vol.)	Greater than or equal to 0,02 % abs.	Greater than or equal 0,001 % vol.
Measurement NO_x (sensor)	Greater than or equal (0 a 4000 ppm)	Greater than or equal 25 ppm abs.	Greater than or equal 1 ppm
Measurement CO_2 (NDIR)	Greater than or equal to (0,01-16 % vol.)	Greater than or equal to 0,30 % abs.	Greater than or equal 0,01 % vol.
Measurement HC (NDIR)	Greater than or equal to (1 a 15 000 ppm)	Greater than or equal 4 ppm abs.	Greater than or equal 1 ppm

2.6. Variable analysis

A multilevel factorial design was implemented to evaluate various fuel mixtures (diesel, B10, and B20) in two vehicles with distinct injection technologies: Common Rail Direct Injection (CRDI) and mechanical injection pump systems. Each vehicle was tested under three driving conditions, ascending, urban, and descending, resulting in multiple combinations for assessing emissions of carbon monoxide (CO), hydrocarbons (HC), nitrogen oxides (NO_x), as well as oxygen (O_2) and carbon dioxide (CO_2) concentrations. Five repetitions were performed for each experimental condition. Control charts were applied to assess the reliability of the experimental data, ensuring consistency by identifying deviations that might cause excessive variability relative to acceptable thresholds [37]. The nomenclature used for the factorial combinations is presented in Tables 5 and 6. The statistical methodology follows the approach proposed by several authors, including that of [23]. According to Serrano et al. [38], the influence of independent variables on response variables can be effectively evaluated using response surface methodology (RSM) [39, 40]. Data analysis was performed using the educational version of Statgraphics Centurion XVI.

Table 5. Factor levels and designation codes

Factors	Levels	Designation 1	Designation 2
Vehicle	M2.5C (2,5 cm^3 CDRI)	1	A2
	H2.5B (2,5 cm^3 injection pump)	-1	A1
Fuel Type	Diesel	1	C1
	B10	0	C2
	B20	-1	C3
Driving condition	Ascent	1	AS
	Urban	0	UR
	Descent	-1	DE

Table 6. Experimental treatment combinations for response surface analysis

Treatment	Vehicle	Fuel	Driving condition
1	A1	C1	AS
2	A1	C2	UR
3	A2	C2	UR
4	A2	C1	AS
5	A1	C3	UR
6	A2	C2	DE
7	A1	C3	DE
8	A2	C3	DE
9	A1	C1	DE
10	A2	C3	UR
11	A2	C1	UR
12	A1	C2	DE
13	A2	C1	DE
14	A1	C3	AS
15	A2	C3	AS
16	A1	C2	AS
17	A1	C1	UR
18	A2	C2	AS

3. Results and Discussion

This section presents the results obtained from the experimental procedures. Tables 7 and 8 summarize the data used for response surface analysis of the two test vehicles. Across all cases, standard deviations were low, and the coefficients of variation remained below 20%, indicating moderate and acceptable levels of variability. The range values, defined as the difference between the maximum and minimum measurements, were also within acceptable limits for most variables.

Response surface methodology (RSM) has been widely used in similar studies to evaluate the influence of multiple independent factors on dependent variables, as well as to construct predictive models of their interactions. This approach has been applied by authors such as Morales-Bayetero et al. [41], Guardia et al. [40], and Rocha-Hoyos et al. [25], among others.

Table 7. Statistical summary of emission measurements for H2.5B vehicle

	Count	**Average**	**Standard Deviation**	**Coefficient of Variation (%)**	**Range**
$ADCO_2$	5	7.76	0.44	5.74	1.06
$AB10CO_2$	5	9.03	0.28	3.13	0.62
$AB20CO_2$	5	8.67	0.34	4.01	0.78
ADCO	5	0.02	0	0	0
AB10CO	5	0.02	0	0	0
AB20CO	5	0.018	0.002	11.29	0.004
ADHC	5	112.41	4.84	4.3	11.79
AB10HC	5	164.74	4.75	2.88	10.23
AB20HC	5	131.47	10.59	8.06	24.03
$ADNO_x$	5	334.47	10.54	3.15	23.67
$AB10NO_x$	5	352.89	7.8	2.21	17.66
$AB20NO_x$	5	360.86	9.89	2.74	22.16
$DDCO_2$	5	3.56	0.29	8.34	0.64
$DB10CO_2$	5	4.22	0.57	13.52	1.26
$DB20CO_2$	5	4.2	0.15	3.75	0.38
DDCO	5	0.017	0.002	16.49	0.005
DB10CO	5	0.015	0.002	18.85	0.006
DB20CO	5	0.011	0.0004	3.97	0.001
ADHC	5	129.63	3.8	2.93	9.06
DB10HC	5	169.55	2.62	1.54	5.82
DB20HC	5	141.45	5.98	4.23	13.68
$DDNO_x$	5	157.18	4.03	2.56	9.65
$DB10NO_x$	5	152.27	5.31	3.48	13.01
$DB20NO_x$	5	182.86	12.96	7.08	30.92
UDCO2	5	3.42	0.32	9.48	0.73
$UB10CO_2$	5	3.92	0.1	2.58	0.22
$UB20CO_2$	5	3.69	0.24	6.56	0.58
UDCO	5	0.011	0.0008	7.42	0.002
UB10CO	5	0.011	0.0012	11.22	0.003
UB20CO	5	0.011	0.0012	11.22	0.003
UDHC	5	75.06	2.47	3.29	5.33
UB10HC	5	126.15	7.11	5.63	16.31
UB20HC	5	112.26	3.33	2.97	8.17
$UDNO_x$	5	167.52	6.13	3.66	14.39
$UB10NO_x$	5	173.45	2.43	1.4	5.36
$UB20NO_x$	5	179.53	8.01	4.46	18.69

Note: ADCO2 (Ascent Diesel CO_2 (%)), AB10CO2 (Ascent B10 CO_2 (%)), AB20CO2 (Ascent B20 CO_2 (%)), ADCO (Ascent Diesel CO (%)), AB10CO (Ascent B10 CO (%)), AB20CO (Ascent B20 CO (%)), ADHC (Ascent Diesel HC (ppm)), AB10HC (Ascent B10 HC (ppm)), AB20HC (Ascent B20 HC (ppm)), $ADNO_x$ (Ascent Diesel NO_x (ppm)), $AB10NO_x$ (Ascent B10 NO_x (ppm)), $AB20NO_x$ (Ascent B20 NO_x (ppm)), DDCO2 (Descent Diesel CO_2 (%)), DB10CO2 (Descent B10 CO_2 (%)), DB20CO2 (Descent B20 CO_2 (%)), DDCO (Descent Diesel CO (%)), DB10CO (Descent B10 CO (%)), DB20CO (Descent B20 CO (%)), ADHC (Descent Diesel HC (ppm)), DB10HC (Descent B10 HC (ppm)), DB20HC (Descent B20 HC (ppm)), $DDNO_x$ (Descent Diesel NO_x (ppm)), $DB10NO_x$ (Descent B10 NO_x (ppm)), $DB20NO_x$ (Descent B20 NO_x (ppm)), UDCO2 (Urban Diesel CO_2 (%)), UB10CO2 (Urban B10 CO_2 (%)), UB20CO2 (Urban B20 CO_2 (%)), UDCO (Urban Diesel CO (%)), UB10CO (Urban B10 CO (%)), UB20CO (Urban B20 CO (%)), UDHC (Urban Diesel HC (ppm)), UB10HC (Urban B10 HC (ppm)), UB20HC (Urban B20 HC (ppm)), $UDNO_x$ (Urban Diesel NO_x (ppm)), $UB10NO_x$ (Urban B10 NO_x (ppm)), $UB20NO_x$ (Urban B20 NO_x (ppm)).

Table 8. Statistical summary of emission measurements for M2.5C vehicle

	Count	**Average**	**Standard Deviation**	**Coefficient of Variation (%)**	**Range**
$ADCO_2$	5	8.71	0.62	7.13	1.42
$AB10CO_2$	5	8.17	0.24	3.04	0.61
$AB20CO_2$	5	8.85	0.46	5.3	0.99
ADCO	5	0.45	0.03	7.94	0.08
AB10CO	5	0.29	0.02	9.78	0.07
AB20CO	5	0.43	0.03	8.9	0.09
ADHC	5	143.02	1.33	0.92	3.03
AB10HC	5	107.46	1.89	1.76	4.01
AB20HC	5	86.82	2.82	3.25	6.48
ADNOx	5	469	15.71	3.34	32.97
AB10NOx	5	542.2	10.43	1.92	22.98
AB20NOx	5	494.52	3.22	0.65	6.7
$DDCO_2$	5	4.32	0.311	7.219	0.55
$DB10CO_2$	5	4.76	0.11	2.46	0.27
$DB20CO_2$	5	5.13	0.19	3.84	0.46
DDCO	5	0.15	0.02	14.54	0.05
DB10CO	5	0.23	0.03	12.79	0.07
DB20CO	5	0.22	0.02	9.74	0.05
ADHC	5	219.93	5.7	2.59	13.38
DB10HC	5	234.55	4.43	1.88	9.7
DB20HC	5	136.5	3.6	2.63	6.68
DDNOx	5	299.88	8.18	2.72	15.29
DB10NOx	5	322.53	9.31	2.88	21.62
DB20NOx	5	256.29	9.19	3.58	20.72
$UDCO_2$	5	4	0.06	1.51	0.14
$UB10CO_2$	5	3.86	0.15	3.93	0.37
$UB20CO_2$	5	4.39	0.16	3.74	0.39
UDCO	5	0.19	0.01	8.64	0.04
UB10CO	5	0.17	0.02	11.61	0.04
UB20CO	5	0.2	0.009	4.61	0.02
UDHC	5	145.08	7.86	5.41	17.98
UB10HC	5	174.43	1.71	0.98	3.71
UB20HC	5	122.78	2.39	1.94	5.7
UDNOx	5	275.74	8.52	3.09	19.18
UB10NOx	5	339.06	17.19	5.07	36.23
UB20NOx	5	322.82	11.51	3.56	24.1

3.1. Experimental Analysis of CO_2 and CO emissions

Figure 2 illustrates the carbon dioxide (CO_2) emission patterns of the H2.5B vehicle (2.5 L injection pump engine) across different fuel types and driving conditions. The lowest CO_2emissions were recorded during descent with conventional diesel fuel, reaching values of approximately 2.8% by volume, indicating improved combustion efficiency under reduced engine load and favorable operating conditions. Regarding carbon monoxide (CO) emissions, the most favorable results were also observed when using diesel during descent, as well as during ascent with B20 biodiesel, where CO concentrations dropped to approximately 0.0008% by volume.

In the case of the M2.5C vehicle (2.5 L CRDI engine), the CO_2 emission behavior is consistent with that observed in the H2.5B vehicle, as illustrated in Figure 3a. The lowest CO_2 concentrations were recorded under descent conditions when conventional diesel was used. However, for CO emissions, fuel type did not appear to be a significant influencing factor. Instead, driving conditions played a more critical role. The lowest CO values were again observed during descent, reaching approximately 0.0008%, identical to the minimum values recorded for the H2.5B vehicle (Figure 3b) [42].

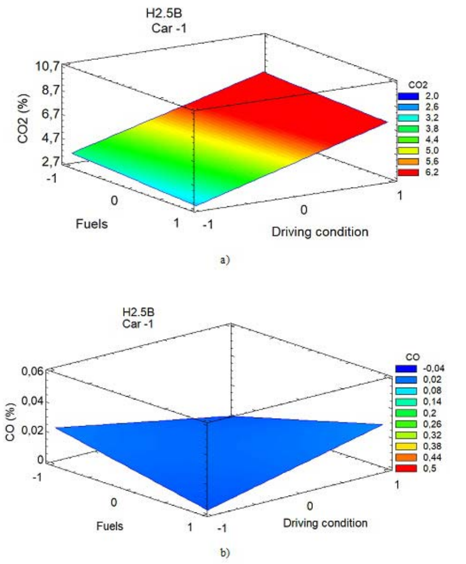

Figure 2. CO_2 emissions (a) and CO emissions (b) from the H2.5B vehicle as a function of fuel type and driving conditions.

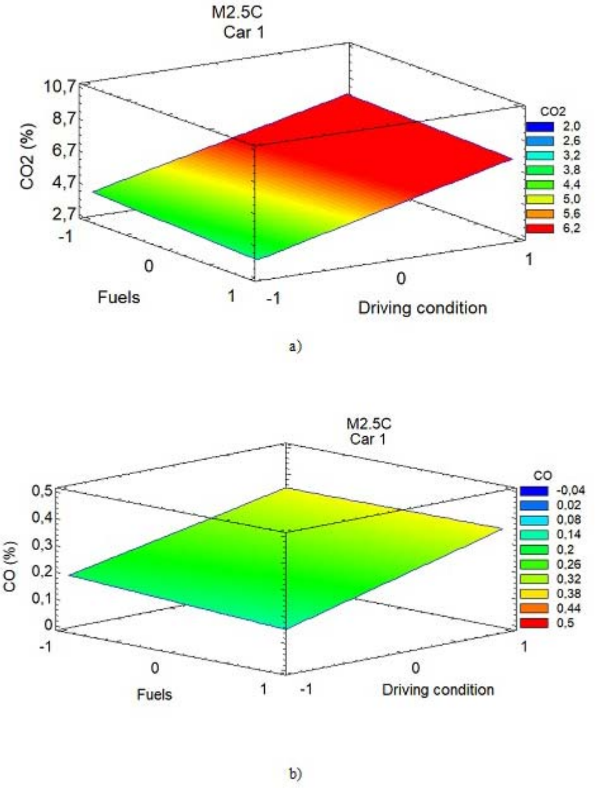

Figure 3. CO_2 emissions (a) and CO emissions (b) from the M2.5C vehicle as a function of fuel type and driving conditions.

The Pareto diagram presented in Figure 4 illustrates the relative influence of experimental factors on CO_2 emissions. The diagram includes the main effects and two-factor interactions: AC (Vehicle–Driving Condition), BC (Fuel–Driving Condition), and AB (Vehicle–Fuel). Among these, driving conditions emerged as the most significant factor affecting CO_2 levels. This result is further supported by the trends shown in Figure 5. In the case of CO emissions, the most influential variables were the vehicle type, driving conditions, and their interaction, as depicted in Figure 6.

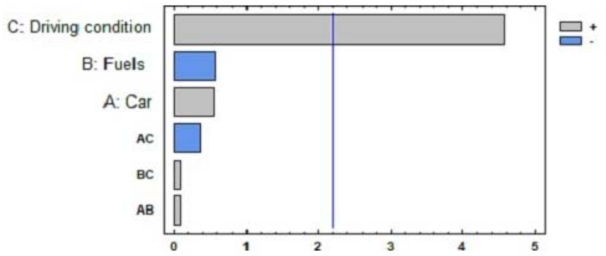

Figure 4. Effects of factors on CO_2 emissions.

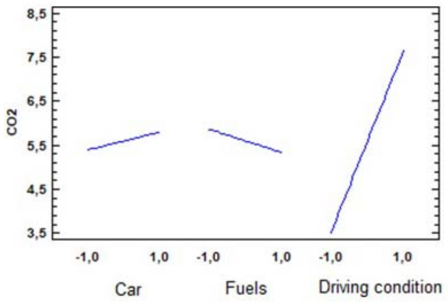

Figure 5. Main effects of factors on CO_2 emissions.

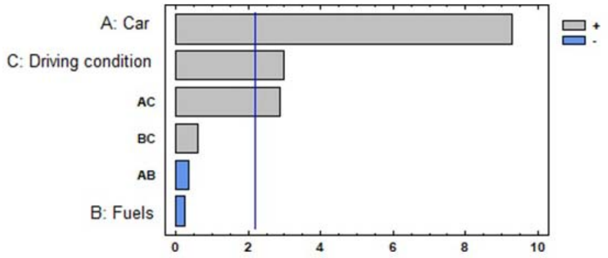

Figure 6. Effects of factors on CO emissions.

3.2. Experimental Analysis of HC emissions

Figure 7 presents the hydrocarbon (HC) emission behavior of the H2.5B vehicle (2.5 L injection pump engine) as a function of fuel type and driving condition. The lowest HC concentrations were observed when using conventional diesel, regardless of the driving condition, suggesting that in this vehicle configuration, fuel type has a greater influence on HC emissions than operating mode. In contrast, the M2.5C vehicle (2.5 L CRDI engine) exhibited a different trend, as shown in Figure 8.

The lowest HC emissions were recorded when operating with B20 biodiesel during ascent conditions.

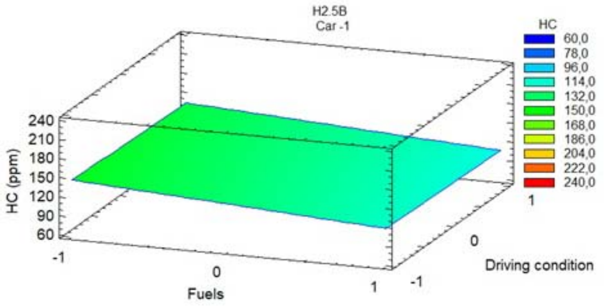

Figure 7. HC emissions from the H2.5B vehicle as a function offuel and driving conditions.

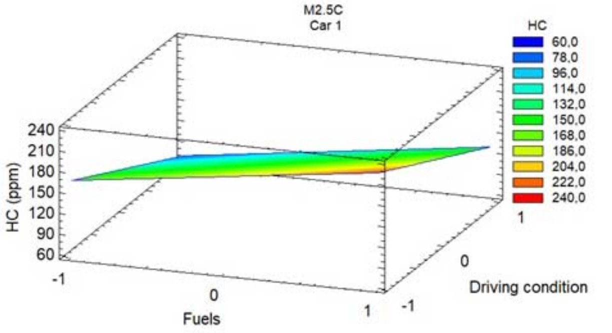

Figure 8. HC emissions from the M2.5C vehicle as a function of fuel and driving conditions.

The Pareto diagram in Figure 9 illustrates the influence of individual factors and their interactions on HC emissions. The most significant contributors were the driving conditions, followed by the interaction between vehicle type, fuel type, and driving conditions. In Figure 10, the main effects of each variable are shown independently, providing a clearer understanding of the relative impact of each factor on HC emissions.

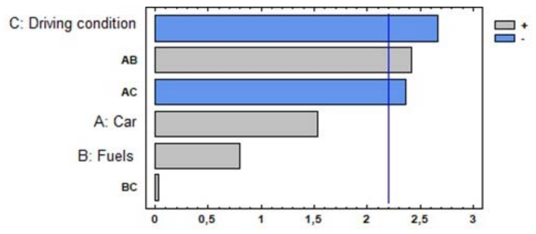

Figure 9. Effects of factors on HC emissions.

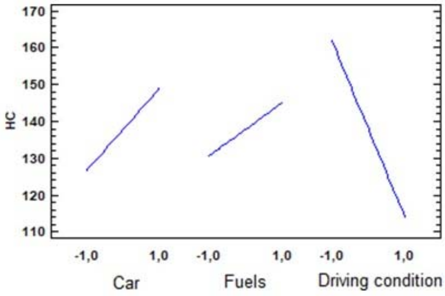

Figure 10. Main effects of factors on HC emissions.

3.3. Experimental Analysis of NO_x Emissions

Figure 11 illustrates the nitrogen oxide (NO_x) emission behavior of both the M2.5C (2.5 L CRDI) and H2.5B (2.5 L injection pump) vehicles as a function of fuel type and driving condition. The lowest NO_x emissions were observed during descent conditions, with fuel type showing no statistically significant effect in this context. Previous studies, such as that by Rocha-Hoyos et al. [25], have reported that biodiesel combustion tends to lower particulate matter, carbon monoxide, and smoke opacity, while slightly increasing NO_x emissions relative to conventional diesel. Similarly, findings by Tesfa, Mishra, and Ball [28] suggest that biodiesel use generally results in increased NO_x levels, irrespective of the feedstock source. However, in the present study, these increases were not statistically significant, likely due to the high-altitude driving conditions and real-world measurement approach, which reflect actual vehicle operation more accurately than laboratory conditions. Additional strategies, such as biodiesel–ethanol blending, have been proposed to mitigate NO_x emissions more effectively [43].

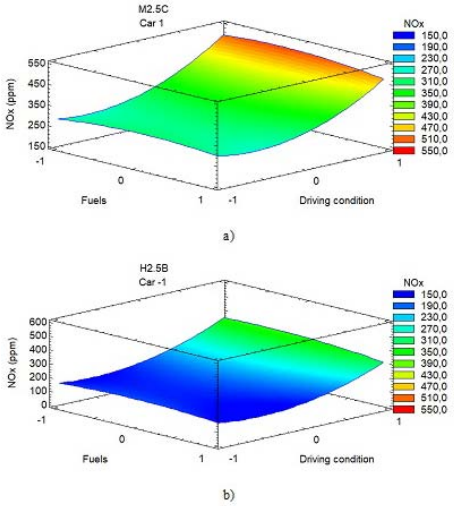

Figure 11. NO_x emissions as a function of fuel type and driving conditions for the M2.5C vehicle (a) and the H2.5B vehicle(b).

4. Conclusions

The chemical characterization of waste frying oil revealed a cetane number of 47, confirming its suitability for biodiesel production through transesterification.

Biodiesel blends (B10 and B20) met the quality criteria outlined in INEN Standard 1489:2012, validating their potential use as alternative fuels in compression ignition engines.

CO_2 and CO emissions from both the H2.5B and M2.5C vehicles were lowest under descent conditions when fueled with conventional diesel. This is attributed to reduced engine load, operation in coasting or injection cutoff modes, and overall improved combustion efficiency in such scenarios.

HC emissions were minimized in ascent conditions when using B20 biodiesel in both vehicles. The increased oxygen content in the biodiesel likely enhanced combustion under high load, thereby reducing unburned hydrocarbons.

NO_x emissions were also lowest during descent, regardless of the fuel type, due to the reduced combustion chamber temperature and lower engine load in these operating conditions.

Acknowledgments

The authors express their gratitude to the following institutions for their support during the experimental phase of this study: the Mechanical Engineering / Efficiency, Environmental Impact, and Innovation Research Group in Industry and Transport at SEK International University, and the Faculty of Mechanics / Science Production Research Group with Modern Technology in the Automotive Field (INVELECTRO) at the Higher Polytechnic School of Chimborazo.

Contributor Roles

- **Edilberto Antonio Llanes-Cedeño:** Conceptualization, supervision,data curation.
- **Andrés Cárdenas-Yánez:** Methodology.
- **Edwin Chamba:** Validation, data curation.
- **Juan Carlos Castelo:** Writing – original draft.
- **Juan Carlos Rocha-Hoyos:** Writing – review & editing.

References

[1] WHO. (2019) How air pollution is destroying our health. World Health Organization. [Online]. Available: https://upsalesiana.ec/ing34ar6nr1

[2] C. Henríquez and H. Romero, *Urban Climates in Latin America.* Springer International Publishing, 2019. [Online]. Available: https://doi.org/10.1007/978-3-319-97013-4

[3] H. Jorquera, L. D. Montoya, and N. Y. Rojas, *Urban Air Pollution.* Springer International Publishing, 2019, pp. 137–165. [Online]. Available: http://dx.doi.org/10.1007/978-3-319-97013-4_7

[4] R. O. McClellan, T. W. Hesterberg, and J. C. Wall, "Evaluation of carcinogenic hazard of diesel engine exhaust needs to consider revolutionary changes in diesel technology," *Regulatory Toxicology and Pharmacology*, vol. 63, no. 2, pp. 225–258, Jul. 2012. [Online]. Available: https://doi.org/10.1016/j.yrtph.2012.04.005

[5] L. D. Claxton, "The history, genotoxicity, and carcinogenicity of carbon-based fuels and their emissions. part 3: Diesel and gasoline," *Mutation Research/Reviews in Mutation Research*, vol. 763, pp. 30–85, Jan. 2015. [Online]. Available: https://doi.org/10.1016/j.mrrev.2014.09.002

[6] L. E. Tipanluisa, A. P. Remache, C. R. Ayabaca, and S. W. Reina, "Emisiones contaminantes de un motor de gasolina funcionando a dos cotas con combustibles de dos calidades," *Información tecnológica*, vol. 28, no. 1, pp. 03–12, 2017. [Online]. Available: http://dx.doi.org/10.4067/S0718-07642017000100002

[7] D. Krajzewicz, M. Behrisch, P. Wagner, R. Luz, and M. Krumnow, *Second Generation of Pollutant Emission Models for SUMO.* Springer International Publishing, 2015, pp. 203–221. [Online]. Available: http://dx.doi.org/10.1007/978-3-319-15024-6_12

[8] M. Balali-Mood, A. Ghorani-Azam, and B. Riahi-Zanjani, "Effects of air pollution on human health and practical measures for prevention in iran," *Journal of Research in Medical Sciences*, vol. 21, no. 1, p. 65, 2016. [Online]. Available: https://doi.org/10.4103/1735-1995.189646

[9] R. J. Wild, W. P. Dubé, K. C. Aikin, S. J. Eilerman, J. A. Neuman, J. Peischl, T. B. Ryerson, and S. S. Brown, "On-road measurements of vehicle NO_2/NO_x emission ratios in Denver, Colorado, USA," *Atmospheric Environment*, vol. 148, pp. 182–189, Jan. 2017. [Online]. Available: https://doi.org/10.1016/j.atmosenv.2016.10.039

[10] V. Bermúdez, J. R. Serrano, P. Piqueras, J. Gómez, and S. Bender, "Analysis of the role of altitude on diesel engine performance and emissions using an atmosphere simulator," *International Journal of Engine Research*, vol. 18, no.

1–2, pp. 105–117, Jan. 2017. [Online]. Available: http://dx.doi.org/10.1177/1468087416679569

[11] L. Mena Navarrete, M. Román, E. A. Llanes Cedeño, N. Barreno, S. Mena Palacio, and J. C. Rocha-Hoyos, "Estudio de rugosidad por análisis de fourier de las toberas de inyectores en sistemas riel común (CRDI)," *Ingeniare. Revista chilena de ingeniería*, vol. 26, no. 4, pp. 654–662, Dec. 2018. [Online]. Available: http://dx.doi.org/10.4067/S0718-33052018000400654

[12] B. Karolys, E. A. Cedeño, W. Vega, S. Cevallos, and J. Rocha-Hoyos, "Effect of injection parameters and emission characteristics in a common-rail direct injection diesel engine in height conditions: A review," *Journal of Engineering Science and Technology Review*, pp. 164–171, 08 2019. [Online]. Available: https://upsalesiana.ec/ing34ar6nr14

[13] G. Triantafyllopoulos, A. Dimaratos, L. Ntziachristos, Y. Bernard, J. Dornoff, and Z. Samaras, "A study on the CO_2 and NO_x emissions performance of Euro 6 diesel vehicles under various chassis dynamometer and on-road conditions including latest regulatory provisions," *Science of The Total Environment*, vol. 666, pp. 337–346, May 2019. [Online]. Available: https://doi.org/10.1016/j.scitotenv.2019.02.144

[14] L. Ntziachristos, G. Papadimitriou, N. Ligterink, and S. Hausberger, "Implications of diesel emissions control failures to emission factors and road transport NO_x evolution," *Atmospheric Environment*, vol. 141, pp. 542–551, Sep. 2016. [Online]. Available: https://doi.org/10.1016/j.atmosenv.2016.07.036

[15] Z. Kan, Z. Hu, D. Lou, P. Tan, Z. Cao, and Z. Yang, "Effects of altitude on combustion and ignition characteristics of speed-up period during cold start in a diesel engine," *Energy*, vol. 150, pp. 164–175, May 2018. [Online]. Available: https://doi.org/10.1016/j.energy.2017.12.103

[16] G. Fontaras, B. Ciuffo, N. Zacharof, S. Tsiakmakis, A. Marotta, J. Pavlovic, and K. Anagnostopoulos, "The difference between reported and real-world CO_2 emissions: How much improvement can be expected by WLTP introduction?" *Transportation Research Procedia*, vol. 25, pp. 3933–3943, 2017. [Online]. Available: https://doi.org/10.1016/j.trpro.2017.05.333

[17] E. A. Llanes Cedeño, J. C. Rocha-Hoyos, D. B. Peralta Zurita, and J. C. Leguísamo Milla, "Evaluación de emisiones de gases en un vehículo liviano a gasolina en condiciones de altura. Caso de estudio Quito, Ecuador," *Enfoque UTE*, vol. 9, no. 2, pp. 149–158, Jun. 2018. [Online]. Available: https://doi.org/10.29019/ENFOQUEUTE.V9N2.201

[18] M. Kousoulidou, G. Fontaras, L. Ntziachristos, P. Bonnel, Z. Samaras, and P. Dilara, "Use of portable emissions measurement system (PEMS) for the development and validation of passenger car emission factors," *Atmospheric Environment*, vol. 64, pp. 329–338, Jan. 2013. [Online]. Available: https://dx.doi.org/10.1016/j.atmosenv.2012.09.062

[19] W. Litwin, W. Leśniewski, D. Piątek, and K. Niklas, "Experimental research on the energy efficiency of a parallel hybrid drive for an inland ship," *Energies*, vol. 12, no. 9, p. 1675, May 2019. [Online]. Available: https://doi.org/10.3390/en12091675

[20] ISO. (1975) ISO 2533:1975 - Standard Atmosphere. International Organization for Standardization. [Online]. Available: https://upsalesiana.ec/ing34ar6nr11

[21] F. S. Mirhashemi and H. Sadrnia, "Nox emissions of compression ignition engines fueled with various biodiesel blends: A review," *Journal of the Energy Institute*, vol. 93, no. 1, pp. 129–151, Feb. 2020. [Online]. Available: https://doi.org/10.1016/j.joei.2019.04.003

[22] S. Dharma, H. C. Ong, H. Masjuki, A. Sebayang, and A. Silitonga, "An overview of engine durability and compatibility using biodiesel–bioethanol–diesel blends in compression-ignition engines," *Energy Conversion and Management*, vol. 128, pp. 66–81, Nov. 2016. [Online]. Available: https://doi.org/10.1016/j.enconman.2016.08.072

[23] H. How, H. Masjuki, M. Kalam, and Y. Teoh, "Influence of injection timing and split injection strategies on performance, emissions, and combustion characteristics of diesel engine fueled with biodiesel blended fuels," *Fuel*, vol. 213, pp. 106–114, Feb. 2018. [Online]. Available: https://doi.org/10.1016/j.fuel.2017.10.102

[24] A. Gharehghani, M. Mirsalim, and R. Hosseini, "Effects of waste fish oil biodiesel on diesel engine combustion characteristics and emission," *Renewable Energy*, vol. 101, pp. 930–936, Feb. 2017. [Online]. Available: https://doi.org/10.1016/j.renene.2016.09.045

[25] J. C. Rocha-Hoyos, E. A. Llanes-Cedeño, S. F. Celi-Ortega, and D. C. Peralta-Zurita, "Efecto de la adición de biodiésel en el rendimiento y la opacidad de un motor diésel,"

Información tecnológica, vol. 30, no. 3, pp. 137–146, Jun. 2019. [Online]. Available: http://dx.doi.org/10.4067/S0718-07642019000300137

[26] M. Kousoulidou, G. Fontaras, L. Ntziachristos, and Z. Samaras, "Biodiesel blend effects on common-rail diesel combustion and emissions," *Fuel*, vol. 89, no. 11, pp. 3442–3449, Nov. 2010. [Online]. Available: https://doi.org/10.1016/j.fuel.2010.06.034

[27] K. J. Godri Pollitt, D. Chhan, K. Rais, K. Pan, and J. S. Wallace, "Biodiesel fuels: A greener diesel? A review from a health perspective," *Science of The Total Environment*, vol. 688, pp. 1036–1055, Oct. 2019. [Online]. Available: https://doi.org/10.1016/j.scitotenv.2019.06.002

[28] B. Tesfa, F. Gu, R. Mishra, and A. Ball, "Emission characteristics of a CI engine running with a range of biodiesel feedstocks," *Energies*, vol. 7, no. 1, pp. 334–350, Jan. 2014. [Online]. Available: https://doi.org/10.3390/en7010334

[29] J. Medrano-Barboza, K. Herrera-Rengifo, A. Aguirre-Bravo, J. R. Ramírez-Iglesias, R. Rodríguez, and V. Morales, "Pig slaughterhouse wastewater: Medium culture for microalgae biomass generation as raw material in biofuel industries," *Water*, vol. 14, no. 19, p. 3016, Sep. 2022. [Online]. Available: https://doi.org/10.3390/w14193016

[30] A. Broch, U. Jena, S. Hoekman, and J. Langford, "Analysis of solid and aqueous phase products from hydrothermal carbonization of whole and lipid-extracted algae," *Energies*, vol. 7, no. 1, pp. 62–79, Dec. 2013. [Online]. Available: https://doi.org/10.3390/en7010062

[31] A. Demirbas, "Biodiesel from waste cooking oil via base-catalytic and supercritical methanol transesterification," *Energy Conversion and Management*, vol. 50, no. 4, pp. 923–927, Apr. 2009. [Online]. Available: https://doi.org/10.1016/j.enconman.2008.12.023

[32] G. Knothe, J. Krahl, and J. Van Gerpen, *The Biodiesel Handbook*, 2nd ed. Urbana, IL, USA: AOCS Press/Academic Press, 2010. [Online]. Available: https://upsalesiana.ec/ing34ar6nr33

[33] A. K. Bhonsle, A. Kumar, A. Ray, J. Singh, N. Rawat, and N. Atray, "Biodiesel production from used cooking oil at room temperature using novel solvent – a techno-economic perspective, sensitivity analysis and societal implications," *Energy Conversion and Management*, vol. 324, p. 119282, Jan. 2025. [Online]. Available: https://doi.org/10.1016/j.enconman.2024.119282

[34] AEADE, *Yerabook 2017*. Asociación de Empresas Automotrices del Ecuador, 2018. [Online]. Available: https://upsalesiana.ec/ing34ar6nr36

[35] F. E. Quinchimbla Pisuña and J. M. Solís Santamaría, *Development of city, road and combined driving cycles to evaluate the actual fuel performance of an Otto cycle-powered vehicle in the Metropolitan District of Quito. 2017*. Quito, Ecuador: Escuela Politécnica Nacional, 2017. [Online]. Available: https://upsalesiana.ec/ing34ar6nr37

[36] J. I. Huertas, M. Giraldo, L. F. Quirama, and J. Díaz, "Driving cycles based on fuel consumption," *Energies*, vol. 11, no. 11, p. 3064, Nov. 2018. [Online]. Available: https://doi.org/10.3390/en11113064

[37] J. C. Leguísamo, E. A. Llanes-Cedeño, S. F. Celi-Ortega, and J. C. Rocha-Hoyos, "Evaluación de la conducción eficiente en un motor de encendido provocado, a 2810 msnm," *Información tecnológica*, vol. 31, no. 1, pp. 227–236, Feb. 2020. [Online]. Available: http://dx.doi.org/10.4067/S0718-07642020000100227

[38] J. R. Serrano, P. Piqueras, A. Abbad, R. Tabet, S. Bender, and J. Gómez, "Impact on reduction of pollutant emissions from passenger cars when replacing Euro 4 with Euro 6d diesel engines considering the altitude influence," *Energies*, vol. 12, no. 7, p. 1278, Apr. 2019. [Online]. Available: https://doi.org/10.3390/en12071278

[39] V. Kolanjiappan, "Reduction of amine and biological antioxidants on NO_x emissions powered by mango seed biodiesel," *Revista Facultad de Ingeniería Universidad de Antioquia*, no. 84, pp. 46–54, Sep. 2017. [Online]. Available: http://doi.org/10.17533/udea.redin.n84a06

[40] Y. Guardia-Puebla, J. Márquez-Delgado, V. Sánchez-Girón, E. A. Llanes-Cedeño, J. C. Rocha-Hoyos, and D. B. Peralta-Zurita, "Enhancements to the subject statistical design of experiments for students of the mechanical engineering career," *Revista ESPACIOS*, vol. 39, no. 30, p. 10, 2018, [En línea]. [Online]. Available: https://upsalesiana.ec/ing34ar6nr42

[41] C. F. Morales-Bayetero, E. A. Llanes-Cedeño, C. Mafla-Yépez, and A. Rodríguez-Rodríguez, "Assessment of the mechanical and environmental behavior of diesel engines operating with biodiesel mixtures," *Revista Facultad de Ingeniería Universidad de Antioquia*, Feb. 2023.

[42] G. Belgiorno, G. Di Blasio, S. Shamun, C. Beatrice, P. Tunestål, and M. Tunér, “Performance and emissions of diesel-gasoline-ethanol blends in a light duty compression ignition engine,” *Fuel*, vol. 217, pp. 78–90, Apr. 2018. [Online]. Available: https://doi.org/10.1016/j.fuel.2017.12.090

[43] H.-H. Riojas-González, L.-J. Bortoni-Anzures, J.-J. Martínez-Torres, and H. A. Ruiz, “Avances y estrategias para mejorar el desempeño del biodiésel en motor diésel,” *Ingenius*, no. 30, pp. 90–105, Jul. 2023. [Online]. Available: https://doi.org/10.17163/ings.n30.2023.08

Scientific Paper / Artículo Científico

UNIVERSIDAD POLITÉCNICA SALESIANA ECUADOR
INGENIUS
Revista de Ciencia y Tecnología
https://doi.org/10.17163/ings.n34.2025.06
pISSN: 1390-650X / eISSN: 1390-860X

IoT AND MQTT-BASED CARDIOVASCULAR PARAMETER MONITORING SYSTEM FOR MEDICAL ALERTS

SISTEMA DE MONITOREO DE PARÁMETROS CARDIOVASCULARES BASADO EN IoT Y MQTT PARA ALERTAS MÉDICAS

Marcia Bayas Sampedro[1,*], Ángela Parra Fernández[1], Ronald Rovira Jurado[1], Manuel Montaño Blacio[1], Óscar Gómez Morales[1], Junior Figueroa Olmedo [1]

Received: 25-02-2025, Received after review: 01-04-2025, Accepted: 29-04-2025, Published: 01-07-2025

Abstract

This paper presents the development of a computing platform for the real-time monitoring of cardiovascular parameters derived from bioelectrical signals. A comprehensive analysis of primary users was conducted, leading to the identification of both technical and functional requirements. The interface design was guided by Sommerville's methodology. The system architecture is based on a microservices model, incorporating a relational database and enabling integration with data transmitted from Internet of Things (IoT) devices. The platform was evaluated through incremental stress testing, starting with zero users and increasing in steps of 100 up to 5,000. A total of 22,132 requests were processed at a peak rate of 440.4 requests per second, with an average response time of 930 ms and 95% of responses occurring within 2,300 ms. The system demonstrated error-free performance with up to 1,700 concurrent users. At 5,000 users and 26,393 total requests, a minimal error rate of 0.16% was recorded, confirming the platform's stability under high workloads. These findings validate the feasibility of the proposed solution for remote biomedical monitoring, offering an efficient, scalable, and robust tool for real-time health supervision.

Keywords: HTTP, MQTT, biomedical parameters, Computing platform

Resumen

Este artículo describe el desarrollo de una plataforma informática destinada al monitoreo en tiempo real de parámetros cardiovasculares a partir de señales bioeléctricas. Se realizó un análisis de los usuarios principales y se identificaron los requisitos técnicos y funcionales necesarios. Asimismo, las interfaces fueron diseñadas aplicando la metodología propuesta por Sommerville. La arquitectura del sistema se basa en microservicios, incorporando una base de datos relacional y permitiendo la integración con datos provenientes de dispositivos del Internet de las Cosas (IoT). La evaluación del sistema se llevó a cabo mediante pruebas de simulación de carga, iniciando con 0 usuarios y aumentando en intervalos de 100 hasta alcanzar los 5000 usuarios. Durante las pruebas, se procesaron 22 132 solicitudes, con una tasa promedio de 440,4 solicitudes por segundo, manteniendo un tiempo de respuesta medio de 930 ms y logrando que el 95 % de las respuestas se ubicaran por debajo de los 2300 ms. Se comprobó que el sistema opera sin errores hasta un umbral de 1700 usuarios concurrentes. Con 5000 usuarios y un total de 26 393 solicitudes, se registró un porcentaje mínimo de error del 0,16 %, lo que evidencia su capacidad para gestionar altas cargas de trabajo de manera estable. Estos resultados confirman la viabilidad de la plataforma para el monitoreo remoto de parámetros biomédicos, ofreciendo una solución eficiente y escalable para la supervisión de la salud en tiempo real.

Palabras clave: HTTP, MQTT, parámetros biomédicos, plataforma informática

---

[1,*] Grupo de investigación TECED, Facultad de Sistemas y Telecomunicaciones, Universidad Estatal Península de Santa Elena, Ecuador. Corresponding author ✉: mbayas@upse.edu.ec.

Suggested citation: M. Bayas Sampedro, A. Parra Fernández, R. Rovira Jurado, M. Montaño Blacio, O. Gómez Morales and J. Figueroa Olmedo, "IoT and MQTT-based cardiovascular parameter monitoring system for medical alerts," *Ingenius, Revista de Ciencia y Tecnología*, N.° 34, pp. 75-88, 2025, DOI: https://doi.org/10.17163/ings.n34.2025.06.

1. Introduction

Experts in Information and Communication Technology (ICT) are increasingly transforming biomedical research to enhance disease prevention and monitoring efforts [1,2]. Interdisciplinary collaboration among specialists in ICT, electronics, automation, and medicine is essential to drive technological innovation in the healthcare sector.

In Ecuador, there is substantial potential for the development and implementation of information platforms tailored to the healthcare sector. However, current initiatives often lack effective integration between Internet of Things (IoT) capabilities and real-time monitoring systems. This gap underscores the need for a technological solution that facilitates accessible, efficient, and continuous monitoring of vital signs using IoT-enabled devices.

Dr. Tedros Adhanom, Director-General of the World Health Organization (WHO), has emphasized the importance of leveraging digital technologies to ensure universal access to healthcare services. According to his perspective, these tools should not be regarded as ends in themselves, but rather as essential means to advance public health [3]. Among their most impactful applications is the monitoring of vital signs, which plays a critical role in enhancing medical care [4].

A systematic review conducted by García et al. evaluated the clinical effectiveness of ICT-based interventions in the management of chronic diseases. The study included 24 investigations focused on asthma, hypertension, diabetes, heart failure, and cardiovascular prevention. The findings indicated that the use of ICT enhances the detection and monitoring of cardiovascular conditions, reduces mortality rates, and improves the efficiency of healthcare services [5].

Cardiovascular parameters such as heart rate and blood pressure provide critical insights into a patient's systemic condition, particularly following clinical procedures [6]. This highlights the need to develop both software and hardware tools specifically designed to support cardiovascular healthcare [7].

In this context, the Internet of Medical Things (IoMT) has emerged as a key technology, enabling the interconnection of medical devices with software applications via network infrastructures [8]. IoMT significantly enhances healthcare by facilitating remote patient monitoring, diagnosis, and treatment [9,10].

Additionally, applications integrated into smartwatches and smart rings have been developed to record data such as heart rate, oxygen saturation, and body temperature. However, these devices are primarily intended for tracking physical activity and sleep patterns. Their specifications explicitly state that they are not classified as medical devices; consequently, the data they provide are for informational purposes only and should not be used for clinical, diagnostic, or research applications.

In the province of Santa Elena, a device was developed for home-based monitoring of biomedical parameters. Although the acquired data were displayed on a test IoT platform, a customized information system for comprehensive data management was not implemented [11]. Nevertheless, such devices hold considerable potential to actively engage physicians and specialists in the continuous monitoring of patients' health status.

This article presents the progress of a multidisciplinary research project titled "Research on IoT Applications in Bioelectric Signal Acquisition" (CUP: 91870000.0000.389571), led by the Technology, Science, and Education (TECED) research group of the Faculty of Systems and Telecommunications at the State University Peninsula of Santa Elena. The project supports the specific objective of integrating the bioelectric signal acquisition system with a database-free platform. Within this framework, information technologies are leveraged to develop an innovative tool for continuous patient monitoring, incorporating clinical evaluation of the patient's health status.

The primary objective was to develop an information platform for monitoring heart rate, oxygen saturation, and body temperature, which are derived from bioelectric signals.

This article is structured as follows: Section 2 details the materials and methods employed in the design, development, and evaluation of the mobile application and web platform; Section 3 presents the results obtained following the implementation of the proposed infrastructure; and Section 4 outlines the conclusions and acknowledgments.

2. Materials and Methods

2.1. Methodology

This article addresses the design and development of an information platform for visualizing data transmitted from an IoT device that reports heart rate, oxygen saturation, and body temperature, which are derived from bioelectric signals [11,12].

As part of the user analysis, two primary profiles were identified: physicians and patients. According to a 2023 report published by the United Nations, over 75% of the global population owns a mobile phone, and 65% has internet access [13]. These figures supported the decision to prioritize the development of a mobile application for patients. Furthermore, recent studies [14,15] show that physicians spend most of their workday using computers, justifying the implementation of a web-based application tailored to healthcare professionals.

For data transmission, the Message Queuing Telemetry Transport (MQTT) protocol was selected, as it is widely used in IoT applications at the application layer [16]. This protocol is distinguished by its ability to support continuous data transmission while optimizing bandwidth and minimizing latency [17].

Asaad et al. demonstrated that an IoT-based remote health monitoring system, integrating GSM, Wi-Fi, and MQTT, is highly effective for patient follow-up in rural areas beyond the coverage of hospital networks. The system achieved a 99.89% success rate in data transmission, with a round-trip time of 7.5 ms and a total energy consumption of 900 mWh, using MQTT as the primary communication protocol [8].

For real-time data visualization in the user interface, MQTT over WebSocket was implemented, drawing on findings from the Internet Engineering Task Force (IETF) working group, which identifies WebSocket as an efficient solution for bidirectional client-server communications, eliminating the need for multiple HTTP requests in web applications [18]. Oliveira et al. compared MQTT and WebSocket using ESP8266 modules and Node.js servers for data exchange, concluding that WebSocket is preferable in environments with round-trip times exceeding 1 ms [19].

Similarly, in the IoT system design proposed by Jun-Oh Seo, MQTT was employed for sensor data collection, and WebSocket for bidirectional communication in low-energy scenarios, thereby validating the combined efficiency of both protocols. Accordingly, in this project, MQTT over WebSocket was adopted for real-time data visualization in the user interface, while MQTT was also used for communication between the broker and the PHP service responsible for database storage, as illustrated in Figure 1. This configuration prevents the generation of multiple HTTP requests that would otherwise occur if data were sent directly from the application to the database.

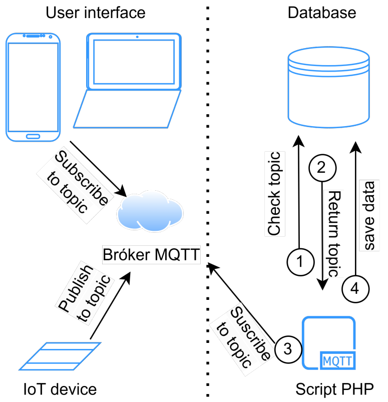

Figure 1. Data connection architecture

Once the corresponding analysis was completed, the system's functional requirements were defined. These requirements provide an overview of the platform, promote clear and consistent communication among stakeholders, support a comprehensive understanding of the system, and establish a robust foundation for the design phase. Additionally, the general use case of the system is depicted in Figure 2.

The functional requirements were organized into specific modules tailored to specific user roles, such as physician or patient, as well as general modules applicable to all users.

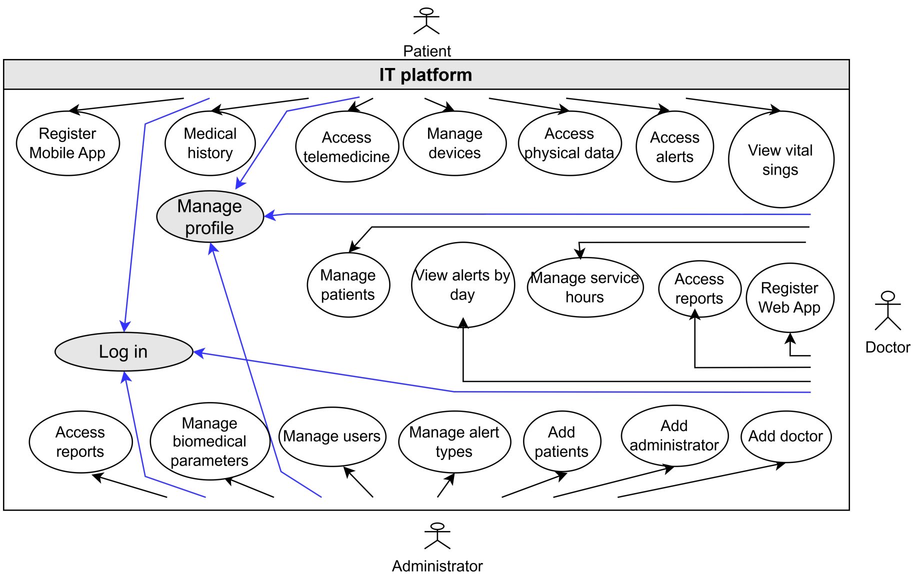

Figure 2. System Use Case

General Modules.

- **Authentication Module:** All users (physicians, patients, or administrators) must authenticate to access the system. Access permissions and visible information vary depending on the assigned role, ensuring both privacy and security. Patients may create their accounts exclusively through the mobile application, while physicians are required to register via the web platform. The system also supports credential recovery by allowing users to enter their email address. A verification code is then sent, which, once validated, permits the user to update their login credentials.

- **Profile Module:** This module allows users to customize and update their personal information, including phone number, email address, and profile picture. It also enables users to modify authentication parameters.

- **Reports Module:** Physicians can access detailed reports on the number of patients seen and consultations conducted. Patients can view their medical prescriptions and clinical history. Administrators can query aggregated system data, including the total number of registered devices, patients, and physicians. Information is presented in both tabular and graphical formats to support data analysis.

Administrator Role Modules.

- **Administration Module:** Administrators are provided with tools for comprehensive user management, including physicians, patients, and other administrators. They can create, enable, disable, and edit user accounts. Additionally, administrators can manage alert types and define new biomedical parameters.

Patient Role Modules.

- **Medical Module:** This module allows patients to select physicians by specialty and healthcare facility, and to configure access permissions for their medical data.

- **Telemedicine Module:** This module enables redirection to WhatsApp and Telegram for conducting consultations, video calls, and sending direct messages to the physician via the platform.

- **Biomedical Data Module:** This module displays real-time values for heart rate, body temperature, and oxygen saturation. It also allows patients to manage additional health data, such as weight and height, annotate alerts, and view their complete alert history. Only the assigned physician has access to the patient's data. Patients can disable a malfunctioning device and register a replacement.

Physician Role Modules.

- **Patient Module:** Physicians can access the complete list of assigned patients and review their vital signs, including heart rate, temperature, and oxygen saturation, along with the history of generated alerts. During consultations, physicians can record clinical observations, issue electronic medical prescriptions, and generate detailed reports for each biomedical parameter. They can also communicate with patients via WhatsApp, Telegram, or through direct messaging on the platform.

One of the core functionalities represented in the general use case diagram is the visualization of biomedical parameters, as shown in Figure 2. To illustrate the underlying system logic, a channel diagram was developed and is presented in Figure 3. This diagram outlines the sequence of activities required to perform this function, along with the actors or components involved in the process: patient, system, server, and user interface.

Each actor is responsible for specific actions, represented by activity rectangles that illustrate the flow from data acquisition to its presentation to the end user. The diagram is vertically segmented into parallel lanes, each delineating the responsibilities of a given actor. This structure enables a clear visualization of the vital signs display process and how it unfolds sequentially [20].

To visualize vital signs on the interface, the user must first place their finger on the IoT device. Once the device processes the data, it is published to the MQTT broker. On the platform, the user then selects the option corresponding to vital signs, which triggers an internal connection to the user's specific topic. The data are subsequently received and displayed in real time on the interface.

In addition to visualizing vital signs, the acquired data are stored in the database and used to automatically generate alerts. To identify abnormal values for heart rate, oxygen saturation, and body temperature, reference ranges were established based on prior studies [21–23]. These thresholds served as the basis for defining the criteria that trigger alert activation.

Once the values are transmitted from the IoT device, they pass through a series of validation filters. If any parameter falls outside the defined normal range, an alert is generated, recorded in the database, and simultaneously sent to both the emergency contact and the assigned physician.

For heart rate, the system first verifies the type of parameter received. If the parameter corresponds to heart rate, the system analyzes the patient's gender and age to classify the value as either appropriate or abnormal. The thresholds established for this classification are presented in Table 1.

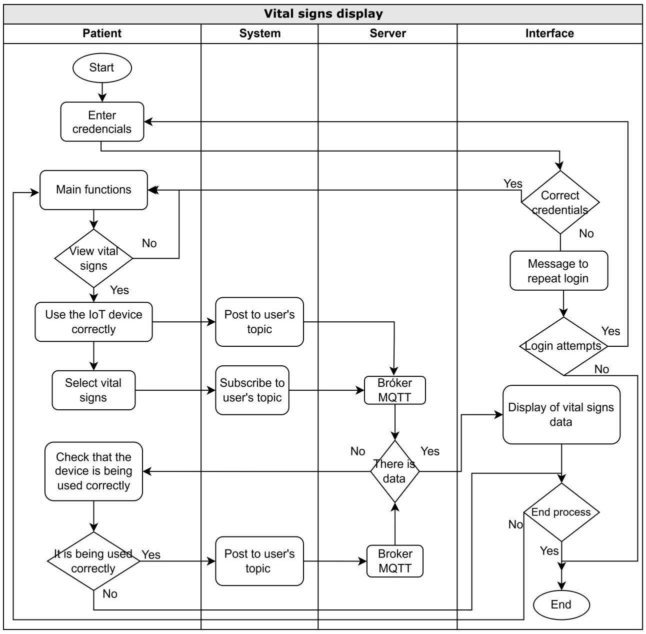

Figure 3. Channel Diagram

Table 1. Heart Rate thresholds by age and gender (beats per minute)

Heart rate		
Age (years)	**Men**	**Women**
20-29	86 or more	96 or more
30-39	86 or more	98 or more
40-49	90 or more	100 or more
50 or more	90 or more	104 or more

If the parameter corresponds to oxygen saturation and the recorded value is below 90%, an automatic alert is triggered, as this level is classified as severe hypoxemia, as shown in Table 2.

Table 2. Oxygen Saturation

Oxygen Saturation Thresholds for Hypoxemia	
Age (years)	**Value**
Mild hypoxemia	90-94 %
Severe hypoxemia	< 90 %

Finally, if the parameter corresponds to body temperature, the system can generate two types of alerts: hypothermia and fever, based on the thresholds established in Table 3.

Table 3. Body Temperature Thresholds for Alert Classification

Temp Body temperature	
Age (years)	**Value**
Hypothermia	< 35 °C
Low-grade fever / Fever	37,2 a 38,9 °C
Hyperthermia	> 40,6 °C

To support a clearer understanding of the alert generation process, the diagram shown in Figure 4 was developed.

After the system requirements were clearly defined, the architecture type was selected. The information platform adopts a microservices architecture model. In this approach, the client layer communicates via HTTP, enabling request and response handling through a FHIR-compatible API developed using Node.js and PHP. This API implements resources such as Patient in accordance with the HL7 FHIR specification and provides RESTful endpoints that consume data in the application/fhir+json format, integrated with a MySQL database.

Additionally, when clients access the application, they subscribe to the topics published on the MQTT broker. The connection is established using the MQTT protocol over WebSocket, enabling real-time data visualization. A PHP script retrieves the relevant topics from the database, manages the subscription process, and stores the received values.

Additionally, a separate PHP script is responsible for automatically sending email alerts once the data have been stored. This architecture was chosen for its ability to manage resources in a distributed manner through independent services. In this model, the client requests a resource over the network, and the corresponding server processes the request and returns a response based on the requested service, as illustrated in Figure 5.

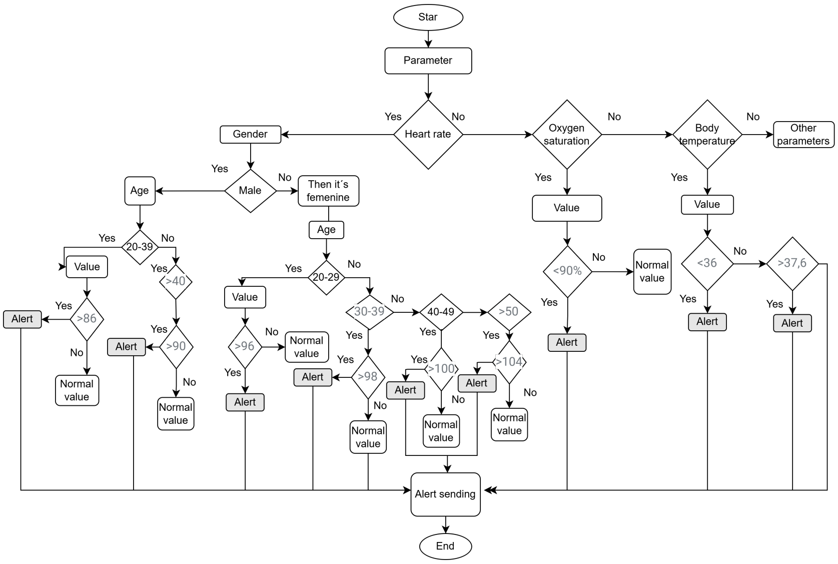

Figure 4. Alert Generation Diagram

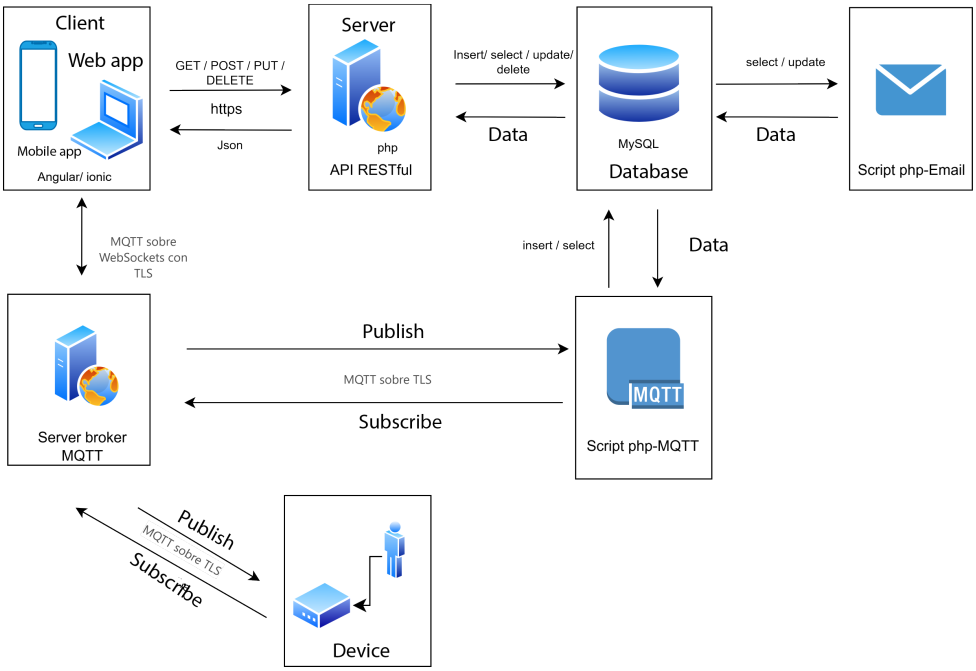

Figure 5. System Architecture

To support real-time data handling and prevent API saturation caused by multiple queries, a PHP script was developed to subscribe to the MQTT broker, retrieve the data, and store it in the database. This process activates triggers that generate additional information, which is subsequently processed by other independent scripts to execute specific actions.

This architectural model allows multiple users to access system resources simultaneously without causing saturation. The various advantages of this approach are detailed in reference [24].

Although this article primarily focuses on the development of the software application, this section describes the components used to build the device responsible for acquiring three bioelectrical signals: heart rate, oxygen saturation, and body temperature, as illustrated in Figure 6.

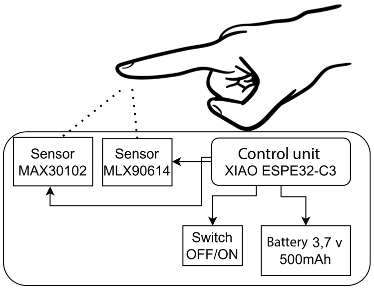

Figure 6. Device components

The device is powered by a 3.7 V battery and a switch, and it includes an XIAO ESP32C3 control unit, a high-performance IoT development mini board designed for low-power applications and wireless wearable devices.

Additionally, the MAX30100 sensor was integrated to measure heart rate and oxygen saturation. This sensor incorporates a discrete-time filter that rejects 50/60 Hz interference, as well as low-frequency and ambient noise.

To measure body temperature, the MLX90614 sensor was used. This sensor offers high accuracy over a wide temperature range (-70 °C to + 380 °C), with a resolution of 0,02 °C, a 90° field of view, and an accuracy of up to ± 0,5 °C at ambient temperature.

Each sensor acquires its respective biomedical parameter values and publishes them to the MQTT broker. The platform communicates with the device via this intermediary. The time required to visualize the data depends on the device itself, as it performs internal calculations to prevent the transmission of erroneous values. Once the device is operational, data are typically received within approximately one minute and are then immediately displayed on the user interface.

To support platform functionality, data modeling was conducted using a relational database model, as shown in Figure 7 [25]. Given the existence of two primary user roles, patients and physicians, a relational structure was required to define their associations and store user-specific data. The advantages of relational databases were leveraged, particularly their ability to link tables through primary and foreign keys.

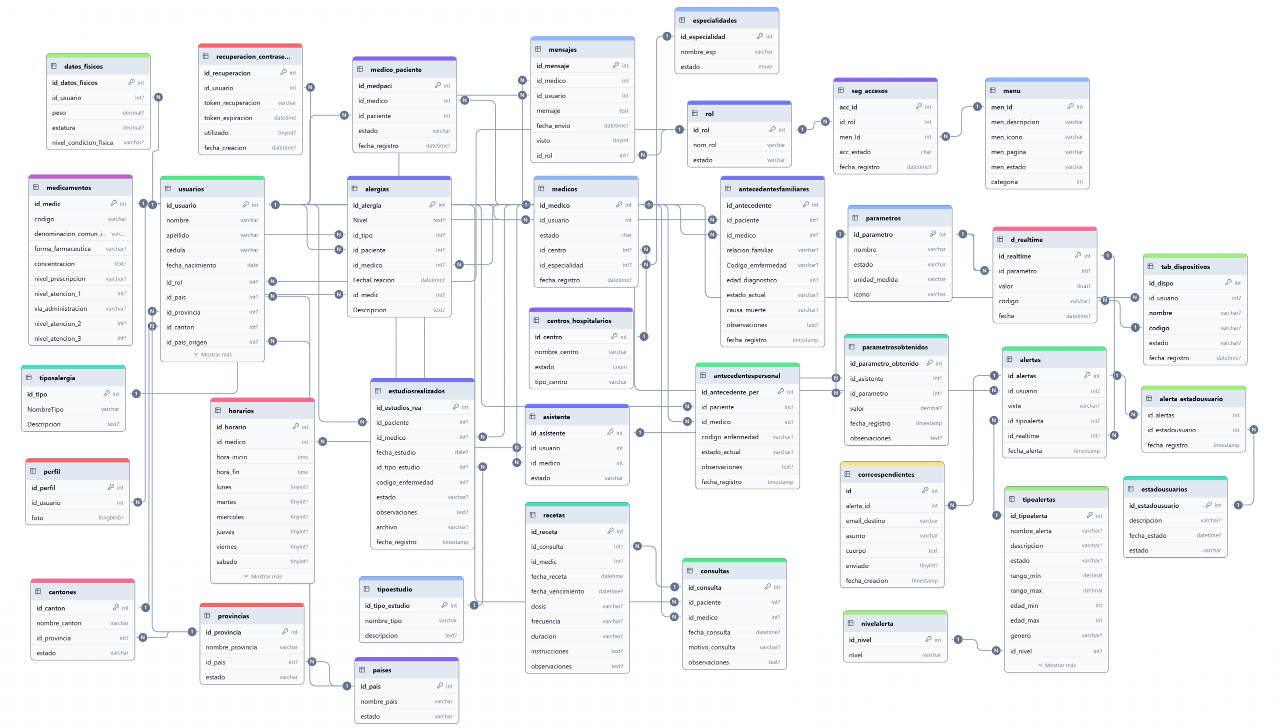

Figure 7. Data model

To ensure proper data modeling, normalization principles were applied to organize information efficiently and eliminate redundancies and inconsistencies. Normalization, introduced by Edgar F. Codd, establishes a set of rules that promote the separation of concepts and minimize anomalies caused by attribute dependencies, thereby reducing data redundancy.

The model design incorporates the first three normal forms: First Normal Form (1NF), Second Normal Form (2NF), and Third Normal Form (3NF). The First Normal Form ensures that all attributes are atomic, meaning they contain indivisible values with no duplications or internal subdivisions. The Second Normal Form eliminates partial dependencies by requiring that all non-key attributes depend solely on the primary key. The Third Normal Form removes transitive dependencies to further enhance data integrity.

These principles guided the construction of the database model, allowing redundancy to be avoided and enabling the use of relationships to implement triggers that execute various functions.

2.2. Interface Design

The interface design for the platform was guided by the methodology proposed by Sommerville. This approach identifies three essential activities required to develop an effective user interface: user analysis, system prototyping, and interface evaluation. Through the completion of these activities, the final product is achieved [26].

For the user analysis, the most frequently used device types were taken into consideration. Additionally, random surveys were conducted with individuals involved in the research project and with potential patients to understand their expectations for an information system. Based on the insights gathered, the interface model was designed, including the selection of color schemes, core functionalities, login screen, and main interface layout. Key elements such as the display of biomedical parameters, alert functionality, and doctor–patient integration were also incorporated into the design process.

The mockups were developed using the Justin mind tool. This stage enabled a clear visualization of the interface design for both the web and mobile applications, facilitating the necessary adjustments to align with the functional requirements and meet the needs of the primary users.

An evaluation was then conducted with members of the TECED research group, which includes faculty, external specialists, and students. Feedback was collected and used to implement targeted improvements. Once these modifications were completed, the final interface design was approved.

The prototype was developed using the incremental development methodology, which structures the project into a series of successive increments [27], as illustrated in Figure 8.

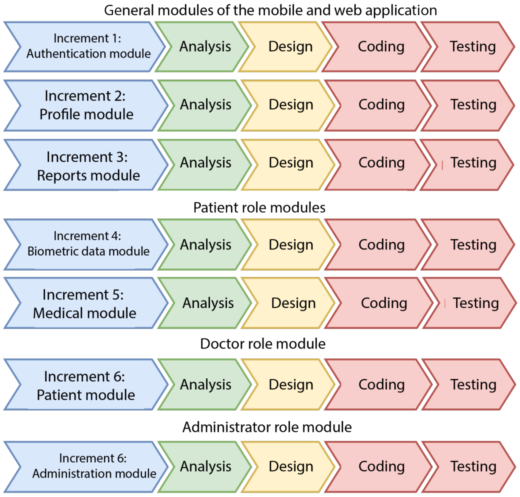

Figure 8. Incremental Methodology

This approach consists of segmenting the overall system functionality according to the requirements provided by subject-matter specialists and performing the corresponding phases of analysis, design, coding, and testing.

2.3. Development Materials of the Software Platform

For the development of the software platform, a computer with 32 GB of RAM and 500 GB of storage was used. The interface designs for both the mobile application and the web version were created using the Justin mind prototyping tool.

For front-end development, Angular and Ionic were used due to their ability to streamline the implementation of both mobile and web applications. This choice facilitated the integration of multiple features and responsive components, allowing the interface to adapt effectively to various screen sizes.

According to the platform's functional requirements, the relationships between physician and patient data were considered. In the design, user roles are queried directly from the database, which informed the selection of a MySQL relational database. For back-end development, PHP, the Fat-Free Framework, and Node.js were used, along with the Visual Studio Code text editor, since both PHP and Node.js offer high compatibility with MySQL.

To compile and deploy the mobile application to production, Android Studio was used. This development environment requires a minimum of 8 GB of RAM to operate efficiently.

For real-time data acquisition, records were collected from two IoT devices [11,12], using the MQTT communication protocol over WebSocket. To store the incoming data, a service was implemented that subscribes to the broker via the MQTT protocol. During the testing phase, data were simulated using Node-RED, alongside real data transmitted by the first device [11] and by another version of the bioelectrical signal acquisition device [12].

3. Results and discussion

3.1. Results

During the development of the software platform, several key aspects were addressed, including communication protocols, user analysis, interface design, system architecture, and database modeling. Upon completion of the development phase, the primary functions associated with the physician profile were defined. These include viewing the patient list, monitoring alerts generated throughout the day, recording consultation data, and generating reports that summarize the number of patients treated and consultations performed.

Figure 9 shows one of the main interfaces designed for physicians, which enables graphical visualization of stored vital sign values and allows users to consult the most recent records. Additionally, the system provides a summary that applies basic statistical calculations such as the mean, median, and mode to support clinical data analysis.

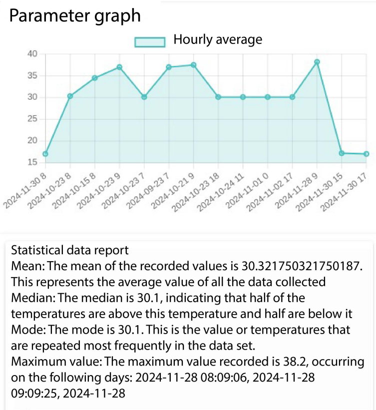

Statistical data report
Mean: The mean of the recorded values is 30.321750321750187. This represents the average value of all the data collected
Median: The median is 30.1, indicating that half of the temperatures are above this temperature and half are below it
Mode: The mode is 30.1. This is the value or temperatures that are repeated most frequently in the data set.
Maximum value: The maximum value recorded is 38.2, occurring on the following days: 2024-11-28 08:09:06, 2024-11-28 09:09:25, 2024-11-28

Figure 9. Main interface for the physician

Figure 10 displays the interface for the patient profile, showing recorded vital sign values along with additional features such as alert notifications, access to telemedicine services, and consultation of physical data.

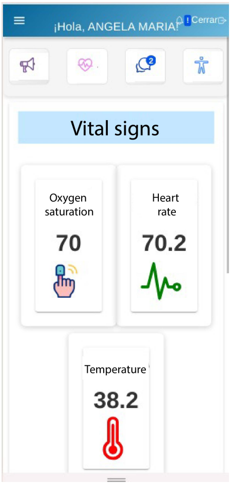

Figure 10. Main interface for the patient

In addition to having a well-designed interface, it is essential to perform stress testing to determine the number of users or requests the system can effectively support.

Resource usage tests for the mobile application were conducted on a smartphone. These performance evaluations were necessary due to the high number of applications commonly installed on mobile devices, which can negatively impact overall performance when running concurrently. To carry out these tests, specialized tools available on the market were used to monitor the resource consumption of installed applications [28].

The Android operating system includes built-in features for monitoring the resource consumption of installed applications. Table 4 presents the data collected during the application's use, demonstrating low energy consumption. This aspect is critical, as users typically prefer devices with extended battery life. Therefore, it is essential for mobile applications to be optimized for energy efficiency [29].

Table 4. Resource usage of the mobile application

Category	Item	Usage
Storage	Application	104 MB
	Data	4,53 MB
	Cache	455 MB
	Total	**109 MB**
RAM	Current usage	143 MB
	Duration	1 minute
	Total memory	**4 GB**
Battery	Foreground usage	8 minutes
	Background usage	5 minutes
	Total usage time	14 minutes
	CPU	6 minutes
	Wifi	6430 packets
	Consumption percentage	0.60%

Stress tests of the platform was carried out using the Locust tool to simulate real-time user traffic. The test began with zero users and progressively increased in increments of 100, reaching up to 5,000 simultaneous users. Each virtual user generated requests and interacted with the platform throughout the test.

Figure 11 shows the blue line representing the number of successful responses per second, which peaked at 600. The red line indicates the number of rejected requests per second. The error rate remained at zero until the test reached 5,000 simultaneous users and a total of 26,393 requests. Beyond this point, a minimal error rate of 0.16% was recorded, corresponding to requests rejected by the server.

Figure 12 shows the progressive increase in the number of users, starting from zero and rising in increments of 100. The platform demonstrated optimal performance, supporting up to 1,700 simultaneous users without generating errors. When the load reached 5,000 users, a minimal percentage of rejected requests was observed, indicating strong overall system performance even under high-demand conditions.

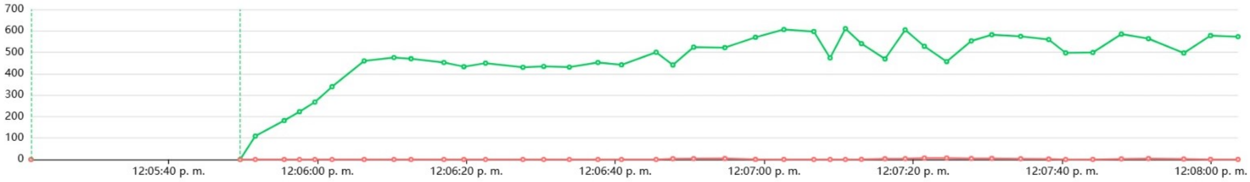

Figure 11. Stress test showing total responses per second

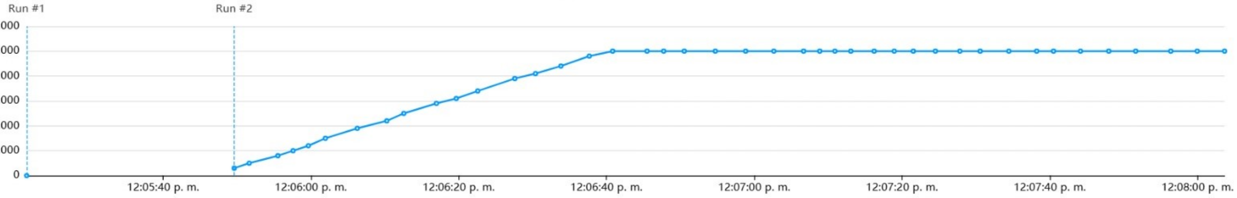

Figure 12. Stress test showing the total number of users

3.2. Discussion

Several studies have focused on the development and implementation of platforms for monitoring physical parameters [30] and biomedical parameters [31]. However, in platforms designed for biomedical monitoring, the doctor–patient relationship is often overlooked. Alerts are typically sent only to the user's device and their designated companion, without direct notification to the attending physician. This omission is significant, as certain data may require specialized medical interpretation.

In [31], data transmission is conducted via Bluetooth, limiting the system's functionality to short-range proximity, as the user must remain near the device to receive information. In contrast, the platform developed in this study transmits data not only to the user and a designated family member but also directly to the attending physician through email and integrated notifications within the information platform. To overcome the range limitations inherent to Bluetooth communication, the system employs a Wi-Fi connection in combination with the MQTT protocol, enabling real-time transmission and remote visualization of vital signs over the internet.

In [30], a backend service for IoT was developed using Microsoft Azure, with a focus on managing data transmitted by an IoT device. However, the scope of that work was limited to backend implementation; no web or mobile applications were developed to support data customization or user interaction, and the API's functionality was validated exclusively using Postman. To overcome these limitations, the platform proposed in this study incorporates not only a database and API but also a comprehensive information system that supports real-time visualization of data acquired from the IoT device, which captures three bioelectrical signals as well as efficient and scalable management of that information.

Numerous studies related to the monitoring of biomedical parameters have been identified; however, most of them primarily focus on the design and implementation of the IoT device, without addressing the development of the accompanying information platform [**?**, 32–38]. During the literature review, commercial devices such as smartwatches and the Galaxy Ring smart ring were also considered, both of which are supported by proprietary applications.

Table 5 presents a comparison of the functionalities offered by existing applications associated with commercial devices such as smartwatches and the Galaxy Ring, in relation to the platform proposed in this study. It is important to note that these commercially available devices use the collected data solely for informational purposes and are not intended for the detection, diagnosis, or treatment of medical conditions.

Table 5. Comparison of the Proposed Information Platform with Similar Systems

Feature	Smart Wristband 3	Samsung Health	Proposed Platform
Web application available for physicians	-	-	✓
Sends vital sign data to physicians or specialists	-	-	✓
Records user's weight	-	✓	✓
Displays heart rate data	✓	✓	✓
Displays oxygen saturation data	✓	✓	✓
Displays body temperature data	✓	✓	✓

The applications linked to these commercial devices are not designed to integrate with medical platforms or transmit data directly to a physician. In contrast, the proposed information platform allows users to designate a healthcare professional who can access information related to their vital signs, generated alerts, and medical history.

Additionally, according to [39], 70% of the evaluated systems exhibit response times between 1.0 and 2.0 seconds. The performance of the proposed platform slightly exceeds this range. However, as Echeverría observes, user-perceived latency tends to increase as system response times lengthen. Therefore, while there is room for performance optimization, the platform still offers a competitive user experience in terms of response speed.

Regarding energy consumption, the mobile application recorded a usage rate of 0.6% over a 14-minute period, aligning with the growing concern about the environmental impact of mobile software. Recent studies [40, 41] emphasize the importance of evaluating the energy consumption of applications on mobile devices.

Although mobile device manufacturers continue to improve energy efficiency through hardware and software innovations, it is equally critical for application developers to address power consumption in their designs. While the energy usage of an individual application may seem negligible, its cumulative impact across millions of devices underscores the importance of optimizing efficiency. Future research could focus on strategies such as interface simplification and code optimization to promote more sustainable software development.

The software platform presented in this study represents its initial version and forms part of the multidisciplinary research project titled "Research on IoT Applications in the Acquisition of Bioelectric Signals" (CUP: 91870000.0000.389571), led by the Technology, Science, and Education (TECED) research group from the Faculty of Systems and Telecommunications.

4. Conclusions

This study presents the development of a scalable software platform that integrates HTTP and MQTT communication protocols for real-time monitoring of biomedical parameters. The system supports comprehensive user management, including both medical professionals and patients, to facilitate continuous remote health supervision.

The platform enables the acquisition and visualization of key biomedical indicators, including heart rate, oxygen saturation, and body temperature. It also supports alert generation, facilitates secure communication between users, and allows physicians to maintain detailed oversight of patients' health status. Designed for scalability, the platform supports the future integration of additional biomedical parameters and the management of high request volumes without compromising performance. Simulation tests confirmed this capability, with an average response time of 930 milliseconds and 95% of responses delivered in under 2.3 seconds.

During load testing, the system successfully processed up to 22,132 requests at the communication endpoint, reaching a rate of 440.4 requests per second without errors. When the number of concurrent users increased to 5,000 and the system handled 26,393 requests, a minimal error rate of 0.16% was recorded, which is considered acceptable given the high concurrency. The platform was confirmed to operate without errors with up to 1,700 simultaneous users.

Compared to previous studies, such as that of González, which indicates that 25% of users abandon applications with load times exceeding 3 seconds [29], the developed platform demonstrated response times well within acceptable thresholds, ensuring a seamless user experience. Similarly, the recorded mobile resource usage data were appropriate, considering the broad range of functionalities provided by the application.

These findings confirm that the proposed system effectively manages high request volumes without compromising stability, positioning it as a reliable tool for the remote monitoring of biomedical parameters.

Acknowledgments

This study is part of the funded research project titled "Research on IoT Applications in the Acquisition of Bioelectric Signals" (CUP 91870000.0000.389571), led by the TECED (Technology, Science, and Education) research group from the Faculty of Systems and Telecommunications at the State University Península de Santa Elena.

The authors express their gratitude to the members of the TECED project, whose contributions and objectives have been instrumental in advancing innovative solutions through the application of information technologies in healthcare.

Contributor Roles

- **Marcia Bayas Sampedro:** Conceptualization, data curation, formal analysis, funding acquisition, investigation, methodology, project administration, resources, software, supervision, validation, visualization, writing – original draft, writing – review & editing.
- **Ángela Parra Fernández:** Data curation, formal analysis, investigation, methodology, resources, software, validation, visualization, writing – original draft, writing – review & editing.
- **Ronald Rovira Jurado:** Conceptualization, funding acquisition, investigation, methodology, project administration, resources, supervision, validation, writing – original draft, writing – review & editing.
- **Manuel Montaño Blacio:** Investigation, validation, visualization, writing – review & editing.
- **Óscar Gómez Morales:** Conceptualization, investigation, validation.
- **Junior Figueroa Olmedo:** Investigation, validation.

References

[1] C. C. Y. Poon, M. D. Wang, P. Bonato, and D. A. Fenstermacher, "Editorial: Special issue on health informatics and personalized medicine," *IEEE Transactions on Biomedical Engineering*, vol. 60, no. 1, pp. 143–146, Jan. 2013. [Online]. Available: https://doi.org/10.1109/TBME.2012.2233593

[2] J. Yang, "Editorial: Flexible biosensors and intelligent medical devices in health and disease," *Frontiers in Bioengineering and Biotechnology*, vol. 10, Jun. 2022. [Online]. Available: https://doi.org/10.3389/fbioe.2022.849617

[3] WHO. (2019) Who releases first guideline on digital health interventions. World Health Organization. [Online]. Available: https://upsalesiana.ec/ing34ar6r3

[4] M. Weenk, S. J. Bredie, M. Koeneman, G. Hesselink, H. van Goor, and T. H. van de Belt, "Continuous monitoring of vital signs in the general ward using wearable devices: Randomized controlled trial," *Journal of Medical Internet Research*, vol. 22, no. 6, p. e15471, Jun. 2020. [Online]. Available: https://doi.org/10.2196/15471

[5] F. García-Lizana and A. Sarría-Santamera, "New technologies for chronic disease management and control: a systematic review," *Journal of Telemedicine and Telecare*, vol. 13, no. 2, pp. 62–68, Mar. 2007. [Online]. Available: https://doi.org/10.1258/135763307780096140

[6] J. Vázquez, A. Secchi, H. Moris, N. Reyne, F. Rivera, F. Astorga, J. Moreno, and P. Amorin, "Parámetros cardiovasculares y su variación posterior a una atención de urgencia odontológica," *International journal of odontostomatology*, vol. 15, no. 4, pp. 1019–1025, Dec. 2021. [Online]. Available: http://dx.doi.org/10.4067/S0718-381X2021000401019

[7] J. J. Pastoriza Beltrán, *Desarrollo de un módulo para la teledetección automática del estado de las funciones cardiovasculares.* Universidad Estatal Península de Santa Elena, 2017. [Online]. Available: https://upsalesiana.ec/ing34ar6r7

[8] B. A. Mubdir and H. M. A. Bayram, "Adopting MQTT for a multi protocols IoMT system," *International Journal of Electrical and Computer Engineering (IJECE)*, vol. 12, no. 1, p. 834, Feb. 2022. [Online]. Available: http://doi.org/10.11591/ijece.v12i1.pp834-844

[9] I. Al Khatib, A. Shamayleh, and M. Ndiaye, "Healthcare and the internet of medical things: Applications, trends, key challenges, and proposed resolutions," *Informatics*, vol. 11, no. 3, p. 47, Jul. 2024. [Online]. Available: https://doi.org/10.3390/informatics11030047

[10] R. Uddin and I. Koo, "Real-time remote patient monitoring: A review of biosensors integrated with multi-hop IoT systems via cloud connectivity," *Applied Sciences*, vol. 14, no. 5, p. 1876, Feb. 2024. [Online]. Available: https://doi.org/10.3390/app14051876

[11] M. E. Alomoto Tomalá, *Diseño e implementación de un sistema de monitoreo domiciliario para la gestión integral de la salud cardiovascular.* Unviersidad Estatal Península de Santa Elena, 2024. [Online]. Available: https://upsalesiana.ec/ing34ar6r11

[12] A. S. Villón Quimi, *Diseño e implementación de un dispositivo IoT para la toma de variables bioeléctricas.* Universidad Estatal Península de Santa Elena, 2025. [Online]. Available: https://upsalesiana.ec/ing34ar6r12

[13] ONU. (2023) Más del 75 % de la población mundial tiene un teléfono celular y más del 65 % usa el internet. Organización de las Naciones Unidas. [Online]. Available: https://upsalesiana.ec/ing34ar6r13

[14] B. G. Arndt, J. W. Beasley, M. D. Watkinson, J. L. Temte, W.-J. Tuan, C. A. Sinsky, and V. J. Gilchrist, "Tethered to the EHR: Primary care physician workload assessment using EHR event log data and time-motion observations," *The Annals of Family Medicine*, vol. 15, no. 5, pp. 419–426, Sep. 2017. [Online]. Available: https://doi.org/10.1370/afm.2121

[15] S. Munday, J. Pinchin, and J. Blakey, "Time spent using computers and impact on clinical work among doctors," *Future Healthcare Journal*, vol. 4, p. s12, Jun. 2017. [Online]. Available: https://doi.org/10.7861/futurehosp.4-2-s12

[16] M. Saqib and A. H. Moon, "A novel lightweight multi-factor authentication scheme for MQTT-based IoT applications," *Microprocessors and Microsystems*, vol. 110, p. 105088, Oct. 2024. [Online]. Available: https://doi.org/10.1016/j.micpro.2024.105088

[17] M. Domingues, J. N. Faria, and D. Portugal, "Dimensioning payload size for fast retransmission of MQTT packets in the wake of network disconnections," *EURASIP Journal on Wireless Communications and Networking*, vol. 2024, no. 1, Jan. 2024. [Online]. Available: https://doi.org/10.1186/s13638-023-02327-3

[18] I. Fette and A. Melnikov, *The WebSocket Protocol.* RFC 6455, Dec. 2011. [Online]. Available: https://doi.org/10.17487/RFC6455

[19] G. Oliveira, D. Costa, R. Cavalcanti, J. Oliveira, D. Silva, M. Nogueira, and M. Rodrigues, "Comparison between mqtt and websocket protocols for iot applications using esp8266," in *2018 Workshop on Metrology for Industry 4.0 and IoT.* IEEE, Apr. 2018. [Online]. Available: https://doi.org/10.1109/METROI4.2018.8428348

[20] S. Al-Fedaghi, *Ingienería de software I.* UNEMI ONLINE, 2019. [Online]. Available: https://upsalesiana.ec/ing34ar6r20

[21] E. M. Jamieson, L. A. Whyte, and J. M. McCall, *Procedimientos de enfermería clínica.* ElSevier Churchill Livingstone, 2007. [Online]. Available: https://upsalesiana.ec/ing34ar6r21

[22] R. Gómez Arribas and B. Blasco Colmenarejo, *Técnicas básicas de enfermería.* EDITEX, 2021. [Online]. Available: https://upsalesiana.ec/ing34ar6r22

[23] A. Pittaras, P. Kokkinos, C. Faselis, C. Grassos, M. Doumas, E. Kallistratos, A. Manolis, and I. B. Samuel, "Resting heart rate and mortality risk in hypertensive patients with no atrial fibrillation," *Journal of Hypertension*, vol. 42, no. Suppl 1, p. e50, May 2024. [Online]. Available: https://doi.org/10.1097/01.hjh.0001019736.22833.da

[24] D. López and E. Maya, "Arquitectura de software basada en microservicios para desarrollo de aplicaciones web," in *Séptima Conferencia de Directores de Tecnología de Información, TICAL 2017 Gestión de las TICs para la Investigación y la Colaboración*, 2017. [Online]. Available: https://upsalesiana.ec/ing34ar6r24

[25] F. L. Osorio Rivera, *Base de datos relacionales Textos Académicos.* ITM, 2008. [Online]. Available: https://upsalesiana.ec/ing34ar6r25

[26] I. Sommerville, *Software engineering.* Pearson Education, 2004. [Online]. Available: https://upsalesiana.ec/ing34ar6r26

[27] S. Martinez Escuredo, *Metodología de Implantación del ERP Microsot Dynamics NAV.* Lulu, 2018. [Online]. Available: https://upsalesiana.ec/ing34ar6r27

[28] S. Khan, Z. Jiangbin, and A. Wahab, "Design and development of android performance testing tool," in *2020 IEEE Conference on Big Data and Analytics (ICBDA).* IEEE, Nov. 2020, pp. 57–60. [Online]. Available: https://doi.org/10.1109/ICBDA50157.2020.9289714

[29] S. Fresneda González, *Gestión del consumo energético en el desarrollo de aplicaciones para dispositivos móviles.* Universitat Politècnica de València, 2017. [Online]. Available: https://upsalesiana.ec/ing34ar6r29

[30] S. Rahman, *Development of an IoT backend service with Azure.* Centria University of Applied Sciences, 2025. [Online]. Available: https://upsalesiana.ec/ing34ar6r30

[31] I. D. Torres-Pardo, J. A. Guzmán-Luna, C. M. Barros-Ligan, and J. P. Gutiérrez-López, "Medición de parámetros de signos vitales para emisión de alertas móviles," *Revista Politécnica*, vol. 19, no. 37, pp. 43–56, Mar. 2023. [Online]. Available: https://doi.org/10.33571/rpolitec.v19n37a4

[32] M. R. Olivas-Martínez and R. Ruiz-Márquez, "Monitor biomédico portátil con comunicación vía bluetooth a dispositivos móviles con sistema operativo Windows," *Memorias Del Congreso Nacional De Ingeniería Biomédica*, vol. 2, no. 1, pp. 323–327, 2017. [Online]. Available: https://upsalesiana.ec/ing34ar6r33

[33] R. E. Cañon Clavijo, *Diseño e implementación de un sistema de monitoreo remoto de ritmo cardíaco y generación de alertas preventivas para la supervisión de pacientes en riesgo potencial.* Universidad Distrital Francisco José de Caldas, 2021. [Online]. Available: https://upsalesiana.ec/ing34ar6r34

[34] C. Mundt, K. Montgomery, U. Udoh, V. Barker, G. Thonier, A. Tellier, R. Ricks, R. Darling, Y. Cagle, N. Cabrol, S. Ruoss, J. Swain, J. Hines, and G. Kovacs, "A multiparameter wearable physiologic monitoring system for space and terrestrial applications," *IEEE Transactions on Information Technology in Biomedicine*, vol. 9, no. 3, pp. 382–391, Sep. 2005. [Online]. Available: https://doi.org/10.1109/TITB.2005.854509

[35] M. Moreno Caballero, *Diseño y programación de un sistema de monitorización de parámetros biomédicos.* PFC/TFG-Escuela Técnica Superior de Ingeniería Industrial, 2021. [Online]. Available: https://upsalesiana.ec/ing34ar6r36

[36] V. Becerra Tapia, V. Téllez Victoria, J. M. Ramos Medina, G. R. Peñaloza Mendoza, and M. S. Castro Zenil, "Sistema de transferencia de datos biomédicos con protocolos de comunicación de bajo consumo," *Revista de Ciencias Tecnológicas*, vol. 6, no. 4, p. e284, Nov. 2023. [Online]. Available: https://doi.org/10.37636/recit.v6n4e284

[37] Z. Rebolledo Nandi, *Monitor de signos vitales portátil.* Universidad Autónoma de Guerrero, 2016. [Online]. Available: https://upsalesiana.ec/ing34ar6r32

[38] E. I. Tintín Durán, *Diseño y elaboración de un prototipo de monitor de signos vitales aplicando métodos no invasivos con comunicación de datos a dispositivos móviles.* Universidad Politécnica Salesiana, 2015. [Online]. Available: https://upsalesiana.ec/ing34ar6r39

[39] D. Echeverría, "Tiempo de respuestas y experiencia de usuario estudio experimental," *Revista Latinoamericana de Ingeniería de Software*, vol. 4, no. 5, p. 231, Dec. 2016. [Online]. Available: https://doi.org/10.18294/relais.2016.231-234

[40] P. Sala del Real, *Análisis de consumo energético para aplicaciones de visión artificial en Android.* UAM. Departamento de Ingeniería Informática, 2017. [Online]. Available: https://upsalesiana.ec/ing34ar6r41

[41] A. Meneses-Viveros, E. Hernández-Rubio, S. Mendoza, J. Rodríguez, and A. B. Márquez Quintos, "Energy saving strategies in the design of mobile device applications," *Sustainable Computing: Informatics and Systems*, vol. 19, pp. 86–95, Sep. 2018. [Online]. Available: https://doi.org/10.1016/j.suscom.2018.07.011

Scientific Paper / Artículo Científico

UNIVERSIDAD POLITÉCNICA SALESIANA ECUADOR
INGENIUS
Revista de Ciencia y Tecnología
https://doi.org/10.17163/ings.n34.2025.07
pISSN: 1390-650X / eISSN: 1390-860X

HYDROPOWER DEVELOPMENT IN ETHIOPIA, TANZANIA, ZAMBIA, AND ZIMBABWE: A COMPREHENSIVE REVIEW

UNA REVISIÓN DEL DESARROLLO DE LA HIDROELECTRICIDAD EN ETIOPÍA, TANZANIA, ZAMBIA Y ZIMBABUE

Sebastián Naranjo-Silva[1,*]

Received: 25-09-2024, Received after review: 06-05-2025, Accepted: 10-05-2025, Published: 01-07-2025

Abstract

All continents are currently undergoing energy transitions toward low-carbon economies driven by renewable technologies. Africa is no exception; with its rapidly growing population and expanding economy, it represents nearly one-fifth of the global demographic. Although the African continent contributes less than 3% of global carbon emissions, it is already experiencing severe and disproportionate impacts from climate change. This manuscript aims to analyze the hydropower development in Ethiopia, Tanzania, Zambia, and Zimbabwe, with the objective of assessing the current use and projected role of this renewable resource. These countries were selected for their significant hydroelectric potential and ongoing investment in renewable energy infrastructure. While these nations have made substantial commitments to hydropower, climate-induced shifts in hydrological patterns, particularly increased drought risk, pose serious challenges to energy security and sustainability. Consequently, electric utilities must not only project future energy generation but also implement robust mitigation and adaptation strategies to safeguard long-term investments. Given the critical role of climate change as an external variable influencing energy planning, it is essential to evaluate hydropower and reservoir operations through a multidimensional lens encompassing parameters such as temperature, precipitation, humidity, river flow, watershed characteristics, and related factors.

Keywords: Africa; energy; hydroelectric; projections; sustainable.

Resumen

Todos los continentes están atravesando actualmente transiciones energéticas hacia una economía baja en carbono desde las renovables. Uno de estos continentes es África, donde la población y el crecimiento económico impulsan una quinta parte del mundo. Si bien el continente africano tiene la menor responsabilidad por el calentamiento global, con menos del 3% de las emisiones, ya enfrenta severos impactos del cambio climático. Por lo tanto, este manuscrito tiene como objetivo analizar el desarrollo de hidroeléctrico en Etiopía, Tanzania, Zambia y Zimbabwe para conocer el uso de esta renovable y sus proyecciones. Estos países fueron seleccionados de acuerdo con información que tienen una amplia proyección hidroeléctrica. En estos países se ha invertido una cantidad valiosa en hidroelectricidad, pero, el impacto del cambio climático aumenta el riesgo de sequías, lo que preocupa debido a una variación en los patrones. Las compañías eléctricas no solo necesitan pronosticar la generación futura de energía, sino que también tomar medidas de mitigación y adaptación para mantener sus inversiones. Además, el cambio climático es un parámetro externo que juega un papel importante al proporcionar datos de referencia para futuros proyectos, siendo necesario evaluar las operaciones de energía hidroeléctrica y embalses bajo un conjunto de parámetros (temperatura, precipitación, humedad, caudal de ríos, cuencas y otros).

Palabras clave: África; energía; hidroeléctrica; proyecciones; sostenible.

[1,*] Department of Sustainability, Polytechnic University of Catalonia, Barcelona, Spain.
Corresponding author✉: hector.sebastian.naranjo@upc.edu.

Suggested citation: S. Naranjo-Silva, "Hydropower Development in Ethiopia, Tanzania, Zambia, and Zimbabwe: A Comprehensive Review," *Ingenius, Revista de Ciencia y Tecnología*, N.° 34, pp. 89-102, 2025, DOI: https://doi.org/10.17163/ings.n34.2025.07.

1. Introduction

Globally, renewable-based electric power systems have played an increasingly critical role in improving energy access, particularly in rural and remote regions where electricity availability remains limited. According to the Global Status Report of Renewables, global investment in renewable energy capacity increased by 2% in 2020, demonstrating resilience amid the economic disruptions caused by the COVID-19 pandemic. Distributed renewable energy systems have continued to expand access, contributing up to 10% of electricity generation in some countries [1].

In 2020, global investment in renewable power and fuels, excluding hydropower projects larger than 50 MW, totaled USD 303.5 billion. For the sixth consecutive year, developing and emerging economies surpassed developed countries in renewable energy capacity investment, reaching a combined total of USD 153.4 billion. That same year, funding in developed economies increased by 13%, while investment in emerging markets declined by 7%, reflecting broader trends in global renewable energy financing, excluding large-scale hydropower projects [2, 3].

Focusing specifically on hydropower, which remains the leading source among renewable technologies, the International Hydropower Association (IHA) reported that global hydropower generation reached an estimated 4,252 TWh in 2021, following a 1.9% increase in 2020. Despite the disruptive effects of the pandemic-induced recession, which impacted many of the world's major hydropower technology providers, the global hydropower market continued to grow. Notably, China accounted for more than half of all new capacity additions in 2021, contributing an increase of 20,840 MW [4].

However, renewable energy use is increasing across all economic sectors, reflecting a growing reliance on electricity to meet societal and industrial demands. According to the REN21 Group, much of the recent progress in expanding the share of renewables in global electricity production has resulted in renewables contributing nearly one-third (30%) of total electricity generation in 2022 [5], as shown in Figure 1.

Figure 1 illustrates that hydropower remains a leading source among renewable energy technologies, and that the industry is expected to face both challenges and opportunities in the years to come. These challenges include operational and technical constraints, environmental and social acceptance issues, declining global wholesale electricity prices, and adverse climate impacts, all of which directly affect hydropower generation [5, 6].

Investing in hydropower development offers substantial economic benefits by accelerating growth and contributing to the reduction of greenhouse gas emissions. Hydropower plays a critical role in advancing clean energy technologies within national economies, which is why this paper examines the current status and future potential of hydropower in selected African countries [7].

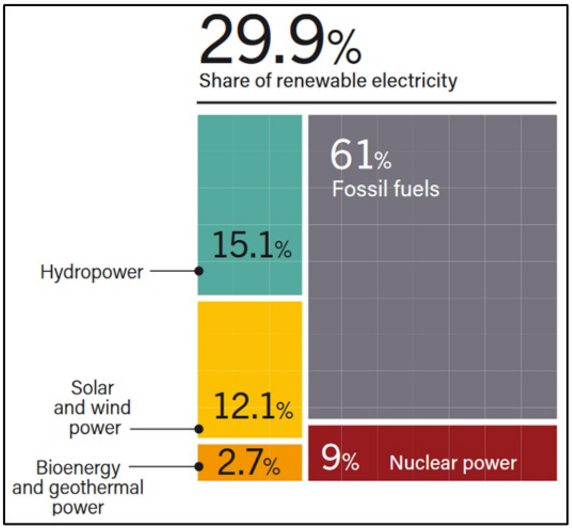

Figure 1. Global energy grid composition [8], p. 1

Currently, approximately 40% of the population in Africa lacks access to electricity, with the majority of those affected living in sub-Saharan Africa. Countries such as Ghana, Kenya, and Rwanda are on track to achieve universal electricity access by 2030, serving as examples for others to follow. Africa also has the lowest per capita consumption of modern energy in the world, particularly from renewable sources. As population and income levels continue to rise, demand for modern energy is expected to increase by one-third between 2020 and 2030, according to the Sustainable Africa Scenario. In parallel, several African countries have committed to reducing emissions by approximately 550 Mt.CO2 by 2030, equivalent to 40% of the continent's current emissions [9, 10].

In Africa, hydropower currently accounts for approximately 17% of total electricity generation. In some countries, including the Democratic Republic of Congo, Ethiopia, Malawi, Mozambique, Uganda, and Zambia, hydropower supplies as much as 80% of total energy consumption [11]. According to the World Bank, Africa's installed hydropower capacity is expected to reach approximately 40 gigawatts (GW) by 2030 [12]. However, nearly 25% of existing plants are not operational due to inadequate maintenance and poor infrastructure. Additionally, the International Hydropower Association (IHA) estimates that the continent has a development pipeline of 117 GW and a remaining hydropower potential of 478 GW [13].

According to data from organizations involved in collecting information on renewable energy, particularly hydroelectricity, this energy source is generally perceived positively due to its reliance on non-depleting natural resources. However, hydropower also entails environmental and social impacts that must be carefully considered. This manuscript aims to analyze hydropower development in Ethiopia, Tanzania, Zambia, and Zimbabwe (Figure 2), focusing on its current use and future projections through a comprehensive review of relevant documents and energy sector policies. These countries were selected based on the available data indicating their significant hydroelectric potential. Additionally, multiple investigative sources were consulted to support and consolidate the information presented in this review.

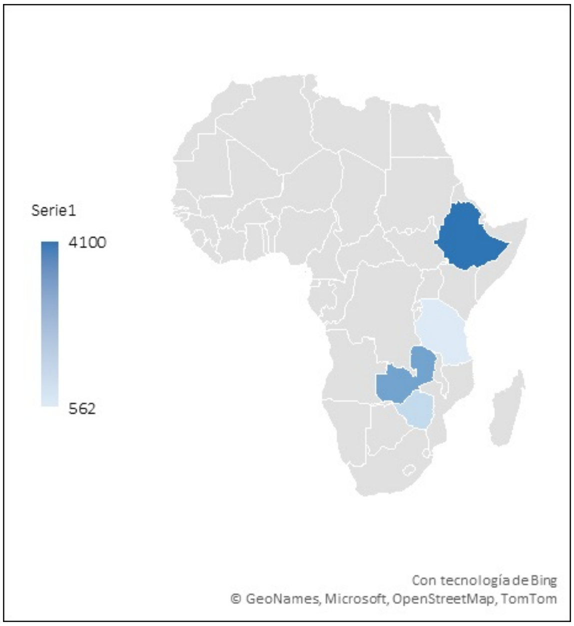

Figure 2. Countries selected for this study [14]

2. Materials and Methods

To analyze hydropower development in Ethiopia, Tanzania, Zambia, and Zimbabwe, the methodology begins with a comprehensive review of literature and documents, guided by an investigative approach. This first step involves collecting relevant sources, including scientific studies, government reports, and energy and environmental policy documents specific to the selected countries. The review focuses on studies that address both hydropower development and climate change impacts in the region, with an emphasis on recent publications, preferably from the past five years, to ensure relevance and timeliness. Priority is given to reliable sources, including academic databases, reports from international organizations, and official government documents.

The second step of the methodology involves a detailed analysis of each country's energy policies and regulatory frameworks. This analysis aims to assess how national policies support hydropower development by identifying key environmental regulations, government incentives, and climate change adaptation strategies. A comparative analysis is then conducted to examine similarities and differences in how climate considerations are integrated into national energy policies, which is essential for understanding the broader context in which hydropower projects are being developed.

The third step involves assessing major hydropower projects in the selected countries. This analysis includes the collection of data on each project's installed capacity, technological configuration, annual energy production, and future generation projections. Additionally, the efficiency and sustainability of these projects are evaluated, considering their vulnerability to climate variability, including droughts and shifts in precipitation patterns, which are becoming increasingly frequent due to climate change.

The fourth step of the methodology involves a comparative case study of the four selected countries, presented in the discussion section. This approach facilitates the assessment of each country's challenges and achievements in developing hydropower under changing climate conditions. Both qualitative and quantitative methods are employed to analyze national experiences, with a particular focus on best practices and lessons learned.

Overall, this article outlines the methodology used to select and analyze scientific documents, providing a detailed account of the keywords applied: "African hydropower development," "Hydropower development in Ethiopia, Tanzania, Zambia, and Zimbabwe," and "Energy matrix in Ethiopia, Tanzania, Zambia, and Zimbabwe." It also specifies the search strings employed, the specific databases and digital libraries consulted, including SCOPUS, Web of Science, and other sources relevant to hydropower research, as well as the time frame of the literature review, which spans from 2017 to 2024.

Finally, the results will be discussed, as validation is essential to ensure the reliability and relevance of the study's conclusions. The combination of these methodological steps provides a comprehensive and rigorous basis for analyzing the current state and future prospects of hydropower in these African countries, within the broader context of accelerating climate change.

3. Results and discussion

According to data from British Petroleum, hydropower generation by continent in 2021 shows that Asia produced the largest share, generating 2,176 TWh. This upward trend has continued since 2003. In comparison, the Americas generated 1,239 TWh, Europe produced 659 TWh, and Africa generated only 146 TWh, indicating significantly lower output. When comparing

Africa's generation to that of Asia [15], the continent accounted for just 7% of Asia's hydropower production, confirming Africa as the region with the lowest level of hydropower development in 2021 [16]. As shown in Figure 3, global hydropower development in 2021 is represented by total installed capacity across regions.

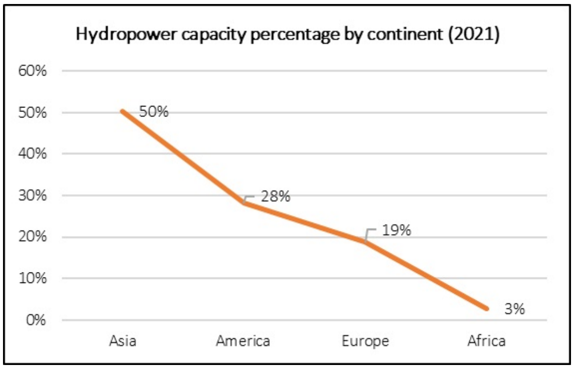

Figure 3. Global hydropower installed capacity by continent in 2021

As shown in Figure 3, hydropower installed capacity in 2021 varied significantly across continents, with Asia leading with 655 MW, followed by the Americas with 382 MW, Europe with 254 MW, and Africa with only 38 MW. These figures reveal substantial disparities in hydropower development, particularly in regions with limited energy infrastructure. Africa presents considerable opportunities for expanding this key renewable energy source [15], [17]. Additionally, the study includes a figure that displays the top 18 African countries by hydropower installed capacity, including pumped storage, as well as the countries selected for this review.

As shown in Figures 3 and 4, hydropower development varies significantly across continents and among African countries. Based on these disparities, this study focuses on Ethiopia, Tanzania, Zambia, and Zimbabwe, selected for their considerable hydroelectric development potential and projected growth. To support this analysis, several investigative sources were reviewed to consolidate relevant information and assess the current state and projected use of hydropower in the selected countries.

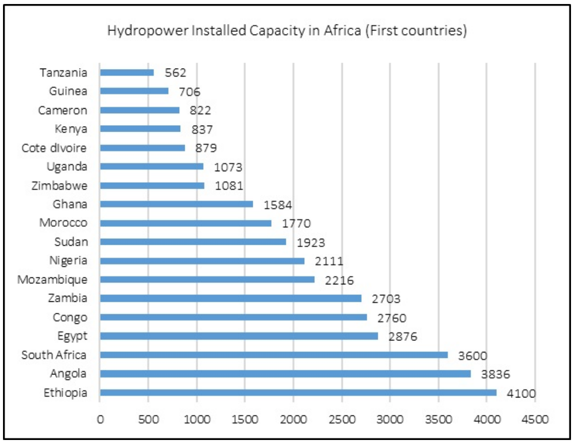

Figure 4. Hydropower installed capacity in Africa [4]

Ethiopia

Ethiopia is a developing country endowed with abundant water resources. Consequently, its hydropower production capacity increased from 850 MW in 2010 to 4,100 MW in 2021. The government is currently undertaking several major hydropower projects aimed at positioning Ethiopia as a key power hub in East Africa. Notable among these projects are the Gibe III Hydropower Plant, constructed on the Omo-Gibe River with a capacity of 1,870 MW, and the Grand Ethiopian Renaissance Dam, built on the Abay River with a capacity of 6,000 MW [18, 19].

Hydropower development has been prioritized as a key driver of economic growth in Ethiopia. However, to ensure the optimal efficiency of both existing and planned reservoirs, it is essential to assess the potential impacts of hydropower expansion. Ongoing changes in temperature, precipitation, and streamflow patterns increasingly affect hydropower schemes, influencing dam and reservoir design horizons as well as the operational life cycles of these facilities [20, 21]. Additionally, reservoir operating rules are widely applied to guide the effective management of hydropower systems [22]. Accordingly, several relevant studies have been conducted and are referenced in this review.

Tewodros Mekonnen (2022) analyzed hydropower development in Ethiopia and concluded that the country is already experiencing the adverse effects of climate change-induced droughts, which are negatively impacting its hydroelectric resources. To mitigate these effects, a 30% increase in total installed capacity would be required to compensate for an anticipated 50% reduction in hydro plant output due to drought. According to projections, by 2065, Ethiopia's electricity supply will comprise 9% from hydropower, 13% from nuclear energy, 3.4% from heavy fuel oil, 7% from geothermal, 6% from wind, and 5% from biomass. Despite the growing diversification of the energy mix, hydropower is expected to remain the dominant source of electricity generation until 2057, accounting for 25.2% of total output [23].

A prospective analysis of the power–water nexus indicates that the rapid construction of large-scale hydroelectric dams imposes environmental costs on downstream communities by altering natural water flow patterns. Simulation scenarios from the analysis reveal that, among Ethiopia's hydropower development pathways, two distinct modeling approaches are required to achieve projected outputs of 71 and 87 TWh per year by 2050 under a climate change mitigation scenario. These findings underscore the need to significantly increase installed capacity in Ethiopia to make a meaningful contribution to global efforts aimed at achieving the 2°C target of the Paris Agreement [24]. For comparison, Ethiopia's hydropower production stood at approximately 21 TWh per year in 2022 [4].

Kinfe Mirani (2022) evaluated the hydropower potential at the Kesem Reservoir, which spans an area of 2,974 km^2. The study applied Representative Concentration Pathways (RCPs), specifically RCP4.5 and RCP8.5, to assess projected climate impacts over short- and long-term periods. Under RCP4.5, the maximum estimated energy production is 376.2 MWh in the short term and 370.5 MWh in the long term. Under RCP8.5, the corresponding values are 368.6 MWh and 363.5 MWh, respectively. It is important to note that the original baseline for hydropower generation was projected at 380 MWh [25]. Additional research supports these findings, showing that climate variability across 200 locations in Ethiopia's Nile sub-basin could result in precipitation changes ranging from - 14% to + 27% by 2050. These findings underscore the significant vulnerability of large-scale hydropower infrastructure to unpredictable climatic events, including both tangible and intangible construction-related costs [26].

Ethiopia's transmission network is undergoing significant expansion and modernization to support the country's ambitious electrification goals. The government now aims to achieve universal electricity access by 2030, revising its earlier target of 2025, with plans to connect 96% of the population to the national grid by that year. Transmission infrastructure is being reinforced through the construction of new substations, the upgrading of transmission lines, and the modernization of grid systems to accommodate increased loads and integrate variable renewable energy sources [27, 28].

Ethiopia possesses substantial hydroelectric potential, with a significant surplus available for export. However, the majority of the population resides in remote areas with limited access to electricity. Currently, the country generates approximately 4 GW of electricity from 11 large and 7 small hydroelectric plants. To achieve universal electricity access, national energy policy should prioritize small-scale hydropower, which may offer a more practical and decentralized solution to meet rural energy needs while promoting economic development in these communities [29].

However, Ethiopia's expansion of large-scale hydroelectric projects has raised concerns among neighboring countries, particularly those dependent on the Nile River. For instance, Egypt has strongly opposed these developments, citing potential disruptions to its historical water rights.

Tanzania

Tanzania, located in East Africa, is known for its cultural diversity, national parks, and rich historical heritage. One of the country's key strengths lies in its abundance of renewable energy resources. Consequently, Tanzania has successfully harnessed various sources, including biomass, hydropower, geothermal, solar, and wind energy. According to the 2021 Energy Resource Guide, the country's total installed electricity generation capacity was 1,602 MW. Of this total, 244 MW were added over the previous four years, with capacity distributed as follows: hydropower – 568 MW, thermal – 951.6 MW, and other renewable sources – 82.4 MW [30].

Tanzania's electricity generation is primarily sourced from natural gas (48%), hydropower (31%), oil (18%), solar energy (1%), and biofuels (1%). This energy mix has contributed to improved electricity access, reaching 36.4% of the urban population and 11% of the rural population [31]. However, the country's continued reliance on hydropower, combined with frequent droughts, often results in power outages. In addition, Tanzania's average per capita electricity consumption remains low at 108 kWh per year, compared to the global average of 2,500 kWh per year [30].

According to Baraka Kichonge (2018), Tanzania is among the fastest-growing economies in Africa. To meet its rapidly increasing energy demands, the country requires affordable, clean, and, most importantly, sustainable electricity. Although thermal generation continues to dominate global electricity production, Tanzania has substantial hydropower potential, estimated at 38,000 MW. Nevertheless, as of 2021, only a small portion of this potential had been developed, with an installed capacity of just 562 MW [4], [32].

Research indicates that in Tanzania, the construction of hydroelectric plants and reservoirs has effects that extend well beyond direct environmental impacts. These developments often require the resettlement of communities and the displacement of wildlife, underscoring the competition for water resources between local populations and hydropower operators. Furthermore, the expansion of infrastructure associated with such projects is frequently linked to increased deforestation [33].

On the other hand, Tanzania's untapped hydroelectric potential, supported by feasibility studies estimating approximately 4,765 MW for development in the short to medium term, should be evaluated within the broader context of an integrated energy grid incorporating various renewable sources. However, frequent climatic challenges can negatively impact large- and medium-scale hydropower projects. The research highlights the important role that small-scale hydroelectric plants can play in both electricity generation and environmental conservation [32].

Reuben Kadigi (2008), in a study of the Great Ruaha River in Tanzania, assessed the value of water in irrigated paddy fields and hydropower generation using a residual imputation model. The estimated productivity of water (PW) in irrigated paddy ranged from 0.126 to 0.265 kg/m^3 while in hydropower generation it ranged from 0.45 to 1.68 kWh/m^3. These results underscore the importance of evaluating water's value across alternative uses to guide effective resource management and allocation [34]. Matthew England (2019) further emphasizes the need to integrate water use decisions across sectors, particularly in agriculture-based economies. In such contexts, resource reallocation can result in substantial transfers from agriculture to sectors with higher economic returns, such as hydropower and industrial production, potentially maximizing pro-poor outcomes [34, 35].

Tanzania is actively expanding its energy grid and transmission network to meet growing demand, with a focus on integrating renewable energy sources and enhancing regional interconnections. However, current conditions vary considerably across the country due to regional economic disparities, which affect the pace and effectiveness of infrastructure development [36, 37].

Given its geographical position and substantial hydroelectric potential, Tanzania is well-positioned to leverage clean, domestic energy resources. These assets can play a significant role in advancing national development goals and mitigating the effects of climate change. Nonetheless, to ensure sustainable progress, it is essential that hydropower initiatives provide meaningful and equitable benefits to both local communities and the environment, thereby supporting long-term growth in sustainable electricity generation.

Zambia

In 2020, Zambia's total installed energy capacity reached 2,800 MW, with hydropower accounting for 2,380 MW, or 85% of the total. In 2019, hydropower generation totaled 13,678 GWh [38]. Hydropower is a key component of Zambia's energy system due to its clean, renewable nature and its effectiveness in regulating power frequency. Zambia, a landlocked country in Southern Africa, borders eight neighboring nations. Its location near the equator gives it a tropical climate, with annual rainfall ranging from approximately 600 mm in the south to 1,400 mm in the north. December and January are typically the wettest months. In recent years, the country has increasingly faced extreme weather events, including recurrent droughts and floods [11], [39].

Nevertheless, research by Frank Mudenda (2022) indicates that fluctuating climate cycles are having increasingly adverse effects on Zambia's rivers, streams, and infrastructure. In recent years, the country has faced a growing electricity deficit caused by persistent power shortages. As of 2019, more than 1.9 million households (57.6%) remained without access to electricity, and over 96% of the rural population was still unelectrified. These figures underscore the critical need to address energy access and pursue sustainable electrification strategies [40].

Damaseck Chirwa (2023) observes that as Zambia's population grows, so does the demand for energy services, particularly electricity. This demand is expected to increase significantly, with the population projected to reach 26.9 million by 2035. Statistically, energy consumption is rising at an estimated rate of 6% per year, driven by demographic and socioeconomic factors [41]. As of 2020, the country's energy generation mix included coal (10.96%), heavy fuel oil (3.65%), diesel (2.78%), and solar (2.96%) [41, 42].

Scott Winton (2021) analyzed the Zambezi River Basin in Southern Africa, a region undergoing rapid development and population growth. Agricultural intensification, urban expansion, and the planned development of additional hydropower dams are likely to degrade the quality of surface water. However, there have been limited comprehensive assessments identifying where, how, and why specific water quality parameters are being affected, especially using in situ data across large regions. To address this gap, Winton conducted four field campaigns in 2018 and 2019, sampling a wide range of biogeochemical water quality parameters at 14 sites across central and southern Zambia. The findings indicate that while the major rivers, Zambezi and Kafue, exhibit low solute concentrations and are generally clean, they are impacted by thermal alterations, hypoxia, and the depletion of suspended sediments downstream of dams. Zambia currently hosts several large hydropower projects on these rivers, with a combined potential capacity exceeding 2,800 GWp, and additional feasibility studies are underway. Although such infrastructure is essential to strengthening the national energy grid and promoting clean energy development, it is recommended that these projects adhere to sustainable development criteria to minimize environmental impacts [43, 44].

Zambia's electricity grid depends largely on hydropower. The country is actively expanding and modernizing its transmission infrastructure to minimize energy losses and enhance reliability, often in coordination with regional power pools. Reports indicate that Zambia has achieved a low transmission loss rate of just 4%, and its national grid now covers nearly the entire country [45, 46].

At the same time, the country faces growing risks of water quality degradation due to increasing agricultural intensification, urbanization, and continued hydropower development. To address these challenges, it is essential for the Zambian government to invest in sustainable infrastructure and environmental management practices. These include wastewater treatment systems, ecologically sound dam operations, and the protection of watershed areas to preserve water quality and ecosystem health.

Zimbabwe

Zimbabwe has made notable progress in developing its energy infrastructure; however, this progress has not kept pace with the country's economic growth. As a result, Zimbabwe continues to face an energy shortfall, with an estimated national demand of 2,200 MW that it has yet to meet [47, 48].

Given the favorable climate conditions and the abundance of water bodies, Zimbabwe possesses substantial potential for hydropower development. However, this potential remains largely untapped due to the high capital investment required and a transmission grid that does not adequately reach viable generation sites. Furthermore, aging infrastructure and frequent power outages further limit access to renewable energy. Ongoing efforts to rehabilitate and expand the transmission network aim to improve both energy access and reliability [49].

According to the Zimbabwe Power Company, most of the country's electricity is generated by coal-fired thermal plants and hydroelectric projects, which are owned either directly or indirectly by Zimbabwe Electricity Supply Authority (ZESA) Holdings. However, due to constrained domestic supply, caused by economic challenges and insufficient investment in key infrastructure, Zimbabwe continues to import electricity from South Africa, Namibia, and Mozambique [50].

In Zimbabwe, forests are essential for both absorbing greenhouse gases and supplying energy, particularly in rural areas where 94% of the population depends on wood fuel. As a result, reconciling climate change mitigation with the goals of energy security and expanded electricity access presents a complex and pressing challenge that requires careful analysis [47].

Anesu Maronga (2021) examined the effects of drought on Zimbabwe's electricity supply, focusing on the Hwange hydropower station. The drought reduced the reliability of electricity generation, resulting in load-shedding that negatively impacted mining operations reliant on a constant power supply. The study evaluated the technical and economic viability of deploying concentrated solar power with thermal storage, as well as photovoltaic systems with battery storage, at a mining site in Zimbabwe. The findings concluded that integrating battery storage with a photovoltaic system significantly increases the proportion of the electrical load met by the renewable energy system [51].

Ekandjo (2018), in a study conducted along the Zambezi River within the renowned Mana Pools National Park, observed significant ecological and morphological changes over the past decade due to the construction of upstream hydroelectric dams. The study found that reservoir operations reduced average peak flows by 17% and increased average low flows by 5% in the Mana Pools area [52]. This analysis focused on Zambia and Zimbabwe, two Southern African countries that share the Zambezi River. In 2021, Zambia reported 2,703 MW of installed hydropower capacity, while Zimbabwe had 1,081 MW [4]. The study also confirmed that dams in and around both countries present various vulnerabilities. To mitigate ecological disruption, the study recommends aligning hydroelectric operations with wildlife management practices, particularly during flood control releases. Sudden gate openings were found to significantly disturb ecosystems, threatening both terrestrial and aquatic species [52].

Randall Spalding-Fecher (2016), in a study on the Zambezi River, highlights that water flow patterns are likely to shift in the future due to the significant impacts of climate change. These changes have serious implications for hydropower potential, as the financial viability and repayment of loans for related projects will depend on the stability of hydropower generation and revenue from energy sales. For example, the Kariba Hydropower Plant, shared by Zambia and Zimbabwe, is projected to be highly vulnerable to dry climate scenarios, with average electricity generation potentially decreasing by 12% between 2050 and 2070 [53].

In Zimbabwe, efforts to expand hydropower through renewable systems face additional challenges. The COVID-19 pandemic has led to higher infrastructure costs and increased land requirements, nearly doubling initial estimates. As a result, while the country gradually invests in new renewable energy projects, it is essential to keep all existing hydroelectric plants fully operational.

3.1. Discussion

Across the globe, continents are transitioning toward low-carbon economies centered on renewable energy technologies. In Africa, rapid population growth and economic development are driving a substantial increase in electricity demand. Consequently, the coordinated development of renewable energy offers a strategic opportunity for the continent to meet its growing energy needs while preserving environmental sustainability [54].

Although the African continent contributes the least to global warming, it is already facing some of the most severe impacts of climate change. Africa is home to nearly one-fifth of the world's population, yet it is responsible for less than 3% of global energy-related carbon dioxide emissions, with the lowest per capita emissions of any continent [9].

Although the adverse effects of climate change are being felt across Africa, countries such as Ethiopia, Tanzania, Zambia, and Zimbabwe are experiencing these impacts disproportionately. These include water stress, reduced food production, more frequent extreme weather events, and fluctuating economic growth. Despite these challenges, it is evident that these nations must continue pursuing economic and social development while contributing to the global clean energy transition [55, 56]. Hydropower is widely regarded as a clean, renewable energy source that offers benefits such as water supply, flood control, economic growth, and recreation [57]. However, the relationship between hydropower and external environmental factors is characterized by constant and often unpredictable fluctuations [58].

Comparing the findings from Ethiopia, Tanzania, Zambia, and Zimbabwe with broader global projections, Hamududu (2012) analyzed data from 12 global circulation models and found that significant changes in runoff are expected globally. For instance, large increases are projected in Quebec, Canada, while notable decreases are anticipated in Turkey and Venezuela, regions that previously exhibited high runoff levels. These changes are likely to have a direct impact on hydropower generation due to shifting hydrological patterns. The models further suggest that by 2050, hydropower production could decline by approximately 0.48% in Southern Africa, 0.83% in Northern Africa, 1.43% in Western Asia, and about 2% in Europe [59].

In comparison with other countries, a study in India projects a significant temperature increase of 6,25 ± 1,62 °C, which is expected to reduce river flows and negatively affect hydropower production during May and June, particularly at the Nathpa Jhakri and Bhakra Nangal plants, both located in snow-dominated regions [60]. In North America, reductions in hydropower output are also anticipated, driven primarily by hydrological changes rather than economic factors such as recessions. This is because hydropower systems generally operate continuously when sufficient water is available; however, increasing climate variability is affecting streamflow reliability [61].

Nevertheless, Africa holds the largest untapped hydropower potential in the world. According to a report published in June 2022 by the International Hydropower Association, this potential is estimated at 474 gigawatts (GW), compared to 73 GW in Europe, 275 GW in South America, 387 GW in North and Central America, 359 GW in East Asia and the Pacific, and 355 GW in South and Central Asia. While Africa's hydropower potential exceeds the continent's current and medium-term energy demand, the cost of electricity generated from hydropower remains among the lowest of all renewable sources globally [62, 63]. Therefore, it is recommended that Ethiopia, Tanzania, Zambia, and Zimbabwe coordinate the development of feasible hydropower resources and consider the findings of various studies, particularly those addressing the current and projected impacts of climate change.

According to the International Renewable Energy Agency, an additional 850 GW of hydropower capacity must be developed by 2050 to meet the climate goals outlined in the Paris Agreement. In 2020, 53 African countries submitted nationally determined contributions (NDCs) to the United Nations Framework Convention on Climate Change, collectively committing to mitigate 550 million tonnes of CO_2 by 2030. This target represents approximately 40% of the continent's current carbon dioxide emissions [9].

Moreover, the Africa Energy Outlook projects that by 2030, renewable sources, including solar, wind, hydropower, and geothermal, will account for over 80% of new power generation capacity. However, a key issue that warrants attention is the development of non-conventional renewables, particularly solar and geothermal energy. Although Africa holds 60% of the world's highest-quality solar resources, it accounts for just 1% of installed solar photovoltaic capacity. Solar energy, already the most cost-effective power source in many regions of Africa, must outcompete all other energy sources across the continent by 2030 to ensure sustainable development [64, 65].

Derrick Danso (2021) notes that hydroelectric power plants with large reservoirs are often used to support the integration of significant amounts of renewable energy, despite the inherent variability and intermittency of these sources. An evaluation of large hydropower reservoirs in West Africa indicates that when electricity demand increases by less than 25%, the combined contribution of solar and wind energy to total generation remains below 20%. This suggests that rising electricity demand can lead to instability in energy networks, particularly when they rely on a complex mix of renewables, fossil fuels, and other sources [66].

The energy transmission network in each country plays a fundamental role in enabling the efficient delivery of electricity from generation sources, including renewables, to demand centers, thereby ensuring a reliable power supply. For Ethiopia, Tanzania, Zambia, and Zimbabwe, a robust and modern transmission infrastructure is especially important to support economic growth, facilitate the integration of renewable energy, and achieve national development and electrification targets. Inadequate transmission systems can lead to bottlenecks, increased energy losses, and limited access expansion, ultimately hindering progress toward each country's development goals [67, 68].

This review highlights hydropower as a promising energy source with significant development potential across Africa. The analysis, which focuses on Ethiopia, Tanzania, Zambia, and Zimbabwe, underscores the need for broader integration of sustainability criteria. However, by covering only four of Africa's 56 nations, the review offers a limited perspective on the continent's overall hydropower landscape.

4. Conclusions

In Ethiopia, Tanzania, Zambia, and Zimbabwe, where hydropower has received substantial investment, climate change poses a significant challenge due to increasingly variable hydrological patterns. Power utilities in these countries must not only project future energy outputs but also implement comprehensive mitigation and adaptation strategies to protect infrastructure. Across all climate scenarios, projections indicate a declining trend in hydropower capacity driven by climatic variability.

In Ethiopia, concerns over transboundary water rights have sparked regional tensions, particularly with countries such as Egypt that depend heavily on Nile waters. Tanzania, by contrast, regards hydropower as a key driver of clean energy development, given its potential to support economic growth and reduce vulnerability to climate change.

In Zambia, the intensification of hydropower development raises concerns about declining water quality, highlighting the need for sustainable infrastructure investments such as wastewater treatment facilities, environmentally conscious dam operations, and basin protection zones. Zimbabwe, meanwhile, faces mounting challenges related to high installation costs, land requirements, and post-pandemic constraints, all of which hinder the expansion of its hydropower sector.

Given the critical role of climate change as an external variable, it is essential to evaluate hydropower generation and reservoir operations using key parameters such as temperature, precipitation, humidity, river flow, and basin characteristics. These indicators provide foundational data for designing resilient and efficient hydropower systems. In addition, African countries are encouraged to explore solar energy, as the continent holds 60% of the world's most valuable solar resources, offering a complementary path toward sustainable energy development.

While hydropower offers a reliable pathway to energy access and socioeconomic advancement for countries like Ethiopia, Tanzania, Zambia, and Zimbabwe, its development must ensure tangible benefits for local communities and ecosystems to be truly sustainable. Future research should explore the integration of other renewable sources across the continent, supported by green financial mechanisms that can accelerate Africa's transition to a diversified and sustainable clean energy future.

Contributor Roles

- **Sebastián Naranjo-Silva:** Conceptualization, data curation, formal analysis, investigation, writing – original draft, writing – review & editing.

References

[1] IRENA. (2020) Renewable energy statistics 2020. renewable hydropower (including mixed plants). International Renewable Energy Agency. [Online]. Available: https://upsalesiana.ec/ing34ar7r1

[2] ——. (2021) Renewable power generation costs in 2020. International Renewable Energy Agency. [Online]. Available: https://upsalesiana.ec/ing34ar7r2

[3] ——, *Renewable Energy Capacity Highlights 2019*. International Renewable Energy Agency, 2019. [Online]. Available: https://upsalesiana.ec/ing34ar7r3

[4] IHA. (2022) Hydropower status report 2022. International Hydropower Association. [Online]. Available: https://upsalesiana.ec/ing34ar7r4

[5] S. Naranjo-Silva, D. Punina-Guerrero, L. Rivera-Gonzalez, K. Escobar-Segovia, J. D. Barros-Enríquez, J. A. Almeida-Domínguez, and J. Álvarez del Castillo, "Hydropower scenarios in the face of climate change in Ecuador," *Sustainability*, vol. 15, no. 13, p. 10160, Jun. 2023. [Online]. Available: https://doi.org/10.3390/su151310160

[6] M. M. Uamusse, K. Tussupova, and K. M. Persson, "Climate change effects on hydropower in Mozambique," *Applied Sciences*, vol. 10, no. 14, p. 4842, Jul. 2020. [Online]. Available: http://doi.org/10.3390/app10144842

[7] A. Mayer, L. Castro-Díaz, M. C. López, G. Leturcq, and E. F. Morán, "Is hydropower worth it? Exploring Amazonian resettlement, human development and environmental costs with the Belo Monte project in Brazil," *Energy Research & Social Science*, vol. 78, p. 102129, Aug. 2021. [Online]. Available: http://doi.org/10.1016/j.erss.2021.102129

[8] REN21. (2023) Renewables 2023 global status report energy supply collection. REN21

Renewables now. [Online]. Available: https://upsalesiana.ec/ing34ar7r5

[9] IEA. (2022) World energy outlook special report Africa energy outlook. International Energy Agency. [Online]. Available: https://upsalesiana.ec/ing34ar7r11

[10] E. Mutambara, "Examining organizational politics as the cause of the crisis in energy generation in developing countries: the instance of Zimbabwe," *International Journal of Research in Business and Social Science (2147- 4478)*, vol. 12, no. 4, pp. 01–14, Jun. 2023. [Online]. Available: http://doi.org/10.20525/ijrbs.v12i4.2432

[11] C. Wang, D. Wang, and J. Zhang, "Experimental study on isolated operation of hydro-turbine governing system of Lunzua hydropower station in Zambia," *Renewable Energy*, vol. 180, pp. 1237–1247, Dec. 2021. [Online]. Available: https://doi.org/10.1016/j.renene.2021.09.014

[12] WBG. (2011) The world bank in Viet Nam. World Bank Group. All Rights Reserved. [Online]. Available: https://upsalesiana.ec/ing34ar7r12

[13] IHA. (2021) Hydropower status report 2021. International Hydropower Association. [Online]. Available: https://upsalesiana.ec/ing34ar7r13

[14] MapChart. (2021) World map: Advanced. the advanced world map adds political and geographical features to the basic world map. MapChart. [Online]. Available: https://upsalesiana.ec/ing34ar7r14

[15] B. P., *Statistical Review of World Energy 2022. Globally Consistent Data on World Energy Markets.* British Petroleum P. L. C., 2022. [Online]. Available: https://upsalesiana.ec/ing34ar7r15

[16] M. Roni, T. Mosier, B. Li, S. S. Alam, V. Durvasulu, B. Lawson, D. Steindorf, B. Pracheil, and V. Chalishazar, "Hydropower flexibility valuation tool for flow requirement evaluation," *Energy Reports*, vol. 9, pp. 217–228, Dec. 2023. [Online]. Available: http://doi.org/10.1016/j.egyr.2022.11.172

[17] IEA. (2022) Hydropower special market report. International Energy Agency. [Online]. Available: https://upsalesiana.ec/ing34ar7r17

[18] G. A. Tiruye, A. T. Besha, Y. S. Mekonnen, N. E. Benti, G. A. Gebreslase, and R. A. Tufa, "Opportunities and challenges of renewable energy production in Ethiopia," *Sustainability*, vol. 13, no. 18, p. 10381, Sep. 2021. [Online]. Available: http://doi.org/10.3390/su131810381

[19] F. Abera, D. Asfaw, A. Engida, and A. Melesse, "Optimal operation of hydropower reservoirs under climate change: The case of Tekeze Reservoir, Eastern Nile," *Water*, vol. 10, no. 3, p. 273, Mar. 2018. [Online]. Available: https://doi.org/10.3390/w10030273

[20] B. Khaniya, C. Karunanayake, M. B. Gunathilake, and U. Rathnayake, "Projection of future hydropower generation in Samanalawewa power plant, Sri Lanka," *Mathematical Problems in Engineering*, vol. 2020, pp. 1–11, Oct. 2020. [Online]. Available: http://doi.org/10.1155/2020/8862067

[21] Y. Meng, J. Liu, Z. Wang, G. Mao, K. Wang, and H. Yang, "Undermined co-benefits of hydropower and irrigation under climate change," *Resources, Conservation and Recycling*, vol. 167, p. 105375, Apr. 2021. [Online]. Available: https://doi.org/10.1016/j.resconrec.2020.105375

[22] A. K. Belay, D. Atenafu, S. Birhan, and T. Tegengn, "Techno-economic feasibility study of the gunde teklehaymanote micro-hydropower plant at Tindwat River, Central Gondar, Ethiopia," *Iranica Journal of Energy & Environment*, vol. 11, no. 2, pp. 130–136, 2020. [Online]. Available: https://doi.org/10.5829/ijee.2020.11.02.06

[23] T. W. Mekonnen, S. T. Teferi, F. S. Kebede, and G. Anandarajah, "Assessment of impacts of climate change on hydropower-dominated power system—the case of Ethiopia," *Applied Sciences*, vol. 12, no. 4, p. 1954, Feb. 2022. [Online]. Available: http://doi.org/10.3390/app12041954

[24] B. van der Zwaan, A. Boccalon, and F. Dalla Longa, "Prospects for hydropower in Ethiopia: An energy-water nexus analysis," *Energy Strategy Reviews*, vol. 19, pp. 19–30, Jan. 2018. [Online]. Available: http://doi.org/10.1016/j.esr.2017.11.001

[25] K. B. Mirani, M. A. Ayele, T. K. Lohani, and T. Y. Ukumo, "Evaluation of hydropower generation and reservoir operation under climate change from Kesem Reservoir, Ethiopia," *Advances in Meteorology*, vol. 2022, pp. 1–14, Jun. 2022. [Online]. Available: http://doi.org/10.1155/2022/3336257

[26] X. Zhang, H.-Y. Li, Z. D. Deng, C. Ringler, Y. Gao, M. I. Hejazi, and L. R. Leung, "Impacts of climate change, policy and water-energy-food nexus on hydropower development," *Renewable Energy*, vol. 116, pp. 827–834, Feb. 2018. [Online]. Available: http://doi.org/10.1016/j.renene.2017.10.030

[27] T. F. Agajie, A. Fopah-Lele, I. Amoussou, B. Khan, M. Bajaj, I. Zaitsev, and E. Tanyi, "Enhancing ethiopian power distribution with novel hybrid renewable energy systems for sustainable reliability and cost efficiency," *Scientific Reports*, vol. 14, no. 1, May 2024. [Online]. Available: http://doi.org/10.1038/s41598-024-61413-8

[28] M. T. Boke, S. A. Moges, and Z. A. Dejen, "Optimizing renewable-based energy supply options for power generation in Ethiopia," *PLOS ONE*, vol. 17, no. 1, p. e0262595, Jan. 2022. [Online]. Available: http://doi.org/10.1371/journal.pone.0262595

[29] A. D. Hailu, "Ethiopia hydropower development and Nile basin hydro politics," *AIMS Energy*, vol. 10, no. 1, pp. 87–101, 2022. [Online]. Available: http://doi.org/10.3934/energy.2022006

[30] ITA. (2023) Energy resource guide. Tanzania - renewable energy. International Trade Administration. [Online]. Available: https://upsalesiana.ec/ing34ar7r30

[31] O. J. Mdee, T. K. Nielsen, C. Z. Kimambo, and J. Kihedu, "Assessment of hydropower resources in Tanzania. A review article," *Renewable Energy and Environmental Sustainability*, vol. 3, p. 4, 2018. [Online]. Available: http://doi.org/10.1051/rees/2018004

[32] B. Kichonge, "The status and future prospects of hydropower for sustainable water and energy development in Tanzania," *Journal of Renewable Energy*, vol. 2018, pp. 1–12, 2018. [Online]. Available: http://doi.org/10.1155/2018/6570358

[33] G. Ardizzon, G. Cavazzini, and G. Pavesi, "A new generation of small hydro and pumped-hydro power plants: Advances and future challenges," *Renewable and Sustainable Energy Reviews*, vol. 31, pp. 746–761, Mar. 2014. [Online]. Available: http://doi.org/10.1016/j.rser.2013.12.043

[34] R. M. Kadigi, N. S. Mdoe, G. C. Ashimogo, and S. Morardet, "Water for irrigation or hydropower generation?—complex questions regarding water allocation in Tanzania," *Agricultural Water Management*, vol. 95, no. 8, pp. 984–992, Aug. 2008. [Online]. Available: http://doi.org/10.1016/j.agwat.2008.03.008

[35] M. I. England, "Contested waterscapes: Irrigation and hydropower in the Great ruaha river basin, Tanzania," *Agricultural Water Management*, vol. 213, pp. 1084–1095, Mar. 2019. [Online]. Available: http://doi.org/10.1016/j.agwat.2018.08.018

[36] R. J. Mwifunyi, D. C. Mnyanghwalo, and S. J. Kawambwa, "Enhancing service restoration in tanzanian power grid using internet of things sensors and renewable energy sources," *Tanzania Journal of Science*, vol. 49, no. 3, pp. 664–676, Sep. 2023. [Online]. Available: http://doi.org/10.4314/tjs.v49i3.10

[37] A. Abdalla and K. Ibwe, "Smart grid in Tanzania: Research opportunities," *Tanzania Journal of Engineering and Technology*, vol. 42, no. 2, pp. 170–183, Jun. 2023. [Online]. Available: http://doi.org/10.52339/tjet.v42i2.838

[38] USAID, *Power Africa: Zambia Energy Sector Overview.* African Power Platform, 2016. [Online]. Available: https://upsalesiana.ec/ing34ar7r38

[39] UCS. (2014) How hydroelectric energy works. Union of Concerned Scientists. [Online]. Available: https://upsalesiana.ec/ing34ar7r39

[40] F. Mudenda, M. van Dijk, and A. Bekker, "Development of evaluation framework for the selection of run-of-river hydropower potential sites to be included in the Zambian Hydropower Atlas," *Journal of Water and Climate Change*, vol. 13, no. 11, pp. 4000–4018, Oct. 2022. [Online]. Available: http://doi.org/10.2166/wcc.2022.262

[41] D. Chirwa, R. Goyal, and E. Mulenga, "Floating solar photovoltaic (FSPV) potential in Zambia: Case studies on six hydropower power plant reservoirs," *Renewable Energy Focus*, vol. 44, pp. 344–356, Mar. 2023. [Online]. Available: http://doi.org/10.1016/j.ref.2023.01.007

[42] ERB, *Energy Sector Report 2020 of Zambia.* Energy Regulatiom Board, 2020. [Online]. Available: https://upsalesiana.ec/ing34ar7r44

[43] R. S. Winton, C. R. Teodoru, E. Calamita, F. Kleinschroth, K. Banda, I. Nyambe, and B. Wehrli, "Anthropogenic influences on Zambian water quality: hydropower and land-use change," *Environmental Science: Processes & Impacts*, vol. 23, no. 7, pp. 981–994, 2021. [Online]. Available: http://doi.org/10.1039/D1EM00006C

[44] A. Levenda, I. Behrsin, and F. Disano, "Renewable energy for whom? A global systematic review of the environmental justice implications of renewable energy technologies," *Energy Research & Social Science*, vol. 71, p. 101837, Jan. 2021. [Online]. Available: http://doi.org/10.1016/j.erss.2020.101837

[45] K. J. Nyoni, A. Kaonga, G. Muyunda, H. Phiri, and A. C. Mumba, "System studies to assess preparedness of the Zambian electrical grid for

the energy transition through integration of large-scale variable renewable energy sources," *Journal of Electrical Electronics Engineering*, vol. 2, no. 2, pp. 168–186, 2022. [Online]. Available: https://upsalesiana.ec/ing34ar7r45

[46] E. Mulenga, A. Kabanshi, H. Mupeta, M. Ndiaye, E. Nyirenda, and K. Mulenga, "Techno-economic analysis of off-grid PV-Diesel power generation system for rural electrification: A case study of Chilubi district in Zambia," *Renewable Energy*, vol. 203, pp. 601–611, Feb. 2023. [Online]. Available: http://doi.org/10.1016/j.renene.2022.12.112

[47] T. Linah Ruwa, T. Ruwa, and S. Abbasoglu, "Exploration and modelling of renewable energy sources and mini-grid installation opportunities in Zimbabwe," in *16th International Conference on Clean Energy (ICCE-2018)*, 2018. [Online]. Available: https://upsalesiana.ec/ing34ar7r48

[48] M. Howells, B. Boehlert, and P. C. Benítez, "Potential climate change risks to meeting Zimbabwe's NDC goals and how to become resilient," *Energies*, vol. 14, no. 18, p. 5827, Sep. 2021. [Online]. Available: http://doi.org/10.3390/en14185827

[49] J. Akpan, H. Kumba, and O. Olanrewaju, "Sustainable energy in Zimbabwe - Status, challenges and solutions," *Renewable Energies*, vol. 2, no. 2, Jul. 2024. [Online]. Available: http://doi.org/10.1177/27533735241276201

[50] T. Murombo, *Climate Change and Energy in Zimbabwe: Towards a Low Carbon Energy Industry*, 10 2019, pp. 205–242. [Online]. Available: https://upsalesiana.ec/ing34ar7r50

[51] A. Maronga, K. J. Nyoni, P. G. Tuohy, and A. Shane, "Evaluation of PV and CSP systems to supply power in the Zimbabwe mining sector," *Energies*, vol. 14, no. 13, p. 3740, Jun. 2021. [Online]. Available: http://doi.org/10.3390/en14133740

[52] M. Ekandjo, H. Makurira, E. Mwelwa, and W. Gumindoga, "Impacts of hydropower dam operations in the Mana Pools National Park floodplains," *Physics and Chemistry of the Earth, Parts A/B/C*, vol. 106, pp. 11–16, Aug. 2018. [Online]. Available: https://doi.org/10.1016/j.pce.2018.05.009

[53] R. Spalding-Fecher, A. Chapman, F. Yamba, H. Walimwipi, H. Kling, B. Tembo, I. Nyambe, and B. Cuamba, "The vulnerability of hydropower production in the Zambezi river basin to the impacts of climate change and irrigation development," *Mitigation and Adaptation Strategies for Global Change*, vol. 21, no. 5, pp. 721–742, Nov. 2014. [Online]. Available: http://doi.org/10.1007/s11027-014-9619-7

[54] A. Salazar, "Caracterización del potencial térmico RSU, para la generación de energía eléctrica, utilizando carbonización hidrotérmica," *Ingenius, Revista de Ciencia y Tecnología*, no. 29, pp. 58–65, Jan. 2023. [Online]. Available: http://doi.org/10.17163/ings.n29.2023.05

[55] S. Obahoundje and A. Diedhiou, "Potential impacts of climate, land use and land cover changes on hydropower generation in West Africa: a review," *Environmental Research Letters*, vol. 17, no. 4, p. 043005, Mar. 2022. [Online]. Available: http://doi.org/10.1088/1748-9326/ac5b3b

[56] H. Kling, P. Stanzel, and M. Fuchs, "Regional assessment of the hydropower potential of rivers in west africa," *Energy Procedia*, vol. 97, pp. 286–293, Nov. 2016. [Online]. Available: http://doi.org/10.1016/j.egypro.2016.10.002

[57] J. Hartmann, *Manual de Entrenamiento sobre Cambio Climático e Hidroenergía.* Proyecto AICCA, Ministerio del Ambiente y Agua de Ecuador – CONDESAN, 2020. [Online]. Available: https://upsalesiana.ec/ing34ar7r57

[58] S. Naranjo-Silva and J. Álvarez del Castillo, "Hydropower: Projections in a changing climate and impacts by this "clean" source," *CienciAmérica*, vol. 10, no. 2, pp. 32–45, Jul. 2021. [Online]. Available: http://doi.org/10.33210/ca.v10i2.363

[59] B. Hamududu and A. Killingtveit, "Assessing climate change impacts on global hydropower," *Energies*, vol. 5, no. 2, pp. 305–322, Feb. 2012. [Online]. Available: https://doi.org/10.3390/en5020305

[60] S. A. Ali, S. Aadhar, H. L. Shah, and V. Mishra, "Projected increase in hydropower production in India under climate change," *Scientific Reports*, vol. 8, no. 1, Aug. 2018. [Online]. Available: http://doi.org/10.1038/s41598-018-30489-4

[61] M. Jakob, R. Soria, C. Trinidad, O. Edenhofer, C. Bak, D. Bouille, D. Buira, H. Carlino, V. Gutman, C. Hübner, B. Knopf, A. Lucena, L. Santos, A. Scott, J. C. Steckel, K. Tanaka, A. Vogt-Schilb, and K. Yamada, "Green fiscal reform for a just energy transition in Latin America," *Economics*, vol. 13, no. 1, Mar. 2019. [Online]. Available: http://doi.org/10.5018/economics-ejournal.ja.2019-17

[62] S. Alnaqbi, S. Alasad, H. Aljaghoub, A. Alami, M. Abdelkareem, and A. Olabi, "Applicability of hydropower generation and pumped hydro energy

storage in the middle East and North Africa," *Energies*, vol. 15, no. 7, p. 2412, Mar. 2022. [Online]. Available: http://doi.org/10.3390/en15072412

[63] S. Naranjo-Silva and J. Álvarez del Castillo, "The american continent hydropower development and the sustainability: A review," *International Journal of Engineering Science Technologies*, vol. 6, no. 2, pp. 66–79, Apr. 2022. [Online]. Available: http://doi.org/10.29121/ijoest.v6.i2.2022.315

[64] M. Tan-Mullins, F. Urban, and G. Mang, "Evaluating the behaviour of chinese stakeholders engaged in large hydropower projects in Asia and Africa," *The China Quarterly*, vol. 230, pp. 464–488, May 2017. [Online]. Available: http://doi.org/10.1017/S0305741016001041

[65] M. Antwi and D. D. Sedegah, *Climate Change and Societal Change—Impact on Hydropower Energy Generation*. Elsevier, 2018, pp. 63–73. [Online]. Available: http://doi.org/10.1016/b978-0-12-813016-2.00005-8

[66] D. K. Danso, B. François, B. Hingray, and A. Diedhiou, "Assessing hydropower flexibility for integrating solar and wind energy in West Africa using dynamic programming and sensitivity analysis. Illustration with the Akosombo Reservoir, Ghana," *Journal of Cleaner Production*, vol. 287, p. 125559, Mar. 2021. [Online]. Available: http://doi.org/10.1016/j.jclepro.2020.125559

[67] M. Amir and S. Z. Khan, "Assessment of renewable energy: Status, challenges, COVID-19 impacts, opportunities, and sustainable energy solutions in Africa," *Energy and Built Environment*, vol. 3, no. 3, pp. 348–362, Jul. 2022. [Online]. Available: http://doi.org/10.1016/j.enbenv.2021.03.002

[68] K. Ukoba, T. J. Kunene, P. Harmse, V. T. Lukong, and T. Chien Jen, "The role of renewable energy sources and industry 4.0 focus for Africa: A review," *Applied Sciences*, vol. 13, no. 2, p. 1074, Jan. 2023. [Online]. Available: http://doi.org/10.3390/app13021074

Scientific Paper / Artículo Científico

UNIVERSIDAD POLITÉCNICA SALESIANA ECUADOR
INGENIUS
Revista de Ciencia y Tecnología
https://doi.org/10.17163/ings.n34.2025.08
pISSN: 1390-650X / eISSN: 1390-860X

Modeling of an Electromagnetic Cannon using ATP-EMTP and ATPDraw

Modelación de un Cañón Electromagnético utilizando ATP-EMTP y ATPDraw

José Manuel Aller[1,*], Juan José Cordero Cantos[1],
Pedro José León Rojas[1], Johnny Rengifo[2]

Received: 02-04-2025, Received after review: 27-05-2025, Accepted: 29-05-2025, Published: 01-07-2025

Abstract

This study presents a computational model of an electromagnetic cannon developed using the ATP-EMTP simulation tool and its graphical interface, ATPDraw. The system features a cylindrical metallic armature that traverses multiple stages of circular coils. Employing the Voltage Behind Reactance (VBR) methodology, each coil is modeled as a dynamic equivalent circuit comprising a resistance, an inductance, and an electromotive force source. The model parameters are dynamically updated at each simulation time step based on the armature's motion. The coils are energized by pre-charged capacitors and connected through thyristors, which are triggered at specific positions of the moving armature. The model's validity is corroborated by experimental data reported in the literature, confirming the accuracy and robustness of the proposed approach. In addition to supporting the design of electromagnetic cannons, this work provides a methodological foundation for future research and practical applications in this domain.

Keywords: Electromagnetic cannon, Circular coils, Armature, Eletromagnetic Transient Program, ATPDraw

Resumen

Este trabajo presenta un modelo de cañón electromagnético desarrollado mediante la herramienta ATP-EMTP y su entorno gráfico ATPDraw. El diseño incluye varias etapas de bobinas circulares a través de las cuales se desplaza una armadura metálica cilíndrica. Utilizando la técnica VBR, cada bobina se convierte en un equivalente dinámico, conformado por una resistencia, una inductancia y una fuente de fuerza electromotriz. Estos parámetros se determinan instantáneamente según la dinámica del sistema mecánico. Las bobinas se energizan mediante condensadores inicialmente cargados y se conectan a ellas mediante tiristores, que se disparan en momentos específicos, determinados por la posición de la pieza metálica móvil denominada armadura. La validez del modelo se verifica mediante resultados experimentales reportados en la literatura, asegurando la precisión y efectividad del enfoque propuesto. Este estudio, además de contribuir al diseño de cañones electromagnéticos, también establece una metodología de análisis para futuras investigaciones y aplicaciones en este campo.

Palabras clave: cañón electromagnético, bobinas circulares, armadura, electromagnetic transient program, ATPDraw

---

[1,*] Carrera de Electricidad. Universidad Politécnica Salesiana, Ecuador
Corresponding author ✉: jaller@ups.edu.ec.

[2] Departamento de Ingeniería Eléctrica, Universidad Técnica Federico Santa María, Santiago, Chile

Suggested citation: J. M. Aller, J. J. Cordero Cantos, P. J. León Rojas y J. Renjifo, "Modeling of an Electromagnetic Cannon using ATP-EMTP and ATPDraw," *Ingenius, Revista de Ciencia y Tecnología*, N.° 34, pp. 103-115, 2025, doi: https://doi.org/10.17163/ings.n34.2025.08.

1. Introduction

The electromagnetic cannon is a device that harnesses the magnetic field generated within a solenoid, energized by an injected electric current, to accelerate metallic moving components to high velocities. This form of propulsion offers an alternative to traditional systems that rely on chemical fuels or explosives. By employing multiple stages arranged in sequence, electromagnetic cannons enable the achievement of high speeds and significant acceleration [1].

The development of electromagnetic cannons dates back to Fauchon-Villeplee's research in 1918 [2], in which he proposed the use of electrical energy for projectile acceleration. However, the technological constraints of the time, combined with the lack of adequate energy sources and materials, impeded practical implementation. Several decades later, the United States Navy revived the concept, fostering its development for military applications. Since then, advances in power electronics, novel material technologies, and sophisticated control systems have made the practical implementation of electromagnetic cannons increasingly feasible. Nonetheless, significant challenges remain, particularly in scaling the technology, enhancing its efficiency and effectiveness, and reducing associated costs.

Interest in electromagnetic cannons extends beyond military applications. Recent studies have explored their role in the propulsion of artificial satellites, offering an efficient and cost-effective alternative for launching nano-satellites [3]. In this context, Schroeder [4] introduced a model centered on space propulsion, emphasizing its potential to enhance access to space through electromagnetic launch systems.

In recent years, significant advancements have been achieved in electromagnetic cannon technology, particularly with the development of multistage synchronous induction coil systems [5–7], which enhance operational efficiency by enabling contactless projectile propulsion. The effectiveness of this approach relies on precise synchronization between the coil power supply and the projectile's motion. However, achieving such exact synchronization continues to pose a significant technical challenge.

The electromagnetic cannon model presented in this work introduces an analytical approach that integrates an electrical circuit whose parameters are dependent on the dynamics of the electromechanical system. To this end, the Voltage Behind Reactance (VBR) representation [8,9] of the governing differential equations is employed. This method derives a dynamic Thèvenin equivalent based on the system's motion-dependent equations, enabling accurate modeling of its behavior.

The model proposed in this work was implemented using the ATP-EMTP simulation tool and its graphical interface, ATPDraw. The system solves the governing differential equations through programming in MODELS modules, which calculate the parameters of the equivalent VBR circuit. These parameters are interconnected with resistances, inductances, and controlled voltage sources via signal control modules known as TACS (Transient Analysis of Control Systems) [10].

The electromagnetic behavior of the coil-armature interaction is characterized using the filament method [11], which enables the calculation of the self and mutual inductances of the coil and armature for any relative position between them. Numerical differentiation is applied to determine the positional variation of these inductances, which are essential for computing both the electric force and the electromotive force acting on the coil. Although the detailed derivation lies beyond the scope of this work, the resulting inductance values and their spatial derivatives are incorporated into the ATP-EMTP model through MODELS programming.

2. Materials and Methods

2.1. Problem Statement

The electromagnetic cannon converts electrical energy into mechanical energy through forces generated by the interaction between the magnetic field produced by the coil current and the field induced in the armature. This interaction results in the acceleration of the armature as it moves through the coil. The effectiveness of the energy conversion depends on the current, dimensions, and geometry of the coils, as well as the electromagnetic coupling with the armature circuit. The electric force acting on the armature is calculated using the principle of virtual work [12], while the resulting acceleration is determined by applying Newton's second law, accounting for resistive losses and friction.

The mutual inductance between a coil and the armature is a function of their relative position. It can be calculated with high precision using numerical techniques such as finite element analysis or the filament method [11]. These methods enable accurate modeling of the cannon's behavior and support performance optimization through simulations that account for dimensional variations.

2.2. Dynamic Model of the Electromagnetic Cannon

Figure 1 presents the equivalent circuit model of the electromagnetic cannon, which consists of a charged capacitor, a thyristor, the coil, and the moving armature. The system's dynamic behavior is governed by a set of differential equations derived from Kirchhoff's voltage law, Maxwell's equations, Newton's second law, and the principle of virtual work [13]. The resulting dynamic model is expressed as [14].

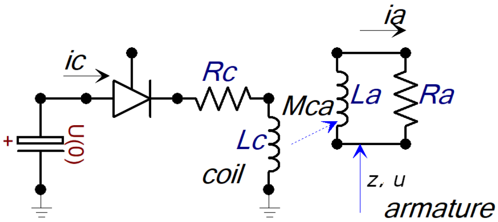

Figure 1. Equivalent circuit model of the electromagnetic cannon

$$\begin{bmatrix} v_c \\ v_a = 0 \end{bmatrix} = \begin{bmatrix} R_c & 0 \\ 0 & R_a \end{bmatrix} \begin{bmatrix} i_c \\ i_a \end{bmatrix} + \frac{d}{dt} \begin{bmatrix} \lambda_c \\ \lambda_a \end{bmatrix} \tag{1}$$

where

$$\begin{bmatrix} \lambda_c \\ \lambda_a \end{bmatrix} = \begin{bmatrix} L_c & M_{ca}(z) \\ M_{ca}(z) & L_a \end{bmatrix} \begin{bmatrix} i_c \\ i_a \end{bmatrix} \tag{2}$$

Equation (2) describes the voltage drops across the coil and the armature, incorporating both the ohmic term and the electromotive forces induced in each circuit, in accordance with Faraday's law. The mutual relationships between the flux linkages and the currents in the system are determined by applying Ampère's law and Gauss's law within the magnetic circuit.

Figure 2 provides a more detailed representation of the electromechanical system comprising the coil, the armature, and its excitation circuit. According to Newton's second law, the force acting on the armature is given by.

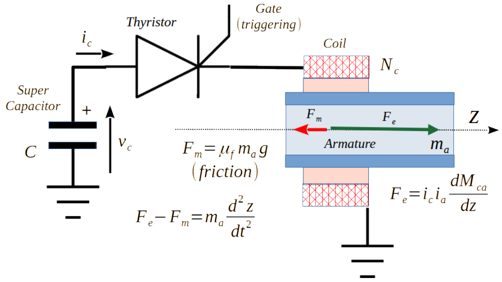

Figure 2. Electromechanical representation of the coil–armature system in the electromagnetic cannon

$$\sum F = F_e - F_m = m_a \tag{3}$$

where

$$F_e = i_c i_a \frac{\partial M_{ca}}{\partial z}; \quad F_m = \mu_f m_{ag} \tag{4}$$

and,

m_a is the mass of the armature,

μ_f is the friction coefficient,

g is the acceleration due to gravity,

The current through the coil discharges the capacitor according to the following expression:

$$C_c \frac{dv_c}{dt} = -i_c, \tag{5}$$

And due to the continuity of space, the following kinematic equation is derived:

$$\frac{dz}{dt} = u \tag{6}$$

2.3. Parameter Calculation

2.3.1. Resistance

The resistance of the coil is calculated using the following expression:

$$R_c = \rho \frac{L}{A} = \rho \frac{\pi N D}{\pi r^2} = \rho \frac{N D}{r^2}, \tag{7}$$

where $\rho = 1.68 \times 10^{-8} \Omega \cdot m$ is the resistivity of copper, N is the number of turns of the coil, D is the diameter of the circular coil, and r is the radius of the copper cross-section.

2.3.2. Friction

The dynamic friction coefficient μ_d is determined from the angle α of the inclined plane at which the moving part begins to slide [15].

$$\mu_d = \tan \alpha. \tag{8}$$

2.3.3. Dimensions of the Coil and Armature

The dimensions of the coil and armature used in this study are based on the work of Niu [7], who analyzed the timing of the shot as the armature travels through the coil. The electromagnetic cannon developed by Niu features certain dimensional variations compared to the present model. Figure 3 and Table 1 present the dimensions adopted in this work. Figure 3 illustrates a cross-sectional view at a representative azimuthal position around the z-axis, which serves as the axis of symmetry. The positions of two circular coils, each with 55 turns, are shown in red to indicate their copper composition. The solid tube representing the armature, shown in blue, moves within the coils and is assumed to be made of aluminum.

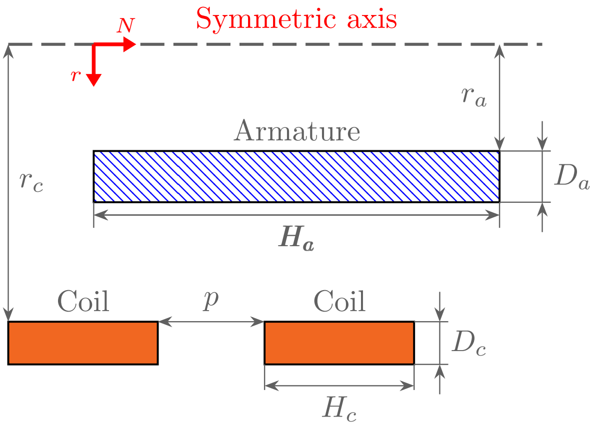

Figure 3. Geometric dimensions of the coils and armature in the electromagnetic cannon.

Table 1. Geometric and electrical parameters of the electromagnetic cannon

	Parameters	**Values**
Coil	r_c	10.5cm
	H_c	6cm
	p	10.5mm
	N	55
Armature	m_a	1.46kg
	r_a	8cm
	H_a	19cm
	D_a	1cm
External Excitation Circuit	C	4mF
	U_0	1.87kV
	R_c	20mΩ

2.3.4. Mutual Inductance Between the Coil and the Armature

The mutual inductances between two concentric rings separated by a distance z are calculated using the following expression:

$$M_{ij} = \frac{2\mu_0\sqrt{R_i R_j}}{k}\left[\left(1 - \frac{k^2}{2}\right)K(k) - E(k)\right], \tag{9}$$

where,

$$k^2 = \frac{4R_i R_j}{(R_i + R_j)^2 + c^2}, \tag{10}$$

$K(k)$ is the complete elliptic integral of the first kind, and $E(k)$ is the complete elliptic integral of the second kind.

To determine the mutual inductance, it is necessary to compute the total magnetic flux linkage between all filaments and divide it by the current that generates this flux [11, 16].

$$M_{ac} = \frac{\lambda_{ac}}{I_{\text{coil}}} = \frac{N_{\text{coil}} N_{\text{arm}}}{n\ m\ v\ w}\sum_j \sum_i M_{ij} \tag{11}$$

The mutual inductance between the coil and the armature is calculated by accounting for the varying current densities in each filament of the armature. The equivalent inductance between the coil and the armature is then obtained using matrices of mutual and self-inductances, followed by the application of Krön reduction [17]. Consequently, the self-inductance and the mutual inductance of the armature are given by:

$$[L_{aa}] = \begin{bmatrix} L_f & M_{a1a2} & \cdots & M_{a1(v\,w)} \\ M_{a2a1} & L_f & \cdots & M_{a2(v\,w)} \\ \vdots & \vdots & \ddots & \vdots \\ M_{a(v\,w)a1} & M_{a(v\,w)a2} & \cdots & L_f \end{bmatrix} \tag{12}$$

where:

$n\,m$ is the dimension of the coil filament matrix, and

$v\,w$ is the dimension of the filament matrix representing the armature. Since all armature filaments are short-circuited, the application of Krön reduction enables the determination of the self-inductance of the equivalent circuit.

2.3.5. Self-Inductance of the Coil

The self-inductance of the coil is calculated using an expression derived from the Biot–Savart law, based on the numerical evaluation of complete elliptic integrals for a solenoidal geometry [18]. The expression is given by:

$$L_{\text{coil}} = \mu_0 \left(\frac{N_{\text{coil}}}{l_{\text{coil}}}\right)^2 \left\{ l_{\text{coil}}^4 + \frac{4L_{\text{coil}}^2 R_{\text{coil}}^2}{3D} K(k_{\text{coil}}) \right\} + \ldots$$

$$\left\{ (+4R_{\text{coil}}^2 - L_{\text{coil}}^2)\,\frac{D}{3} E(k_{\text{coil}}) - \frac{8}{3} R_{\text{coil}}^3 \right\}, \tag{13}$$

where,

$$k_{\text{coil}} = \sqrt{\frac{4R_{\text{coil}}^2}{D}} \quad \text{and} \quad D = \sqrt{4R_{\text{coil}}^2 + l_{\text{coil}}^2}, \tag{14}$$

with $K(k)$ as the complete elliptic integral of the first kind and $E(k)$ as the complete elliptic integral of the second kind.

2.3.6. Self-Inductance of an Armature Filament:

The self-inductance of an individual filament is calculated using Maxwell's expression, which considers the mutual inductance between two identical circular filaments separated by the Geometric Mean Distance (GMD) [19]. The GMD is defined as:

$$\mathrm{GMD} = e^{-\frac{1}{4}} r = 0.7788 r \tag{15}$$

$$L_{ai} = \mu_0 r_i \left((1 + 0.1137 \frac{R_i^2}{r_i^2}) \ln \left(\frac{8 r_i}{R_i} \right) \right) + \ldots \\ + \left(-0.0095 \frac{R^2}{r^2} - 1.75 \right) \tag{16}$$

2.3.7. VBR Model of the Cannon

The VBR model [9,14] provides an electrical and mathematical representation of the electromagnetic cannon, effectively capturing how the coil's equivalent resistance and inductance vary as the projectile traverses its trajectory. These variations are governed by the projectile's position, since the proximity of the metallic armature alters the circuit's impedance.

From (2), the flux linkage of the armature λ_a is calculated as,

$$\lambda_a = M_{ca}\left(z\right) i_c + L_a i_a, \tag{17}$$

obtaining i_a from (17),

$$i_a = \frac{\lambda_a - M_{ca}\left(z\right) i_c}{L_a}, \tag{18}$$

and substituting (18) into the armature equation (1) yields,

$$\frac{\lambda_a}{t} = -\frac{R_a}{L_a} \lambda_a + \frac{R_a}{L_a} M_{ca} i_c. \tag{19}$$

Equation (19) enables the computation of the armature flux linkage λ_a through numerical integration.

Substituting Equations (18) and (19) into the coil expression in Equation (1) results in:

$$v_c = R_{eq}\, i_c + L_{eq} \frac{i_c}{t} + e_e \tag{20}$$

$$R_{eq} = R_c + \frac{M_{ca}^2}{L_a^2} R_a \tag{21}$$

$$L_{eq} = L_c - \frac{M_{ca}^2}{L_a} \tag{22}$$

$$e_e = \left(v \frac{1}{L_a} \frac{dM_{ca}}{dz} - \frac{M_{ca} R_a}{L_a^2} \right) \lambda_a - 2v \frac{M_{ca}}{L_a} \frac{dM_{ca}}{dz} i_c \tag{23}$$

And from the principle of virtual work,

$$F_e = i_a\, i_c\, \frac{dM_{ca}}{dz} \tag{24}$$

Figure 4 illustrates the VBR model developed for the electromagnetic cannon, derived from expressions (21), (22), and (23). This model represents a dynamic Thèvenin equivalent that facilitates simulation within circuit analysis tools such as ATP-EMTP, Simulink, and PSIM, among other specialized platforms.

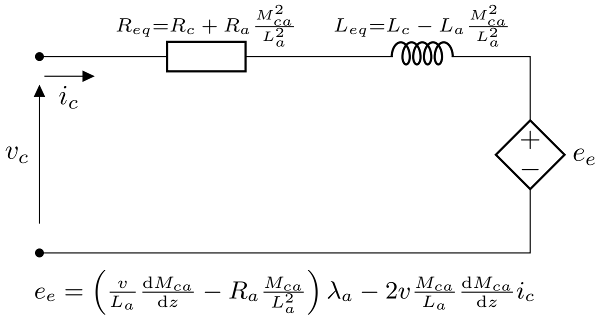

Figure 4. VBR-based equivalent circuit representing the electromagnetic interaction between the coil and the armature

2.4. Modeling in ATPDraw

The ATPDraw program is a human–machine graphical interface that facilitates the efficient use of the ATP-EMTP simulation tool. Within this environment, users can integrate complex electrical circuits, control systems (TACS), and programmable components written in the MODELS language. To simulate the behavior of the electromagnetic cannon, these three components are combined. The electrical circuit, comprising the capacitor, thyristor, and coil, is modeled using ATP-EMTP's native circuit elements. The controls for the sources and the thyristor firing are activated through TACS modules. Additionally, system dynamics and the position-dependent calculation of inductances are implemented using MODELS programming.

2.5. Equivalent Circuit of the Electromagnetic Cannon

Figure 5 shows the circuit implemented in ATPDraw to model a single stage of the electromagnetic cannon. The circuit includes a capacitor used to store the energy required for firing, a thyristor triggered via TACS, and its associated snubber circuit to mitigate transient overvoltages. Additionally, the equivalent resistance R_{eq}, inductance L_{eq}, and electromotive force E_{eq} are represented as variable components, whose instantaneous values are determined through dynamic computation using MODELS programming.

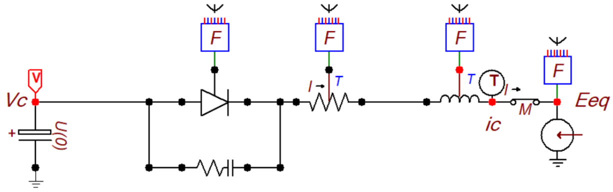

Figure 5. Equivalent circuit based on the VBR model

2.5.1. Modeling of Mutual Inductance

The mutual inductance was modeled using the filament method [11], in which the coil was discretized into $n \times m$ segments and the armature into $v \times w$ circular elements. Each segment possesses a self-inductance as defined in equation (16), while mutual inductances between segments are computed using equation (9). These expressions were implemented in a MATLAB script to evaluate the electromagnetic coupling between the coil and the armature for arbitrary relative positions along their axes. Figure 6 illustrates a representative position z at which the inductances are calculated; blue markers denote coil filaments, and red markers represent those of the armature.

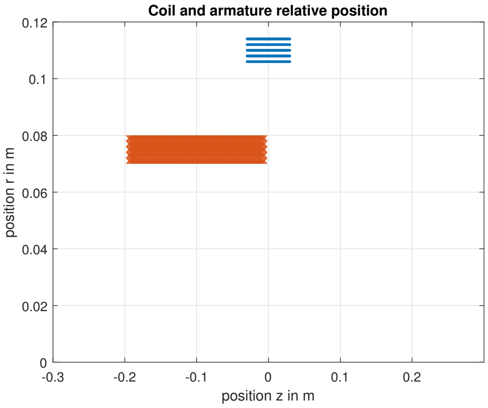

Figure 6. Representative relative position between coil and armature for mutual inductance calculation

Starting from the inductance calculations, where the electromagnetic coupling between the coil and the armature is evaluated at each separation distance between their centers, the mutual inductance as a function of position z is obtained, as illustrated in Figure 7. By applying numerical differentiation to this position-dependent mutual inductance, its spatial derivative is determined, as shown in Figure 8.

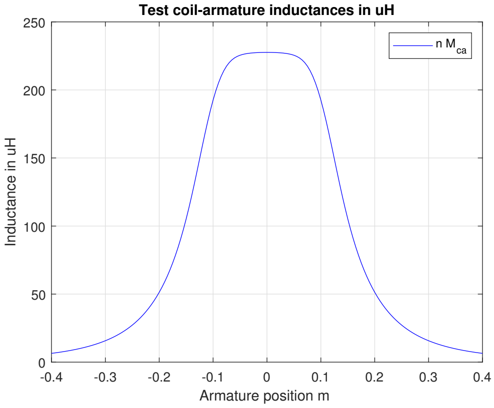

Figure 7. Mutual inductance between the coil and the armature as a function of position z, obtained from equation (11).

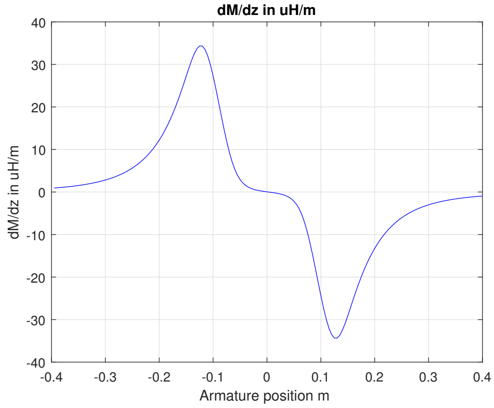

Figure 8. Spatial derivative of the mutual inductance between the coil and the armature as a function of position z

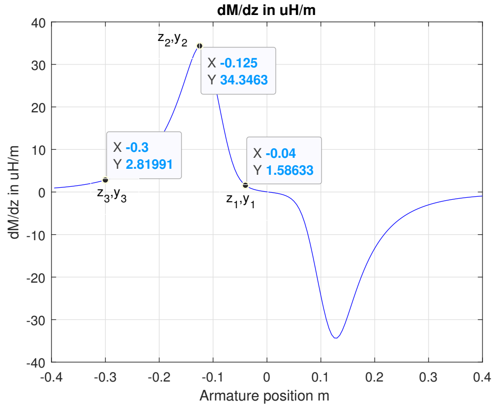

Figure 9. Extraction of key data points for graphical reconstruction

The behavior of the derivative of the mutual inductance with respect to position is subsequently reconstructed within the ATPDraw programming interface. To this end, key data points are extracted from the curve in Figure 8, as illustrated in Figure 9. The derivative is modeled using three distinct functions: a horizontal line between zero and z_1, a line between z_1 and z_2, and an exponential decay between z_2 and infinity. After defining these segments based on the selected points, they are integrated to generate a continuous representation of the mutual inductance as a function of position.

2.6. Modeling of the First-Stage Coil–Armature System

The first model developed aims to replicate the interaction between a coil and the armature. To achieve this, an electrical circuit is programmed in ATPDraw, comprising a pre-charged capacitor, a thyristor with its corresponding overvoltage protection circuit, the equivalent resistance R_{eq} as defined by equation (21), the equivalent inductance L_{eq} from equation (22), and the electromotive force e_e according to equation (23).

These three quantities, R_{eq}, L_{eq}, and e_e, are dynamically computed using the MODELS module dm-m, which takes as input the armature's position, velocity, and the current in the coil. Additionally, this module calculates the electric force F_e acting on the armature. The resulting force is fed back into the MODELS module *dinamica*, which numerically integrates equations (19), (3), (5), and (6) to determine the armature's position z, velocity u, and flux linkage λ_a.

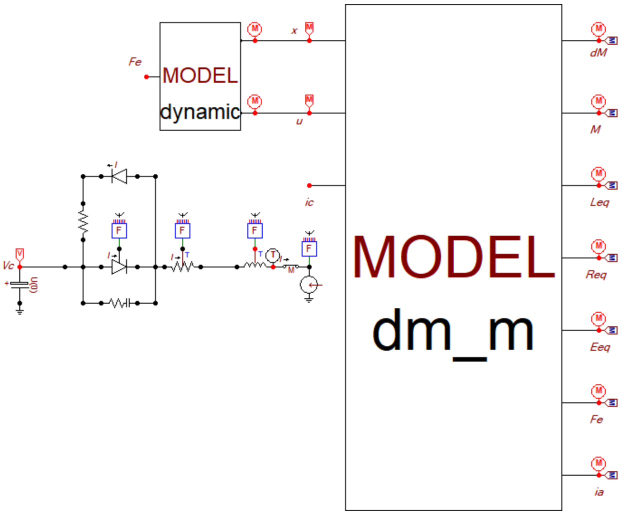

Figure 10. ATPDraw circuit used to model the first-stage coil–armature interaction

Figures 11, 12, and 13 present the simulation results for the armature velocity u, the electric force F_e acting on it, and the coil current, respectively.

Figure 11 illustrates the acceleration profile of the armature resulting from the electromagnetic force generated by current injection into the coil, as depicted in Figure 12. The electric force initially exhibits a positive peak, followed by a negative component of lower magnitude, leading the armature velocity to reach a maximum before gradually decreasing.

Figure 13 shows the behavior of the coil current. While the current follows a sinusoidal trend, characteristic of oscillations between the capacitor and the coil, it is notably influenced by the armature's motion. As the armature traverses the coil, it alters the equivalent inductance and induces an electromotive force, which delays the current's zero crossing and the subsequent deactivation of the excitation thyristor.

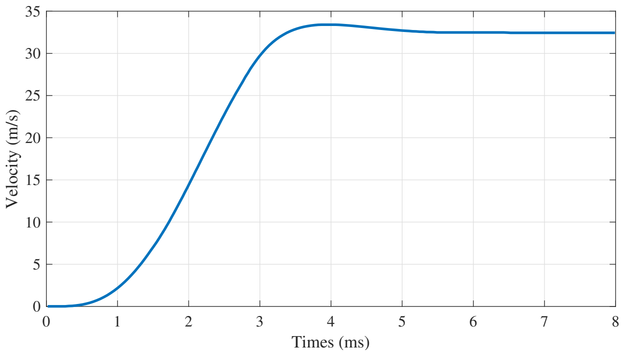

Figure 11. Velocity u of the armature for one stage cannon

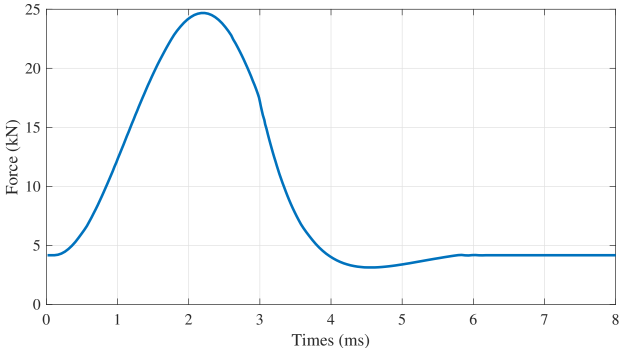

Figure 12. Electric force F_e on the armature

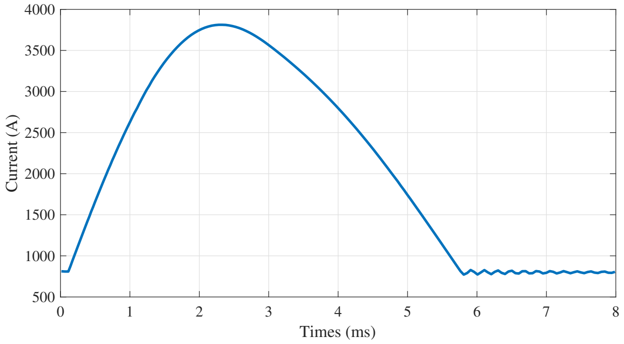

Figure 13. Current in the coil i_c

Figure 14 illustrates the reversal of current in the armature circuit relative to the coil current, a phenomenon arising from the electromagnetic action–reaction process. Despite the reversal, the system continues to exert force on the armature, contributing to its acceleration during this interval.

Figure 15 shows the voltage behavior across the capacitor when it is connected to the coil. The system exhibits an $L - C$ type oscillation that begins at approximately 1800 V and reaches a minimum of –1500V. This voltage swing reflects both the transfer of energy to the armature and the inherent energy losses in the electrical circuit.

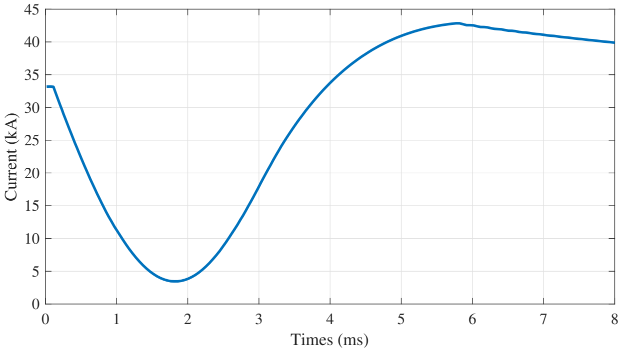

Figure 14. Armature current i_a

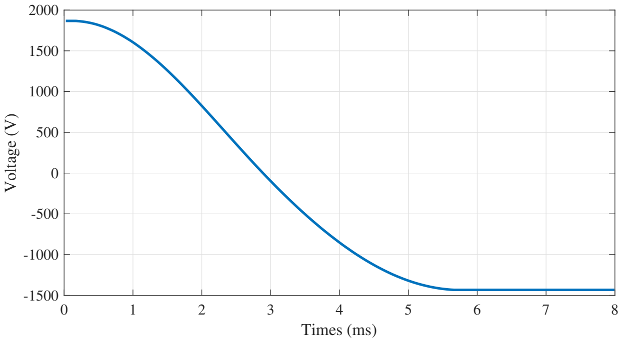

Figure 15. Voltage across the capacitor v_c during the first-stage electromagnetic cannon discharge

2.7. Cannon Model with Multiple Stages

The implementation of a multistage electromagnetic cannon involves replicating the initial single-stage model across successive stages. Each stage requires feedback of the coil current i_{ci} and the corresponding mutual inductance M_{cai}. The total electromagnetic force is computed by summing the contributions from all stages, a process carried out using a TACS module.

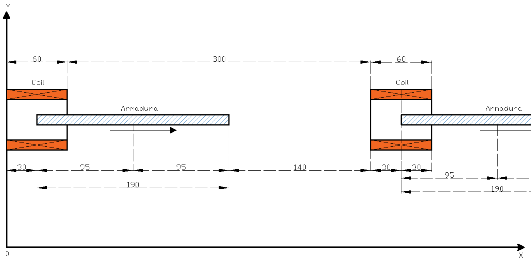

Figure 16. Definition of parameters and positions of the coils and the armature

To trigger the thyristors, it is necessary to identify the specific positions of the armature at which the activation signals are applied. The first thyristor is triggered at a predefined moment, positioning the armature optimally, typically at the midpoint of the coil when its velocity is zero. Subsequent stages are activated based on the real-time position of the armature. Improper timing of thyristor activation can negatively impact the final velocity of the projectile. A common activation criterion is to fire the thyristor when the rear end of the armature aligns with the midpoint of each coil. However, as the armature's velocity increases, advancing the firing position can enhance energy conversion efficiency. The selected trigger positions for each stage are summarized in Table 2. These values serve as reference points for coil activation and can be adjusted to optimize the system's final velocity.

Table 2. Geometric and electrical parameters of the electromagnetic cannon

Coil	Position calculation	Triggering position
1	$z + 95 - 390$	$z - 295\,mm$
2	$z + 95 - 750$	$z - 655\,mm$
3	$z + 95 - 1110$	$z - 1015\,mm$
4	$z + 95 - 1470$	$z - 1375\,mm$
5	$z + 95 - 1830$	$z - 1925\,mm$

Figure 17 presents the complete model of the electromagnetic cannon configured with five stages, constructed following the same methodology employed in the single-coil model. In this multistage configuration, an individual electrical circuit is replicated for each stage, along with corresponding MODELS modules to compute the mutual inductances and electric forces generated by each coil. Additionally, a dynamic module is employed to integrate the equations of motion and calculate the armature's flux linkage. This module receives the cumulative effect of the instantaneous forces generated by each coil of the electromagnetic cannon.

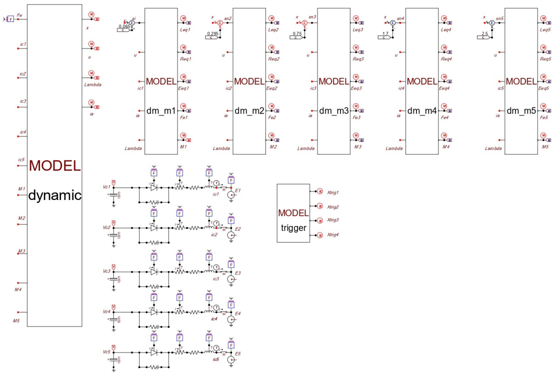

Figure 17. Five-stage Electromagnetic Cannon

Figures 18, 19, and 20 present the simulation results for the five-stage electromagnetic cannon model, depicting the armature velocity u, the electric forces F_{ei} exerted by each coil, and the corresponding coil currents i_{ci}. The velocity profile of the armature exhibits a stepped behavior, attributable to the spatial separation between the coils.

Figure 18 illustrates five distinct acceleration phases, each corresponding to the armature's passage through a coil. These accelerations result from the electromagnetic forces generated by the coils, as shown in Figure 19. Each acceleration phase resembles the behavior observed in the single-stage case (Figures 11 and 12); however, the armature's velocity progressively increases with each stage. This progression modifies the acceleration dynamics due to the varying electromotive forces induced in the coils.

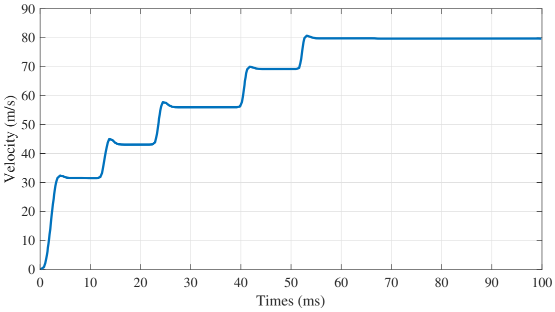

Figure 18. Velocity u during the five stages

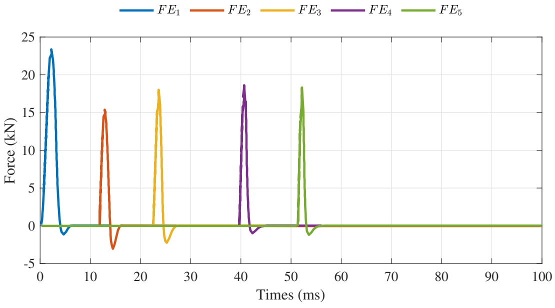

Figure 19. Electric force of the five stages

Figure 20 shows the evolution of the currents in each coil as the armature's velocity increases. At higher speeds, a noticeable change in shape occurs because the armature exits the coil entirely before the current can reach zero, thereby preventing the proper deactivation of the corresponding thyristor.

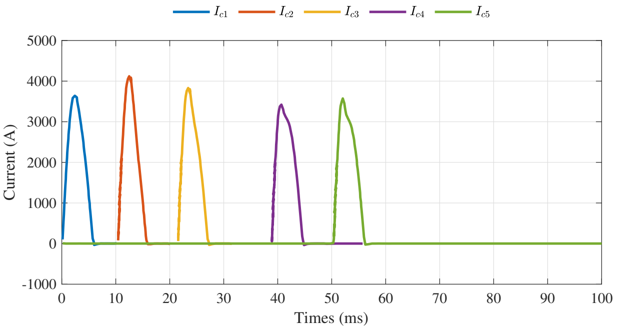

Figure 20. Current in the coil during the five stages

Figures 22 and 21 present the simulation results for the armature current and the voltages across the capacitors in each stage of the converter. The observed behavior is similar to that of a single-coil system; however, in the multistage configuration, the armature current exhibits an initial value at each triggering event. This initial current influences the generation of electromagnetic force and, consequently, the acceleration of the moving armature.

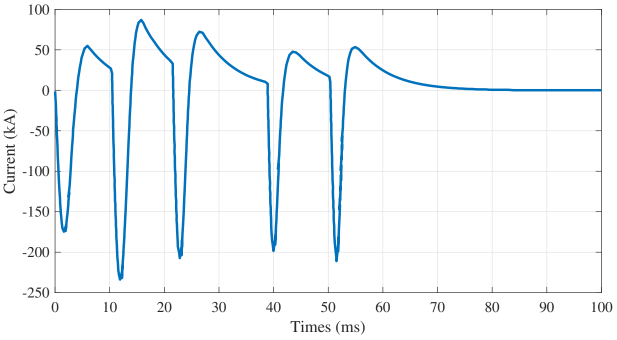

Figure 21. Armature current of the five stages.

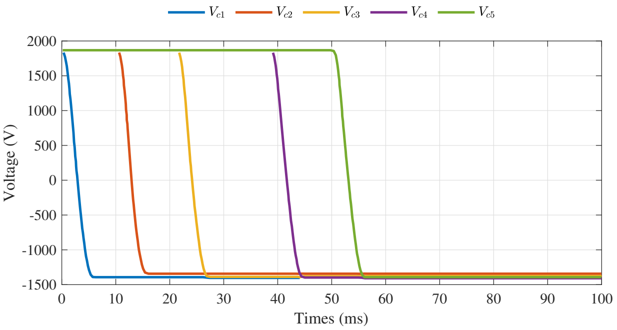

Figure 22. Capacitor voltage in the five stages

3. Results and discussion

This section summarizes the simulation results obtained using the developed model for both the single-stage and five-stage electromagnetic cannons. Additionally, the outcomes are compared with experimental data reported in the literature for a five-stage cannon [7].

3.1. Results of the First Stage

Table 3 presents the steady-state or peak values of the key variables obtained for the first-stage electromagnetic cannon model.

Table 3. Results of the first stage

Variable	Results
Velocity	$32.47\,m/s$
I_c	$3769.3\,A$
I_a	$56.8\,kA$
F_e	$24.64\,kN$

In the specific case of velocity, the steady-state value reported in Table 3 corresponds to the final value attained after the peak has been surpassed. This slight decline is attributed to the negative electric force that emerges toward the end of the coil's current pulse.

The obtained results are consistent in both form and magnitude with simulations and experiments reported in previous studies [7].

3.2. Results of the Multiple Stages

Table 4 presents the steady-state or peak values of the key variables for the five-stage electromagnetic cannon. In this configuration, the velocity increases in a stepwise manner across each stage, ultimately reaching 79.7 m/s, owing to the precise synchronization of the thyristor triggers. While this final velocity could be improved by adjusting the firing positions, such optimization lies beyond the scope of the present study. In the first stage, firing is scheduled based on time, whereas in subsequent stages it is controlled by the armature's position using a MODELS block with a triggering mechanism. The firing is slightly advanced to minimize errors and enhance energy transfer.

The relationship between velocity and force shown in Figure 19 confirms that the force peaks align with the velocity increments, underscoring the critical role of precise switching activation. A summary of the corresponding results is provided in Table 4.

Table 4. Results of each stage of the process

Stage	Variable	Result
Stage 1	Velocity	$32.47\,m/s$
	I_c	$3769.3\,A$
	I_a	$56.8\,kA$
	F_e	$24.64\,kN$
Stage 2	Velocity	$44.32\,m/s$
	I_c	$4169.23\,A$
	I_a	$88.91\,kA$
	F_e	$15.516\,kN$
Stage 3	Velocity	$58.032\,m/s$
	I_c	$3879\,A$
	I_a	$73.124\,kA$
	F_e	$18.174\,kN$
Stage 4	Velocity	$70\,m/s$
	I_c	$3467.4\,A$
	I_a	$48.189\,kA$
	F_e	$18.797\,kN$
Stage 5	Velocity	$80\,m/s$
	I_c	$3601.4\,A$
	I_a	$54.06\,kA$
	F_e	$17.9\,kN$

3.3. Comparison with Experimental Results

Experimental results for a five-stage electromagnetic cannon with dimensions similar to those used in this study are presented in [7]. The system specifically focuses on optimizing the firing synchronization of the electromagnetic cannon. The results from Niu's experiment are reproduced in Table 5.

Table 5. Results of coil current and experimental velocity

Stage	Results
Stage 1	$I_c \approx 5.66\,kA$
Stage 2	$I_c \approx 6.82\,kA$
Stage 3	$I_c \approx 7.38\,kA$
Stage 4	$I_c \approx 8.11\,kA$
Stage 5	$I_c \approx 9\,kA$
Velocity	$88\,m/s$

The comparison between Niu's model and the one developed in this work reveals that the coil currents in the proposed model are lower and exhibit a pulsating profile, whereas in Niu's model [7], the currents increase progressively. The present model reaches a final velocity of 80 m/s, slightly below the 88 m/s achieved in Niu's system. This difference may be attributed to the higher efficiency of Niu's configuration; however, both models demonstrate comparable performance in terms of energy conversion. Further improvements could be made to the proposed model and thyristor firing system, particularly in the optimization of switching times.

3.4. Discussion

3.4.1. Evaluation of the Method Used

The modeling approach employed in this work provides a robust and reliable tool for designing electromagnetic cannons. It demonstrates strong agreement with experimental data, exhibiting discrepancies of less than 10% in critical measurable variables such as coil currents, projectile velocity, and capacitor voltages. Other parameters, including the acceleration force and armature currents, are inherently difficult to measure directly; however, they can be effectively estimated through the predictive capabilities of the proposed model.

3.4.2. Evaluation of the VBR Method

The Voltage Behind Reactance (VBR) method provides an effective framework for representing the electromagnetic behavior of the cannon through equivalent electrical circuits, transforming the coil and armature into a voltage source behind a reactance. Unlike its conventional application in induction machines, where the reactance remains constant and only the induced electromotive force varies, this implementation requires real-time adjustments to both resistance and equivalent inductance as functions of the projectile's position z. Consequently, it becomes necessary to simultaneously solve the coupled electrical and mechanical differential equations, given their strong interdependence.

3.4.3. Evaluation of the ATP-EMTP Tool

The ATP-EMTP simulation tool, along with its graphical interface ATPDraw, proved highly effective for modeling the electromagnetic cannon. These programs enable fast and efficient computation by employing the trapezoidal integration method, which models system components as networks of conductances powered by current sources at each integration step.

Given the complexity of the electromagnetic system, accurately simulating the behavior of self and mutual inductances requires the use of the filament method. To incorporate these results into the simulation, functional approximations or tabulated values are implemented within the MODELS programming environment in ATP-EMTP. In this work, precise outcomes were achieved by selecting three representative points from the derivative profile of mutual inductance between the coil and the armature. These points were then used to perform the analytical integration of these functions into MODELS programs for each coil.

The system dynamics were also successfully modeled within a MODELS module by integrating the system's state variables to compute the armature's position, velocity, and flux linkage.

3.4.4. Challenges associated with electromagnetic cannon development

The development of electromagnetic cannons presents several critical challenges that must be addressed to enable their practical deployment:

- They require high-power, compact energy sources.
- Significant energy losses, primarily converted into heat, must be efficiently managed to prevent thermal conditions that exceed the limits of structural materials.
- There are mechanical and thermal stress limits that current materials cannot exceed.
- The high projectile velocities introduce challenges for the control systems across the entire structure.
- The electromagnetic fields generated can interfere with control and communication systems, potentially disrupting their operation.
- High development and implementation costs may limit the scalability and practical adoption of these technologies.
- The reaction forces generated in the coils, comparable in magnitude to those acting on the projectile, require support systems capable of absorbing substantial mechanical stress.

4. Conclusions

This study presents the development of a computational model of an electromagnetic cannon, constructed using an analytical–numerical methodology for the calculation of self and mutual inductances in both the coils and the armature. The inductance profiles were implemented within the ATP-EMTP simulation environment using linear and exponential approximations.

The proposed model is structured into four interconnected subsystems: 1. The representation of the electrical circuit. 2. The integration of the differential equations governing the dynamic behavior of key state variables. 3. A module responsible for computing the inductances and their derivatives, as well as the electromagnetic force exerted on the armature by each coil. 4. A triggering module that activates each thyristor at appropriate armature positions. This architecture is scalable to any number of stages and emulates, with high fidelity, the principal components and dimensions of electromagnetic cannon systems.

Simulation results derived from this model exhibit deviations of less than 10% compared to experimental data reported in [7], demonstrating the approach's accuracy and robustness. Coupled with the user-friendly programming environment and visual interface offered by ATP-EMTP and ATPDraw, the proposed modeling framework constitutes a powerful tool for the analysis and design of electromagnetic launch systems. These systems hold growing relevance in diverse application areas, including military technologies, aerospace propulsion, and plasma generation for advanced scientific research.

Acknowledgments

The authors would like to express their gratitude to the Universidad Politécnica Salesiana and the Energy Research Group GIE for their invaluable support in the development and execution of this work.

Contributor Roles

- **José Manuel Aller Castro:** Conceptualization, formal analysis, investigation, methodology, supervision, writing – original draft.

- **Juan José Cordero Cantos:** Data curation, formal analysis, investigation, software, validation, visualization.

- **Pedro José León Rojas:** Data curation, formal analysis, software, validation, visualization.

- **Johnny Rengifo:** Conceptualization, methodology, visualization, writing – original draft, writing – review & editing.

References

[1] K. McKinney and P. Mongeau, "Multiple stage pulsed induction acceleration," *IEEE Transactions on Magnetics*, vol. 20, no. 2, pp. 239–242, Mar. 1984. [Online]. Available: https://doi.org/10.1109/TMAG.1984.1063089

[2] I. McNab, "Early electric gun research," *IEEE Transactions on Magnetics*, vol. 35, no. 1, pp. 250–261, 1999. [Online]. Available: https://doi.org/10.1109/20.738413

[3] E. N. Zapico, G. J. Torresán, and R. J. Garay, "Análisis estructural preliminar de un nanosatélite lanzado por cañón electromagnético," in *Mecánica Computacional*, vol. XXIV, no. 12, Córdoba, Argentina, Nov. 2005, pp. 2075–2085. [Online]. Available: https://upsalesiana.ec/ing34ar10r3

[4] J. Schroeder, J. Gully, and M. Driga, "Electromagnetic launchers for space applications," *IEEE Transactions on Magnetics*, vol. 25, no. 1, pp. 504–507, 1989. [Online]. Available: https://doi.org/10.1109/20.22590

[5] X. Niu, K. Liu, Y. Zhang, G. Xiao, and Y. Gong, "Multiobjective optimization of multistage synchronous induction coilgun based on NSGA-II," *IEEE Transactions on Plasma Science*, vol. 45, no. 7, pp. 1622–1628, Jul. 2017. [Online]. Available: https://doi.org/10.1109/TPS.2017.2706522

[6] X. Niu, W. Li, and J. Feng, "Nonparametric modeling and parameter optimization of multistage synchronous induction coilgun," *IEEE Transactions on Plasma Science*, vol. 47, no. 7, pp. 3246–3255, Jul. 2019. [Online]. Available: https://doi.org/10.1109/TPS.2019.2918157

[7] X. Niu, L. Chen, Y. An, and Y. Hu, "Research on critical trigger criterion of multistage synchronous induction coilgun," *IEEE Transactions on Plasma Science*, vol. 51, no. 9, pp. 2667–2675, Sep. 2023. [Online]. Available: https://doi.org/10.1109/TPS.2023.3306329

[8] L. Wang, J. Jatskevich, and S. D. Pekarek, "Modeling of induction machines using a voltage-behind-reactance formulation," *IEEE Transactions on Energy Conversion*, vol. 23, no. 2, pp. 382–392, Jun. 2008. [Online]. Available: https://doi.org/10.1109/TEC.2008.918601

[9] J. M. Aller, J. A. Restrepo, and J. C. Viola, "Voltage behind reactance model of induction machines using ATPDraw and MODELS," in *2021 IEEE Fifth Ecuador Technical Chapters Meeting (ETCM)*. IEEE, Oct. 2021. [Online]. Available: http://doi.org/10.1109/ETCM53643.2021.9590817

[10] H. K. Høidalen, L. Prikler, and J. Hall, "Atpdraw-graphical preprocessor to atp, windows version," in *Proceedings of International Conference on Power Systems Transients, IPST*, 1999, pp. 20–24. [Online]. Available: https://upsalesiana.ec/ing34ar10r10

[11] L. Shoubao, R. Jiangjun, P. Ying, Z. Yujiao, and Z. Yadong, "Improvement of current filament method and its application in performance analysis of induction coil gun," *IEEE Transactions on Plasma Science*, vol. 39, no. 1, pp. 382–389, Jan. 2011. [Online]. Available: http://doi.org/10.1109/TPS.2010.2047276

[12] D. C. White, *Electromagnetic energy conversion.* Wiley, 1959. [Online]. Available: https://upsalesiana.ec/ing34ar10r12

[13] J. M. Aller, “Máquinas eléctricas rotativas: Introducción a la teoría general,” *Editorial Equinoccio*, 2006. [Online]. Available: https://upsalesiana.ec/ing34ar10r13

[14] J. M. Aller, J. A. Restrepo, J. C. Viola, and J. R. Mayor, “Simplified voltage behind reactance model for the six-phase open-end salient pole PMSM,” in *2020 International Conference on Electrical Machines (ICEM).* IEEE, Aug. 2020, pp. 2216–2221. [Online]. Available: https://doi.org/10.1109/ICEM49940.2020.9270701

[15] Wikipedia. (2020, Apr.) Coefficient of friction. Wikipedia, the free encyclopedia. Accessed: 2025-06-12. [Online]. Available: https://upsalesiana.ec/ing34ar10r15

[16] W. G. Hurley, M. C. Duffy, J. Zhang, I. Lope, B. Kunz, and W. H. Wolfle, “A unified approach to the calculation of self- and mutual-inductance for coaxial coils in air,” *IEEE Transactions on Power Electronics*, vol. 30, no. 11, pp. 6155–6162, Nov. 2015. [Online]. Available: http://doi.org/10.1109/TPEL.2015.2413493

[17] G. Kron, *A short course in tensor analysis for electrical engineers*, I. Dover Publications, Ed. CONSTABLE and CO, LTD, 1959. [Online]. Available: https://upsalesiana.ec/ing34ar10r17

[18] E. Rosa and F. Grover, *Formulas and tables for the calculation of mutual and self-inductance.* US Government Printing Office, 1912. [Online]. Available: https://upsalesiana.ec/ing34ar10r18

[19] R. Weaver, *Geometric Mean Distance - Its Derivation and Application in Inductance Calculations.* Electronbunker.ca, 06 2016. [Online]. Available: https://upsalesiana.ec/ing34ar10r19

Scientific Paper / Artículo Científico

UNIVERSIDAD POLITÉCNICA SALESIANA ECUADOR
INGENIUS
Revista de Ciencia y Tecnología
https://doi.org/10.17163/ings.n34.2025.09
pISSN: 1390-650X / eISSN: 1390-860X

Exploring deep generative models for improved data generation in hypertrophic cardiomyopathy

Exploración de modelos generativos profundos para una mejor generación de datos en la miocardiopatía hipertrófica

Swarajya Madhuri Rayavarapu[1,*], Gottapu Sasibhushana Rao[1]

Received: 06-08-2024, Received after review: 05-06-2025, Accepted: 10-06-2025, Published: 01-07-2025

Abstract

Data generation strategies are essential for addressing the challenge of limited training data in deep learning-based medical image analysis, particularly for hypertrophic cardiomyopathy (HCM) using magnetic resonance imaging (MRI). Unlike traditional augmentation techniques, deep generative models can synthesize novel and diverse MRI images, enriching the training datasets. This study evaluates several generative models, including Variational Autoencoders (VAEs), Generative Adversarial Networks (GANs), Deep Convolutional GANs (DCGANs), Auxiliary Classifier GANs (ACGANs), InfoGANs, and Diffusion Models, using the Structural Similarity Index Measure (SSIM) and Cross-Correlation Coefficient (CC) to assess image quality and structural fidelity. While VAEs demonstrated limitations such as noticeable noise and blurriness, GAN-based models, particularly DCGANs and ACGANs, generated higher-quality and anatomically accurate images. Diffusion models achieved the highest image fidelity among all the methods evaluated, but required longer generation times. These findings underscore the trade-off between image quality and computational efficiency and highlight the potential of deep generative models to augment MRI datasets, thereby improvingdeep learning applications for HCM diagnosis.

Keywords: Data Generation, Diffusion models, Generative Adversarial networks, Variational autoencoders.

Resumen

Las estrategias de generación de datos son fundamentales para superar el desafío de los datos de entrenamiento limitados en el análisis de imágenes médicas basado en aprendizaje profundo, en particular para la miocardiopatía hipertrófica (HCM) mediante resonancia magnética (MRI). A diferencia de los métodos de aumento tradicionales, los modelos generativos profundos pueden sintetizar imágenes de MRI novedosas y diversas. Este estudio evalúa múltiples modelos generativos: autocodificadores variacionales (VAE), redes generativas adversarias (GAN), GAN convolucionales profundas (DCGAN), GAN con clasificador auxiliar (ACGAN), InfoGAN y modelos de difusión, utilizando el índice de similitud estructural (SSIM) y el coeficiente de correlación cruzada (CC) para evaluar la calidad de imagen y la fidelidad estructural. Si bien los VAE mostraron limitaciones como el ruido y la borrosidad, los modelos basados en GAN, especialmente DCGAN y ACGAN, produjeron imágenes de mayor calidad y precisión anatómica. Los modelos de difusión lograron la mayor fidelidad de imagen, aunque a expensas de tiempos de generación más prolongados. Estos resultados destacan la compensación entre la calidad de imagen y la eficiencia computacional, y demuestran el potencial de los modelos generativos para ampliar los conjuntos de datos de MRI, mejorando así las aplicaciones de aprendizaje profundo para el diagnóstico de HCM.

Palabras clave: generación de datos, modelos de difusión, redes generativas adversarias, codificadores automáticos variacionales

---

[1,*] Department of Electronics and Communication Engineering, Andhra University, India.
Corresponding author ✉: madhurirayavarapu.rs@andhrauniversity.edu.in.

Suggested citation: S. Madhuri Rayavarapu and G. Sasibhushana Rao, “Exploring deep generative models for improved data generation in hypertrophic cardiomyopathy,” *Ingenius, Revista de Ciencia y Tecnología*, N.° 34, pp. 116-125, 2025, DOI: https://doi.org/10.17163/ings.n34.2025.09.

1. Introduction

Artificial intelligence (AI) has become an increasingly powerful tool for analyzing medical data, including images, text, and signals, to support disease interpretation, identification, classification, and diagnosis [1]. The development of AI-based medical software relies heavily on large volumes of diverse data, such as electrocardiograms, X-rays, magnetic resonance imaging (MRI), computed tomography (CT), echocardiography, and dermatological images [2–8]. However, the collection and annotation of these datasets remain costly and time-consuming, often requiring expert clinicians to manually label the data [9].

Although numerous medical datasets are available, publicly accessible data for rare cardiac conditions such as hypertrophic cardiomyopathy (HCM) remain scarce. This limitation stems from factors including the low prevalence of the disease, privacy restrictions, and class imbalance within existing datasets. Consequently, there is an urgent need for advanced techniques capable of generating high-quality synthetic medical images to augment current datasets. Deep learning models, particularly those developed for medical image analysis, benefit greatly from large, balanced, and precisely labeled datasets, which improve diagnostic accuracy and generalizability [10]. Moreover, diverse training data are essential for mitigating overfitting and enhancing model robustness.

Developing effective deep learning models for medical imaging poses several challenges. First, acquiring sufficient data is difficult due to patient confidentiality constraints and limited data sharing among institutions. Second, manual annotation of medical images is labour-intensive, time-consuming, and susceptible to variability across different imaging modalities. Third, datasets often exhibit class imbalance, as pathological cases typically constitute a minority compared to normal or healthy instances [11]. Collectively, these challenges complicate the development of reliable automated diagnostic systems.

To address these issues, researchers have adopted data augmentation techniques to increase dataset size and variability. Traditional augmentation methods include geometric transformations, kernel operations, and colour space adjustments [12–14]. While useful, these methods yield only limited variation because they manipulate existing images rather than creating entirely new ones. In contrast, deep learning-based augmentation approaches, such as Variational Autoencoders (VAEs), Neural Style Transfer, Diffusion Models, and Generative Adversarial Networks (GANs), have demonstrated superior capability in generating diverse and realistic synthetic images [15–17]. Unlike conventional methods, these generative models learn the underlying high-dimensional data distribution, enabling the creation of novel samples that closely resemble real-world data. As a result, deep generative models are particularly effective for mitigating data scarcity and class imbalance, especially for rare diseases such as HCM, thereby enhancing the training and generalization performance of diagnostic models.

Section 2 reviews the deep generative models used for synthetic image generation and describes the methodology, section 3 presents the results and discussion, and section 4 summarizes the conclusions.

2. Materials and methods

2.1. Deep generative models

This section provides a concise description of the different deep generative models employed for generating medical images. It focuses on three main types of models: Variational Autoencoders, Generative Adversarial Networks, and Diffusion Models.

2.1.1. Variational autoencoder

Max Welling and Diederik P. Kingma introduced the concept of the variational autoencoder (VAE) in 2013 [18]. A VAE describes an observation in latent space in a probabilistic manner. Instead of producing a single value for each latent state attribute, the encoder generates a probability distribution for each attribute. Applications of VAEs include data compression and the generation of synthetic data. Figure 1 illustrates the VAE architecture, with its main components detailed below.

- **Input**: The input to a VAE depends on the specific application and the domain of interest. For image-based VAEs, the input typically consists of entire images or image patches.

- **Encoder**:The encoder transforms the input data into the parameters of the latent space, which define the associated probability distribution. It typically consists of multiple neural network layers, such as convolutional or fully connected layers, that work together to reduce the dimensionality of the input. The output of the encoder is a set of mean and variance vectors that approximate the characteristics of a multivariate Gaussian distribution in the latent space.

- **Latent space**: Each point in the latent space represents a latent code, which is a reduced-dimensional description of the input data. During training, the encoder learns to generate latent codes that accurately capture the essential features of the input.

- **Decoder**: Before mapping the transformed data back to the input space, the decoder extracts a relevant subset from the latent space. Like the encoder, it consists of several neural network layers that progressively sample the latent code and generate the output. The goal of the decoder is to reproduce the original input data as accurately as possible.

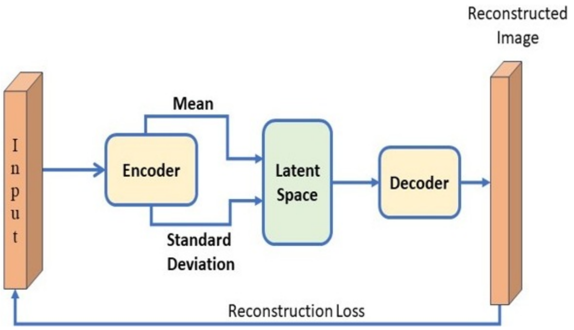

Figure 1. Variational autoencoder

VAEs rely on the mathematical representation of the latent space learned by the encoder network to approximate the data distribution, while the decoder network uses this representation to generate samples similar to the training data.

The encoder network maps an input sample x to a latent representation z according to Equation (1), while the decoder network uses Equation (2) to reconstruct the input space from the latent representation z. The functions f and g denote the encoder and decoder networks, respectively.

$$z = f(x) \tag{1}$$

$$x' = g(z) \tag{2}$$

The loss function of the VAE is defined in Equation (3). In this equation, the first term represents the reconstruction loss, while the second term corresponds to the Kullback–Leibler (KL) divergence.

$$Loss = E\left[L\left(x, x'\right)\right] - D_{KL}\left(q\left(z \mid x\right) || \, p\left(z\right)\right) \tag{3}$$

$$Where \; L\left(x, x'\right) = logp\left(x \mid x'\right) \tag{4}$$

2.1.2. Generative adversarial networks

Generative Adversarial Networks (GANs) are an unsupervised learning method that leverages the well-established zero-sum game theory framework for two players. This concept was introduced by Goodfellow in 2014 [19]. In a GAN, the generator creates new samples based on real data, while the discriminator estimates the underlying data distribution by distinguishing between real and generated samples, see figure 2.

- **Generator**: The generator component of a GAN creates synthetic data by transforming random noise into samples that resemble real data.
- **Discriminator**: The discriminator component of a GAN acts as a classifier that distinguishes between real data and artificially generated data produced by the generator.

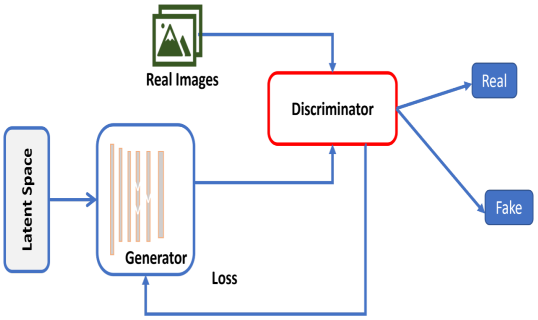

Figure 2. Architecture of a generative adversarial network (GAN)

GANs operate based on a mathematical framework in which the discriminator network provides feedback on the realism of generated samples, while the generator network maps latent space representations to the original data space. This adversarial process enables GANs to learn a generative model of the data and produce diverse, realistic synthetic samples. Compared to other generative methods, GANs offer notable advantages, including the ability to handle complex data distributions and generate high-resolution images [20].

The loss function of the GAN is defined in Equation (5).

$$\begin{aligned} min_G max_D V(D,G) = E_x log(D(x)) + \\ E_z log(1 - D(G(z))) \end{aligned} \tag{5}$$

In Equation (5), Zepresents the latent space or noise input, which is supplied to the generator. The discriminator is denoted by D, and the generator is denoted by G. The discriminator receives both the generated images and the real data samples. The representation of real data is expressed as $D(x)$, while the representation of generated data is expressed as $D(G(z))$. Both the discriminator and generator networks are trained simultaneously: the discriminator aims to minimize the classification score of generated samples, whereas the generator seeks to maximize it.

Several variants of GANs have been introduced in recent years. Some of these variants are described in the following sections.

2.1.3. Deep convolutional GANs

Deep Convolutional Generative Adversarial Networks (DCGANs) are a novel variant of convolutional neural networks (CNNs) designed with specific architectural constraints, as introduced in [21]. To meet these requirements, DCGANs incorporate three key architectural modifications. First, they replace fully connected hidden layers and pooling layers with convolutional layers, using fractional-strided convolutions in the generator and strided convolutions in the discriminator to enhance network performance. Second, they apply ReLU activations to all layers of the generator except the output layer, while employing LeakyReLU activations throughout the discriminator. Third, batch normalization is applied consistently in both the generator and the discriminator.

2.1.4. Auxiliary classifier GAN

Odena et al. [22] introduced the Auxiliary Classifier Generative Adversarial Network (ACGAN), which incorporates an additional classifier to enhance the model's performance. The ACGAN discriminator includes a classifier that categorizes samples into discrete classes, thereby improving training stability. In an ACGAN, the generator G uses both noise Z and a category label C sampled from a distribution to generate a synthetic sample, denoted as $x_{fake} = G(c, z)$. The discriminator D distinguishes between real and fake samples while also considering both the authenticity and the class labels.

The objective functions of the ACGAN are defined in Equations (6) and (7).

$$\begin{aligned} L_s = E\left[log(P(S = real \mid Xreal))\right] + \\ E\left[log(P(S = fake \mid Xfake))\right] \end{aligned} \tag{6}$$

$$\begin{aligned} L_c = E\left[log(P(C = c \mid Xreal))\right] + \\ E\left[log(P(C = c \mid Xfake))\right] \end{aligned} \tag{7}$$

The terms L_s and L_c denote the probabilities of correctly identifying the source and the class, respectively. X denotes the input image, C is the class label, and S is the source.

When training the discriminator D, the primary objective is to maximize the total loss $(L_s + L_c)$. In contrast, the generator G is trained to maximize the difference $L_s - L_c$ between the losses.

2.1.5. Information Maximizing GAN (Info GAN)

InfoGAN was proposed by Chen et al. [23] as an information-theoretic approach to improve interpretability in GANs by learning meaningful latent variables. The term "info" indicates the mutual information shared between the generated distribution $G(z, c)$ and the latent code c. To reduce the correlation between x and c, InfoGAN maximizes the mutual information $I(c; G(z, c))$. A regularization term incorporating this information objective is added to the standard GAN loss function. To estimate a tractable lower bound of the mutual information $P(c \mid x)$, an auxiliary distribution $Q(c \mid x)$ is introduced to approximate $P(c \mid x)$.

The objective function of InfoGAN is defined in Equation (8):

$$\frac{min}{G, Q} \frac{max}{D} L(D, G, Q) = V(D, G) - \lambda I(G, Q) \tag{8}$$

Where λ is the regularization constant, typically set to one.

2.2. Diffusion models

Sohl-Dickstein et al. were the first to introduce diffusion models [24]. Building on this idea, Ho et al. [25] proposed Denoising Diffusion Probabilistic Models (DDPMs), marking the first demonstration that diffusion models can achieve performance comparable to other generative models for image synthesis tasks.

Diffusion models are advanced machine learning algorithms that generate high-quality data by gradually adding noise to a dataset and then learning how to reverse this process [26]. As a subset of deep learning-based generative models, their primary objective is to produce synthetic data that is both realistic and plausible given a set of input conditions. Due to their many advantages over other generative methods, such as the ability to generate highly diverse data, handle high-dimensional datasets, and learn complex distributions effectively, diffusion-based generative models have recently gained significant popularity across various scientific disciplines [27].

A diffusion model is a probabilistic generative framework that involves two multi-step processes: forward diffusion and reverse diffusion. In the forward diffusion process, noise is gradually added to the input data until the original information is completely obscured. In contrast, the reverse diffusion process employs a trainable neural network to progressively remove the noise and reconstruct the original data distribution. Synthetic outputs are generated by applying this trained neural network to noisy samples, see figure 3.

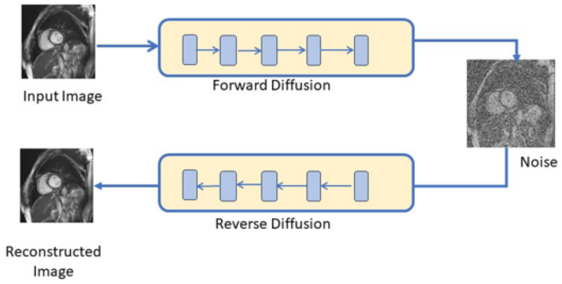

Figure 3. Architecture of a diffusion model

To initiate the forward diffusion process, samples are drawn from a simple distribution, typically a Gaussian. This initial sample then undergoes a sequence of small, reversible transformations. Through a Markov chain, each step incrementally increases the complexity of the sample, which can be interpreted as the progressive addition of structured noise.

In a forward diffusion process, small amounts of Gaussian noise are progressively added to a data point x drawn from the true data distribution $q(x)$, producing a series of increasingly noisy samples denoted by $x_1, x_2, x_3, \ldots, x_T$. This process is mathematically defined by Equations (9) and (10).

$$q(x_t \mid x_{t-1}) = N(x_i, \sqrt{1-\beta_t}x_{t-1,}\beta_t I) \tag{9}$$

$$q(x_{1:T} \mid x_0) = \prod_{t}^{T} = q(x_t \mid x_{t-1}) \tag{10}$$

The reverse diffusion process is defined by Equations (11) and (12).

$$p\theta(x_{0:T}) = p(x_T) \cdot \prod_{l=1}^{\bar{I}} p\theta(x_{t-1} \mid x_t) \tag{11}$$

$$p\theta(x_{t-1} \mid x_t) = W(x_{t-1}; u_\theta(x_t, t), \sum \theta(x_t, t)) \tag{12}$$

2.3. Methodology

Images of hypertrophic cardiomyopathy (HCM) are generated using various deep generative models, with Magnetic Resonance Imaging (MRI) serving as the primary modality for detecting and evaluating the disease. MRI provides detailed and high-resolution images of the heart's structure and function without the use of ionizing radiation, making it particularly well-suited for cardiac assessment. Key features of HCM, such as ventricular wall thickening and myocardial fibrosis, can be effectively evaluated through MRI scans. This imaging technique also enables assessment of disease severity and progression, supporting clinical decision-making. Furthermore, the MRI data serve as the basis for developing and validating automated techniques for HCM detection and analysis.

The dataset for hypertrophic cardiomyopathy was obtained from the Cardiac ACDC Dataset.

2.3.1. Dataset

The cardiac MRI scans used in this study were sourced from the open-source Cardiac ACDC dataset [28]. The real clinical examinations that form the ACDC dataset were provided by the University Hospital of Dijon. To protect patient privacy, all data underwent thorough anonymization and processing in accordance with the criteria established by the local ethics committee of the French Hospital of Dijon. The dataset includes a sufficient number of examples to train machine learning algorithms and to reliably assess changes in key physiological parameters derived from cine-MRI, such as diastolic volume and ejection fraction. It encompasses a range of diverse cardiac pathologies and is divided into five categories with an equal proportion of cases in each. In total, the dataset comprises 150 examinations, each obtained from a different patient.

2.3.2. Experimental setup and training process

The Python programming language and the PyTorch framework were used to implement the various deep generative models. Model training was performed in an Anaconda Navigator and Jupiter Notebook environment, with Graphics Processing Unit (GPU) acceleration enabled on an Intel I7 laptop.

Each generative model, including VAE, GAN, Deep Convolutional GAN (DCGAN), InfoGAN, ACGAN, and Diffusion Models, was trained using the Adam optimizer with an initial learning rate of $0,0002$, $\beta_1 = 0,5$ y $\beta_2 = 0,999$. The batch size was set to 32, and models were trained for up to 100 epochs unless early stopping was triggered based on validation loss. For the diffusion models, training was extended to approximately 115 epochs. For GAN-based architectures, the appropriate adversarial loss functions were applied; InfoGAN additionally optimized a mutual information loss term, and ACGAN incorporated an auxiliary classification loss. VAEs were trained by minimizing a combination of reconstruction loss and Kullback–Leibler (KL) divergence. Training stability was enhanced through techniques such as gradient penalty and label smoothing where applicable. Model checkpoints were saved regularly to preserve the best-performing weights according to validation metrics.

Upon completion of training, approximately 1,000 images were generated. These images were then subjected to a qualitative evaluation to assess their similarity to the original dataset.

2.3.3. Evaluation metrics

The SSIM, cross-correlation, and mean squared error (MSE) metrics were used to evaluate the deep generative models, as they capture different aspects of image quality and similarity that are crucial in medical imaging contexts.

2.3.4. Structural similarity index (SSIM)

The Structural Similarity Index (SSI), also known as SSIM, is a widely used metric for quantifying the similarity between two images [29]. SSIM evaluates the similarity of structural information by considering luminance, contrast, and structural patterns within the images. It works by performing three comparisons between corresponding patches: luminance comparison, contrast comparison, and structural comparison. These results are then combined to produce an overall SSIM index, which ranges from -1 to 1, where a value of 1 indicates perfect structural similarity.

For two images, x and y, SSIM is computed using the equation (13):

$$(x, y) = \frac{(2 \cdot \mu_x \mu_y + c_1) \cdot (2 \cdot \sigma_{xy} + c_2)}{(c_1 2 + \mu_x 2 + \mu_y 2) \cdot (c_2 2 + \sigma_x 2 + \sigma_y 2)} \quad (13)$$

$\sigma_y 2$, $\sigma_x 2$ are the variances of images y and x, respectively.

$\sigma_{x,y}$ is the covariance between y and x.

μ_x, μ_y are the mean values of images x and y, respectively.

The constants c_1 and c_2 are determined based on the dynamic range of the pixel values. The SSIM value equals one if and only if both x and y are identical.

2.3.5. Cross correlation coefficient

In image processing, cross-correlation is a technique used to measure the similarity between two signals or images [30]. It involves sliding one image (or signal) over another and calculating a similarity measure at each position.

2.3.6. Mean square error

One of the most widely used and straightforward full-reference metrics is the mean squared error (MSE), which is calculated by squaring the intensity differences between corresponding pixels in the distorted and reference images [31].

3. Results and discussion

The comparison between real and generated images produced by different deep generative models was conducted using three metrics: SSIM, cross-correlation coefficient, and mean squared error (MSE). These metrics quantify the degree of similarity between the generated images and the original ones.

The performance of the generated images for hypertrophic cardiomyopathy using different deep generative models is summarized in Table 1. The similarity index of the images generated by the VAE is lower than that of all the GAN-based and diffusion models. The generated images produced by the various deep generative models for hypertrophic cardiomyopathy are presented in Figure 4. The first image shows the original MRI scan, followed by the VAE-generated image, the GAN-generated image, the DCGAN- and InfoGAN-generated images, and finally the image generated using the diffusion model.

Table 1. Performance Analysis between Real and Generated Images using different deep generative models (VAE, GAN, DCGAN, ACGAN, and Diffusion Models)

Method	SSIM	Cross- Correlation Coefficient	MSE
VAE	0.903	0.8421	0.39
GAN	0.941	0.8821	0.1
DCGAN	0.958	0.9204	0.1
ACGAN	0.969	0.9371	0.09
Diffusion models	0.972	0.9403	0.06

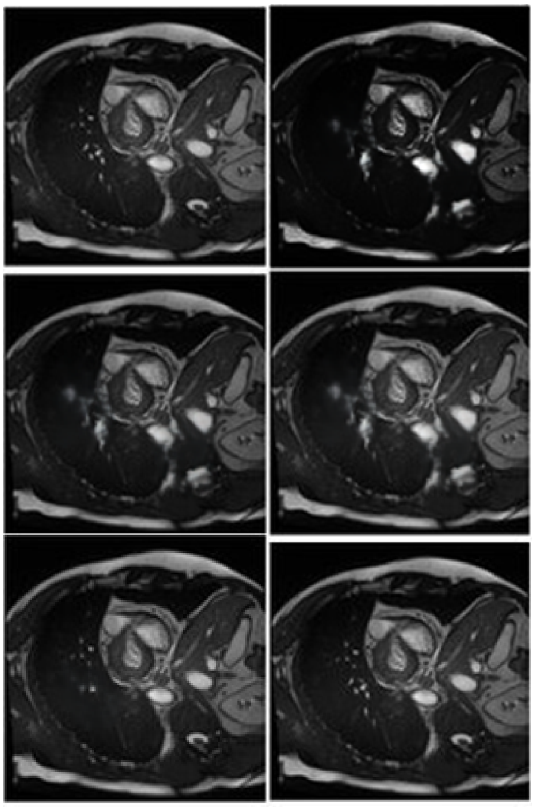

Figure 4. Original Image and Synthesized cardiac images generated using VAE, GAN, DCGAN, ACGAN, and Diffusion model, respectively

In addition to these similarity results, the training loss graphs for the various deep generative models are also presented. The loss function results for the VAE are shown in Figure 5, where it can be observed that the loss decreases as the number of epochs increases.

Figure 6 shows that the generator loss in the GAN increases initially, while the discriminator loss decreases as the number of epochs increases up to approximately 18 epochs. After that point, both losses converge around the 62nd epoch, which yields the best results. The training losses for the DCGAN and diffusion models are shown in Figures 7 and 8, respectively.

When compared to GANs, VAEs perform better during training due to their resilience against mode collapse and their ability to produce more diverse outputs. However, a major drawback is that the generated images are generally blurry and lack sharp detail.

Although diffusion models can produce highly realistic results and maintain stable training, the extensive diffusion process requires a lengthy sampling period, which can limit their practicality for generating images efficiently. This trade-off is evident in the performance metrics presented in Table 1.

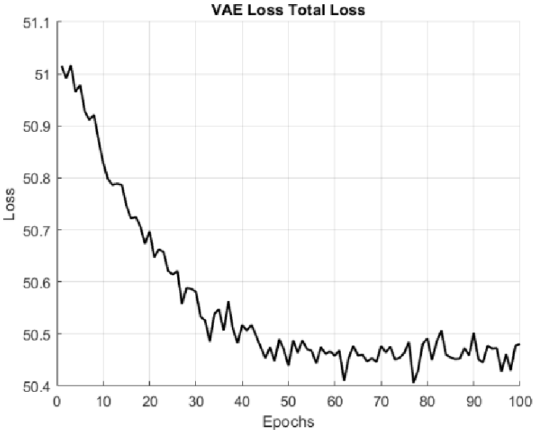

Figure 5. Training Loss of the VAE

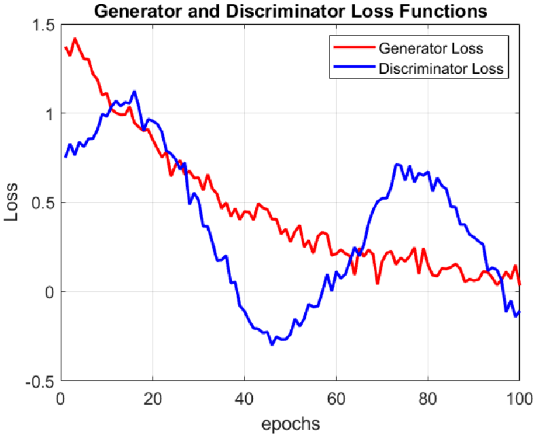

Figure 6. Training Loss of the GAN

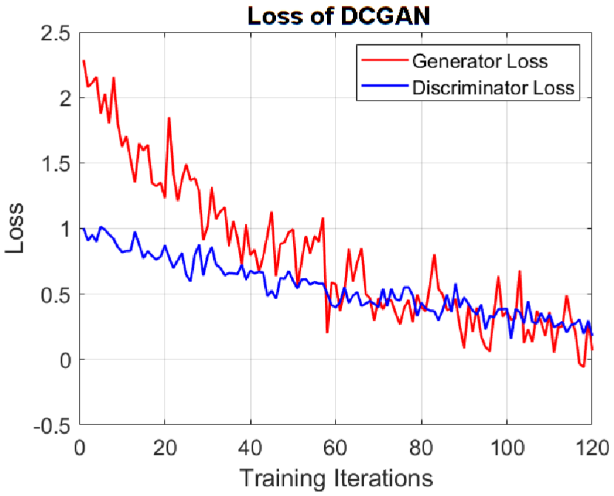

Figure 7. Training Loss of the DCGAN

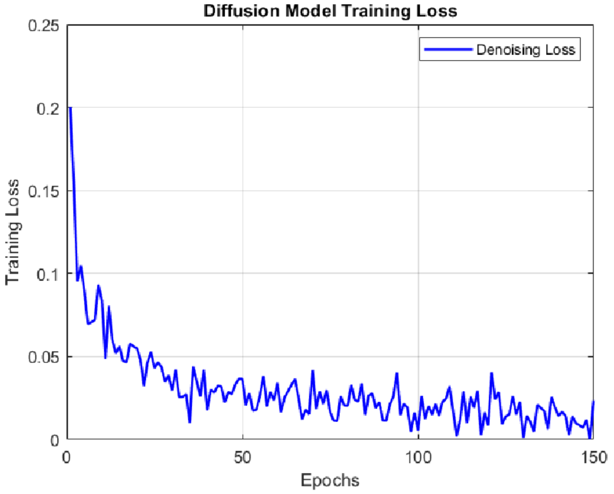

Figure 8. Training Loss of the Diffusion model

4. Conclusions

Data generation strategies are critical for overcoming the challenge of limited training data in deep learning-based medical image analysis. Unlike conventional data augmentation techniques commonly applied in cardiac diagnostics, deep generative models can synthesize entirely new and diverse data samples. In this study, the performance of various data generation approaches was evaluated using the Structural Similarity Index Measure (SSIM) and the Cross-Correlation Coefficient (CC), both of which are standard metrics for assessing image quality and structural fidelity.

The variational autoencoder (VAE) approach achieved an SSIM of 0.9028 and a CC of 0.8421; however, the generated images exhibited noticeable noise and blurriness, revealing limitations in visual realism. In contrast, generative adversarial networks

(GANs) demonstrated improved performance, achieving an SSIM of 0.9428 and the same CC of 0.8421. Among the GAN variants, both deep convolutional GANs (DCGANs) and auxiliary classifier GANs (AC-GANs) produced superior results, with SSIM values of 0.9576 and 0.9687, respectively, indicating a greater capability to generate high-quality and structurally accurate images.

Diffusion models outperformed both GANs and VAEs in terms of similarity metrics, achieving the highest SSIM scores; however, their practicality is constrained by substantially longer sampling times. This trade-off between image quality and computational efficiency should be carefully weighed when selecting an appropriate generative model for medical data augmentation in cardiac diagnostics, particularly for conditions such as hypertrophic cardiomyopathy.

Contributor roles

- **Swarajya Madhuri Rayavarapu:** Conceptualization, methodology, software.
- **Gottapu Sasibhushana Rao:** Investigation, supervision.

References

[1] C. González García, E. Núñez-Valdez, V. García-Díaz, C. Pelayo G-Bustelo, and J. M. Cueva-Lovelle, "A review of artificial intelligence in the internet of things," *International Journal of Interactive Multimedia and Artificial Intelligence*, vol. 5, no. 4, p. 9, 2019. [Online]. Available: http://dx.doi.org/10.9781/ijimai.2018.03.004

[2] Y. Shen, L. Chen, J. Liu, H. Chen, C. Wang, H. Ding, and Q. Zhang, "PADS-Net: GAN-based radiomics using multi-task network of denoising and segmentation for ultrasonic diagnosis of Parkinson disease," *Computerized Medical Imaging and Graphics*, vol. 120, p. 102490, Mar. 2025. [Online]. Available: https://doi.org/10.1016/j.compmedimag.2024.102490

[3] H. Zhang and Y. Qie, "Applying deep learning to medical imaging: A review," *Applied Sciences*, vol. 13, no. 18, p. 10521, Sep. 2023. [Online]. Available: https://doi.org10.3390/app131810521

[4] M. Rana and M. Bhushan, "Machine learning and deep learning approach for medical image analysis: diagnosis to detection," *Multimedia Tools and Applications*, vol. 82, no. 17, pp. 26 731–26 769, Dec. 2022. [Online]. Available: https://doi.org/10.1007/s11042-022-14305-w

[5] X. Liu, H. Wang, Z. Li, and L. Qin, "Deep learning in ECG diagnosis: A review," *Knowledge-Based Systems*, vol. 227, p. 107187, Sep. 2021. [Online]. Available: https://doi.org/10.1016/j.knosys.2021.107187

[6] S. K. Mathivanan, S. Srinivasan, M. S. Koti, V. S. Kushwah, R. B. Joseph, and M. A. Shah, "A secure hybrid deep learning framework for brain tumor detection and classification," *Journal of Big Data*, vol. 12, no. 1, Mar. 2025. [Online]. Available: https://doi.org/10.1186/s40537-025-01117-6

[7] C. Chola, P. Mallikarjuna, A. Y. Muaad, J. V. Bibal Benifa, J. Hanumanthappa, and M. A. Al-antari, "A hybrid deep learning approach for COVID-19 diagnosis via CT and X-ray medical images," in *The 1st International Electronic Conference on Algorithms*, ser. IOCA 2021. MDPI, Sep. 2021, p. 13. [Online]. Available: https://doi.org/10.3390/IOCA2021-10909

[8] F. Y. Shih and H. Patel, "Deep learning classification on optical coherence tomography retina images," *International Journal of Pattern Recognition and Artificial Intelligence*, vol. 34, no. 08, p. 2052002, Oct. 2019. [Online]. Available: https://doi.org/10.1142/S0218001420520023

[9] P. Gupta, S. Nandakumar, M. Gupta, and G. Panda, "Data programming enabled weak supervised labeling for ECG time series," *Biomedical Signal Processing and Control*, vol. 87, p. 105540, Jan. 2024. [Online]. Available: https://doi.org10.1016/j.bspc.2023.105540

[10] S. U. Amin, A. Hussain, B. Kim, and S. Seo, "Deep learning based active learning technique for data annotation and improve the overall performance of classification models," *Expert Systems with Applications*, vol. 228, p. 120391, Oct. 2023. [Online]. Available: https://doi.org/10.1016/j.eswa.2023.120391

[11] T. Liu, W. Fan, and C. Wu, "A hybrid machine learning approach to cerebral stroke prediction based on imbalanced medical dataset," *Artificial Intelligence in Medicine*, vol. 101, p. 101723, Nov. 2019. [Online]. Available: https://doi.org/10.1016/j.artmed.2019.101723

[12] T. Islam, M. S. Hafiz, J. R. Jim, M. M. Kabir, and M. Mridha, "A systematic review of deep learning data augmentation in medical imaging: Recent advances and future research directions," *Healthcare Analytics*, vol. 5, p. 100340, Jun. 2024. [Online]. Available: https://doi.org/10.1016/j.health.2024.100340

[13] N. Nonaka and J. Seita, "Data augmentation for electrocardiogram classification with deep neural network," *arXiv*, 2020. [Online]. Available: https://doi.org/10.48550/arXiv.2009.04398

[14] M. M. Rahman, M. W. Rivolta, F. Badilini, and R. Sassi, "A systematic survey of data augmentation of ECG signals for AI applications," *Sensors*, vol. 23, no. 11, p. 5237, May 2023. [Online]. Available: http://doi.org/10.3390/s23115237

[15] F. J. Moreno-Barea, J. M. Jerez, and L. Franco, "Improving classification accuracy using data augmentation on small data sets," *Expert Systems with Applications*, vol. 161, p. 113696, Dec. 2020. [Online]. Available: https://doi.org/10.1016/j.eswa.2020.113696

[16] J. Saldanha, S. Chakraborty, S. Patil, K. Kotecha, S. Kumar, and A. Nayyar, "Data augmentation using variational autoencoders for improvement of respiratory disease classification," *PLOS ONE*, vol. 17, no. 8, p. e0266467, Aug. 2022. [Online]. Available: https://doi.org/10.1371/journal.pone.0266467

[17] D. Bhattacharya, S. Banerjee, S. Bhattacharya, B. Uma Shankar, and S. Mitra, *GAN-Based Novel Approach for Data Augmentation with Improved Disease Classification.* Springer Singapore, Dec. 2019, pp. 229–239. [Online]. Available: https://doi.org/10.1007/978-981-15-1100-4_11

[18] D. P. Kingma and M. Welling, "Auto-encoding variational bayes," *arXiv*, 2013. [Online]. Available: https://doi.org/10.48550/arXiv.1312.6114

[19] I. J. Goodfellow, J. Pouget-Abadie, M. Mirza, B. Xu, D. Warde-Farley, S. Ozair, A. Courville, and Y. Bengio, "Generative adversarial networks," *arXiv*, 2014. [Online]. Available: https://doi.org/10.48550/arXiv.1406.2661

[20] Y. Skandarani, P.-M. Jodoin, and A. Lalande, "GANs for medical image synthesis: An empirical study," *Journal of Imaging*, vol. 9, no. 3, p. 69, Mar. 2023. [Online]. Available: https://doi.org10.3390/jimaging9030069

[21] A. Radford, L. Metz, and S. Chintala, "Unsupervised representation learning with deep convolutional generative adversarial networks," *arXiv*, 2015. [Online]. Available: https://doi.org/10.48550/arXiv.1511.06434

[22] A. Odena, C. Olah, and J. Shlens, "Conditional image synthesis with auxiliary classifier GANs," *arXiv*, 2016. [Online]. Available: https://doi.org/10.48550/arXiv.1610.09585

[23] X. Chen, Y. Duan, R. Houthooft, J. Schulman, I. Sutskever, and P. Abbeel, "InfoGAN: interpretable representation learning by information maximizing generative adversarial nets," *arXiv*, 2016. [Online]. Available: https://doi.org/10.48550/arXiv.1606.03657

[24] J. Sohl-Dickstein, E. A. Weiss, N. Maheswaranathan, and S. Ganguli, "Deep unsupervised learning using nonequilibrium thermodynamics," *arXiv*, 2015. [Online]. Available: https://doi.org/10.48550/arXiv.1503.03585

[25] J. Ho, A. Jain, and P. Abbeel, "Denoising diffusion probabilistic models," *arXiv*, 2020. [Online]. Available: https://doi.org/10.48550/arXiv.2006.11239

[26] F.-A. Croitoru, V. Hondru, R. T. Ionescu, and M. Shah, "Diffusion models in vision: A survey," *IEEE Transactions on Pattern Analysis and Machine Intelligence*, vol. 45, no. 9, pp. 10 850–10 869, Sep. 2023. [Online]. Available: https://doi.org/10.1109/TPAMI.2023.3261988

[27] Z. Guo, J. Liu, Y. Wang, M. Chen, D. Wang, D. Xu, and J. Cheng, "Diffusion models in bioinformatics: A new wave of deep learning revolution in action," *arXiv*, 2023. [Online]. Available: https://doi.org/10.48550/arXiv.2302.10907

[28] O. Bernard, A. Lalande, C. Zotti, F. Cervenansky, X. Yang, P.-A. Heng, I. Cetin, K. Lekadir, O. Camara, M. A. Gonzalez Ballester, G. Sanroma, S. Napel, S. Petersen, G. Tziritas, E. Grinias, M. Khened, V. A. Kollerathu, G. Krishnamurthi, M.-M. Rohé, X. Pennec, M. Sermesant, F. Isensee, P. Jäger, K. H. Maier-Hein, P. M. Full, I. Wolf, S. Engelhardt, C. F. Baumgartner, L. M. Koch, J. M. Wolterink, I. Išgum, Y. Jang, Y. Hong, J. Patravali, S. Jain, O. Humbert, and P.-M. Jodoin, "Deep learning techniques for automatic mri cardiac multi-structures segmentation and diagnosis: Is the problem solved?" *IEEE Transactions on Medical Imaging*, vol. 37, no. 11, pp. 2514–2525, Nov. 2018. [Online]. Available: http://doi.org/10.1109/TMI.2018.2837502

[29] H. Sheikh, M. Sabir, and A. Bovik, "A statistical evaluation of recent full reference image quality assessment algorithms," *IEEE Transactions on Image Processing*, vol. 15, no. 11, pp. 3440–3451, Nov. 2006. [Online]. Available: http://doi.org/10.1109/TIP.2006.881959

[30] G. Prieto, E. Guibelalde, M. Chevalier, and A. Turrero, "Use of the cross-correlation component of the multiscale structural similarity metric (R* metric) for the evaluation of medical images," *Medical Physics*, vol. 38, no. 8,

pp. 4512–4517, Jul. 2011. [Online]. Available: https://doi.org/10.1118/1.3605634

[31] A. Borji, "Pros and cons of GAN evaluation measures: New developments," *arXiv*, 2021. [Online]. Available: https://doi.org/10.48550/arXiv.2103.09396

Scientific Paper / Artículo Científico

UNIVERSIDAD POLITÉCNICA SALESIANA ECUADOR
INGENIUS
Revista de Ciencia y Tecnología
https://doi.org/10.17163/ings.n34.2025.10
pISSN: 1390-650X / eISSN: 1390-860X

IMPLEMENTATION AND EVALUATION OF A WHEELED-LEGGED LOCOMOTION ROBOT FOR OPTIMIZING THE PREFLIGHT AIR INTAKE INSPECTION PROTOCOL OF FIGHTER AIRCRAFT

IMPLEMENTACIÓN Y EVALUACIÓN DE UN ROBOT CON SISTEMA DE LOCOMOCIÓN *WHEELED-LEGGED* PARA LA OPTIMIZACIÓN DEL PROTOCOLO DE INSPECCIÓN DE TOMAS DE AIRE EN AVIONES CAZA EN ESTADO PREVIO AL VUELO

Mayki Mamani[1,*], Jhonathan Uchamaco[1], David Meneses[1],
Yuri Silva[1], Jorge Apaza[1]

Received: 12-05-2025, Received after review: 02-06-2025, Accepted: 11-06-2025, Published: 01-07-2025

Abstract

Maintenance and inspection protocols in the aerospace industry are designed to safeguard the structural integrity of aircraft and ensure pilot safety. However, the air intakes of fighter aircraft pose significant access challenges for maintenance technicians during preflight inspections. To address this limitation, this study presents an innovative solution: the implementation and evaluation of a robot equipped with a wheeled-legged locomotion system. This system enables efficient access to the air intakes, significantly enhancing the inspection protocol. The robot was developed in close alignment with the operational requirements of Peruvian Air Force (FAP) technicians, which was critical to defining its design specifications and manufacturing parameters. Its adaptive and compact architecture allows it to navigate confined intake structures effectively, optimizing inspection time and resource utilization. The prototype's performance was rigorously assessed through standardized tests, demonstrating its capability to reliably access and inspect air intakes under preflight conditions. This advancement contributes to the modernization of conventional aircraft maintenance procedures by integrating robotic technologies into the aeronautical inspection process.

Keywords: Robot, design, inspection, air intake, fighter aircraft, locomotion, wheeled-legged

Resumen

Los protocolos de mantenimiento e inspección en la industria aeroespacial están diseñados para salvaguardar la integridad estructural de las aeronaves y la seguridad de los pilotos. Las tomas de aire de los aviones caza presentan un acceso limitado para los técnicos de mantenimiento durante la inspección en estado previo al vuelo. Ante esta limitación, se propone una solución innovadora mediante la implementación de un robot con sistema de locomoción *wheeled-legged*, que permite acceder a dichas tomas de aire y optimizar significativamente el protocolo de inspección. En esta investigación se desarrolló e implementó un robot con tecnología de locomoción *wheeled-legged*, cuyo propósito específico es facilitar la inspección de las tomas de aire en aviones caza previo al vuelo. Para su diseño y fabricación se consideraron cuidadosamente los requerimientos operativos de los técnicos de la Fuerza Aérea del Perú (FAP), lo que resultó fundamental en la definición de las especificaciones del sistema. El resultado fue un diseño adaptativo y compacto que permite al robot desplazarse con eficacia a través de las tomas de aire, optimizando el tiempo y los recursos empleados en las inspecciones. Mediante pruebas estandarizadas se evaluó el rendimiento del prototipo, demostrando su capacidad para acceder e inspeccionar eficazmente dichas estructuras. Esto permite mejorar el protocolo de mantenimiento tradicional mediante la incorporación de tecnología avanzada en los procesos de inspección aeronáutica.

Palabras clave: robot, diseño, inspección, tomas de aire, aviones caza, locomoción, wheeled-legged

---

[1,*] Mechanical Engineering Professional School, Production and Services Faculty, Universidad Nacional de San Agustín de Arequipa, Arequipa, Perú. Corresponding author ✉: mmamanimar@unsa.edu.pe.

Suggested citation: M. Mamani, J. Uchamaco, D. Meneses, Y. Silva and J. Apaza, "Implementation and evaluation of a wheeled-legged locomotion robot for optimizing the preflight air intake inspection protocol of fighter aircraft," *Ingenius, Revista de Ciencia y Tecnología*, N.° 34, pp. 126-139, 2025, DOI: https://doi.org/10.17163/ings.n34.2025.10.

1. Introduction

Currently, in the aeronautical industry, the optimal performance of aircraft is ensured through specialized maintenance protocols designed to uphold the highest safety standards [1]. Among the critical components addressed in these procedures are the air intakes. These structures, characterized by their complex geometry, contain multiple peripheral gates that redirect airflow toward the engine, thereby enhancing the aircraft's overall performance [2] and [3].

In the Peruvian Air Force (FAP), accessing the air intakes of fighter aircraft presents specific challenges that complicate inspection tasks for maintenance personnel. This limitation can result in overlooked structural defects or the presence of foreign object debris (FOD) [4], posing a significant risk of catastrophic incidents, potential loss of life, and substantial material damage with severe economic repercussions [5].

In the FAP, daily and weekly maintenance routines include engine removal to facilitate thorough inspection of the air intakes [6]. However, during preflight inspections, the available time is limited, and disassembling the engine is impractical, which prevents technicians from adequately inspecting the air intakes [7].

The use of periscopes as tools to visually access hard-to-inspect areas of aircraft has been explored and implemented within the FAP. However, their limited reach and the complex geometry of the air intakes continue to pose a risk of undetected fuselage defects or the presence of FOD [8,9]. Although these devices provide partial enhancements to maintenance protocols, the possibility of missed faults during the preflight phase remains.

On the other hand, advances in additive manufacturing technologies, such as 3D printing, have grown significantly across various industrial sectors [10], particularly in robotics, where they enable the rapid and cost-effective creation of complex designs for inspecting hard-to-reach areas [11–15].

Similarly, robotics has been increasingly integrated into aircraft maintenance processes. Notable examples include the use of unmanned aerial vehicles (UAVs) for aircraft inspections by the Spanish Air Force in collaboration with Airbus [16]; the application of vortex technology for inspecting fuselages and wings [17]; octopod robots capable of adhering to aircraft surfaces to inspect rivets [18,19]; the development of continuum robots that navigate cavities to inspect engines [20,21]; and modular robots designed to examine the interior of wings and their internal structures [22].

Although these technologies have been explored for general aircraft maintenance, they do not specifically address the inspection of air intakes, which are confined spaces with complex geometries and limited accessibility. Currently, there is a lack of studies and experimental validation supporting the deployment of robots within these structures.

To address this limitation, various locomotion technologies have been investigated for accessing air intakes, including tracks, conventional wheels, adaptive designs, omnidirectional systems, continuum robots, electroadhesive mechanisms, and unmanned aerial vehicles (UAVs) [23]. Among these alternatives, wheeled-legged locomotion technology stands out [24], as it combines wheels and legs in mobile platforms, enabling stable movement over irregular surfaces such as those found inside air intakes.

This approach is supported by developments such as the Centauro robot from the German Aerospace Center (DLR), which employs a hybrid locomotion system to operate on rough terrain during search and rescue missions [25]; and the Roller Walker [26], which combines wheels for movement on smooth surfaces with articulated legs to overcome obstacles. However, none of these systems have been designed for the deployment of hybrid robots within confined spaces inside aircraft.

This study presents the implementation and evaluation of the ALLQU robot, equipped with a wheeled-legged locomotion system designed to optimize maintenance protocols by enabling access to and inspection of air intakes. For its validation, three methodological frameworks are employed: the NIST-ASTM testing protocol for evaluating robots in complex environments [23]; the FAP POCHE maintenance protocol; and the NASA TLX methodology, which analyzes operator workload to assess the system's usability, advantages, and limitations within the operational context.

2. Materials and methods

2.1. Wheeled-Legged Robots

As illustrated in Figure 1, wheeled-legged robots combine wheels and legs to enhance mobility across varied terrains. These systems employ actuators that enable switching between different locomotion modes depending on the terrain characteristics. However, this versatility can increase operational complexity, an aspect evaluated in this study using the NASA TLX methodology [27].

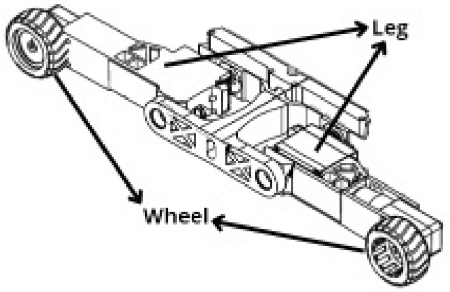

Figure 1. Wheeled-legged robot

Some of the advantages and disadvantages of this type of robot, as reported by Li et al. [27], are summarized in Table 1.

In general, their adaptability and stability, defined as the ability to maintain position and orientation without tipping over or excessive slipping, make them a suitable option for applications in hard-to-reach environments, such as the one addressed in this study.

Table 1. Examples of wheeled-legged robots

	Previous work	Characteristics
[28]	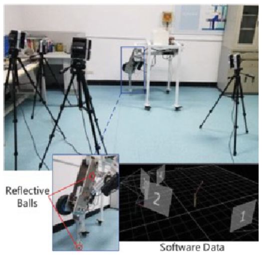 	**Advantages** High mobility High stability Great obstacle avoidance capability **Disadvantages** High level of control required
[29]	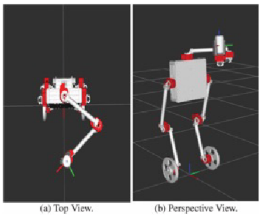 (a) Top View. (b) Perspective View.	
[30]	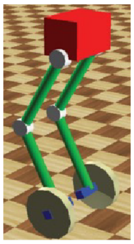	
[31]	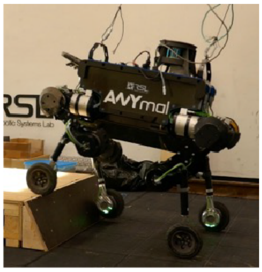 	
[32]	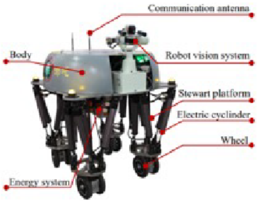 	

2.2. Study of the Work Environment

The air intake environment of the Mirage 2000, whose structure is primarily composed of aluminum, was analyzed. Its location is shown in Figure 2(a), and its main components, including inlets, outlets, gates, and critical sections, are mapped in Figure 2(b).

The air intake entrance has a height of 16 cm Figure 2(c), while the outlet, which connects to the compressor area, has a diameter of 78 cm Figure 2(d). In one critical section, the maximum recorded height is 14 cm.

Peripheral Gate 1 features a drop of 12 cm, an opening of 35 cm, and a slope of 30° Figure 2(e), whereas Gate2 has a height of 5 cm Figure 2(f).

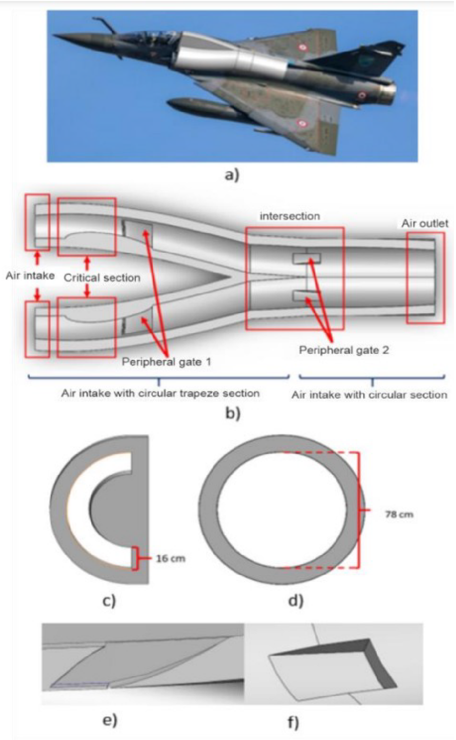

Figure 2. Characteristics of the air intakes of Mirage 2000 fighter aircraft: (a) Location of the air intake on the fighter aircraft. (b) Components of the air intake. (c) Section at the air intake entrance. (d) Section at the air intake outlet. (e) Peripheral Gate 1. (f) Peripheral Gate 2.

The preflight maintenance protocol for the Mirage 2000, as outlined in the POCHE manual, includes six main components, which are shown in Figure 3. Among these, the air intake, characterized by restricted access, constitutes the primary focus of this study.

Maintenance includes inspecting the internal fuselage, verifying that the gates are properly closed, and ensuring the absence of FOD within the system.

The requirements of FAP technical personnel were collected and analyzed through surveys and structured interviews, using rating scales. The results were classified into two categories: technical requirements (dimensions, reach, FOD detection, stability, maneuverability, and speed) and economic requirements (cost and availability).

Interviews were conducted with three key groups of FAP personnel involved in the inspection of air intakes:

1. Technicians responsible for the manual inspection of the aircraft.

2. Personnel responsible for the removal of foreign objects.

3. Supervisors responsible for documenting and recording inspection activities.

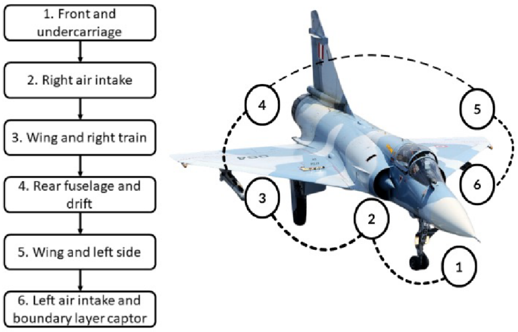

Figure 3. Preflight maintenance procedure for Mirage 2000 fighter aircraft.

The averages obtained from the surveys and interviews are presented in Table 2. The final score represents the mean value of both sources and is illustrated in the bar chart in Figure 4.

The order of importance assigned to the evaluated criteria for the prototype design was as follows: Effectiveness (4.8), Reach (4.6), Maneuverability (4.4), Adaptability (4.05), Dimensions (3.5), Availability (3.4), Stability (2), Speed (1.15), and Cost (0).

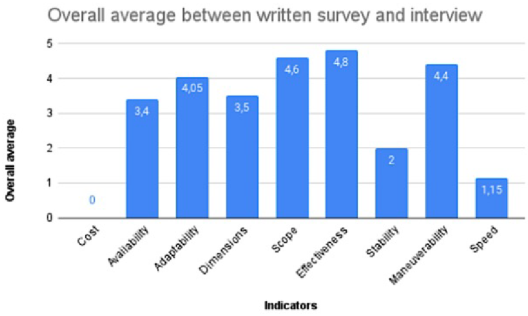

Figure 4. Average scores from the written surveys and interviews of FAP personnel

Table 2. Analysis of results from the written surveys and interviews

Indicator	Average		Overall
	Written sruvey	Interview	Average
Cost	0	0	0
Availability	3.3	3.5	3.4
Adaptability	3.8	4.3	4.05
Dimensions	3	4	3.5
Range	4.6	4.6	4.6
Effectiveness	4.8	4.8	4.8
Stability	4	0	2
Maneuverability	4.1	4.7	4.4
Speed	2.3	0	1.15

Note: The score ranges from 1 to 5 depending on of growing importance.

Based on the analysis of the air intake environment, the FAP's preflight maintenance protocol, and the results of surveys and interviews with technical personnel, the requirements that the ALLQU robot must meet were defined and are presented in Table 3.

Table 3. List of requirements

Characteristic	Requirement
Main function	Inspection of the internal fuselage of the air intakes and detection of FOD
Dimensioning	The size of the robot is based on the critical section, with a height of up to 140 mm and a minimum length of 350 mm.
Mobility	Movement throughout the interior of the air intakes.
Adaptability	The system must adapt to the shape of the air intake.
Stability	The robot must be stable throughout its entire journey.

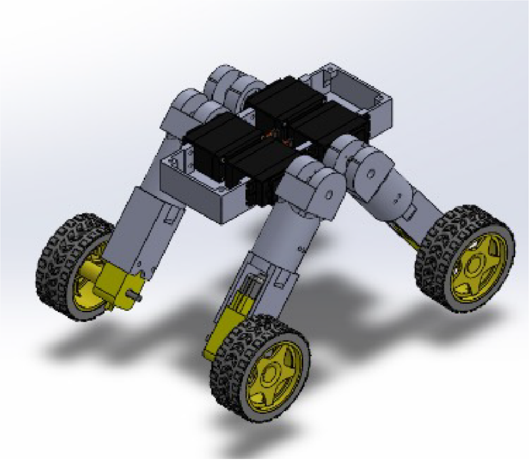

Figure 6. Three-dimensional assembly of the ALLQU robot in SolidWorks.

3. Results and discussion

3.1. Design, Construction, and Implementation of a Robot with a Wheeled-Legged System

Based on the established requirements, the robot's dimensions are shown in Figure 5: a maximum height of 140 mm, a width of 250 mm, and a length of 400 mm. The length slightly exceeds the 350 mm opening of Peripheral Gate 1, ensuring that the robot can pass through this section without the risk of jamming.

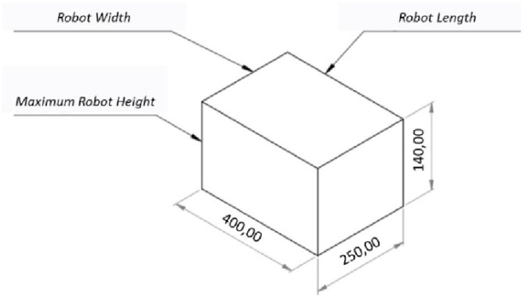

Figure 5. Conceptual dimensions of the robot relative to the available space in the critical section of the Mirage 2000 fighter aircraft air intake

3.2. Design of the wheeled-legged system

The design and assembly of the ALLQU robot's mechanical components were performed using three-dimensional modeling software, as illustrated in Figure 6. The design prioritizes compactness and adaptability, which are essential for operationin confined spaces.

A hybrid wheeled-legged locomotion system was selected for its demonstrated ability to combine the efficiency of wheels with the adaptability of legs. This configuration enables the robot to contract and extend its structure, ensuring stable and efficient movement through the complex geometries of the air intakes, including peripheral gates and critical sections.

To balance weight, strength, and functionality, 14 lightweight yet robust structural components were fabricated using 3D printing. The final design has a total weight of 1.350 kg and dimensions of 140 mm in height, 250 mm in width, and 400 mm in length, ensuring precise adaptation to the critical section, which has a height of 14 cm and a 35 cm opening at Peripheral Gate1.

This configuration was designed to maximize maneuverability and access capability in restricted environments while balancing these attributes against the inherent complexity of control and manufacturing cost.

The robot comprises six main mechanical components, as illustrated in Figure 7. It is equipped with four rubber wheels, each with a radius of 22.5 mm, which are mounted using the couplings shown in Figure 7(a) that connect them to the geared motors.

The structural legs, which support the motors, are shown in Figure 7(b) and are attached to pivots, as depicted in Figure 7(c), allowing movement via independent servomotors. The chassis, shown in Figure 7(d), provides structural stability and overall support for the assembly. The cover, shown in Figure 7(e), protects the servomotors and serves as a mount for the electronic system, which is housed within the module shown in Figure 7(f).

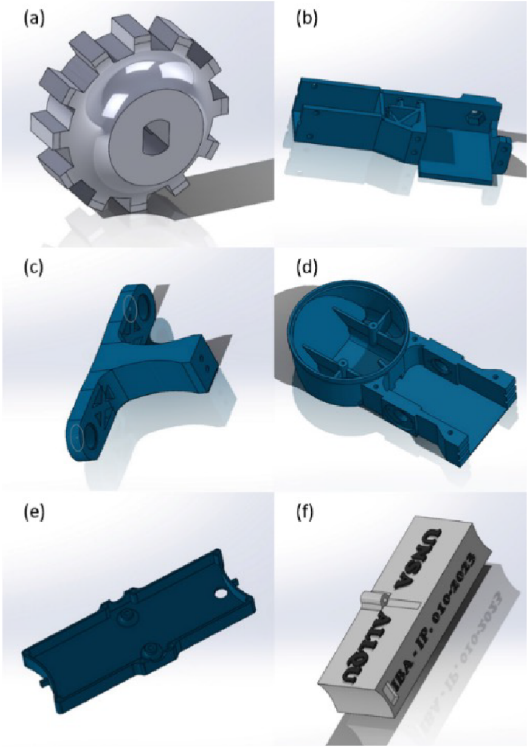

Figure 7. Three-dimensional modeling of the ALLQU robot components in SolidWorks: (a) Wheel coupling, (b) Leg, (c) Pivot structure, (d) Chassis, (e) Cover, (f) Electronics module

Two operational scenarios were evaluated in the critical section of the system, as shown in Figure 8: the robot's entry with all four wheels on a 30° slope Figure 8(a), and its exit with two wheels on a flat surface Figure 8(b).

With a mass of 1.35 kg and static and rolling friction coefficients of $C_f = 0.74$ and $C_r = 0.005$, respectively, the required forces were calculated to be 6.679 N for ascending the incline and 0.066 N for movement on a flat surface. Considering a wheel radius of 22.5 mm, the required torque was determined to be 0.038 Nm, which is below the maximum allowable limit of 0.052 Nm, thereby ensuring sufficient traction and preventing slippage.

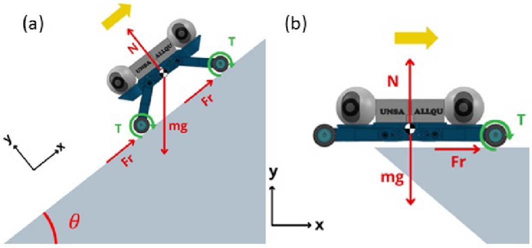

Figure 8. Free body diagram of the robot: (a) Inclined at 30° with 4 wheels in contact, (b) Horizontal plane at 0° with 2 wheels in contact

Table 4. Required torque values

Torques	Description	Torque Parameters (Nm)
Torque on motor	2 wheels in contact and inclination 0º.	Treq 0º = 0,002 Nm
of wheels required	4 wheels in contact or inclination 30º.	Treq 45º = 0,038 Nm
Maximum torque of	2 wheels in contact nd inclination 0º.	Tmax.tractivo 0º = 0,104 Nm
wheel tractions	4 wheels in contact and inclination 30º.	Tmax.tractivo 45º = 0,052 Nm

The robot's movement was simulated in the critical section of the air intake (Figure 9). The simulation confirmed that its dimensions, along with the wheeled-legged system, allow it to traverse this section effectively.

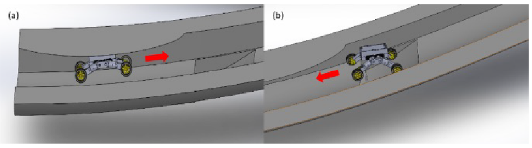

Figure 9. SolidWorks motion simulation of the robot in the critical section of the air intake: (a) Robot entry, (b) Robot exit.

Figure 9(a) shows the robot's entry using only its wheels, while Figure 9(b) depicts its exit using its legs.

3.3. Construction and implementation

The ALLQU robot was constructed in the manufacturing laboratory of the National University of San Agustín de Arequipa, as shown in Figure 10. The design includes a total of 14 structural components fabricated using 3D printing, along with 4 wheel couplings, 4 legs, 2 pivots, 2 chassis structures, a cover, and a central electronic module.

The robot is equipped with 4 high-grip rubber wheels, coupled to 3–6 V DC gear motors. Each leg is driven by 4.8–7.2 V DC servomotors. Additionally, it has 2 wireless cameras with integrated LED and infrared lighting systems to facilitate inspections in low-visibility environments.

Figure 10. Assembly of the ALLQU robot

The dimensions of the ALLQU robot and the Operational Control Unit (OCU) are shown in Figure 11 and detailed in Table 5. These measurements were recorded with the robot in its extended configuration, as depicted in Figure 8(b). The resulting dimensions enable effective maneuvering in confined spaces, such as the air intakes of fighter aircraft.

Figure 11. ALLQU robot and Operational Control Unit (OCU)

Table 5. Specifications of the ALLQU robot and THE Operational Control Unit (OCU)

Characteristics	Description	Parameter
Robot characteristics	Robot weight	1,350 kg
	Robot length	350 mm
	Robot width	150 mm
	Robot height	110 mm
Operator Control Unit (OCU) characteristics	Weight OCU	300 grams
	length OCU	150 mm
	width OCU	175 mm
	height OCU	40 mm

The robot's structure, built from 3D-printed components, is lightweight and durable, which enhances operational efficiency. The integrated cameras, described in Table 6, were specifically selected to enable recording in low-light conditions, such as those inside the Mirage 2000 air intake.

Table 6. Camera Characteristics

Description	Parameter
Connectivity technology	Wireless
Connectivity protocol	Wifi
Camera weight	20 grams
Light source type	LED e infrared
Power	15 watts

The assembled version of the ALLQU robot is shown in Figure 12, which also illustrates the maximum angles that can be formed between the legs and the body of the system. In Figure 12(a), an angle of 70° is observed when the legs are positioned below the body. In Figure 12(b), angles of 25° between the body and the front leg in the upward direction, and 15° between the body and the rear leg in the same direction, are measured.

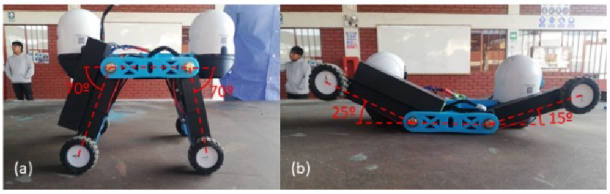

Figure 12. ALLQU robot with wheeled-legged locomotion system: (a) Maximum angle between the body and the legs in the downward position. (b) Maximum angles between the body and the legs in the upward position

Table 7 presents the technical specifications of the robot.

Table 7. Especificaciones técnicas del robot

Characteristics	Description
Type of locomotion	Wheeled-Legged
Robot dimensions	Length: 350 mm
	Width: 150 mm
	Height: 110 mm
Robot weight	1,350 kg
Wheels	4 rubber wheels
	Radius: 22,5 mm
Legs	4 servomotors
Inspection cameras	2 wireless cameras
Connectivity	Wifi
Camera weight	20 g
Light source (camera)	Infrared LED
Power (camera)	15W
OCU dimensions	Length: 150 mm
	Width: 175 mm
	Height: 40 mm
OCU weight	300 g

3.4. Analysis of the Test Setup and Testing Methodology

This section describes the characteristics of the two tests conducted on the ALLQU robot. The first test evaluates the turning performance of the wheeled-legged system and the camera's effectiveness under real operating conditions. The second test assesses the overall performance of the wheeled-legged locomotion system and the mental workload perceived by the operator while controlling the robot.

3.4.1. Test of the turning effectiveness of the wheeled-legged system and camera performance

A ventilation duct was used, as shown in Figure 13 and detailed in Table 8, to simulate a narrow space with low lighting conditions. This environment enabled the evaluation of the ALLQU robot's turning capability and the quality of the video captured by its camera.

Figure 13. Ventilation duct used for the tests

The test was repeated ten times, varying the angles between the robot's body and its legs. Subsequently, the robot advanced toward the chart, capturing images at different distances, and then returned to the starting point along the same path.

Table 8. Characteristics of the ventilation duct

Characteristics	Value
Profile	Circular
Length	1,83 m
Diameter	0,62 m
Surface material	Steel

3.4.2. Test of the effectiveness of the wheeled-legged locomotion system and analysis of mental workload using NASA TLX

The test of the wheeled-legged locomotion system and the operator's mental workload was conducted at the air base, specifically at the air intakes of the Mirage 2000. Due to the environmental conditions, there were limitations on both the test range and the number of trials performed. Details of the experimental environment are illustrated in Figure 14.

The evaluation included an analysis of displacement effectiveness and travel time in the sections previously identified in Figure 2: the two lateral air intakes and the central intersection. Following the FAP's POCHE maintenance protocol, the robot was initially positioned at the right intake, moved toward the intersection, and then returned through the left intake.

Eight tests were conducted with four trained operators. Subsequently, the NASA TLX methodology was applied to assess the mental workload perceived by the participants, taking into account factors such as physical and mental effort, perceived performance, frustration level, and the demands of the operational environment.

Figure 14. Ventilation duct of the Mirage aircraft

3.5. Results Analysis

This section presents the results obtained from the tests conducted with the robot equipped with the wheeled-legged locomotion system, as described previously.

3.5.1. Test of the turning effectiveness of the wheeled-legged system and camera performance

The turning effectiveness of the ALLQU robot and the performance of the integrated camera were evaluated. For the turning test, ten trials were conducted inside the ventilation duct, using different angles between the robot's body and its legs oriented toward its underside.

The results are presented in Table 9, detailing the robot's turning performance under the described conditions.

Table 9 shows that the ALLQU robot can perform turns effectively when the angle between the body and the legs exceeds 50°. However, it fails to complete a turn at angles below 45° due to the physical constraints of the test environment. The turning capability is directly influenced by the available space and becomes increasingly limited in narrower areas.

Table 9. Results of the robot turning test

Angle between legs and body	Turn achieved?
70°	Yes
65°	Yes
60°	Yes
55°	Yes
50°	Yes
45°	No
40°	No
35°	No
30°	No
25°	No

Figure 15 shows the test conducted using the Snellen chart and an example of an image captured by the robot's camera. The visual acuity results from this evaluation are summarized in Table 10.

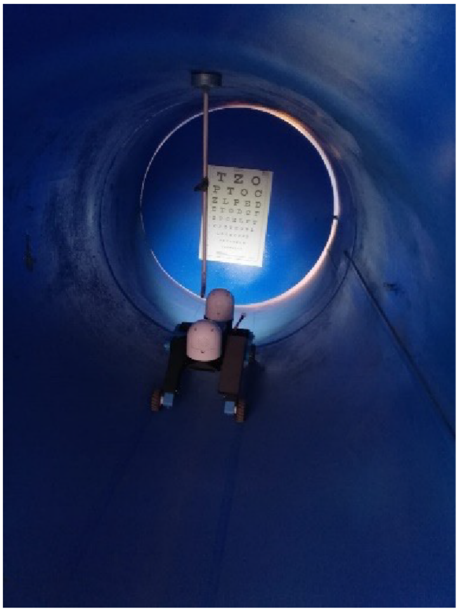

Figure 15. ALLQU robot in the ventilation duct, performing vision tests using a SNELLEN chart.

The visual acuity achieved by the robot's camera varied depending on the light source, distance, and use of zoom. With LED lighting and at a distance of 0.4 m, an acuity of 20/12.5 was achieved, both with and without zoom. At 1.5m , the acuity was 20/20 without zoom, improving to 20/16 when zoom was activated, demonstrating its effectiveness at greater distances.

Under infrared lighting at 0.4 m, the visual acuity was likewise 20/12.5 in both cases. At 1.5 m without zoom, a value of 20/16 was recorded, which remained unchanged when zoom was applied.

These results indicate that the robot's vision system performs reliably at short distances, while the use of zoom significantly enhances visual accuracy at longer ranges. Overall, the system demonstrates robust adaptability to varying lighting conditions and environments.

Table 10. Resultados de prueba de giro del robot

Light source type	Distance	Zoom	Visual acuity	Last letter
LED	0,4 m	No	20/12,5	P
		Yes	20/12,5	P
	1,5 m	No	20/20	P
		Yes	20/16	E
Infrared	0,4 m	No	20/12,5	P
		Yes	20/12,5	P
	1,5 m	No	20/16	E
		Yes	20/16	E

3.5.2. Test of the effectiveness of the wheeled-legged locomotion system and analysis of mental workload using NASA TLX

A test consisting of eight runs performed by four operators was conducted to evaluate the effectiveness of the wheeled-legged locomotion system within the air intakes of the Mirage 2000, following the POCHE protocol established by the FAP. Figure 16 illustrates the robot's positions during the runs.

The results of this locomotion test, including system effectiveness, distances traveled, and travel times, are presented in Table 11.

The operation of the robot by four operators in the air intakes of the Mirage 2000, as shown in Figure 17, was assessed using the NASA TLX methodology. The results include the individual scores, the pairwise comparison chart used to calculate the weighted score, and the final ranking of mental workload.

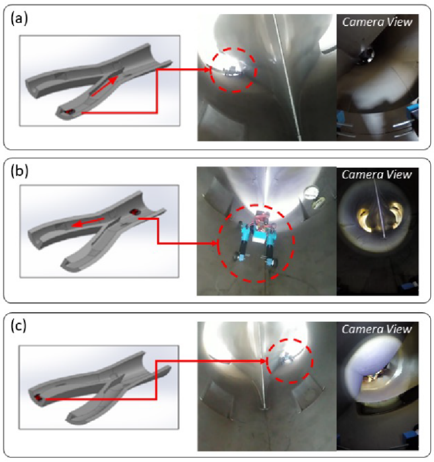

Figure 16. ALLQU robot in the air intake of a Mirage 2000 fighter aircraft, conducting locomotion and inspection tests: (a) Robot entering through the right air intake. (b) Robot at the intersection. (c) Robot exiting through the left air intake

Table 11. Locomotion test results in the air intake of a fighter aircraft

Air intake component	Distance Traveled	Time	Remarks
Right air intake	0,94 m	55,6 s	The circuit was completed in all 8 trials.
Engine intersection	3,36 m	36,4 s	
Left air intake	0,94 m	48,7 s	

Figure 17. Operators preparing the tests

These results are presented in Tables 12, 13, and 14, respectively.

Table 12. NASA TLX methodology scores

Dimension	Person 1	Person 2	Person 3	Person 4
Mental demand	12	20	10	20
Physical demand	4	20	5	17
Temporal demand	12	20	13	14
Performance	20	20	16	18
Effort	14	20	11	18
Frustration level	10	10	15	10

Table 12 shows that the perceived mental and physical workload varied among participants, with Person 2 reporting the highest values in most of the evaluated categories. Temporal demands showed moderate variation, while performance was consistently high, particularly for Persons 1 and 2, who achieved the maximum score of 20.

Effort and frustration levels also varied among operators; however, frustration remained generally low. Overall, these results indicate a high workload accompanied by a moderate emotional response from the participants.

Table 13 presents the weighting values assigned to each dimension of the NASA TLX index, reflecting the perceived importance of each factor contributing to workload. Temporal demand received the highest relative weight, particularly for Person 1 (weight 5) and Person 3 (weight 4), due to the times exceeding 30 seconds recorded in the critical sections of the route.

Mental demand also stood out, with Person 4 assigning it a weight of 4. Frustration had a greater impact on Persons 3 and 4, while physical demand was more significant for Persons 1 and 2.

Table 13. Pairwise comparison chart

Dimension	Person 1	Person 2	Person 3	Person 4
Mental demand	3	2	2	4
Physical demand	1	4	0	0
Temporal demand	5	4	4	1
Performance	4	1	2	3
Effort	2	1	3	4
Frustration level	0	3	4	3

Table 14 shows a high mental workload for most participants, except for Person 3, who recorded a medium level of 985 units. This difference is attributed to the robot's operation in the critical section, as illustrated in Figure 2(b). The tests conducted in both the ventilation duct and the Mirage 2000 validated the operational performance of the ALLQU robot and confirmed the user's perception of cognitive workload.

Table 14. Mental workload

Level	Person 1	Person 2	Person 3	Person 4
Low				
Medium			985	
High	1040	1350		1250

The robot demonstrated its capability to optimize inspection time, reducing both aircraft downtime and the need for highly specialized personnel. The standardized tests were conducted in two scenarios:

1. Turning and vision test, performed in a circular steel ventilation duct with a diameter of 0.62 m and a length of 1.83 m under low-light conditions. A Snellen chart was used to assess the image quality captured by the robot's camera.
2. Locomotion and mental workload test, carried out in the air intakes of an operational Mirage 2000 fighter aircraft located in a FAP hangar. This test evaluated the robot's performance in critical inlet geometries, such as sections with a height of 16 cm and an outlet width of 78 cm, under real field conditions defined by the POCHE protocol.

4. Conclusions

This work presented the development and implementation of the ALLQU robot, equipped with a wheeled-legged locomotion system, specifically designed to enhance preflight inspection of air intakes in fighter aircraft. The robot demonstrated its effectiveness in navigating and inspecting these confined structures, optimizing maintenance resources by reducing aircraft downtime and the need for highly specialized personnel, as validated through tests conducted in a controlled ventilation duct and within the air intakes of an operational Mirage 2000 fighter aircraft.

The main findings of this study are summarized as follows:

- The wheeled-legged locomotion system enabled stable and reliable movement within all three evaluated sections of the Mirage 2000, with average traversal times of 36.4 at the engine intersection and 52.15 s in the lateral air intakes.
- Turning capability in confined spaces was directly dependent on the available area. In a duct with a diameter of 0.62 m, turning was feasible only when the body-to-leg angle exceeded 50°.
- The visual system, comprising optical sensors with integrated LED and infrared lighting, delivered high visual acuity even under low-light conditions. The optical zoom significantly enhanced resolution in areas with limited visibility.

The NASA TLX analysis indicated a high mental workload, particularly in critical sections of the route where operators were required to control multiple elements of the robot simultaneously.

The experimental results confirm the operational feasibility of the ALLQU robot for air intake inspection in fighter aircraft; however, certain technical limitations were identified, including:

- Limited turning ability at angles below45°.
- Visual inspection limited to surface-level observation, with no subsurface detection.
- Limited operational autonomy due to current battery capacity.
- Structural robustness not yet validated under extreme environments (high temperatures, dust, or vibrations).
- High cognitive load on the operator when maneuvering in critical sections.

To address these limitations, future improvements should focus on developing more agile control algorithms, integrating non-destructive testing (NDT) sensors, extending energy autonomy, validating structural performance under diverse operational conditions, and designing a more intuitive user interface to reduce the operator's mental workload.

Beyond its operational efficiency, the ALLQU robot offers qualitative advantages over traditional methods. It reduces the risks associated with manual inspection in confined spaces and provides consistent, objective visual records that improve traceability and support long-term monitoring of potential structural anomalies.

Conflict of Interest

The authors declare that they have no conflict of interest regarding the development of this research. All tests were conducted directly on the developed robot and did not involve human subjects.

Funding

This work is part of the research project "Prototype of an inspection robot for fighter aircraft air intakes during preflight," funded by the Universidad Nacional de San Agustín de Arequipa under contract number PI-010-2023-UNSA.

Acknowledgments

The authors express their deepest gratitude to the Universidad Nacional de San Agustín de Arequipa for its invaluable support throughout this research. Its commitment and backing were essential to the project's development and success.

The authors also thank the Communications and Electronics Squadron and the Aircraft Maintenance Squadron of Air Group No. 4 of the Peruvian Air Force, whose support was crucial for conducting the necessary tests and advancing this research.

Contributor Roles

- **Mayki Mamani**: Methodology, writing – original draft.
- **Jhonathan Uchamaco**: Methodology, writing – original draft.
- **David Meneses**: Validation, visualization.
- **Yuri Silva**: Writing – review & editing, visualization.
- **Jorge Apaza**: Validation, visualization.

References

[1] V. Madonna, P. Giangrande, and M. Galea, "Electrical power generation in aircraft: Review, challenges, and opportunities," *IEEE Transactions on Transportation Electrification*, vol. 4, no. 3, pp. 646–659, Sep. 2018. [Online]. Available: http://doi.org/10.1109/TTE.2018.2834142

[2] A. V. Chatzi, "Safety management systems: an opportunity and a challenge for military aviation organisations," *Aircraft Engineering and Aerospace Technology*, vol. 91, no. 1, pp. 190–196, Jan. 2018. [Online]. Available: http://doi.org/10.1108/AEAT-05-2018-0146

[3] Y. D. Yasuda, F. A. Cappabianco, L. E. G. Martins, and J. A. Gripp, "Aircraft visual inspection: A systematic literature review," *Computers in Industry*, vol. 141, p. 103695, Oct. 2022. [Online]. Available: https://doi.org/10.1016/j.compind.2022.103695

[4] T. Chauhan, C. Goyal, D. Kumari, and A. K. Thakur, "A review on foreign object debris/damage (FOD) and its effects on aviation industry," *Materials Today: Proceedings*, vol. 33, pp. 4336–4339, 2020. [Online]. Available: https://doi.org/10.1016/j.matpr.2020.07.457

[5] K. K. R. Yadav, A. R. Paul, A. Jain, and F. Alam, "Effects of synthetic jets on swirl inflow in a variable-geometry twin air-intake," *Flow, Turbulence and Combustion*, vol. 111, no. 4, pp. 1193–1225, Sep. 2023. [Online]. Available: https://doi.org/10.1007/s10494-023-00481-8

[6] M. Maddox, *Human Factors Guide for Aviation Maintenance.* Washington, DC: Aviation Medicine, Federal Aviation Administration, U.S. Department of Transportation, 1996. [Online]. Available: https://upsalesiana.ec/ing34ar10r1

[7] M. Tsakalerou, D. Nurmaganbetov, and N. Beltenov, "Aircraft maintenance 4.0 in an era of disruptions," *Procedia Computer Science*, vol. 200, pp. 121–131, 2022. [Online]. Available: https://doi.org/10.1016/j.procs.2022.01.211

[8] D. Xie, M. Xu, and H. Dai, "Effects of damage parametric changes on the aeroelastic behaviors of a damaged panel," *Nonlinear Dynamics*, vol. 97, no. 2, pp. 1035–1050, Jun. 2019. [Online]. Available: https://doi.org/10.1007/s11071-019-05029-y

[9] S. Bowling, S. Kaewkuekool, M. Khasawneh, R. Desai, and K. Gramopadhye, "Confined space work in aircraft maintenance industry: Scope for improving safety and reducing errors," 05 2002. [Online]. Available: https://upsalesiana.ec/ing34ar10r9

[10] M. Verhoeff, W. Verhagen, and R. Curran, "Maximizing operational readiness in military aviation by optimizing flight and maintenance planning," *Transportation Research Procedia*, vol. 10, pp. 941–950, 2015. [Online]. Available: https://doi.org/10.1016/j.trpro.2015.09.048

[11] S. Fu and N. P. Avdelidis, "Prognostic and health management of critical aircraft systems and components: An overview," *Sensors*, vol. 23, no. 19, p. 8124, Sep. 2023. [Online]. Available: https://doi.org/10.3390/s23198124

[12] M. Siegel, P. Gunatilake, and G. Podnar, “Robotic assistants for aircraft inspectors,” *Industrial Robot: An International Journal*, vol. 25, no. 6, pp. 389–400, Dec. 1998. [Online]. Available: https://doi.org/10.1108/01439919810240234

[13] Y. Zhang, P. Li, J. Quan, L. Li, G. Zhang, and D. Zhou, “Progress, challenges, and prospects of soft robotics for space applications,” *Advanced Intelligent Systems*, vol. 5, no. 3, Jun. 2022. [Online]. Available: https://doi.org/10.1002/aisy.202200071

[14] A. H. Alami, A. Ghani Olabi, A. Alashkar, S. Alasad, H. Aljaghoub, H. Rezk, and M. A. Abdelkareem, “Additive manufacturing in the aerospace and automotive industries: Recent trends and role in achieving sustainable development goals,” *Ain Shams Engineering Journal*, vol. 14, no. 11, p. 102516, Nov. 2023. [Online]. Available: https://doi.org/10.1016/j.asej.2023.102516

[15] J. S. Bennett, B. E. Vyhnalek, H. Greenall, E. M. Bridge, F. Gotardo, S. Forstner, G. I. Harris, F. A. Miranda, and W. P. Bowen, “Precision magnetometers for aerospace applications: A review,” *Sensors*, vol. 21, no. 16, p. 5568, Aug. 2021. [Online]. Available: https://doi.org/10.3390/s21165568

[16] D. A. Rodríguez, C. Lozano Tafur, P. F. Melo Daza, J. A. Villalba Vidales, and J. C. Daza Rincón, “Inspection of aircrafts and airports using UAS: A review,” *Results in Engineering*, vol. 22, p. 102330, Jun. 2024. [Online]. Available: https://doi.org/10.1016/j.rineng.2024.102330

[17] M. Kaur Dhoot, I.-S. Fan, and Z. Skaf, “Review of robotic systems for aircraft inspection,” *SSRN Electronic Journal*, 2020. [Online]. Available: https://dx.doi.org/10.2139/ssrn.3718054

[18] J. Shang, T. Sattar, S. Chen, and B. Bridge, “Design of a climbing robot for inspecting aircraft wings and fuselage,” *Industrial Robot: An International Journal*, vol. 34, no. 6, pp. 495–502, Oct. 2007. [Online]. Available: http://dx.doi.org/10.1108/01439910710832093

[19] M. Fujita, S. Ikeda, T. Fujimoto, T. Shimizu, S. Ikemoto, and T. Miyamoto, “Development of universal vacuum gripper for wall-climbing robot,” *Advanced Robotics*, vol. 32, no. 6, pp. 283–296, Mar. 2018. [Online]. Available: https://doi.org/10.1080/01691864.2018.1447238

[20] Y. L. Silva Vidal, E. D. Supo Colquehuanca, D. F. Meneses Huanca, E. J. Valdeiglesias Flores, F. J. Uchamaco Noa, J. A. Guevara Mamani, J. L. Apaza Gutierrez, and G. W. Galdos Alvarez, “Analysis of robotics applied to mobility in the air intakes of a fighter aircraft,” *International Journal of Mechanical Engineering and Robotics Research*, vol. 11, no. 12, pp. 937–947, Dec. 2022, [En línea]. [Online]. Available: https://upsalesiana.ec/ing34ar10r20

[21] D. M. Helevera, *Visual examinations and manual checks to determine the condition of an aircraft and its component.* National Aviation University, Ukraine, 2022. [Online]. Available: https://upsalesiana.ec/ing34ar10r21

[22] S. Kumar Thukaram, *Robot based 3D welding for jet engine blade repair and rapid prototyping of small components.* University of Manitoba, 2010. [Online]. Available: https://upsalesiana.ec/ing34ar10r22

[23] R. M. Groves, *3.12 Inspection and Monitoring of Composite Aircraft Structures.* Elsevier, 2018, pp. 300–311. [Online]. Available: https://doi.org/10.1016/B978-0-12-803581-8.10340-6

[24] M. Bjelonic, V. Klemm, J. Lee, and M. Hutter, *A Survey of Wheeled-Legged Robots.* Springer International Publishing, Aug. 2022, pp. 83–94. [Online]. Available: https://doi.org/10.1007/978-3-031-15226-9_11

[25] T. Klamt, D. Rodríguez, M. Schwarz, C. Lenz, D. Pavlichenko, D. Droeschel, and S. Behnke, “Supervised autonomous locomotion and manipulation for disaster response with a centaur-like robot,” in *2018 IEEE/RSJ International Conference on Intelligent Robots and Systems (IROS).* IEEE, Oct. 2018, pp. 1–8. [Online]. Available: https://doi.org/10.1109/IROS.2018.8594509

[26] G. Endo and S. Hirose, “Study on roller-walker – Improvement of locomotive efficiency of quadruped robots by passive wheels,” *Advanced Robotics*, vol. 26, no. 8–9, pp. 969–988, May 2012. [Online]. Available: https://doi.org/10.1163/156855312X633066

[27] J. Li, Y. Liu, Z. Yu, Y. Guan, Y. Zhao, Z. Zhuang, and T. Sun, “Design, analysis, and experiment of a wheel-legged mobile robot,” *Applied Sciences*, vol. 13, no. 17, p. 9936, Sep. 2023. [Online]. Available: https://doi.org/10.3390/app13179936

[28] J. Niu, H. Wang, Z. Jiang, L. Chen, J. Zhang, Y. Feng, and S. Guo, “Kinematic analysis of a serial-parallel hybrid mechanism and its application to a wheel-legged robot,” *IEEE Access*, vol. 8, pp. 111 931–111 944, 2020. [Online]. Available: https://doi.org/10.1109/ACCESS.2020.3001653

[29] F. Raza, W. Zhu, and M. Hayashibe, "Balance stability augmentation for wheel-legged biped robot through arm acceleration control," *IEEE Access*, vol. 9, pp. 54 022–54 031, 2021. [Online]. Available: https://doi.org/10.1109/ACCESS.2021.3071055

[30] Y. Xin, H. Chai, Y. Li, X. Rong, B. Li, and Y. Li, "Speed and acceleration control for a two wheel-leg robot based on distributed dynamic model and whole-body control," *IEEE Access*, vol. 7, pp. 180 630–180 639, 2019. [Online]. Available: https://doi.org/10.1109/ACCESS.2019.2959333

[31] V. S. Medeiros, E. Jelavic, M. Bjelonic, R. Siegwart, M. A. Meggiolaro, and M. Hutter, "Trajectory optimization for wheeled-legged quadrupedal robots driving in challenging terrain," *IEEE Robotics and Automation Letters*, vol. 5, no. 3, pp. 4172–4179, Jul. 2020. [Online]. Available: https://doi.org/10.1109/LRA.2020.2990720

[32] H. Peng, J. Wang, S. Wang, W. Shen, D. Shi, and D. Liu, "Coordinated motion control for a wheel-leg robot with speed consensus strategy," *IEEE/ASME Transactions on Mechatronics*, pp. 1–1, 2020. [Online]. Available: https://doi.org/10.1109/TMECH.2020.2975083

GUIDELINES FOR PUBLICATION IN INGENIUS JOURNAL

1. General Information

INGENIUS is a scientific publication of the *Universidad Politécnica Salesiana* of Ecuador, published since January 2007, with a fixed biannual periodicity, specialized in Mechanical Engineering, Electrical Engineering, Electronics, Computer Science and its integration in what is now known as Mechatronics; these lines of action strengthen areas such as automation, control, robotics, among others..

It is a scientific journal, which uses the peer-review system, under double-blind review methodology, according to the publication standards of the Institute of Electrical and Electronics Engineers (IEEE). Compliance with this system allows authors to guarantee an objective, impartial and transparent review process, which facilitates the publication of their inclusion in reference databases, repositories and international indexing.

INGENIUS is indexed in the directory and selective catalog of the Regional Online Information System for Scientific Journals of Latin America, the Caribbean, Spain and Portugal (Latindex), in the Directory of Journals of Open Access DOAJ, In the Information Matrix for the Analysis of Journals, MIAR, In the Ibero-American Network of Innovation and Scientific Knowledge, REDIB and in repositories, libraries and specialized catalogs of Latin America.

The journal is published in a double version: printed (ISSN: 1390-650X) and digital (e-ISSN: 1390-860X), in Spanish, each work being identified with a DOI (Digital Object Identifier System. The articles sent to INGENIUS magazine must comply with the following criteria:

2. Scope and policy

2.1. Theme

Original contributions in Mechanical Engineering, Electrical and Electronic Engineering, Computer Science and its integration in what is now known as Mechatronics, as well as related areas: Automation, Control, Domotics, Robotics in their different fields of action and all those related disciplines with the same central theme.

All the work carried out by national or foreign researchers may be published once they meet the required scientific quality criteria.

2.2. Contributions

INGENIUS Journal preferably publishes articles related to empirical research, and also reports of technological development, proposals for models and innovations, products for the elaboration of graduate and postgraduate thesis that contribute to the field of science and technology, as well as select revisions of literature. (state-of-the-art).

- **Research:** 5,000 to 6,500 words of text, including title, abstracts, descriptors, charts and references.
- **Reports:** 5,000 to 6,500 words of text, including title, abstracts, charts and references.
- **Reviews:** 6,000 to 7,000 words of text, including charts and references. Current, selective and justified references, would be specially valued from among 40 works

The INGENIUS Journal publishes original and unpublished works written in Spanish and English, they may not have been published through any printed or electronic media, nor be in the process of arbitration or publication.

Every article will be subjected to a rigorous arbitration process; the evaluation of the article will be made according to criteria of originality, relevance, relevance, contributions, scientific rigor and compliance with established editorial guidelines.

Being an arbitrated publication, the Editorial Board approves its publication based on the concept of specialized pairs. The reception of a document does not imply commitment of publication.

It is essential to present a letter of presentation and grant of rights which can be downloaded from: <
urlhttps://goo.gl/ZNkMRD>.

Contributions must be exclusively sent and through the OJS (Open Journal System) <`https://goo.gl/JF7dWT`>. In which all authors must previously register as a user. For any consultation of the procedure you should contact:

<revistaingenius@ups.edu.ec>,
<jcalle@ups.edu.ec> ó
<mquinde@ups.edu.ec>.

To promote diversity in publications, the author(s) may not publish more than one (1) article per issue, nor in consecutive issues. In order for the author(s) to submit their research again to Ingenius, a minimum of 3 published issues must have elapsed.

3. Presentation and structure of the manuscripts

For those works that are empirical investigations, the manuscripts will follow the IMRDC structure (Introduction, Materials and Methods, Results and Discussion and Conclusions), being optional the Notes and Supports. Those papers that, on the contrary, deal with reports, studies, proposals and reviews may be more flexible in their epigraphs, particularly in material and methods, analysis, results, discussion and conclusions. In all typologies of works, references are mandatory.

Articles may be written on Microsoft Word (.doc or .docx) or LaTeX(.tex). The template to be used can be downloaded from the journal's website, a, <`https://goo.gl/gtCg6m`>, while for LaTeX in <`https://goo.gl/hrHzzQ`>, it is necessary that the file be anonymised in Properties of File, so that the author(s) ID is not displayed.

Figures, Graphs and/or Illustrations, as well as Charts shall be numbered sequentially including an explanatory description for each. The equations included in the article must also be numbered; the figures, charts and equations must be cited in the text.

Use space after point, commas and question marks.

Use "enter" at the end of each paragraph and title heading. Do not use .^{en}ter.^{a}nywhere else, let the word processor program automatically break the lines.

Do not center headings or subheadings as they should be aligned to the left.

Charts must be created in the same program used for the document body, but must be stored in a separate file. Use tabs, not spaces, to create columns. Remember that the final size of printed pages will be 21 x 28 cm, so the tables must be designed to fit the final print space.

3.1. Structure of the manuscripts

3.1.1. Presentation and cover letter

1. **Título (español) / Title (inglés):** Concise but informative, in Spanish on the front line and in English on the second, when the article is written in Spanish and vice versa if it is written in English.

2. **Authors and affiliations:** Full name and surname of each author, organized by order of priority and their institutional affiliation with reference to the end of the first sheet, where it must include: Dependency to which belongs within the institution, Institution to which he/she belongs, country, ORCID. A maximum of 5 authors will be accepted, although there may be exceptions justified by the complexity and extent of the topic.
3. **Abstract (Spanish) / Abstract (English):** It will have a maximum extension of 230 words, first in Spanish and then in English. : 1) Justification of the topic; 2) Objectives; 3) Methodology and sample; 4) Main results; 5) Main conclusions.
4. **Keywords (Spanish) / Keywords (English):** 6 descriptors must be presented for each language version directly related to the subject of the work. The use of the key words set out in UNESCO's Thesaurus will be positively valued.
5. **Presentation (Cover Letter):** A statement that the manuscript is an original contribution, not submission or evaluation process in another journal, with the confirmation of the signatory authors, acceptance (if applicable) of formal changes in the manuscript according to the guidelines and partial assignment of rights to the publisher, according to the format established in: <`https://goo.gl/ZNkMRD`>

3.1.2. Manuscript

1. **Título (español) / Title (inglés):** Concise but informative, in Spanish on the front line and in English on the second, when the article is written in Spanish and vice versa if it is written in English.
2. **Authors and affiliations:** Full name and surname of each author, organized by order of priority and their institutional affiliation with reference to the end of the first sheet, where it must include: Dependency to which belongs within the institution, Institution to which he/she belongs, country, ORCID. A maximum of 5 authors will be accepted, although there may be exceptions justified by the complexity and extent of the topic.
3. **Abstract (Spanish) / Abstract (English):** It will have a maximum extension of 230 words, first in Spanish and then in English. : 1) Justification of the topic; 2) Objectives; 3) Methodology and sample; 4) Main results; 5) Main conclusions.
4. **Keywords (Spanish) / Keywords (English):** 6 descriptors must be presented for each language version directly related to the subject of the work. The use of the key words set out in UNESCO's Thesaurus will be positively valued.
5. **Introduction:** It should include the problem statement, context of the problem, justification, rationale and purpose of the study, using bibliographical citations, as well as the most significant and current literature on the topic at national and international level.
6. **Material and methods:** It must be written so that the reader can easily understand the development of the research. If applicable, it will describe the methodology, the sample and the form of sampling, as well as the type of statistical analysis used. If it is an original methodology, it is necessary to explain the reasons that led to its use and to describe its possible limitations.
7. **Analysis and results:** It will try to highlight the most important observations, describing, without making value judgments, the material and methods used. They will appear in a logical sequence

in the text and the essential charts and figures avoiding the duplication of data.

8. **Discussion and Conclusions:** It will summarize the most important findings, relating the observations themselves to relevant studies, indicating contributions and limitations, without adding data already mentioned in other sections. It should also include deductions and lines for future research.
9. **Supports and acknowledgments (optional):** The Council Science Editors recommends the author (s) to specify the source of funding for the research. Priority will be given to projects supported by national and international competitive projects.
10. **The notes (optional):** will go, only if necessary, at the end of the article (before the references). They must be manually annotated, since the system of footnotes or the end of Word is not recognized by the layout systems. The numbers of notes are placed in superscript, both in the text and in the final note. The numbers of notes are placed in superscript, both in the text and in the final note. No notes are allowed that collect simple bibliographic citations (without comments), as these should go in the references.
11. **References:** Bibliographical citations should be reviewed in the form of references to the text. Under no circumstances should references mentioned in the text not be included. Their number should be sufficient to contextualize the theoretical framework with current and important criteria. They will be presented sequentially in order of appearance, as appropriate following the format of the IEEE.

3.2. Guidelines for Bibliographical references

Journal articles:

[1] J. Riess, J. J. Abbas, "Adaptive control of cyclic movements as muscles fatigue using functional neuromuscular stimulation". IEEE Trans. Neural Syst. Rehabil. Eng vol. 9, pp.326–330, 2001. [Onine]. Available: https://doi.org/10.1109/7333.948462

Books:

[1] G. O. Young, "Synthetic structure of industrial plastics" in Plastics, 2nd ed., vol. 3, J. Peters, Ed. New York: McGraw–Hill, 1964, pp. 15–64.

Technical reports:

[1] M. A. Brusberg and E. N. Clark, "Installation, operation, and data evaluation of an oblique–incidence ionosphere sounder system," in "Radio Propagation Characteristics of the Washington–Honolulu Path," Stanford Res. Inst., Stanford, CA, Contract NOBSR–87615, Final Rep., Feb. 1995, vol. 1

Articles presented in confeences (unpubished):

[1] Vázquez, Rolando, Presentación curso "Realidad Virtual". National Instruments. Colombia, 2009.

Articles of memories of Conferences (Published):

[1] L. I. Ruiz, A. García, J. García, G. Taboada. "Criterios para la optimización de sistemas eléctricos en refinerías de la industria petrolera: influencia y análisis en el equipo eléctrico," IEEE CONCAPAN XXVIII, Guatemala 2008.

Thesis:

[1] L.M. Moreno, "Computación paralela y entornos heterogéneos," Tesis doctoral, Dep. Estadística, Investigación Operativa y Computación, Universidad de La Laguna, La Laguna, 2005.

Guidelines:

[1] IEEE Guide for Application of Power Apparatus Bushings, IEEE Standard C57.19.100–1995, Aug. 1995.

Patents:

[1] J. P. Wilkinson, “Nonlinear resonant circuit devices,” U.S. Patent 3 624 125, July 16, 1990.

Manuals:

[1] Motorola Semiconductor Data Manual, Motorola Semiconductor Products Inc., Phoenix, AZ, 1989.

Internet resources:

[1] E. H. Miller, “A note on reflector arrays” [Online]. Available. https://goo.gl/4cJkCF

3.3. Epigraphs, Figures and Charts

The epigraphs of the body of the article will be numbered in Arabic. They should go without a full box of capital letters, neither underlined nor bold. The numbering must be a maximum of three levels: 1. / 1.1. / 1.1.1. At the end of each numbered epigraph will be given an enter to continue with the corresponding paragraph.

The charts must be included in the text according to order of appearance, numbered in Arabic and subtitled with the description of the content, the subtitle should go at the top of the table justified to the left.

Figures can be linear drawings, maps or black and white halftone or color photographs in 300 dpi resolution. Do not combine photographs and line drawings in the same figure.

Design the figures so that they fit eventually to the final size of the journal 21 x 28 cm. Make sure inscriptions or details, as well as lines, are of appropriate size and thickness so that they are not illegible when they are reduced to their final size (numbers, letters and symbols must be reduced to at least 2.5 mm in height After the illustrations have been reduced to fit the printed page). Ideally, the linear illustrations should be prepared at about a quarter of their final publication size.

Different elements in the same figure should be spelled a, b, c, etc.

Photographs should be recorded with high contrast and high resolution. Remember that photographs frequently lose contrast in the printing process. Line drawings and maps should be prepared in black.

The text of the figures and maps must be written in easily legible letters.

If the figures have been previously used, it is the responsibility of the author to obtain the corresponding permission to avoid subsequent problems related to copyright.

Each figure must be submitted in a separate file, either as bitmap (.jpg, .bmp, .gif, or .png) or as vector graphics (.ps, .eps, .pdf).

4. Submission process

The manuscript must be sent through the OJS system of the journal, <`https://goo.gl/JF7dWT`>,the manuscript should be uploaded as an original file in .pdf without author data and anonymized according to the above; In complementary files the complete manuscript must be loaded in .doc or .docx (Word file), that is to say with the data of the author (s) and its institutional ascription; Also the numbered figures should be uploaded in independent files according to the corresponding in the manuscript (as bitmap .jpg, .bmp, .gif, or .png or as vector graphics .ps, .eps, .pdf). It is also obligatory to upload the cover letter and grant of rights as an additional file.

All authors must enter the required information on the OJS platform and only one of the authors will be responsible for correspondence.

Once the contribution has been sent the system will automatically send the author for correspondence a confirmation email of receipt of the contribution.

5. Editorial process

Once the manuscript has been received in OJS, a first check by the editorial team of the following points:

- The topic is in accordance with the criteria of the journal.
- Must have the IMRDC structure.
- Must be in the Ingenius format.
- Must use the IEEE citation format.
- All references should be cited in the text of the manuscript as well as charts, figures and equations.
- The manuscript is original; for this, software is used to determine plagiarism.

The assessment described above can take up to 4 weeks.

If any of the above is not complete or there is inconsistency, an email will be sent to the author to make the requested corrections.

The author will make the corrections and resend the contribution through an email in response to the notification and will also upload the corrected manuscript into OJS supplementary files.

The editorial team will verify that the requested corrections have been incorporated, if it complies, the manuscript will start the second part of the process that may be followed by the author through OJS, otherwise the author will be notified and the manuscript will be archived.

The second phase of the process consists of the evaluation under the methodology of double-blind review, which includes national and foreign experts considering the following steps:

- The editor assigns two or more reviewers for the article.
- After reviewing the article, the reviewers will submit the evaluation report with one of the following results.
  - Publishable
  - Publishable with suggested changes
  - Publishable with mandatory changes
  - Non publishable
- The editor once received the evaluation by the reviewers will analyze the results and determine if the article is accepted or denied.
- If the article is accepted, the author will be notified to make corrections if required and the corresponding editorial process will be continued.
- If the article is denied, the author will be notified and the manuscript will be archived.
- In the two previous cases the result of the evaluation of the reviewers and their respective recommendations will be sent.

The second phase of the process lasts at least 4 weeks, after which they will be notified to the author giving instructions to continue with the process.

6. Publication

The Ingenius Journal publishes two issues per year, on January 1st and July 1st, so it is important to consider the dates for sending the articles and their corresponding publication. Articles received until October will be considered for the January publication and those received until April for the July publication.

7. Information on the Use of Artificial Intelligence

Should artificial intelligence be used at any stage of the research presented in the article, authors are required to clearly highlight this in the cover letter associated with the article, specifying the section or sections where artificial intelligence has been used. The purpose of this requirement is to inform readers about the sections where this technology has been employed, providing greater transparency and understanding of its application in the presented research.

INGENUS, Revista de Ciencia y Tecnologia, recognizes the importance of maintaining high ethical standards in scientific research, particularly in the use of artificial intelligence (AI).

The decision to accept a publication that has utilized artificial intelligence rests at the discretion of the editorial team.

UNIVERSIDAD POLITÉCNICA SALESIANA DEL ECUADOR
Juan Cárdenas Tapia, sdb,
Rector

Turuhuayco 3-69 y Calle Vieja
Postal code 2074
Cuenca, Ecuador
Teléfono: (+593 7) 205 00 00
Fax: (+593 7) 408 89 58
Email: srector@ups.edu.ec

Exchange

Exchange with other periodicals is accepted.

Address:
Secretaría Técnica de Comunicación
Universidad Politécnica Salesiana
Turuhuayco 3-69 y Calle Vieja
Postal code 2074
Cuenca, Ecuador
Phone: (+593 7) 205 00 00 Ext. 1182
Fax: (+593 7) 408 89 58
Email: rpublicas@ups.edu.ec
www.ups.edu.ec
Cuenca – Ecuador

INGENIUS, Journal Science of Technology,
Issue 34
july/december 2025
John Calle Siguencia, Editor in chief
revistaingenius@ups.edu.ec

Printed

Centro Gráfico Salesiano: Antonio Vega Muñoz 10-68 y General Torres.
Phone: (+593 7) 283 17 45
Cuenca – Ecuador
Email: centrograficosalesiano@lns.com.ec

OTHER PERIODIC PUBLICATIONS OF THE UNIVERSITY

UNIVERSITAS, Journal of Social and Human Sciences.

LA GRANJA, Journal of the Sciences.

ALTERIDAD, Journal of Education.

RETOS,Journal of Administration Sciences and Economics.

UTOPÍA, University Youth Ministry Magazine.

SOPHIA, Collection of Philosophy of Education.

ABYA YALA
UNIVERSIDAD POLITÉCNICA SALESIANA

ECUADOR
SALESIANOS DON BOSCO